DISS. ETH NO. 30134

Unraveling the Mechano-Molecular Mechanism of Aging:
Insights from CRISPR/Cas9 Cell Reporter & Prematurely
Aging PolgA Mice on Bone Mechanoregulation

A thesis submitted to attain the degree of

DOCTOR OF SCIENCES
(Dr. sc. ETH Zurich)

presented by

DILARA YILMAZ

M.Sc. in Regenerative Biology and Medicine, TU Dresden

born on *07.07.1990*

accepted on the recommendation of

Prof. Dr. Ralph Müller, examiner
Prof. Dr. Michelle McDonald, co-examiner
Dr. Neashan Mathavan, co-examiner

2024

"Not all those who wander are lost." J. R. R. Tolkien

Table of contents

Acknowledgments

Where to begin? This thesis, a labor of love and caffeine, has finally crossed the finish line. The work presented here would not have been possible without the support of several people, to whom I owe my sincere thanks.

First and foremost, I would like to thank Prof. Dr. Ralph Müller for the opportunity to work in the Laboratory of Bone Biomechanics (LBB). His drive, enthusiasm, and particularly his knack for consistently finding effective solutions have been truly inspiring. I deeply value his mentorship, encouragement, and guidance during my Ph.D. journey. The lessons I learned from him (including how to format long documents in Word) are not only for my Ph.D. but also for my future.

I would like to thank Dr. Michelle McDonald for being my co-examiner despite her demanding schedule and responsibilities. I am grateful to Dr. Pedro Souza for his unwavering support and guidance. Thanks to Peter Schwilch for his support with the loading machine and to Dr. Amit Singh for insightful scientific discussions. Special thanks to Dr. Friederike Schulte for her willingness to offer feedback on the sections of my thesis and to Dr. Rada Vukmirovic for her regular check-ins.

I must express my heartfelt thanks to my students: Lorena Gregorio, Jérome Schlatter, Thurga Pararajasingam, Sandra Zimmermann, Gaonhae (Gabby) Hwang, Yannick Fischer, Mirthe Kapmhuis, Gülşade Rabia Çakmak, Abhay Khosla for their hard work and valuable contributions to our research.

My gratitude extends to these current and former members of LBB who have contributed to this journey, each offering unique and invaluable support. To Dr. Elliott Goff, Dr. Ariane Scheuren, Dr. Duncan Tourolle né Betts, Dr. Graeme Paul, and Dr. Nicholas Ohs for their guidance and help. Particularly to Nicholas, for the fun times, including the delightful culinary experiences and enduring horror movie nights. Dr. Penny Atkins for being a beacon of support and kindness, always being there when needed. To Anke de Leeuw for the great adventures we shared and to Margherita Bernero for her willingness to read a section of my thesis. Dr. Daniele Boaretti for providing computational support and showing me the way of Italian. To Wanwan Qiu for her kindness and sweet gestures of feeding me with chocolate.

Summary

Aging is a complex biological process characterized by a gradual decline in physiological functions, leading to an increased susceptibility to diseases such as frailty, sarcopenia, and osteoporosis. This decline significantly impairs the quality of life in older adults. Skeletal integrity deterioration, associated with aging, is primarily due to changes in bone remodeling processes. These processes hinge on the delicate balance between bone-resorbing osteoclasts, bone-forming osteoblasts, and osteocytes–key mechanosensors in bone. Mechanoregulation, the response of bones to mechanical loads, diminishes with age, leading to a decreased ability to handle mechanical loading–a fundamental aspect of age-related osteoporosis. However, the complex molecular dynamics that govern adaptive responses of bone to mechanical loading, and how these responses vary with age and sex, are not well-understood. Therefore, elucidating the molecular mechanisms that regulate load-driven bone adaptation is crucial, not only for discovering targets to prevent and treat bone-related diseases but also for advancing our knowledge of musculoskeletal aging.

Hence, this thesis is presented to address these challenges and organized into three aims: 1) To elucidate the role of tartrate-resistant acid phosphatase (TRAP) in bone adaptation and mechanoregulation utilizing CRISPR/Cas9 mediated fluorescent reporter mice 2) To decipher hallmarks of aging including frailty phenotype and degeneration of bone and osteocytes in prematurely aged PolgA mice 3) To investigate spatially resolved age- and sex-specific differences in bone mechanomics and mechanoregulation in prematurely aged PolgA mice.

In the first aim, we investigated the role of TRAP and osteoclast dynamics in bone adaptation and mechanoregulation by using a novel CRISPR/Cas9-mediated reporter mouse model. These mice exhibited traits of TRAP deficiency, a result of the fusion protein (mCherry with TRAP). This unforeseen outcome provided a unique opportunity to track TRAP-deficient osteoclasts *in vivo* and *in vitro*, thus characterizing the role of TRAP in bone adaptation and mechanoregulation. TRAP is a critical regulator in osteoclast differentiation and bone resorption, thus understanding its function can aid in developing targeted therapies for osteoclast-related diseases. Our study revealed that TRAP-deficient mice responded to mechanical loading equivalently as the controls, and thus suggesting that TRAP is not a main regulator in bone remodeling.

Subsequent parts of the thesis focused on the prematurely aged PolgA mouse model to elucidate hallmarks of aging by characterizing the musculoskeletal aging phenotypes including frailty and changes in bone and osteocyte network. This study offers new insights into frailty in this mouse model since frailty is poorly investigated in prematurely aging mice despite being a critical hallmark of aging. Our study exhibited the prevalence of frailty manifest at around 40 weeks of age in these mice, which corresponds to those observed in aged mice (~20 months) and aged humans (~65 years old). Furthermore, this study elucidates the age- and sex-associated alterations in the bone and osteocyte lacuno-canalicular network (LCN). Our findings highlighted significant deterioration in bone quality and osteocyte morphology in aged PolgA mice, with greater changes observed in males.

Finally, this thesis delves into the age and sex impacts on bone adaptation and mechanoregulation in PolgA mice. Utilizing previously established *in vivo* mechanical loading combined with spatial transcriptomics analysis, our study unravels the spatially resolved gene expression changes associated with age- and sex-related responses to mechanical loading. Our findings elucidated that mechanical loading induced a strong bone-forming response in young, particularly female mice. Conversely, aged PolgA mice exhibited a reduced response to mechanical stimuli with a tendency towards adipogenic rather than osteogenic activity in both sexes, although males displayed earlier signs of physiological aging.

In summary, this thesis provides a comprehensive assessment of osteoclast dynamics, the hallmarks of aging within bone, and age- and sex-related differences in bone adaptation and mechanoregulation. It identifies the role of TRAP in bone adaptation, underscores the manifestation of frailty, and sheds light on the contributing factors to age-related osteoporosis by exhibiting degeneration of the osteocyte network and bone in prematurely aged PolgA mice. Furthermore, it elucidates the age- and sex-specific responses to mechanical stimuli while highlighting the spatial gene expression patterns in response to mechanical loading. This thesis advances our understanding of bone adaptation and mechanoregulation in terms of osteoclast dynamics and the interplay of aging and sex differences and offers insights into the development of the potential therapeutic strategies to mitigate bone-related diseases and age-related bone loss, and ultimately aiming to improve the quality of life for the older individual.

Zusammenfassung

Altern ist ein komplexer biologischer Prozess, der durch einen allmählichen Rückgang der physiologischen Funktionen gekennzeichnet ist und zu einer erhöhten Anfälligkeit für Krankheiten wie Gebrechlichkeit, Sarkopenie und Osteoporose führt. Dieser Rückgang beeinträchtigt die Lebensqualität älterer Menschen erheblich. Die altersbedingte Verschlechterung der Skelettintegrität ist in erster Linie auf Veränderungen der Knochenumbauprozesse zurückzuführen. Diese Prozesse hängen vom empfindlichen Gleichgewicht zwischen knochenresorbierenden Osteoklasten, knochenbildenden Osteoblasten und Osteozyten - den wichtigsten Mechanosensoren im Knochen - ab. Die Mechanoregulation, also die Reaktion des Knochens auf mechanische Belastungen, nimmt mit dem Alter ab, was zu einer verminderten Fähigkeit führt, mechanische Belastungen zu bewältigen - ein grundlegender Aspekt der altersbedingten Osteoporose. Die komplexe molekulare Dynamik, die die adaptive Reaktion des Knochens auf mechanische Belastung bestimmt, und die Art und Weise, wie diese Reaktion mit dem Alter und dem Geschlecht variiert, sind jedoch noch nicht gut verstanden. Daher ist die Aufklärung der molekularen Mechanismen, die die belastungsabhängige Knochenbildung regulieren, von entscheidender Bedeutung, nicht nur um Angriffspunkte für die Vorbeugung und Behandlung knochenbedingter Krankheiten zu finden, sondern auch um unser Wissen über die Alterung des Bewegungsapparats zu erweitern.

Die vorliegende Arbeit ist daher auf diese Herausforderungen ausgerichtet und in drei Ziele gegliedert: 1) Aufklärung der Rolle der tartrate-resistent acid phosphatase (TRAP) bei der Knochenanpassung und Mechanoregulation mit Hilfe von CRISPR/Cas9-vermittelten fluoreszierenden Reportermäusen 2) Entschlüsselung von Alterungsmerkmalen, einschliesslich des Phänotyps der Gebrechlichkeit und der Degeneration von Knochen und Osteozyten in vorzeitig gealterten PolgA-Mäusen 3) Untersuchung von räumlich aufgelösten alters- und geschlechtsspezifischen Unterschieden in der Knochenmechanik und Mechanoregulation in vorzeitig gealterten PolgA-Mäusen.

Im Rahmen des ersten Ziels untersuchten wir die Rolle von TRAP und der Osteoklasten-Dynamik bei der Knochenanpassung und Mechanoregulation mit Hilfe einer neuen CRISPR/Cas9-vermittelten Reportermaus. Diese Mäuse wiesen Merkmale eines TRAP-Mangels auf, was auf das Fusionsprotein (mCherry mit TRAP) zurückzuführen ist. Dieses unvorhergesehene Ergebnis bot eine einzigartige Gelegenheit, TRAP-defiziente Osteoklasten *in vivo* und *in vitro* zu verfolgen und so die Rolle von TRAP bei der Knochenanpassung und

Mechanoregulation zu charakterisieren. TRAP ist ein entscheidender Regulator bei der Osteoklasten-Differenzierung und der Knochenresorption, so dass das Verständnis seiner Funktion bei der Entwicklung gezielter Therapien für osteoklastenbedingte Krankheiten hilfreich sein kann. Unsere Studie zeigte, dass TRAP-defiziente Mäuse auf mechanische Belastung genauso reagierten wie die Kontrolltiere, was darauf hindeutet, dass TRAP kein Hauptregulator für den Knochenumbau ist.

Die nachfolgenden Teile der Arbeit konzentrierten sich auf das vorzeitig gealterte PolgA-Mausmodell, um die Kennzeichen des Alterns durch die Charakterisierung der muskuloskelettalen Alterungsphänotypen, einschliesslich der Gebrechlichkeit und der Veränderungen des Knochen- und Osteozytennetzwerks, zu erforschen. Diese Studie bietet neue Einblicke in die Gebrechlichkeit bei diesen Mäusen, da die Gebrechlichkeit bei vorzeitig alternden Mäusen kaum untersucht wurde, obwohl sie ein entscheidendes Merkmal des Alterns ist. Unsere Studie zeigte, dass sich die Gebrechlichkeit bei diesen Mäusen im Alter von etwa 40 Wochen manifestiert, was den bei älteren Mäusen (~20 Monate) und älteren Menschen (~65 Jahre) beobachteten Werten entspricht. Darüber hinaus werden in dieser Studie die alters- und geschlechtsspezifischen Veränderungen im lacuno-canicular network (LCN) der Knochen und Osteozyten aufgezeigt. Unsere Ergebnisse zeigen eine signifikante Verschlechterung der Knochenqualität und der Morphologie der Osteozyten bei gealterten PolgA-Mäusen, wobei die Veränderungen bei männlichen Tieren stärker ausgeprägt sind.

Schliesslich wird in dieser Arbeit der Einfluss von Alter und Geschlecht auf die Knochenanpassung und Mechanoregulation bei PolgA-Mäusen untersucht. Unter Verwendung der zuvor etablierten *in vivo* mechanischen Belastung in Kombination mit einer räumlichen Transkriptomanalyse enthüllt unsere Studie die räumlich aufgelösten Veränderungen der Genexpression, die mit alters- und geschlechtsspezifischen Reaktionen auf mechanische Belastung einhergehen. Unsere Ergebnisse zeigen, dass die mechanische Belastung bei jungen, insbesondere weiblichen Mäusen eine starke knochenbildende Reaktion hervorruft. Umgekehrt zeigten gealterte PolgA-Mäuse bei beiden Geschlechtern eine geringere Reaktion auf mechanische Stimuli mit einer Tendenz zu adipogener statt osteogener Aktivität, wobei Männchen frühere Anzeichen physiologischer Alterung zeigten.

Zusammenfassend lässt sich sagen, dass diese Arbeit eine umfassende Bewertung der Osteoklastendynamik, der Kennzeichen der Knochenalterung und der alters- und geschlechtsspezifischen Unterschiede in der Knochenanpassung und Mechanoregulation liefert. Sie identifiziert die Rolle von TRAP bei der Knochenanpassung, unterstreicht die

Manifestation von Gebrechlichkeit und beleuchtet die Faktoren, die zur altersbedingten Osteoporose beitragen, indem sie die Degeneration des Osteozytennetzwerks und des Knochens in vorzeitig gealterten PolgA-Mäusen zeigt. Darüber hinaus werden die alters- und geschlechtsspezifischen Reaktionen auf mechanische Stimuli aufgeklärt und die räumlichen Genexpressionsmuster als Reaktion auf mechanische Belastung aufgezeigt. Diese Arbeit verbessert unser Verständnis der Knochenanpassung und der Mechanoregulation im Hinblick auf die Osteoklastendynamik und das Zusammenspiel von Alterung und Geschlechtsunterschieden und bietet Einblicke in die Entwicklung potenzieller therapeutischer Strategien zur Abschwächung knochenbedingter Krankheiten und altersbedingten Knochenverlusts und zielt letztlich auf eine Verbesserung der Lebensqualität älterer Menschen ab.

Chapter 1

Introduction

1.1 Thesis motivation

Aging is an inherently complex process characterized by a progressive decline in physiological functions, with significant implications for the skeletal system [1]. This decline makes older adults more vulnerable to diseases such as sarcopenia, marked by a loss of muscle mass and strength, and osteoporosis, indicated by decreased bone mass and compromised structural integrity, which in turn escalates the risk of fractures [2-5]. These conditions are often interconnected and cumulatively lead to frailty–a syndrome characterized by a diminished physiological reserve and resilience to stressors, ultimately heightening the risk of adverse health outcomes [1, 6-10]. The age-related decline in skeletal integrity can be attributed to disruptions in bone remodeling which is a balance mediated by the critical interaction between bone-resorbing osteoclasts, bone-forming osteoblasts, and osteocytes–the key mechanosensors [11-13]. With advancing age, this delicate balance shifts in favor of bone resorption, resulting in decreased bone mass and strength, thereby increasing fracture risks, which are key contributors to the development of age-related osteoporosis.

While reduced use of the skeleton, a common consequence of aging, significantly contributes to age-related osteoporosis, mechanical loading is known to increase bone formation [13-17]. Mechanoregulation is the ability of bones to adapt their structure in response to mechanical loading, playing a key regulatory role in regulating bone mass and strength [16, 18-28]. Enhancing our knowledge of the molecular processes behind load-induced bone formation is essential for discovering new treatment strategies for bone diseases and gaining insight into musculoskeletal aging.

In this regard, *in vivo* mouse models have become indispensable tools to investigate the molecular mechanisms governing bone loss and mechanoregulation. Their genetic similarities to humans, coupled with the relative ease of genome manipulation make them particularly useful for bone research [5, 29-31]. Specifically, models generated through the CRISPR/Cas9 technology could be pivotal in advancing our ability to visualize and track bone cells during bone adaptation and mechanoregulation processes. Moreover, *in vivo* micro-computed tomography (micro-CT) provides comprehensive evaluations of structural changes in the bone under mechanical loading [19, 32, 33]. When combined with spatial transcriptomics analysis, these techniques enable detailed mapping of gene expression, offering profound insights into the tissue-specific responses of bone to mechanical loading and the underlying molecular mechanisms [34, 35].

Among the *in vivo* mouse models, those that display premature aging are particularly valuable as they allow for studying the hallmarks of aging within a shorter time frame compared to naturally aging mice. Particularly, $Polg^{AD257A/D257A}$ mouse model–referred as PolgA characterized by premature aging phenotypes, presents a unique opportunity to investigate aging and its effects on bone health. By 40 weeks of age, these mice exhibit various clinical signs of aging such as alopecia, kyphosis, osteosarcopenia, and osteoporosis–symptoms arising from a mutation in the proofreading activity of the DNA polymerase γ gene (PolgA) [36-38]. Despite these clear aging signs, including lower bone density and muscle mass, frail phenotype, and the full spectrum of musculoskeletal aging phenotypes in these mice remain underexplored. Thoroughly assessing the suitability of this model for mimicking age-related osteoporosis and frailty is critical for developing effective preventative therapies.

Hence, the goal of this thesis is to elucidate the mechano-molecular mechanism of bone adaptation by studying osteoclast dynamics using a CRISPR/Cas9 mediated reporter mouse model with TRAP deficiency. Additionally, it seeks to characterize the hallmarks of aging in prematurely aged PolgA mice focusing on the frailty phenotype and age-related changes in bone and osteocytes. Moreover, this work aims to understand the age- and sex-specific spatial mechano-adaptive responses in these prematurely aged PolgA mice.

1.2 Specific aims

Aim 1: Elucidating the role of TRAP and osteoclast dynamics in bone mechano-adaptation utilizing CRISPR/Cas9 mediated fluorescent reporter mice.

Aim 2: Deciphering hallmarks of aging and degeneration of bone and osteocytes in prematurely aged PolgA mice.

Aim 3: Investigating spatially resolved age- and sex-specific alterations in bone mechanomics and mechanoregulation in prematurely aged PolgA mice.

1.3 Thesis outline

The thesis consists of six chapters. In addition to the current chapter outlining the motivation and specific aims, the content of the subsequent chapters is the following:

Chapter 2: Background

Chapter 2 provides a comprehensive background on musculoskeletal aging and associated conditions of frailty, osteoporosis, and sarcopenia. It particularly emphasizes the use of accelerated aging mouse models including SAMP, Ercc1$^{-/\Delta}$, Zmpste24$^{-/-}$, and PolgA mice, that exhibit musculoskeletal aging phenotypes associated with these conditions. This chapter discusses a detailed examination of these models offering valuable insight into the underlying mechanism of aging in musculoskeletal research along with their valid assessment methods.

Chapter 3: CRISPR/Cas9 Mediated Reporter Mice to Investigate Mechano-Molecular Dynamics in Bone Mechanoregulation

Chapter 3 focuses on elucidating the role of tartrate-resistant acid phosphatase (TRAP, Acp5) in bone remodeling and mechanoregulation. Utilizing CRISPR/Cas9 technology, the chapter describes the feasibility of identification and tracking of osteoclasts that are TRAP deficient *in vivo* and *in vitro* fluorescently, allowing for a comprehensive assessment of osteoclast activity under mechanically driven bone remodeling. The findings discussed in this chapter provides valuable insight into the role of TRAP activity in bone remodeling and mechanoregulation.

Chapter 4: Hallmarks of Aging of Bone and Bone Cells in Prematurely Aged PolgA Mice

Chapter 4 focuses on the hallmarks of aging of bone in PolgA mice, showcasing them as a robust model for studying age-related diseases. The chapter underscores the utility of the model in investigating frailty and age-related osteoporosis.

Section 4.1 describes the application of the human frailty phenotype approach to assess frailty characteristics in prematurely aged PolgA mice, revealing the sex-specific manifestation of frailty in these mice. The results outlined in this section enhance our understanding of the onset and prevalence of frailty in relation to sex, and thus, underlining the importance of PolgA mice for investigating aging and associated disorders.

Section 4.2 outlines the characterization of age-related osteoporosis through the investigation of age- and sex-related alterations in bone and the osteocyte lacuno-canalicular network (LCN) in prematurely aged PolgA mice. Moreover, the section introduces a novel approach for staining undecalcified fresh frozen bone sections, combined with quantitative *in silico* analysis to assess alterations in osteocyte LCN as a function of age and sex.

Findings in this chapter highlight the pivotal role of the PolgA mouse model in understanding the cellular mechanisms that contribute to age-related bone loss.

Chapter 5: Spatially Resolved Bone Mechanomics and Mechanoregulation in Prematurely Aged Mice

Chapter 5 evaluates the complex interplay of aging, bone adaptation, and mechanosensitivity in prematurely aging male and female PolgA mice. This chapter elaborates on the variation

in bone responses to mechanical loading across different ages and sexes. Additionally, it identifies the contribution of the specific gene alterations that correspond with age- and sex-related responses to mechanical loading in PolgA mice. These findings presented in this chapter underscore the value of the PolgA mouse model in studying the effects of aging and sex on bone adaptation and mechanosensitivity.

Chapter 6: Synthesis

This chapter provides a summary of the subjects covered in previous chapters of the thesis, highlights the key findings, the limitations of the presented work, and an outlook for future research.

References

1. Fulop, T., et al., Aging, frailty and age-related diseases. Biogerontology, 2010. 11(5): p. 547-63.

2. Walston, J.D., Sarcopenia in older adults. Curr Opin Rheumatol, 2012. 24(6): p. 623-7.

3. Demontiero, O., C. Vidal, and G. Duque, Aging and bone loss: new insights for the clinician. Ther Adv Musculoskelet Dis, 2012. 4(2): p. 61-76.

4. Milte, R. and M. Crotty, Musculoskeletal health, frailty and functional decline. Best Pract Res Clin Rheumatol, 2014. 28(3): p. 395-410.

5. Jilka, R.L., The relevance of mouse models for investigating age-related bone loss in humans. J Gerontol A Biol Sci Med Sci, 2013. 68(10): p. 1209-17.

6. Fried, L.P., et al., Frailty in older adults: evidence for a phenotype. J Gerontol A Biol Sci Med Sci, 2001. 56(3): p. M146-56.

7. Hirschfeld, H.P., R. Kinsella, and G. Duque, Osteosarcopenia: where bone, muscle, and fat collide. Osteoporos Int, 2017. 28(10): p. 2781-2790.

8. Greco, E.A., P. Pietschmann, and S. Migliaccio, Osteoporosis and Sarcopenia Increase Frailty Syndrome in the Elderly. Front Endocrinol (Lausanne), 2019. 10: p. 255.

9. Fried, L.P., Interventions for Human Frailty: Physical Activity as a Model. Cold Spring Harb Perspect Med, 2016. 6(6).

10. Fedarko, N.S., The biology of aging and frailty. Clin Geriatr Med, 2011. 27(1): p. 27-37.

11. Henriksen, K., et al., Local communication on and within bone controls bone remodeling. Bone, 2009. 44(6): p. 1026-33.

12. Hadjidakis, D.J. and Androulakis, II, Bone remodeling. Ann N Y Acad Sci, 2006. 1092: p. 385-96.

13. Fang, H., et al., The Mechanism of Bone Remodeling After Bone Aging. Clin Interv Aging, 2022. 17: p. 405-415.

14. Raisz, L.G. and G.A. Rodan, Pathogenesis of osteoporosis. Endocrinol Metab Clin North Am, 2003. 32(1): p. 15-24.

15. Khosla, S. and B.L. Riggs, Pathophysiology of age-related bone loss and osteoporosis. Endocrinol Metab Clin North Am, 2005. 34(4): p. 1015-30, xi.

16. Javaheri, B. and A.A. Pitsillides, Aging and Mechanoadaptive Responsiveness of Bone. Curr Osteoporos Rep, 2019. 17(6): p. 560-569.

17. Gogakos, A.I., et al., Bone signaling pathways and treatment of osteoporosis. Expert Rev Endocrinol Metab, 2009. 4(6): p. 639-650.

18. Schulte, F.A., et al., Local mechanical stimuli regulate bone formation and resorption in mice at the tissue level. PLoS One, 2013. 8(4): p. e62172.

19. Scheuren, A.C., et al., Mechano-Regulation of Trabecular Bone Adaptation Is Controlled by the Local in vivo Environment and Logarithmically Dependent on Loading Frequency. Front Bioeng Biotechnol, 2020. 8: p. 566346.

20. Nagaraja, M.P. and H. Jo, The Role of Mechanical Stimulation in Recovery of Bone Loss-High versus Low Magnitude and Frequency of Force. Life (Basel), 2014. 4(2): p. 117-30.

21. Lambers, F.M., et al., Mouse tail vertebrae adapt to cyclic mechanical loading by increasing bone formation rate and decreasing bone resorption rate as shown by time-lapsed in vivo imaging of dynamic bone morphometry. Bone, 2011. 49(6): p. 1340-50.

22. Klein-Nulend, J., R.G. Bacabac, and M.G. Mullender, Mechanobiology of bone tissue. Pathol Biol (Paris), 2005. 53(10): p. 576-80.

23. Goodship, A.E., T.J. Lawes, and C.T. Rubin, Low-magnitude high-frequency mechanical signals accelerate and augment endochondral bone repair: preliminary evidence of efficacy. J Orthop Res, 2009. 27(7): p. 922-30.

24. Gardinier, J.D., et al., Bone adaptation in response to treadmill exercise in young and adult mice. Bone Rep, 2018. 8: p. 29-37.

25. Duncan, R.L. and C.H. Turner, Mechanotransduction and the functional response of bone to mechanical strain. Calcif Tissue Int, 1995. 57(5): p. 344-58.

26. Turner, C.H., et al., Mechanobiology of the skeleton. Sci Signal, 2009. 2(68): p. pt3.

27. Oftadeh, R., et al., Biomechanics and mechanobiology of trabecular bone: a review. J Biomech Eng, 2015. 137(1): p. 0108021-01080215.

28. Mellon, S.J. and K.E. Tanner, Bone and its adaptation to mechanical loading: a review. International Materials Reviews, 2013. 57(5): p. 235-255.

29. Vandamme, T.F., Use of rodents as models of human diseases. J Pharm Bioallied Sci, 2014. 6(1): p. 2-9.

30. Rydell-Tormanen, K. and J.R. Johnson, The Applicability of Mouse Models to the Study of Human Disease. Methods Mol Biol, 2019. 1940: p. 3-22.

31. Liang, H., et al., Genetic mouse models of extended lifespan. Exp Gerontol, 2003. 38(11-12): p. 1353-64.

32. Schulte, F.A., et al., In vivo micro-computed tomography allows direct three-dimensional quantification of both bone formation and bone resorption parameters using time-lapsed imaging. Bone, 2011. 48(3): p. 433-42.

33. Scheuren, A.C., G.A. Kuhn, and R. Muller, Effects of long-term in vivo micro-CT imaging on hallmarks of osteopenia and frailty in aging mice. PLoS One, 2020. 15(9): p. e0239534.

34. D'Ercole, C., et al., Spatially resolved transcriptomics reveals innervation-responsive functional clusters in skeletal muscle. Cell Rep, 2022. 41(12): p. 111861.

35. Xiao, X., et al., Spatial transcriptomic interrogation of the murine bone marrow signaling landscape. Bone Res, 2023. 11(1): p. 59

36. Trifunovic, A., et al., Premature ageing in mice expressing defective mitochondrial DNA polymerase. Nature, 2004. 429(6990): p. 417-23.

37. Kujoth, G.C., C. Leeuwenburgh, and T.A. Prolla, Mitochondrial DNA mutations and apoptosis in mammalian aging. Cancer Res, 2006. 66(15): p. 7386-9.

38. Scheuren, A.C., et al., Hallmarks of frailty and osteosarcopenia in prematurely aged PolgA((D257A/D257A)) mice. J Cachexia Sarcopenia Muscle, 2020. 11(4): p. 1121-1140.

Chapter 2

Background

2.1 Mouse models of accelerated aging in musculoskeletal research for assessing frailty, sarcopenia, and osteoporosis - a review

Dilara Yılmaz[a], Neashan Mathavan[a], Esther Wehrle[a,b], Gisela A. Kuhn[a], Ralph Müller[a]

[a] Institute for Biomechanics, ETH Zurich, Zurich, Switzerland
[b] AO Research Institute Davos, Davos Platz, Switzerland

Abstract

Musculoskeletal aging encompasses the decline in bone and muscle function, leading to conditions such as frailty, osteoporosis, and sarcopenia. Unraveling the underlying molecular mechanisms and developing effective treatments are crucial for improving the quality of life for those affected. In this context, accelerated aging models offer valuable insights into these conditions by displaying the hallmarks of human aging. Herein, this review focuses on relevant mouse models of musculoskeletal aging with particular emphasis on frailty, osteoporosis, and sarcopenia. Among the discussed models, PolgA mice in particular exhibit hallmarks of musculoskeletal aging, presenting early-onset frailty, as well as reduced bone and muscle mass that closely resemble human musculoskeletal aging. Ultimately, findings from these models hold promise for advancing interventions targeted at age-related musculoskeletal disorders, effectively addressing the challenges posed by musculoskeletal aging and associated conditions in humans.

Keywords

Musculoskeletal aging, accelerated aging mouse models, frailty, osteoporosis, sarcopenia, PolgA

2.1.1. Introduction

Musculoskeletal aging denotes the age-associated alterations that manifest within the bones, muscles, tendons, ligaments, and joints [1]. This natural progression often gives rise to the conditions such as frailty, osteoporosis, and sarcopenia, all of which contribute to reduced physical capabilities and heightened susceptibility to stressors, ultimately increasing the likelihood of adverse health outcomes among older individuals.

The collective state of vulnerability and reduced resilience is commonly referred to as frailty, encompassing the interconnected challenges posed by the musculoskeletal aging [2]. Osteoporosis, on the one hand, a widespread ailment in older adults, is marked by decreased bone density and structural deterioration, significantly increasing the risk of fractures, especially in weight-bearing bones [3]. On the other hand, sarcopenia refers to the progressive loss of muscle mass and strength and further contributes to functional decline, reduced mobility, and an increased risk of falls and fractures [4]. Gaining a deeper understanding of the underlying mechanisms and discovering effective strategies to mitigate these musculoskeletal conditions is crucial for promoting healthy aging and improving the quality of life for older adults. In this regard, mouse models have emerged as valuable tools for investigating musculoskeletal aging, owing to their genetic similarity to humans and the ability to manipulate their genomes easily [5]. In particular, accelerated aging mouse models have received significant attention in recent years through genetically induced alterations that accelerate the aging process, thereby displaying hallmarks of musculoskeletal aging and associated conditions seen in humans [6]. On that note, this review focuses on musculoskeletal aging (Table 2.1) with particular emphasis on mouse models of accelerated aging that exhibit hallmarks of frailty, osteoporosis, and sarcopenia (Table 2.2).

2.1.2. Hallmarks of musculoskeletal aging

Frailty

Frailty is characterized by the loss of physiological function and reduced strength and endurance, leading to increased susceptibility to adverse health outcomes in aged humans [7]. It involves a decline of function in various physiological systems, leading to reduced resilience, diminished functional capacity, and increased risk of disability, morbidity, and mortality. The underlying causes of frailty are not fully understood, but possible mechanisms include

increased oxidative stress, DNA damage, cellular senescence, and mitochondrial dysfunction [7, 8]. Various evaluation methods have been developed to capture the multidimensional nature of frailty. One widely used approach is the frailty phenotype (FP) proposed by Fried et al. This approach considers people frail if they exhibit at least three out of the five characteristics: exhaustion, low physical activity, weakness, slow walking speed, and unintended weight loss [9]. Another method is the frailty index (FI), developed by Rockwood et al., which calculates the ratio of the number of health deficiencies present in an individual divided by the total number of deficiencies evaluated [10, 11]. Rockwood FI method evaluates overall health status, comorbidities, and functional impairments. It has been shown to be a valuable predictor of adverse health outcomes and rapid physical and cognitive deterioration in older adults. Higher FI score indicates greater susceptibility to functional decline, increased risk of falls, hospitalizations, and mortality. It serves as an indicator of the overall vulnerability and frailty of an individual. Building upon the FI, the Clinical Frailty Scale (CFS) is developed to provide a simplified and standardized measure of frailty correlated with the FI method [11]. The CFS categorizes individuals into one of nine categories ranging from "very fit" (level 1) to "terminally ill" (level 9), with each level representing a different degree of frailty. A score of 5 or above indicates that a patient is frail. The CFS offers a quick and practical way to estimate level of frailty of an individual, providing a common language for clinicians, researchers, and healthcare professionals to communicate and make informed decisions about care and interventions. The FI captures a more detailed and nuanced evaluation of health deficits, while the CFS provides a simplified scale to estimate the overall level of frailty. In contrast, FP method focuses on physical features rather than clinical symptoms and signs of diseases. Overall, both approaches demonstrate that frailty increases with age and is associated with morbidity and mortality in old humans and identify individuals who are at higher risk of adverse outcomes.

In preclinical research, efforts have been made to develop mouse models that mimic human frailty [12-14]. Liu et al. assessed the frailty of 27-28 months-old wild-type C57BL/6 male mice applying the human FP approach, evaluating grip strength (inverted grip test), walking speed (rotarod test), physical activity (voluntary wheel running), and endurance (grip strength + rotarod test) [13]. Similar to human criteria, mice were classified as non-frail, mildly or pre-frail, and frail based on the number of characteristics present. Valencia score is another method of assessing frailty in mice based on the human FP [15]. The same criteria were used to define frailty in mice, with weight loss being the only exception: Instead of the lowest 20% of the

mice displaying weight loss, a >5% body weight was used as a cut-off value for being frail [15]. Additionally, Whitehead et al. developed a simplified mouse frailty assessment based on the clinical human FI [16]. The integument (skin), vestibulocochlear/auditory system (hearing and balance), ocular/nasal systems, digestive/urogenital system, respiratory systems, body weight, body surface temperature, and signs of discomfort are 31 parameters assessed by this method [16]. A FI score was calculated for each parameter by assigning a value of 0 to indicate no deficiency, 0.5 to represent a mild deficiency, and 1 to indicate severe deficiency. To determine body weight and surface temperature changes, young adult mice were used as references. FI scoring allows for the quantification of the level of impairment or deficiency in each parameter, providing a comprehensive assessment of frailty in individuals. Thus, this approach showed a progressive increase in FI score on aging C57BL/6 mice (between 5 months and 28 months) [16]. Other groups have used this clinical mouse FI method by modifying the parameters, such as generating a 27-item FI [17], which has shown promise in assessing frailty in aging mice considering factors other than FP (e.g., physical activity). Overall, the two mouse frailty assessment approaches could contribute to developing effective interventions for frailty.

Osteoporosis

Age-related bone loss is a prevalent condition characterized by the gradual decline in bone mass and deterioration of bone tissue over time [18]. It is a natural part of the aging process and can contribute to the development of osteoporosis. Osteoporosis, conversely, is characterized by low bone mass and deterioration of bone tissue, resulting in increased bone fragility and a higher risk of fractures [19].

While age-related bone loss is a broader term that encompasses the natural decline in bone health with aging, osteoporosis refers to a more severe disorder where bone loss reaches a point where it significantly increases the risk of fractures, thereby impacting the quality of life of an individual. In the context of this review, the focus is specifically on age-related bone loss associated with osteoporosis, excluding specific aspects such as fracture risk assessment or postmenopausal osteoporosis. This allows for a more targeted examination of the gradual decline in bone mass and its implications without delving into the more severe manifestations of osteoporosis.

Moreover, age-related bone loss in humans is assoskiated with increased number of marrow adipocytes, which correlates with a decline in BMD. This is attributed to a shift in the

osteogenic differentiation where mesenchymal stem cells (MSCs) favor adipocytes over osteoblasts during aging [24]-[25]. Therefore, dysfunctional osteoblasts with reduced bone formation, rather than increased resorption, is suggested to be the primary mechanism underlying age-related bone loss [26]. One example of a pathway that promotes osteogenic differentiation is Wnt signaling. With age, the level of Wnt signaling declines, resulting in reduced bone formation [27]. Another factor contributing to age-related decreases in bone formation is the increased levels of sclerostin, a Wnt antagonist secreted by osteocytes [27]. Sclerostin inhibits the Wnt signaling pathway, which plays a crucial role in promoting osteogenic differentiation and bone formation. With age, the levels of sclerostin tend to rise and result in reduced bone formation. Additionally, osteocytes produce RANKL, a key mediator of osteoclastogenesis [28]. The increased presence of RANKL in aging individuals leads to an imbalance between bone formation and resorption, ultimately contributing to increased bone resorption and the development of osteoporosis. Thus, osteocytes play a direct role in bone formation events of osteoblasts with aging, thereby promoting osteoporosis. Importantly, as age progresses, the osteocyte lacuna-canalicular network (OLCN) undergoes deterioration characterized by reduced lacunar density, increased apoptosis, and the accumulation of microcracks [29]. These changes in the OLCN negatively impact the communication and signaling between osteocytes and other bone cells, impairing their ability to regulate bone remodeling effectively. Consequently, the compromised functionality of osteocytes hinders the normal bone formation process carried out by osteoblasts, leading to a net loss of bone density and strength. Thereby, the deteriorating OLCN and the associated dysregulation of osteocyte function contribute to the promotion of osteoporosis. Together, the intrinsic mechanisms of age-related osteoporosis in humans involve altered cellular signaling, increased bone marrow adiposity, and the role of osteocytes in bone formation events.

When comparing age-related bone loss between humans and mice, it is important to consider the similarities and differences. Humans typically experience gradual age-related bone loss, while mice often exhibit more rapid bone loss due to their shorter lifespan [5]. Human osteoporosis is influenced by various factors, including hormonal changes, genetics, lifestyle, and nutrition, while mouse models often focus on specific aspects, such as hormonal deficiencies or genetic modifications. Despite these differences, mouse models have proven valuable in understanding the pathophysiology of age-related bone loss. The C57BL/6 mouse, which is one of the most commonly used naturally aging models, exhibits a decline in BMD that affects both cancellous and cortical bone, reflecting changes observed in humans [5]. In

C57BL/6 mice, BMD starts to decline between 16 to 25 months before they reach their median age [5]. Similar age-associated bone loss has also been reported in other mouse strains. For instance, the outbred strains, such as CW1 mice, show a decline in peak bone mass at 12, 15, and 18 months of age, while inbred strains, such as C3H/HeJ and BALB/cByj mice, experience age-associated bone loss between 7 to 28 months of age [30]. In addition to the decline in BMD, C57BL/6 mice exhibit a bone phenotype that closely resembles osteoporotic humans, characterized by reduced bone mass and compromised quality. Specifically, with advanced aging, there is a notable impact on trabecular and cortical bones, as shown by significant decrease in trabecular bone volume fraction observed between 6 to 24 months of age [31]. Moreover, the osteogenic potential of bone marrow stromal cells (BMSCs) was reported to decrease with age in mice. In C57BL/6 mice, the number and differentiation capacity of these stem cells were found to be reduced by 18 months [32]. Similarly, age-related bone loss led to a decrease in the proliferation capacity of stem cells in BALB/c mice at 24 months [33]. Furthermore, RANKL expression increases with age in C57BL/6 mice, suggesting a similar mechanism of bone resorption as observed in humans [34]. Age-related bone loss affects OLCN in mice as well. In C57BL/6 mice, there is a significant decline in osteocyte density and dendriticity accompanied by reduced canaliculi and lacunae, indicating degeneration in the OLCN with aging [35]. These findings highlight the occurrence of age-related bone loss in various mouse strains due to the decreased osteogenic potential of BMSCs, reduced proliferation capacity of stem cells, increased RANKL expression, and alterations in the OLCN, which collectively mirror the process seen in humans.

Sarcopenia

Sarcopenia, loss of skeletal muscle mass and function, is one of the health concerns in aging humans. It leads to reduced physical performance, impaired mobility, and increased risk of falls [36]. It can contribute to the development of frailty, as weakened muscles can make individuals more susceptible to physical limitations and disability. At around age 40, sarcopenia becomes apparent, and by age 80, 30-50% of the muscle mass and function are reported to be lost [4]. Gait speed, grip strength, and lean muscle mass are determinant factors in predicting age-related locomotor activity [37]. Reduced gait speed is considered an indicator of slowness and is often used to assess physical performance in individuals. Weak grip strength, on the other hand, serves as a reliable measure of muscle weakness and can provide valuable insights into overall muscle function)[38] In addition to these assessments, DXA scans are

commonly utilized to determine low lean muscle mass, which is a key characteristic of sarcopenia [39]. Furthermore, imaging techniques such as CT, MRI, and ultrasound can be employed to identify specific alterations in muscle size and function in patients with sarcopenia, providing a more comprehensive evaluation of the condition [40]. In addition to these direct evaluation methods, various functional and clinical indicators are used to identify sarcopenia and assess its impact on the health of an individual. The Short Physical Performance Battery (SPPB), for instance, combines gait speed, chair stands, and balance tests to provide an overall assessment of physical performance [41]. The scoring system for the SPPB ranges from 0 (indicating the worst performance) to 12 (indicating the best performance). Numerous studies have demonstrated the predictive validity of the SPPB, showing that individuals with lower scores are at a higher risk for adverse outcomes such as mortality, nursing home admission, and disability. On the other hand, the European Working Group on Sarcopenia in Older People has established diagnostic criteria for sarcopenia that include the measurement of muscle mass, muscle strength, and physical performance [42]. In accordance with these diagnostic criteria, the identification of probable sarcopenia is based on Criterion 1, which stipulates the presence of low muscle strength. To confirm the diagnosis, additional documentation of Criterion 2 is required, which involves low muscle quantity or quality. If all three criteria, including Criterion 3, which relates to low physical performance, are met, the diagnosis of sarcopenia is considered severe. These criteria provide a comprehensive framework for assessing and categorizing sarcopenia based on different aspects of muscle function and performance [40]. Sarcopenia can be attributed to various underlying factors, including mitochondrial dysfunction, fat infiltration, and decreased satellite cells, leading to reduced muscle regeneration capacity [43]. Consequently, sarcopenia is associated with a decline in type II muscle fibers, myofiber number, and cross-sectional muscle area [37, 44]. Additionally, various signaling pathways are implicated in age-associated changes to the regulation of muscle protein synthesis and regeneration. The phosphatidylinositol 3-kinase (PI3K)/Akt pathway is known to influence protein synthesis and contribute to muscle loss in sarcopenia [45]. Similarly, the transforming growth factor beta (TGFβ) family governs muscle regeneration, while activation of the mammalian target of rapamycin (mTOR) pathway promotes muscle hypertrophy [46]. The age-related decline in Notch signaling affects satellite cell self-renewal capacity, further compromising the muscle regeneration [47]. Furthermore, the shift from canonical to non-canonical Wnt signaling hampers satellite cell function and impairs the muscle regeneration [48]. Collectively, these signaling pathways contribute to the development and progression of sarcopenia, underscoring the need to comprehensively

understand and target these factors for potential interventions and treatments that can mitigate muscle loss in older individuals.

Mouse models of sarcopenia often involve genetically modified mice, age-induced muscle wasting, or disuse-induced muscle atrophy models [49]. Similar to humans, mice are evaluated for muscle strength and physical performance using grip strength and functional performance tests. Additionally, evaluating muscle mass, muscle fiber type distribution, and muscle fiber cross-sectional area are among the methods used to study sarcopenia in mice [50]. For instance, at 18 months of age, grip strength and endurance were considerably lower compared to 10-week-old C57BL/6 mice [51]. Furthermore, hindlimb muscle weight was reduced in 25-month-old C57BL/6 mice compared to 10-month-old mice, accompanied by a significant decline in grip strength and maximum muscle strength [52]. These findings further support the notion that age-related muscle loss develops in C57BL/6 mice as they age.

In addition to naturally aging mice, genetically altered mouse models have played a crucial role in understanding the underlying pathways and mechanisms involved in sarcopenia. For instance, IL-10 knockout mice, also known as frail mice, have been developed to study the impact of IL-10 deficiency, an anti-inflammatory cytokine, on muscle weakness and reduced physical activity [53, 54]. The double knockout of IL-10 leads to the de-repression of nuclear factor kappa light chain enhancer of activated B cells (NF-κB) and contributes to the muscle weakness phenotypes observed in sarcopenia patients [53, 54]. Another commonly used mouse model is the copper-zinc superoxide dismutase knockout mice (Sod1$^{-/-}$), which display symptoms of sarcopenia, including muscle atrophy and weakness, by the age of 5 months [55]. Furthermore, IGF-1, PI3K, and Akt1 knockout mice, have been particularly valuable in studying the pathways involved in the development of sarcopenia [56]. By targeting specific genes and signaling pathways, these models provide insights into the molecular mechanisms underlying age-related muscle loss. In addition to the genetically engineered models, hindlimb unloading models have been utilized to induce muscle disuse and mimic the effects of aging on muscle physiology [57]. These methods allow for the investigation of muscle atrophy, weakness, and other age-related changes associated with sarcopenia.

Table 2.1 summarizes the measurements that define the musculoskeletal aging conditions with the cut-off values in humans and mice.

Table 2.1 Comparison of musculoskeletal aging conditions in humans and mice with emphasis on evaluation methods and criteria

Parameters: Frailty Phenotype (FP), Frailty Index (FI), Clinical Frailty Scale (CFS), Bone Mineral Density (BMD), Dual X-Ray Absorptiometry (DXA), Quantitative Computed Tomography (QCT), micro–Computed Tomography (micro-CT), Magnetic Resonance Imaging

	Condition	**Method**	**Criteria**	**References**
Human	Frailty	FP: evaluating exhaustion, physical activity, weakness, slowness, and weight loss	not frail: 0 criteria present pre-frail: 1-2 criteria present frail ≥ 3 criteria present	[10]
		CFS: based on FI evaluating the cumulative health deficiency score of 70 parameters	1 (very fit) to 9 (terminally ill) frail ≥ 5	[12]
	Osteoporosis	BMD: DXA	T-score < 2.5	[23]
		Bone microarchitecture: QCT HR-pQCT		
	Sarcopenia	Muscle strength: grip strength gait speed chair stand test	grip strength: men < 30 kg women < 20 kg gait speed < 0.8 m/s chair stand test: 5 times to sit to stand	[41-42]
		Muscle mass: DXA	lean muscle mass men < 7.23 kg/m^2 women < 5.67 kg/m^2	
		Muscle quality: CT or MRI		[57-61]
Mouse	Frailty	FP: evaluating grip strength, walking speed, physical activity, and endurance	not frail: 0 criteria present pre-frail: 1-2 criteria present frail ≥ 3 criteria present	[14]
		Valencia score: evaluating weight loss, running time and speed, grip strength, and motor coordination	not frail: 0 criteria present pre-frail: 1-2 criteria present frail ≥ 3 criteria present	[16]
		FI: evaluating cumulative health deficiency score of 31 parameters	0: no deficiency 0.5: mild deficiency 1: severe deficiency	[17]
	Osteoporosis	BMD: DXA		[6]
		Bone microarchitecture: micro-CT		
	Sarcopenia	Muscle strength: grip strength or wire hang test rotarod test		[50]
		Muscle mass: DXA micro-CT		

2.1.3. Accelerated aging mouse models with musculoskeletal aging phenotypes

Accelerated aging mouse models play a crucial role in elucidating the fundamental molecular pathways and mechanisms associated with musculoskeletal aging and associated conditions. These mouse models exhibit accelerating aging due to specifically targeted single gene mutations leading to multiple aging pathologies [6]. They offer distinct advantages over naturally aging mice requiring longer lifespans to exhibit age-related phenotypes, making it costly and challenging to study the progression of musculoskeletal aging over time. In contrast, accelerated aging mouse models enable to study these age-related changes within a relatively short timeframe [63]. These models exhibit accelerated manifestations of age-related phenotypes, including bone and muscle loss, frailty, and other hallmarks of musculoskeletal aging that parallel the physiological decline observed in humans. In this regard, we discuss four specific accelerated aging mouse models that exhibit hallmarks of musculoskeletal aging conditions in depth (Table 2.2).

Senescence accelerated mouse

Senescence accelerated mouse (SAM) is broadly utilized for studying age-related musculoskeletal changes. This model developed by selective inbreeding of the AKR/J mice and, based on their senescent phenotype, categorized into two groups: SAMP (senescence-accelerated prone) mice demonstrate faster aging with a shorter life span, whereas SAMRs (senescence resistant) mice display moderately less accelerated aging and have a typical lifespan [64-66].

Among the SAMP strains, SAMP6 is one of the most extensively characterized models used in research on senile osteoporosis [67, 68]. SAMP6 mice display lower BMD as assessed with DXA compared to the controls [69]. Additionally, micro-CT evaluation of the caudal vertebra revealed trabecular bone loss in these mice [70]. Similar findings have indicated bone loss with aging in the lumbar vertebra and tibia of 3-4 months old SAMP6 mice [70, 71]. This indicates that SAMP6 mice exhibit osteoporotic features, such as reduced bone density and mass which is consistent with the development of osteoporosis during aging. Furthermore, advanced aging in SAMP6 mice is suggested to be associated with increased bone resorption due to increased maturation of osteoclasts, increased adipogenesis, and reduced osteoblastogenesis [72]. In addition, the secretion of the frizzled-related protein (Srfp4), a Wnt pathway antagonist, is

increased in SAMP6 mice, contributing to reduced osteoblastogenesis [73]. Notably, at four months of age, SAMP6 mice demonstrate little or no difference in mechanosensitivity relative to their controls when subjected to *in vivo* tibia loading [74], suggesting that SAMP6 mice do not display significant alterations in their bone's ability to sense and respond to mechanical forces while they exhibit other age-related phenotypes, such as osteoporosis.

Moreover, age-associated musculoskeletal changes in these mice are assessed through physical (open field-home cage activity) and motor activity tests (grip strength, hanging, and rotation rod) [75]. It has been observed that adult SAMP6 (4-6 months old) mice have higher activity compared to old (8-12 months old) and the age-matched controls [75]. However, both adult and old SAMP6 mice display impaired intrinsic motor coordination as evidenced by decreased latency to fall (rotarod test) compared to control animals [75]. These findings suggest age-related decline in neuromuscular function in SAMP6 mice.

In contrast to SAMP6, SAMP8 mice are commonly used in sarcopenia research due to their rapid muscle aging phenotypes compared to normal aging mice and SAMR controls. The aging characteristics of SAMP8 mice have been extensively studied, revealing several age-related alterations in multiple aspects.

Firstly, SAMP8 mice exhibit various physical changes associated with aging, such as a reduction in the body condition score, increased kyphosis (excessive curvature of the spine), and loss of fur color [76]. Additionally, these mice experience a decrease in body weight as they age [76]. These observations indicate that SAMP8 mice manifest visible signs of accelerated aging compared to their control counterparts. When it comes to muscle function, SAMP8 mice demonstrate a decline in motor skills and muscle performance as they age. This has been assessed through various tests, including the treadmill-exhaustion test, grip strength measurements, and voluntary wheel running tests [76]. In each of these assessments, SAMP8 mice perform poorly compared to the controls, indicating an age-related decline in motor abilities and early signs of aging.

Sarcopenic muscle characteristics of SAMP8 mice further support the accelerated muscle aging phenotype. These mice exhibit reduced mass in gastrocnemius and (extensor digitorum longus) EDL, decreased cross-sectional area and decrease in soleus muscle fiber size at approximately 10-12 months [76]. Additionally, SAMP8 mice display lower grip strength, decreased muscle contraction time, increased fatigue rate, and a reduction in type II muscle fibers in the soleus

and gastrocnemius muscles [76]. These findings collectively indicate the development of muscle atrophy and deterioration in SAMP8 mice as they age.

At the cellular level, SAMP8 mice show decreased mTOR and Akt signaling, which leads to the upregulation of genes associated with muscle protein degradation and mitochondrial dysfunctionality [76]. This suggests that molecular mechanisms underlying muscle aging, such as increased protein degradation and impaired mitochondrial function, contribute to the accelerated muscle aging phenotype observed in SAMP8 mice.

It is worth noting that SAMP6 and SAMP8 mouse models have also been extensively utilized in neurodegenerative disease research. These strains exhibit a decline in cognitive skills with aging, suggesting that progressive neurodegenerative conditions may contribute to the observed aging-related muscle and bone phenotypes. Collectively, SAMP6 mice serve as a useful model for studying age-related musculoskeletal changes, including osteoporosis and motor coordination impairments and SAMP8 mice serve as valuable models for studying sarcopenia due to their accelerated muscle aging phenotypes compared to normal aging mice.

Lamin A deficiency

Zmpste24 knockout mice (Zmpste24$^{-/-}$) are widely used as a model to study the effects of impaired Lamin A processing on musculoskeletal aging. Zmpste24 is a zinc metalloproteinase responsible for processing Lamin A, which plays a crucial role in maintaining the integrity of the nuclear envelope and ensuring proper cell proliferation and genome stability [77]. By knocking out Zmpste24 in mice, the normal processing of Lamin A is disrupted, mimicking the defective processing observed in Hutchison-Gilford progeria syndrome (HPGS). The characteristics of this disease involve accelerated aging, including alopecia and cardiovascular complications [78]. Mice deficient with Zmpste24 exhibited an accelerated aging phenotype, displaying gradual weight and hair loss, as well as kyphosis (abnormal curvature of the spine), alopecia, and shortened life span of approximately 20 weeks overall frailty-like characteristics [77, 79]. Additionally, Zmpste24$^{-/-}$ mice exhibit various impairments in bone structure and function, as analyzed by micro-CT. At 3 months of age, these mice demonstrate significantly lower bone volume and density and thinner trabeculae [77, 80]. These findings indicate a substantial loss of bone in Zmpste24$^{-/-}$ mice. Histomorphometry analysis further reveals a notable decrease in the numbers of osteoblasts and osteocytes, suggesting that the accumulation of prelamin A, resulting from Zmpste24 deficiency, contributes to bone loss [77, 80].

Furthermore, the reduced osteoblastogenesis observed in Zmpste24^{-/-} mice is associated with decreased expression of key transcription factors, including Runx2, osteocalcin (OCN), osteopontin (OPN), and bone sialoprotein (BSP) [80]. This shift towards reduced osteoblastogenesis is concurrent with an increase in adipogenesis, suggesting a preference for adipocyte formation over osteoblast differentiation in this mouse model. These musculoskeletal changes observed in Zmpste24^{-/-} mice closely resemble the characteristics of age-related osteoporosis seen in humans.

Muscle-related phenotypes are also observed in Zmpste24^{-/-} mice. One notable finding is the reduction in grip strength and whole-body tension in Zmpste24^{-/-} mice, indicating a decline in locomotor activity [77, 81]. These mice also exhibit decreased ankle mobility and increased passive torque, suggesting the presence of stiff joints [81]. These musculoskeletal impairments contribute to reduced physical activity and compromised movement in Zmpste24^{-/-} mice. In terms of specific muscle groups, Zmpste24^{-/-} mice exhibit dystrophic quadriceps, characterized by the increased presence of abnormal small round muscle fibers [82]. The contractile capacity of the posterior leg muscles (soleus, plantaris, and gastrocnemius) remains unaffected in these mice [81]. However, the anterior leg muscles (extensor hallucis longus, tibialis anterior, extensor digitorum longus) demonstrate significant weakness compared to the controls.

The size and distribution of soleus muscle fibers also show distinct characteristics in Zmpste24^{-/-} mice. Although the mean cross-sectional area of soleus muscle fibers is similar between Zmpste24 knockout and control mice, the fiber size distribution is significantly broader in Zmpste24^{-/-} mice. Additionally, the percentage of myosin heavy chain type I, IIa, and IIx fibers in the soleus muscles is similar between the two groups, but Zmpste24^{-/-} mice have a higher number of myonuclei [81, 83]. These findings suggest altered muscle composition and potential compensatory mechanisms in response to Zmpste24 deficiency. In particular, muscle-derived mesenchymal stem cells (MSCs) in Zmpste24^{-/-} mice exhibit reduced proliferation and myogenic differentiation, which contributes to impaired muscle regeneration. Moreover, the absence of Zmpste24 leads to age-related bone loss and abnormal fat infiltration within the bone marrow without affecting the subcutaneous fat layer [84]. This aberrant fat accumulation within the bone marrow is associated with reduced differentiation of MSCs toward the adipogenic lineage. Furthermore, downstream signaling pathways involved in stem cell differentiation and function, such as Notch and Wnt, are impaired in Zmpste24^{-/-} mice [83]

These signaling pathways play essential roles in regulating the balance between different cell lineages and maintaining tissue homeostasis.

In summary, Zmpste24$^{-/-}$ mice exhibit various muscle-related phenotypes, including decreased grip strength, mobility impairments, muscle weakness in specific muscle groups, altered muscle fiber characteristics, impaired muscle regeneration, and abnormal fat infiltration within the bone marrow. These findings highlight the complex interactions between Zmpste24 deficiency, muscle function, stem cell dynamics, and age-related musculoskeletal changes.

DNA damage repair mechanism dysfunction

Ercc1 mutant mouse (Ercc1$^{-/\Delta}$) is another valuable model for studying musculoskeletal aging. This model exhibits a deficiency in the ERCC1-XPF endonuclease protein complex, which plays a crucial role in DNA repair mechanisms [85]. In humans, mutations, or deletions of Errc1 or XPF gene are associated with accelerated aging, leading to a range of clinical diseases and developmental problems [86].

Notably, Ercc1 knockout mice (Ercc1$^{-/-}$) display significantly accelerated aging, with a remarkably short lifespan of only 3 weeks [87]. These mice show musculoskeletal aging phenotypes and other health abnormalities, including liver abnormalities and neuronal degeneration underscoring the critical role of Ercc1 in DNA repair and overall organismal health. On the other hand, Ercc1$^{-/\Delta}$ mutant mice, which retain 10% of XPF-Ercc1 expression, have normal development until adulthood but subsequently experience accelerated aging with a reduced life span [85, 88].

One of the prominent musculoskeletal changes observed in Ercc1$^{-/\Delta}$ mice is a decline in bone density and structure exhibiting age-related osteoporosis characteristics [89]. Micro-CT analysis of Ercc1$^{-/\Delta}$ mice reveals age-related changes in the bone microarchitecture, including reduced trabecular thickness and number and increased vertebral porosity in the lumbar vertebra [89]. Particularly these mice develop age-related intervertebral disc degeneration (IDD) associated with an osteoporotic bone phenotype characterized by loss of disk height and degenerative changes within the disc [90]. In 20-week-old Ercc1$^{-/\Delta}$ mice, a significantly lower height of the lumbar vertebral disc was observed. This reduction is equivalent to the vertebral height loss observed in mice naturally aged to 2 years [90]. Thus, the osteoporotic phenotype in mutant Ercc1 mice occurs at an earlier age than in normal aging 2-year-old mice.

Additionally, elevated expression of tumor necrosis factor α (TNFα), and receptor activator of NF-Қβ, suggests an early onset of osteoporosis in Ercc1-deficient mice [91, 92]. This is attributed to increased senescence in bone marrow stem cells, leading to reduced osteoblast functionality and increased osteoclastogenesis in these mice.

In terms of muscle-related phenotypes, Ercc1$^{-/\Delta}$ mice exhibit reduced grip strength, poor body condition, gait impairment, kyphosis, and tremors, indicating muscle dysfunction and wasting [93, 94]. Correspondingly, the decline in locomotor activity, assessed through the grip strength, rotarod, and open field test, supports the reduced muscle strength and function in these mice compared to controls [93]. Moreover, at 16 weeks, Ercc1$^{-/\Delta}$ mice demonstrate a sarcopenic muscle phenotype characterized by smaller muscle sizes and decreased mass in muscles like the EDL and soleus [93]. This muscle loss is attributed to age-associated muscle mass decline. In addition, Ercc1$^{-/\Delta}$ mice exhibit a higher proportion of dying muscle fibers due to apoptosis and necrosis compared to aged wild-type mice [93].

Furthermore, Akt pathway, known for its involvement in regulating muscle hypertrophy, is upregulated in mutant Ercc1 mice [93]. This finding suggests that the activation of protein synthesis pathways counteracts the observed atrophic muscle phenotype in these mice. Consequently, it is plausible that stimulating the protein synthesis pathways could potentially serve as a compensatory mechanism to compensate for the severe muscle wasting observed in this mouse model.

Beyond these findings of the musculoskeletal phenotype of mutant Ercc1 mice, several studies have investigated interventions aimed at extending the health span and improving symptoms in mutant Ercc1 mice. These interventions include stem cell transplantation from young wild-type mice, dietary restrictions, and inhibition of the NF-Қβ pathway [95]. These approaches aim to mitigate the effects of accelerated aging and promote healthier aging in Ercc1-deficient mice.

Overall, the Ercc1-XPF complex is crucial for the DNA repair process, and deficiencies in Ercc1 or XPF genes can lead to accelerated aging and various clinical conditions. Mice with Ercc1 gene mutations or deletions exhibit accelerated aging phenotypes with notable effects on the musculoskeletal system, including bone loss and muscle dysfunction.

Mitochondrial dysfunction

PolgA$^{D257A/D257A}$ mice (referred to as PolgA), also known as mutator mice, carry a mutated form of the proofreading domain found exclusively in the mitochondrial DNA (mtDNA) polymerase [96]. This mutation leads to a substantial increase (3-5 times higher) in the accumulation of point mutations within mtDNA compared to normal mice [97]. Consequently, this accelerated mutation rate gives rise to compromised mitochondrial function, affecting various cellular processes and resulting in accelerated aging.

PolgA mice display several hallmarks of aging, including kyphosis, alopecia, hearing impairments, and gradual weight loss. These phenotypes are evident throughout their relatively short lifespan of approximately 48 weeks [96, 98]. The age-related decline in PolgA mice has been assessed through the clinical mouse FI method. Notably, at 40 weeks of age, these mice demonstrate a higher prevalence of aging-associated characteristics, including graying fur, ruffled fur, distended abdomen, kyphosis, etc., when compared to the control group. This observation indicates an increased FI in PolgA mice, reflecting that they experience accelerated frailty progression relative to their aged match counterparts, even at a relatively young age [99]. Additionally, the aging phenotypes observed in PolgA mice are primarily attributed to increased mitotic cell apoptosis rather than elevated oxidative stress, reduced cellular proliferation, or cellular senescence. This suggests that the accumulation of mitochondrial DNA mutations, resulting from the PolgA mutation, drives the accelerated aging phenotype in these mice rather than increased oxidative stress induced by reactive oxygen species (ROS), causing damaged mitochondria and leading to accelerated aging [100].

Moreover, PolgA mice demonstrate a pronounced propensity for the development of osteopenia. These mice display significant alterations in bone density and structure, reflecting the characteristic features of osteoporosis. Specifically, at 40 weeks of age, they display reduced BMD in femurs, which closely resembles the BMD decline observed in aging humans [96]. Micro-CT analysis further confirms age-related impairments in bone microarchitecture evident by the decrease in bone volume and quality together with a reduction in multiple bone morphometric parameters in comparison to the age-matched controls in caudal vertebrae and tibia [99-101]. Similar findings of bone loss were observed in the lumbar vertebrae and femurs of PolgA mice at 4-11 months [97]. In addition, PolgA mice were found to be more susceptible to the development of knee osteoarthritis by showing increased numbers of hypertrophic

chondrocytes, specifically in the articular calcified cartilage. Importantly, Geurts et al. reported the prevalence of low-grade cartilage degeneration primarily characterized by proteoglycan alterations in this mouse model. The study also demonstrated a significant correlation between trabecular thickness and osteocyte apoptosis, along with an elevation in osteoclast numbers [100]. These findings suggest that mitochondrial DNA mutations impact chondrocyte function and subchondral bone dynamics.

Furthermore, Polg A mice with advanced aging show a lack of mechanosensitivity upon *in vivo* mechanical loading of the caudal vertebra, indicating impaired bone response to mechanical stimuli. This is reminiscent of the reduced bone turnover observed in aging humans but without achieving peak bone mass [99]. This impaired bone response and loss in PolgA mice was accompanied by a significant decrease in bone formation rate, reduced densities of osteoblasts, along with increased density of osteoclasts [97]. In this regard, *in vitro* experiments have revealed significant impairments in the formation of mineralized matrix as well as an increased ability to resorb bone through osteoclast activity in these mice [97]. These findings suggest that the PolgA mutation significantly affects bone health, leading to impaired bone formation and increased resorption that contribute to the accelerated rate of bone loss observed in these mice.

Regarding muscle characteristics, PolgA mice demonstrate deficiencies in motor coordination, locomotor activity, and muscle functionality, all of which contribute to their musculoskeletal deterioration phenotype. For instance, rotarod and voluntary wheel running tests showed decreased performance in PolgA mice, including reduced running capacity, decreased distance covered, and diminished overall physical activity compared to wild-type mice [102]. Decline in the grip strength in PolgA mice with aging supported the findings in compromised muscle strength and function, mirroring the characteristics of sarcopenia [99]. Moreover, muscle fiber atrophy and reduced muscle mass were reported in PolgA mice at 40-46 weeks [99]. Such pathological alterations further contribute to the impairment of muscle function and the development of sarcopenia in PolgA mice.

Another important feature of PolgA mice is that they exhibit dysfunctional stem cells starting from embryogenesis. The self-renewal capacity of these cells is reduced *in vitro*, while *in vivo* there is a decrease in quiescent stem cell populations [103]. Treatment with N-acetyl-L-cysteine improved abnormalities, suggesting that mtDNA mutagenesis-induced ROS/redox changes modulate stem cell function. Additionally, PolgA mice showed an enlarged small intestine with apoptosis in the stem cell zones [104]. Stem cell-derived organoids from these

mice exhibited impaired development highlighting the early effects of mtDNA mutagenesis on stem cell function. On that note, voluntary wheel running has been shown to improve the visible aging phenotypes mentioned earlier in PolgA mice, as well as behavioral parameters like locomotion and rearing [102]. The study also investigated the effects of exercise on mtDNA mutation load and mtDNA copy number. It was found that voluntary running resulted in a reduction of mtDNA mutation load in actively running PolgA mice compared to sedentary or exercised wild-type mice. However, mtDNA copy number did not increase with exercise in PolgA mice, possibly due to the presence of defective stem cell populations in these mice [98,103-104]. Furthermore, exercise improved the dysregulated proteins observed in the gastrocnemius muscle and striatum of mtDNA mutator mice [102]. These findings suggest that exercise in aging humans may contribute to a decrease in mtDNA mutation load and the normalization of skeletal muscle protein levels based on the findings in PolgA mice. Overall, these results are consistent with those observed in human sarcopenia patients, suggesting the PolgA mouse model is a promising model for studying musculoskeletal aging.

Table 2.2 Comparing the hallmarks of aging to musculoskeletal conditions observed in accelerated aging mouse models.

Parameters: Frailty Index (FI), Bone Mineral Density (BMD), Intravertebral Disk Degeneration (IDD).

*Only the PolgA mouse model has been shown to be subjected to clinical mouse frailty scoring. The remaining models displayed frailty-like phenotypes based on mouse monitoring.

	SAMP6	SAMP8	Zmpste24 $^{-/-}$	Ercc1$^{-/\Delta}$	PolgA
Life Span	~42 weeks		~30 weeks	~20 weeks	~48 weeks
Mechanism	selective inbreeding [63]		Lamin A deficiency [76]	DNA damage repair impairment [84]	mitochondrial dysfunction [96, 98]
Frailty and associated phenotypes		↑ kyphosis ↑ loss of fur color ↑ body weight ↑ body scoring	↓ body weight ↑ hair loss ↑ kyphosis ↑ scoliosis ↑ alopecia	↑ poor body condition ↑ gait impairment ↑ kyphosis ↑ tremor ↑ hearing loss	↑ FI* ▪ hearing loss ▪ kyphosis ▪ graying ↓ body weight ▪ alopecia ↑ kyphosis
Age-related osteoporosis	↓ bone peak ↓ trabecular bone ↓ BMD		↓ trabecular bone ↓ BMD ▪ stiff joints	↓ trabecular bone ↑ porosity ▪ IDD	↓ trabecular bone ↓ BMD ↓ mechanosensitivity ▪ osteoarthritis development
Sarcopenia		↓ motor activity ▪ muscle weakness ↓ muscle mass ↓ fiber size ↑ fatigue rate	↓ motor activity ▪ muscle weakness ▪ muscle dystrophy ▪ abnormal fibers ↑ number of myonuclear	↓ motor activity ▪ muscle weakness ↓ muscle mass ▪ muscle dystrophy ▪ smaller muscle size ▪ dying fibers	↓ motor activity ▪ muscle weakness ↓ muscle mass ▪ fiber atrophy

2.1.4 Discussion

Musculoskeletal aging is a complex process that involves the deterioration of the skeletal system and muscles, leading to conditions such as frailty, sarcopenia, and osteoporosis. Mouse models that exhibit accelerated aging have become invaluable tools for studying hallmarks of musculoskeletal aging and associated conditions in a shorter time frame than observed in natural aging. With this regard, numerous models of accelerated aging have been developed to aid in the development of interventions for slowing down aging and age-related skeletal and muscle pathologies. From the array of well-established and extensively studied accelerated aging models such as mutant BubR1 hypomorph (BubR1$^{H/H}$) mice, Terc1 and Sod1 knock-out mice, we have carefully selected models that specifically target key pathways involved in musculoskeletal aging, including DNA damage repair, mitochondrial dysfunction, and Lamin A deficiency exhibiting prominent musculoskeletal aging phenotypes similar to humans. Hence, in this comprehensive review, we have focused on discussing the significance and findings of SAMP6, SAMP8, Zmpste24, Ercc1, and PolgA mice, shedding light on their invaluable contributions to the understanding of musculoskeletal aging and associated conditions.

Firstly, SAMP6 and SAMP8 mice exhibit certain characteristics resembling musculoskeletal aging in humans. However, these models possess a polygenic background and exhibit some deviations from the complete spectrum of human musculoskeletal aging. For instance, the lack of mechanosensitivity in SAMP6 mice and slower muscle atrophy observed in SAMP8 mice limits their representation of the full complexity of human musculoskeletal aging.

While Zmpste24$^{-/-}$ model, which provides insights into accelerated aging and nuclear envelope defects, shows a rapid aging phenotype and decreased bone turnover, its applicability to studying sarcopenia and other musculoskeletal aging aspects may be limited due to exhibiting selective muscle weakness.

Additionally, Ercc1$^{-/\Delta}$ model offers the opportunity to investigate the impact of DNA repair deficiency on aging, including its effect on the musculoskeletal system. This model displays aging-related bone and muscle phenotypes; however, its specific emphasis on DNA repair may limit its direct applicability to musculoskeletal aging research. Furthermore, the impact of

Ercc1 deficiency on fertility underscores a crucial factor to consider when utilizing this model to study musculoskeletal aging and its related conditions.

Finally, among the discussed models, PolgA mice appear to best represent the hallmarks of musculoskeletal aging and associated conditions similar to humans. They display early onset frailty, robust reductions in muscle and bone mass, and degeneration of bone cells. However, it is important to acknowledge certain limitations of the PolgA mouse model. These include the need for strategic breeding to prevent mitochondrial accumulation in females and the observed decrease in fertility in both male and female mice by the age of 20 weeks. Additionally, further research, particularly in the areas of transcriptomics and metabolomics, is necessary to fully establish the suitability of PolgA mice as a comprehensive model for investigating musculoskeletal aging and associated conditions.

Future research should focus on further characterizing these mouse models and conducting detailed analyses to gain a comprehensive understanding of the molecular changes associated with musculoskeletal aging research. Moreover, the translation of findings from these mouse models to human clinical applications remains a crucial area of investigation.

2.1.5. Conclusion

In conclusion, mouse models of accelerated aging have proven to be valuable tools in studying musculoskeletal aging and associated conditions (frailty, osteoporosis, and sarcopenia). These mouse models of accelerated aging, in particular the PolgA mouse model, provide important insights due to exhibiting hallmarks of musculoskeletal aging. While these models have limitations and may not fully capture the complexity of human musculoskeletal aging, they offer promise for advancing interventions and improving the quality of life for the aging population.

Acknowledgment

Conflict of interest

The authors have no conflict of interest to declare.

References

1. Roberts, S., et al., Ageing in the musculoskeletal system. Acta Orthop, 2016. 87(sup363): p. 15-25.

2. Milte, R. and M. Crotty, Musculoskeletal health, frailty and functional decline. Best Pract Res Clin Rheumatol, 2014. 28(3): p. 395-410.

3. Demontiero, O., C. Vidal, and G. Duque, Aging and bone loss: new insights for the clinician. Ther Adv Musculoskelet Dis, 2012. 4(2): p. 61-76.

4. Walston, J.D., Sarcopenia in older adults. Curr Opin Rheumatol, 2012. 24(6): p. 623-7.

5. Jilka, R.L., The relevance of mouse models for investigating age-related bone loss in humans. J Gerontol A Biol Sci Med Sci, 2013. 68(10): p. 1209-17.

6. Hasty, P. and J. Vijg, Accelerating aging by mouse reverse genetics: a rational approach to understanding longevity. Aging Cell, 2004. 3(2): p. 55-65.

7. Fedarko, N.S., The biology of aging and frailty. Clin Geriatr Med, 2011. 27(1): p. 27-37.

8. Fulop, T., et al., Aging, frailty and age-related diseases. Biogerontology, 2010. 11(5): p. 547-63.

9. Fried, L.P., et al., Frailty in older adults: evidence for a phenotype. J Gerontol A Biol Sci Med Sci, 2001. 56(3): p. M146-56.

10. Rockwood, K. and A. Mitnitski, Frailty defined by deficit accumulation and geriatric medicine defined by frailty. Clin Geriatr Med, 2011. 27(1): p. 17-26.

11. Rockwood, K., et al., A global clinical measure of fitness and frailty in elderly people. CMAJ, 2005. 173(5): p. 489-95.

12. Parks, R.J., et al., A procedure for creating a frailty index based on deficit accumulation in aging mice. J Gerontol A Biol Sci Med Sci, 2012. 67(3): p. 217-27.

13. Liu, H., et al., Clinically relevant frailty index for mice. J Gerontol A Biol Sci Med Sci, 2014. 69(12): p. 1485-91.

14. Baumann, C.W., D. Kwak, and L.V. Thompson, Phenotypic Frailty Assessment in Mice: Development, Discoveries, and Experimental Considerations. Physiology (Bethesda), 2020. 35(6): p. 405-414.

15. Gomez-Cabrera, M.C., et al., A New Frailty Score for Experimental Animals Based on the Clinical Phenotype: Inactivity as a Model of Frailty. J Gerontol A Biol Sci Med Sci, 2017. 72(7): p. 885-891. 16. Whitehead, J.C., et al., A clinical frailty index in aging

mice: comparisons with frailty index data in humans. J Gerontol A Biol Sci Med Sci, 2014. 69(6): p. 621-32.

17.   Sukoff Rizzo, S.J., et al., Assessing Healthspan and Lifespan Measures in Aging Mice: Optimization of Testing Protocols, Replicability, and Rater Reliability. Curr Protoc Mouse Biol, 2018. 8(2): p. e45.

18.   Raisz, L.G. and G.A. Rodan, Pathogenesis of osteoporosis. Endocrinol Metab Clin North Am, 2003. 32(1): p. 15-24.

19.   Akkawi, I. and H. Zmerly, Osteoporosis: Current Concepts. Joints, 2018. 6(2): p. 122-127.

20.   Raisz, L.G. and E. Seeman, Causes of age-related bone loss and bone fragility: an alternative view. J Bone Miner Res, 2001. 16(11): p. 1948-52.

21.   Ammann, P. and R. Rizzoli, Bone strength and its determinants. Osteoporos Int, 2003. 14 Suppl 3: p. S13-8.

22.   Sheu, A. and T. Diamond, Bone mineral density: testing for osteoporosis. Aust Prescr, 2016. 39(2): p. 35-9.

23.   Engelke, K., et al., Clinical use of quantitative computed tomography and peripheral quantitative computed tomography in the management of osteoporosis in adults: the 2007 ISCD Official Positions. J Clin Densitom, 2008. 11(1): p. 123-62.

24.   Paccou, J., et al., Marrow adiposity and bone: Review of clinical implications. Bone, 2019. 118: p. 8-15.

25.   Fazeli, P.K., et al., Marrow fat and bone--new perspectives. J Clin Endocrinol Metab, 2013. 98(3): p. 935-45.

26.   Almeida, M., Aging mechanisms in bone. Bonekey Rep, 2012. 1.

27.   Kim, J.H., et al., Wnt signaling in bone formation and its therapeutic potential for bone diseases. Ther Adv Musculoskelet Dis, 2013. 5(1): p. 13-31.

28.   Cheng, C.H., L.R. Chen, and K.H. Chen, Osteoporosis Due to Hormone Imbalance: An Overview of the Effects of Estrogen Deficiency and Glucocorticoid Overuse on Bone Turnover. Int J Mol Sci, 2022. 23(3).

29.   Busse, B., et al., Decrease in the osteocyte lacunar density accompanied by hypermineralized lacunar occlusion reveals failure and delay of remodeling in aged human bone. Aging Cell, 2010. 9(6): p. 1065-75.

30.   Beamer, W.G., et al., Genetic variability in adult bone density among inbred strains of mice. Bone, 1996. 18(5): p. 397-403. 31.   Ferguson, V.L., et al., Bone development and age-related bone loss in male C57BL/6J mice. Bone, 2003. 33(3): p. 387-98.

32.   Zhang, W., et al., Age-related changes in the osteogenic differentiation potential of mouse bone marrow stromal cells. J Bone Miner Res, 2008. 23(7): p. 1118-28.

33.   Bergman, R.J., et al., Age-related changes in osteogenic stem cells in mice. J Bone Miner Res, 1996. 11(5): p. 568-77.

34.   Cao, J., et al., Expression of RANKL and OPG correlates with age-related bone loss in male C57BL/6 mice. J Bone Miner Res, 2003. 18(2): p. 270-7.

35.   Tiede-Lewis, L.M., et al., Degeneration of the osteocyte network in the C57BL/6 mouse model of aging. Aging (Albany NY), 2017. 9(10): p. 2190-2208.

36.   Frontera, W.R., A.R. Zayas, and N. Rodriguez, Aging of human muscle: understanding sarcopenia at the single muscle cell level. Phys Med Rehabil Clin N Am, 2012. 23(1): p. 201-7, xiii.

37.   Shefer, G., et al., Satellite-cell pool size does matter: Defining the myogenic potency of aging skeletal muscle. Developmental Biology, 2006. 294(1): p. 50-66.

38.   Zhang, K., et al., The Relationship Between Sarcopenia, Cognitive Impairment, and Cerebral White Matter Hyperintensity in the Elderly. Clin Interv Aging, 2023. 18: p. 547-555.

39.   Messina, C., et al., Diagnostic imaging of osteoporosis and sarcopenia: a narrative review. Quant Imaging Med Surg, 2018. 8(1): p. 86-99.

40.   Cruz-Jentoft, A.J., et al., Sarcopenia: revised European consensus on definition and diagnosis. Age Ageing, 2019. 48(1): p. 16-31.

41.   Puthoff, M.L., Outcome measures in cardiopulmonary physical therapy: short physical performance battery. Cardiopulm Phys Ther J, 2008. 19(1): p. 17-22.

42.   Cruz-Jentoft, A.J., et al., Sarcopenia: European consensus on definition and diagnosis: Report of the European Working Group on Sarcopenia in Older People. Age Ageing, 2010. 39(4): p. 412-23.

43.   Bellanti, F., A. Lo Buglio, and G. Vendemiale, Mitochondrial Impairment in Sarcopenia. Biology, 2021. 10(1).

44.   Narici, M.V. and N. Maffulli, Sarcopenia: characteristics, mechanisms and functional significance. Br Med Bull, 2010. 95: p. 139-59. 45. Ziaaldini, M.M., et al., Biochemical Pathways of Sarcopenia and Their Modulation by Physical Exercise: A Narrative Review. Front Med (Lausanne), 2017. 4: p. 167.

46.   Rommel, C., et al., Mediation of IGF-1-induced skeletal myotube hypertrophy by PI(3)K/Akt/mTOR and PI(3)K/Akt/GSK3 pathways. Nat Cell Biol, 2001. 3(11): p. 1009-13.

47.   Bi, P., et al., Stage-specific effects of Notch activation during skeletal myogenesis. Elife, 2016. 5.

48.   Florian, M.C., et al., A canonical to non-canonical Wnt signalling switch in haematopoietic stem-cell ageing. Nature, 2013. 503(7476): p. 392-+.

49.   Rydell-Tormanen, K. and J.R. Johnson, The Applicability of Mouse Models to the Study of Human Disease. Methods Mol Biol, 2019. 1940: p. 3-22.

50.   Xie, W.Q., et al., Mouse models of sarcopenia: classification and evaluation. J Cachexia Sarcopenia Muscle, 2021. 12(3): p. 538-554.

51.   Kim, C. and J.K. Hwang, The 5,7-Dimethoxyflavone Suppresses Sarcopenia by Regulating Protein Turnover and Mitochondria Biogenesis-Related Pathways. Nutrients, 2020. 12(4).

52.   van Dijk, M., et al., Sarcopenia in older mice is characterized by a decreased anabolic response to a protein meal. Archives of Gerontology and Geriatrics, 2017. 69: p. 134-143.

53.   Akki, A., et al., Skeletal muscle ATP kinetics are impaired in frail mice. Age (Dordr), 2014. 36(1): p. 21-30.

54.   Ko, F., et al., Impaired mitochondrial degradation by autophagy in the skeletal muscle of the aged female interleukin 10 null mouse. Exp Gerontol, 2016. 73: p. 23-7.

55.   Sataranatarajan, K., et al., Molecular changes in transcription and metabolic pathways underlying muscle atrophy in the CuZnSOD null mouse model of sarcopenia. Geroscience, 2020. 42(4): p. 1101-1118.

56.   Baek, K.W., et al., Rodent Model of Muscular Atrophy for Sarcopenia Study. J Bone Metab, 2020. 27(2): p. 97-110.

57.   Morey-Holton, E.R. and R.K. Globus, Hindlimb unloading rodent model: technical aspects. J Appl Physiol (1985), 2002. 92(4): p. 1367-77.

58.   Ruan, X.Y., et al., Estimating whole body intermuscular adipose tissue from single cross-sectional magnetic resonance images. J Appl Physiol (1985), 2007. 102(2): p. 748-54.

59.   Goodpaster, B.H., et al., Skeletal muscle attenuation determined by computed tomography is associated with skeletal muscle lipid content. J Appl Physiol (1985), 2000. 89(1): p. 104-10.

60.   Reinders, I., et al., Muscle Quality and Myosteatosis: Novel Associations With Mortality Risk: The Age, Gene/Environment Susceptibility (AGES)-Reykjavik Study. Am J Epidemiol, 2016. 183(1): p. 53-60.

61.   Grimm, A., et al., Evaluation of 2-point, 3-point, and 6-point Dixon magnetic resonance imaging with flexible echo timing for muscle fat quantification. Eur J Radiol, 2018. 103: p. 57-64.

62.   Distefano, G., et al., Physical activity unveils the relationship between mitochondrial energetics, muscle quality, and physical function in older adults. J Cachexia Sarcopenia Muscle, 2018. 9(2): p. 279-294.

63.   Gurkar, A.U. and L.J. Niedernhofer, Comparison of mice with accelerated aging caused by distinct mechanisms. Exp Gerontol, 2015. 68: p. 43-50.

64.   Takeda, T., Senescence-accelerated mouse (SAM): a biogerontological resource in aging research. Neurobiol Aging, 1999. 20(2): p. 105-10.

65.   Takeda, T., M. Hosokawa, and K. Higuchi, Senescence-accelerated mouse (SAM): a novel murine model of senescence. Exp Gerontol, 1997. 32(1-2): p. 105-9.

66.   Takeda, T., et al., A new murine model of accelerated senescence. Mech Ageing Dev, 1981. 17(2): p. 183-94.

67.   Matsushita, M., et al., Age-Related-Changes in Bone Mass in the Senescence-Accelerated Mouse (Sam) - Sam-R/3 and Sam-P/6 as New Murine Models for Senile Osteoporosis. American Journal of Pathology, 1986. 125(2): p. 276-283.

68.   Silva, M.J., M.D. Brodt, and S.L. Ettner, Long bones from the senescence accelerated mouse SAMP6 have increased size but reduced whole-bone strength and resistance to fracture. Journal of Bone and Mineral Research, 2002. 17(9): p. 1597-1603.

69.   Kasai, S., et al., Consistency of low bone density across bone sites in SAMP6 laboratory mice. J Bone Miner Metab, 2004. 22(3): p. 207-14.

70.   Jilka, R.L., et al., Linkage of decreased bone mass with impaired osteoblastogenesis in a murine model of accelerated senescence. J Clin Invest, 1996. 97(7): p. 1732-40.

71.   Chen, H., et al., Site-specific bone loss in senescence-accelerated mouse (SAMP6): a murine model for senile osteoporosis. Exp Gerontol, 2009. 44(12): p. 792-8.

72.   Kajkenova, O., et al., Increased adipogenesis and myelopoiesis in the bone marrow of SAMP6, a murine model of defective osteoblastogenesis and low turnover osteopenia. J Bone Miner Res, 1997. 12(11): p. 1772-9.

73.   Nakanishi, R., et al., Secreted frizzled-related protein 4 is a negative regulator of peak BMD in SAMP6 mice. J Bone Miner Res, 2006. 21(11): p. 1713-21.

74.   Silva, M.J. and M.D. Brodt, Mechanical stimulation of bone formation is normal in the SAMP6 mouse. Calcified Tissue International, 2008. 82(6): p. 489-497.

75.   Niimi, K. and E. Takahashi, Characterization of Senescence-Accelerated Mouse Prone 6 (SAMP6) as an Animal Model for Brain Research. Experimental Animals, 2014. 63(1): p. 1-9.

76.   Liu, H.W., et al., Dysregulations of mitochondrial quality control and autophagic flux at an early age lead to progression of sarcopenia in SAMP8 mice. Biogerontology, 2020. 21(3): p. 367-380.

77.   Bergo, M.O., et al., Zmpste24 deficiency in mice causes spontaneous bone fractures, muscle weakness, and a prelamin A processing defect. Proc Natl Acad Sci U S A, 2002. 99(20): p. 13049-54.

78.   Denecke, J., et al., A homozygous ZMPSTE24 null mutation in combination with a heterozygous mutation in the LMNA gene causes Hutchinson-Gilford progeria syndrome (HGPS): insights into the pathophysiology of HGPS. Hum Mutat, 2006. 27(6): p. 524-31.

79.   Wang, Y., et al., Abolishing the prelamin A ZMPSTE24 cleavage site leads to progeroid phenotypes with near-normal longevity in mice. Proc Natl Acad Sci U S A, 2022. 119(9).

80.   Rivas, D., et al., Accelerated features of age-related bone loss in zmpste24 metalloproteinase-deficient mice. J Gerontol A Biol Sci Med Sci, 2009. 64(10): p. 1015-24.

81.   Greising, S.M., et al., Skeletal muscle contractile function and neuromuscular performance in Zmpste24 -/- mice, a murine model of human progeria. Age (Dordr), 2012. 34(4): p. 805-19.

82.   Pendas, A.M., et al., Defective prelamin A processing and muscular and adipocyte alterations in Zmpste24 metalloproteinase-deficient mice. Nat Genet, 2002. 31(1): p. 94-9.

83. Song, M., et al., Muscle-derived stem/progenitor cell dysfunction in Zmpste24-deficient progeroid mice limits muscle regeneration. Stem Cell Res Ther, 2013. 4(2): p. 33.

84. Heizer, P.J., et al., Deficiency in ZMPSTE24 and resulting farnesyl-prelamin A accumulation only modestly affect mouse adipose tissue stores. J Lipid Res, 2020. 61(3): p. 413-421.

85. Weeda, G., et al., Disruption of mouse ERCC1 results in a novel repair syndrome with growth failure, nuclear abnormalities and senescence. Curr Biol, 1997. 7(6): p. 427-39.

86. Eriksson, M., et al., Recurrent de novo point mutations in lamin A cause Hutchinson-Gilford progeria syndrome. Nature, 2003. 423(6937): p. 293-8.

87. McWhir, J., et al., Mice with DNA repair gene (ERCC-1) deficiency have elevated levels of p53, liver nuclear abnormalities and die before weaning. Nat Genet, 1993. 5(3): p. 217-24.

88. Dolle, M.E., et al., Broad segmental progeroid changes in short-lived Ercc1(-/Delta7) mice. Pathobiol Aging Age Relat Dis, 2011. 1.

89. Chen, Q., et al., DNA damage drives accelerated bone aging via an NF-kappaB-dependent mechanism. J Bone Miner Res, 2013. 28(5): p. 1214-28.

90. Vo, N., et al., Accelerated aging of intervertebral discs in a mouse model of progeria. J Orthop Res, 2010. 28(12): p. 1600-7.

91. Flores, R.R., et al., Expansion of myeloid-derived suppressor cells with aging in the bone marrow of mice through a NF-kappaB-dependent mechanism. Aging Cell, 2017. 16(3): p. 480-487.

92. Kim, D.E., et al., Deficiency in the DNA repair protein ERCC1 triggers a link between senescence and apoptosis in human fibroblasts and mouse skin. Aging Cell, 2020. 19(3): p. e13072.

93. Alyodawi, K., et al., Compression of morbidity in a progeroid mouse model through the attenuation of myostatin/activin signalling. Journal of Cachexia Sarcopenia and Muscle, 2019. 10(3): p. 662-686.

94. de Waard, M.C., et al., Age-related motor neuron degeneration in DNA repair-deficient Ercc1 mice. Acta Neuropathol, 2010. 120(4): p. 461-75.

95. Lavasani, M., et al., Muscle-derived stem/progenitor cell dysfunction limits healthspan and lifespan in a murine progeria model. Nat Commun, 2012. 3: p. 608.

96.   Trifunovic, A., et al., Premature ageing in mice expressing defective mitochondrial DNA polymerase. Nature, 2004. 429(6990): p. 417-23.

97.   Dobson, P.F., et al., Mitochondrial dysfunction impairs osteogenesis, increases osteoclast activity, and accelerates age related bone loss. Sci Rep, 2020. 10(1): p. 11643.

98.   Kujoth, G.C., C. Leeuwenburgh, and T.A. Prolla, Mitochondrial DNA mutations and apoptosis in mammalian aging. Cancer Res, 2006. 66(15): p. 7386-9.

99.   Scheuren, A.C., et al., Hallmarks of frailty and osteosarcopenia in prematurely aged PolgA((D257A/D257A)) mice. J Cachexia Sarcopenia Muscle, 2020. 11(4): p. 1121-1140.

100.   Geurts, J., et al., Prematurely aging mitochondrial DNA mutator mice display subchondral osteopenia and chondrocyte hypertrophy without further osteoarthritis features. Sci Rep, 2020. 10(1): p. 1296.

101.   Scheuren, A.C., G.A. Kuhn, and R. Muller, Effects of long-term in vivo micro-CT imaging on hallmarks of osteopenia and frailty in aging mice. PLoS One, 2020. 15(9): p. e0239534.

102.   Ross, J.M., et al., Voluntary exercise normalizes the proteomic landscape in muscle and brain and improves the phenotype of progeroid mice. Aging Cell, 2019. 18(6): p. e13029.

103.   Ahlqvist, K.J., et al., Somatic progenitor cell vulnerability to mitochondrial DNA mutagenesis underlies progeroid phenotypes in Polg mutator mice. Cell Metab, 2012. 15(1): p. 100-9.

Chapter 3

CRISPR/Cas9 Cell Reporter Mice to Investigate Mechano-Molecular Dynamics in Bone Mechanoregulation

3.1 Elucidating the mechano-molecular dynamics of TRAP activity using CRISPR/Cas9 mediated fluorescent reporter mice

Dilara Yılmaz[1]*, Francisco C. Marques[1]*, Yannick Fischer[1], Sandra Zimmermann[1], Gaonhae Hwang[1], Penny R. Atkins[1, 2], Neashan Mathavan[1], Amit Singh[1], Pedro P. C. de Souza[1, 3], Gisela A. Kuhn[1], Esther Wehrle[1, 4]*, Ralph Müller[1]*

[1]Institute for Biomechanics, ETH Zürich, Zürich, Switzerland

[2]Department of Orthopaedics, University of Utah 590 Wakara Way, Salt Lake City, USA

[3]Innovation in Biomaterials Laboratory, School of Dentistry, Federal University of Goiás, Goiânia, Brazil

[4]AO Research Institute Davos, Davos Platz, Switzerland

*equal contribution

Abstract

Osteoclasts are essential for bone remodeling by adapting their resorptive activity in response to their mechanical *in vivo* environment. However, the molecular mechanisms underlying this process remain unclear. Here, we demonstrated the role of tartrate-resistant acid phosphatase (TRAP, Acp5), a key enzyme secreted by osteoclasts, in bone remodeling and mechanosensitivity. Using CRISPR/Cas9 reporter mice, we demonstrated bone cell reporter (BCR[Ibsp/Acp5]) mice feature fluorescent TRAP-deficient osteoclasts and examined their activity during mechanically driven trabecular bone remodeling. Although BCR[Ibsp/Acp5] mice exhibited trabecular bone impairments and reduced resorption capacity *in vitro*, RNA sequencing revealed unchanged levels of key osteoclast-associated genes such as *Ctsk, Mmp9,* and *Calcr*. These findings, in conjunction with serum carboxy-terminal collagen crosslinks (CTX) and *in*

vivo mechanical loading outcomes collectively indicated an unaltered bone resorption capacity of osteoclasts *in vivo*. Furthermore, we demonstrated similar mechanoregulation during trabecular bone remodeling in $BCR^{Ibsp/Acp5}$ and wild-type (WT) mice. Hence, this study provides valuable insights into the dynamics of TRAP activity in the context of bone remodeling and mechanosensation.

Keywords

mechanosensitivity, CRISPR/Cas9 mediated reporter mice, fluorescent osteoclasts and osteoblasts, TRAP deficiency, trabecular bone remodeling, micro-computed tomography, micro-finite element analysis, *in vivo* loading, bone remodeling.

3.1.1 Introduction

The skeleton undergoes continuous remodeling as old bone is removed and new bone is formed [1-3]. This intricate process of bone remodeling involves the highly coordinated activity of bone-resorbing osteoclasts and bone-forming osteoblasts both of which are influenced by mechanical strains in the mechanical *in vivo* environment of these cells [4]. Therefore, bone formation has been associated with regions subjected to high strains, while bone resorption was more frequently observed in regions with low strains [5-8]. Notably, this effect is more evident in trabecular bone that is more sensitive to mechanical loading due to its higher metabolic activity and mechanical heterogeneity compared to that of cortical bone. Furthermore, bone resorption was demonstrated to be more tightly regulated by mechanical loading in comparison to bone formation, thus highlighting the key role of osteoclasts in bone remodeling and mediating bone loss. Dysregulation of the function of osteoclast function has been linked to numerous diseases, including osteoporosis, osteopetrosis, and rheumatoid arthritis [9-11]. The precise mechanism underlying their response to mechanical stress is yet to be fully elucidated.

Tartrate-resistant acid phosphatase (TRAP; Acp5) is a pivotal enzyme that is predominantly found in osteoclasts, macrophages, and dendritic cells [12]. TRAP encodes for two distinct isoforms (TRAP 5a and TRAP 5b). TRAP 5a is a peptide loop protein that interacts with the active site of the enzyme to inhibit phosphatase activity. The loop region undergoes proteolytic cleavage that results in the formation of dimeric TRAP 5b with enhanced phosphatase activity[13]. While TRAP 5a is secreted from macrophages and dendritic cells, TRAP 5b is transported through osteoclasts by transcytosis. Therefore, it is released into the bloodstream during bone resorption and serves as a marker for osteoclast activity [3, 14]. Additionally, TRAP 5b has been suggested to regulate osteoclast migration through the dephosphorylation of osteopontin (OPN) [15]. Both of these TRAP isoforms have been demonstrated to be secreted by differentiating osteoclasts and are correlated to C-terminal type I collagen cross-linked peptide (CTX). Increased TRAP 5b release from bone suggests a link to osteoclast resorptive activity, and a peak in the TRAP 5b/5a ratio coincides with a rapid release of CTX[16]. Notably, the inactivation of the human *TRAP* gene (*Acp5*) results in the hyperphosphorylation of OPN [17], thus further emphasizing the intricate relationship between

TRAP isoforms and the modulation of cellular processes. TRAP also plays an important role in facilitating osteoclast migration to bone resorption sites. Once bone remodeling is initiated,

TRAP levels increase in the plasma and initiate crucial processes such as osteoclast differentiation, activation, and proliferation [18, 19].

In TRAP knock-out studies, the absence of TRAP led to widened and disorganized growth plates, skeletal shortening and deformity, and increased mineralization of bones linked to mild osteopetrosis due to dysfunctional osteoclast activity [2, 18]. Thus, osteoclasts are important for remodeling, responding to mechanical signals, and secreting essential markers for resorption, such as TRAP, whose dysregulation is a precursor to significant bone diseases.

Additionally, mouse loading models have enabled controlled experimental conditions to investigate bone adaptation in response to physiological and supraphysiological mechanical loading [20-23]. In combination with imaging techniques possessing improved spatial and temporal resolution, it is possible to monitor bone remodeling *in vivo* at the tissue and cellular levels. Particularly, in-depth characterization of the mechanical *in vivo* environment during bone remodeling was significantly advanced through the time-lapsed *in vivo* micro-computed tomography (micro-CT) measurements with micro-finite element simulations (micro-FE). By registering consecutive micro-CT time points, remodeling sites can be accurately identified and associated with local mechanical signals computed using micro-FE [8, 24]. In this regard, the role of TRAP in bone mechanoregulation, when considering the influence of supraphysiological mechanical loading on trabecular bone adaptation, is yet to be elucidated. Understanding osteoclast biology and the critical function of TRAP in bone turnover is essential to guide the development of TRAP inhibitors, and potential therapeutics for osteoclast-related bone abnormalities.

Here, we provide insights into the function of TRAP in mechanically driven trabecular bone adaptation and mechanosensitivity using *in vivo* loading mouse models. We used BCR[Ibsp/Acp5] mouse model, generated via CRISPR/Cas9 technology, which features osteoclasts that are TRAP-deficient and fluorescently marked with mCherry (*Acp5-mCherry*). Simultaneously, the osteoblasts remain intact and are also fluorescently labeled with GFP (*Ibsp-eGFP*). This dual-tagging approach enables us to track osteoblasts and TRAP-deficient osteoclasts both *in vivo* and *in vitro* effectively. Additionally, BCR[Ibsp/WT] mice expressing only *Ibsp-eGFP* were used as internal controls. By combining *in vivo* loading and time-lapsed micro-CT with *in vitro* cell assays and RNA sequencing, we further demonstrated trabecular bone adaptation at the molecular level in BCR[Ibsp/Acp5] mice. Moreover, we used *in silico* micro-FE simulations to characterize trabecular mechanoregulation at sites of bone remodeling in our TRAP-deficient

mouse model. Our findings revealed that mechanosensitivity was maintained in $BCR^{Ibsp/Acp5}$ mice despite deteriorated trabecular bone structure and reduced osteoclast function.

Overall, this study was motivated by the lack of understanding of the function of TRAP in bone remodeling and mechanosensation. Utilizing CRISPR/Cas9 technology, we have created a reporter mouse model characterized by TRAP deficiency, with osteoclasts and osteoblasts fluorescently labeled, which allows for the tracking of these cells. Our comprehensive methodology includes the characterization of both cell types through *in vivo, in vitro*, and *in silico* approaches aimed to elucidate the dynamics of the TRAP activity in bone remodeling. Insights gained from this study could lead to new treatments targeting diseases associated with osteoclast dysfunction.

3.1.2 Results

In vivo identification and characterization of fluorescent bone cells in $BCR^{Ibsp/Acp5}$ mice

To identify the characteristics and morphology of the fluorescently tagged cells *in vivo,* we performed cell-specific immunostaining in the caudal vertebrae and femurs of $BCR^{Ibsp/Acp5}$ mice and compared them to those of WT mice at ages between 5-25 weeks. While the expression profile of labeled TRAP is broader and encompasses not only osteoclasts but also macrophages and immune cell types, the term "fluorescent osteoblast" similarly denotes not only osteoblasts but also osteoblastic cell types such as lining cells. Fluorescently labeled osteoblasts and TRAP-deficient osteoclasts were primarily located on the trabecular bone surfaces, around the growth plate, and along the cortex of $BCR^{Ibsp/Acp5}$ mice whereas WT mice lacked both signals in the caudal vertebrae and femurs (Figure 3.1A). Calcein Blue stained the mineralized bone surfaces from the caudal vertebrae to outline the bone structure. Multinucleated TRAP-deficient osteoclasts expressing mCherry, and mononucleated lining cells and osteoblasts expressing GFP around the bone surface were identified with Hoechst staining (Figure 3.1B). TRAP staining revealed the absence of TRAP expression in $BCR^{Ibsp/Acp5}$ mice compared to that in WT mice, and mCherry immunostaining confirmed the mCherry signal only in $BCR^{Ibsp/Acp5}$ mice (Figure 3.1F-G). Moreover, Ibsp, GFP, and mCherry immunostainings validated the co-localization of GFP and mCherry signals with the respective stainings and accentuated the specificity of the tagged cells (Figure 3.1C-D, F). The relative fluorescence intensities of GFP and mCherry further verified the expression of mCherry and GFP signals from $BCR^{Ibsp/Acp5}$ in contrast to WT mice lacking fluorescent protein expressions

(Figure 3.1E, H). Additionally, Van Steensel's co-localization analysis quantitatively measured the overlap between fluorescent signals and their respective immunostainings in the BCR[Ibsp/Acp5] mice. The complete colocalization was indicated by a peak at $\delta x = 0$ and a bell-shaped curve [25]. Although differences in fluorescence intensity can decrease the height of this curve, the peak remains at $\delta x = 0$. The specific overlap between GFP and mCherry signals and their corresponding immunostainings was confirmed for BCR[Ibsp/Acp5] in comparison to WT mice through the pronounced bell-shaped curve peak at $\delta x = 0$, with a mean cross-correlation (CCF) of 0.55 ± 0.03 in GFP, 0.50 ± 0.07 in Ibsp, and 0.45 ± 0.09 in mCherry (Figure 3.1I-J). Overall, these data confirmed the presence and specificity of GFP- and mCherry-tagged osteoblasts and TRAP-deficient osteoclasts from BCR[Ibsp/Acp5] mice *in vivo*.

Furthermore, micro-CT analysis of the caudal vertebra in BCR[Ibsp/Acp5] mice demonstrated differences in bone structure between TRAP-deficient mice and controls. Reduced trabecular bone volume fraction (BV/TV), trabecular number and thus increased trabecular space compared to BCR[Ibsp/WT] and WT mice indicated a notably impaired trabecular bone in BCR[Ibsp/Acp5] mice (Figure 3.S1A, C). In addition, BCR[Ibsp/Acp5] mice displayed a significant shortening of the vertebra, as indicated by the longitudinal 3D images comparing the vertebra length of BCR[Ibsp/Acp5] mice with BCR[Ibsp/WT] and WT at 20 weeks (Figure 3.S1A, C). However, no distinct difference was found between the groups regarding cortical bone development, as shown by the 3D cross-sectional images (Figure 3.S1B). Supporting this data, there were no significant differences between BCR[Ibsp/Acp5], BCR[Ibsp/WT] and WT mice in cortical bone parameters, including cortical bone area, total cortical area, cortical area fraction, and cortical thickness (Figure 3.S1E). Similar skeletal deformities were observed in the femurs from BCR[Ibsp/Acp5] mice in comparison to BCR[Ibsp/WT] and WT mice (Figure 3.S2A). 3D reconstructed micro-CT images of femurs showed significant shortening of the femora length and indicated trabecular impairments in BCR[Ibsp/Acp5] mice compared to BCR[Ibsp/WT] and WT (Figure 3.S2A-B). In contrast to vertebra data, trabecular BV/TV significantly increased in BCR[Ibsp/Acp5] mice compared to other groups, while no change was observed in trabecular number and separation (Figure 3.S2B). In agreement with vertebrae data, cortical parameters developed similarly between the groups in femurs, where cortical thickness, cortical bone area, and total cortical area showed no notable differences; however, cortical area fraction was significantly different (Figure 3.S2C). Taken together, this data suggests that BCR[Ibsp/Acp5] mice display deteriorated trabecula and malformation in the skeleton**.**
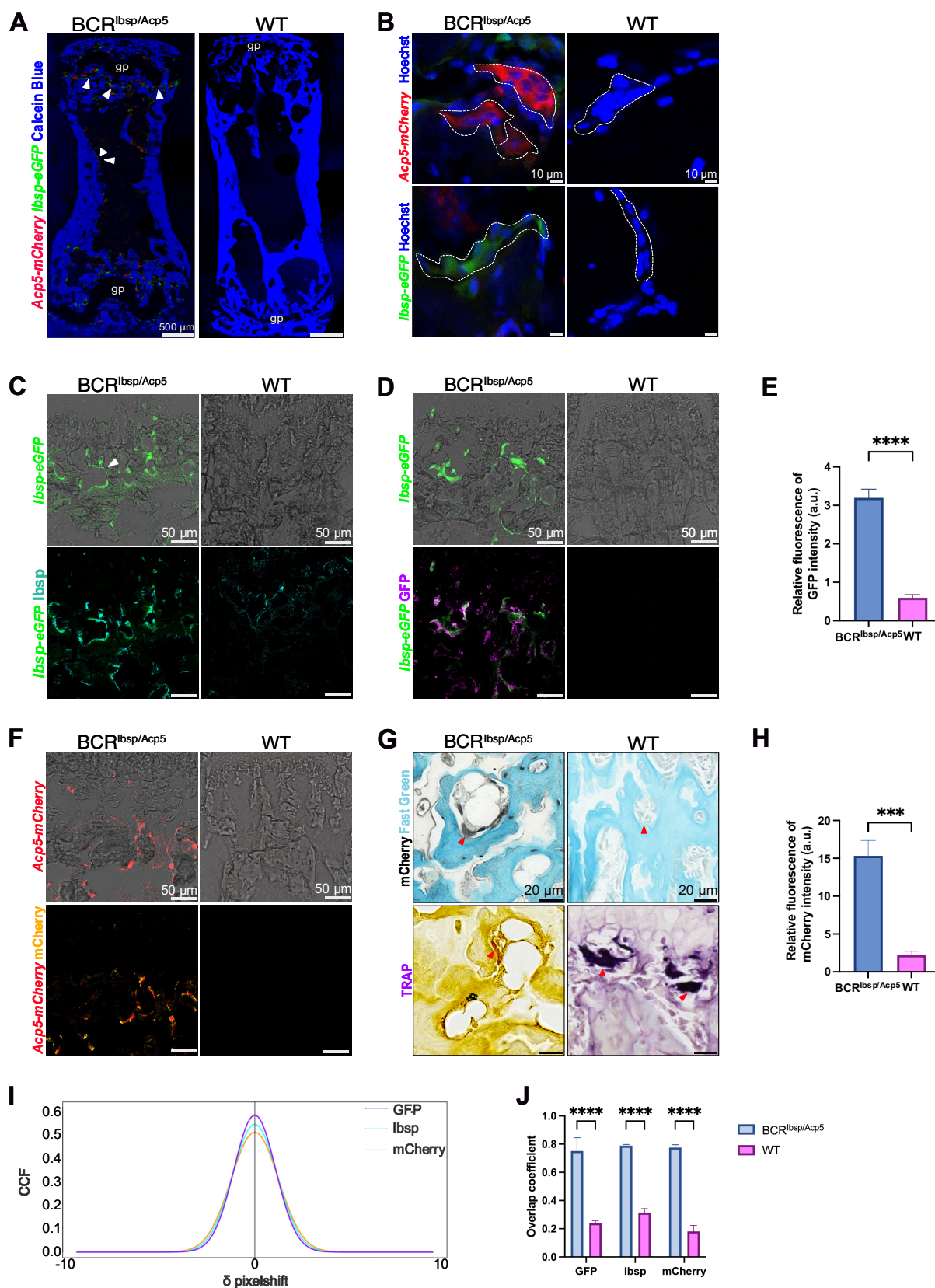
Figure 3.1 Characterization of fluorescent bone cells of BCR[Ibsp/Acp5] mice *in vivo*. A) Representative tile scan confocal images of the caudal vertebra showing mCherry (*Acp5-mCherry*, red), GFP (*Ibsp-eGFP,* green), and Calcein Blue (mineral, blue) staining in 5-week-

old BCR$^{Ibsp/Acp5}$ and WT mice. B) High-magnification images showing fluorescent signals of osteoclasts (Acp5-mCherry, red) and osteoblasts (*Ibsp-eGFP*, green) stained with Hoechst (nuclear, blue) in 5-week-old BCR$^{Ibsp/Acp5}$ and WT mice.C-D) Colocalization of GFP (*Ibsp-eGFP*) with GFP and Ibsp immunostainings. GFP signal (*Ibsp-eGFP*, green) is shown on bright-field images for each staining. C) Representative maximum intensity projections images of BCR$^{Ibsp/Acp5}$ and WT vertebra stained for GFP (purple) and D) Ibsp (cyan). E) Relative fluorescence intensity (a.u.) of GFP (*Ibsp-eGFP*) signals of BCR$^{Ibsp/Acp5}$ and WT vertebra sections. F) Colocalization of mCherry (Acp5-mCherry, red) with mCherry immunostaining (yellow). mCherry (Acp5-mCherry, red) signal is shown on bright-field images. G) mCherry immunostaining co-stained with fast green (turquoise) and TRAP (purple) staining in BCR$^{Ibsp/Acp5}$ and WT mice. Arrowheads indicate osteoclasts. H) Relative fluorescence intensity (a.u.) of mCherry (*Acp5-mCherry*) signals of BCR$^{Ibsp/Acp5}$ and WT vertebra sections. I) Quantitative Van Steensel's analyses and overlap colocalization coefficient. Data represent mean ± s.d., (n=3 mice/group), Significance was determined by two-tailed unpaired t-test, *p<0.05, **p<0.01, ***p<0.001.

TRAP-deficient osteoclasts display an altered morphology and function

Next, we isolated bone marrow macrophages from BCR$^{Ibsp/Acp5}$ and WT mice and cultured them *in vitro* to study the features of TRAP-deficient osteoclasts (Figure 3.2A). The same number of bone marrow macrophages was initially seeded for BCR$^{Ibsp/Acp5}$ and WT mice to differentiate into osteoclasts in the presence of the receptor activator of nuclear factor kappa B ligand (RANKL). Macrophages (cells treated with macrophage colony-stimulating factor (MCSF) and without RANKL) were used as the internal controls (Figure 3.2B-C). Similar to the *in vivo* data, TRAP staining confirmed the expression of TRAP$^+$ osteoclasts in WT mice but not in osteoclasts from BCR$^{Ibsp/Acp5}$ mice (Figure 3.2B). Nonetheless, TRAP-deficient osteoclasts from BCR$^{Ibsp/Acp5}$ mice were positive for Acp5-mCherry, whereas this signal was absent in osteoclasts from WT mice, as expected (Figure 3.2C). Formation of F-actin rings that are characteristic feature of mature osteoclasts were observed by Phalloidin-Hoechst staining in both groups (Figure 3.2C). Multinucleated (>2 nuclei) osteoclasts were identified from BCR$^{Ibsp/Acp5}$ mice and were similar to WT mice; however, these multinucleated osteoclasts in TRAP-deficient mice were smaller in size, irregular in shape (67.5 mm ± 27.0 for BCR$^{Ibsp/Acp5}$; 116.3 mm ± 73.3 for WT, p<0.0001) and more abundant (12.9 ± 4.9 for BCR$^{Ibsp/Acp5}$; 9.5 ± 4.5 for WT, p=0.0014) as presented in Figure 3.2D-E. Moreover, osteoclasts from BCR$^{Ibsp/Acp5}$ mice not only displayed irregular shapes and small sizes but also exhibited lower nuclear counts compared to those of WT osteoclasts (Figure 3.2G). Most of the observed osteoclasts from BCR$^{Ibsp/Acp5}$ mice contained 3-4 nuclei, and the osteoclasts with the highest nuclei count was 29 nuclei. In contrast, osteoclasts from the WT mice, displayed an average of 10 nuclei, whereas the largest osteoclasts contained up to 47 nuclei (Figure 3.2G). Differences in the

number of nuclei per osteoclasts between the groups were confirmed to be statistically significant using the Kolmogorov-Smirnov test ($p<0.000.1$) (Figure 3.2D). However, there was no discernible difference in the number of pre-osteoclasts containing two nuclei between BCR$^{Ibsp/Acp5}$ and WT mice (Figure 3.2H). These data suggested that osteoclasts from BCR$^{Ibsp/Acp5}$ mice are unable to form large highly nucleated osteoclasts, thus indicating a compromised fusion process, whereas the preosteoclast formation remains unaffected.

Additionally, when the cells were cultured on bone disks, the concentration of CTX, a serum marker indicating bone resorption, was decreased by 80% in osteoclasts from BCR$^{Ibsp/Acp5}$ mice compared to those from WT, thus illustrating that the resorption capacity of osteoclasts was reduced in BCR$^{Ibsp/Acp5}$ mice (Figure 3.2F).
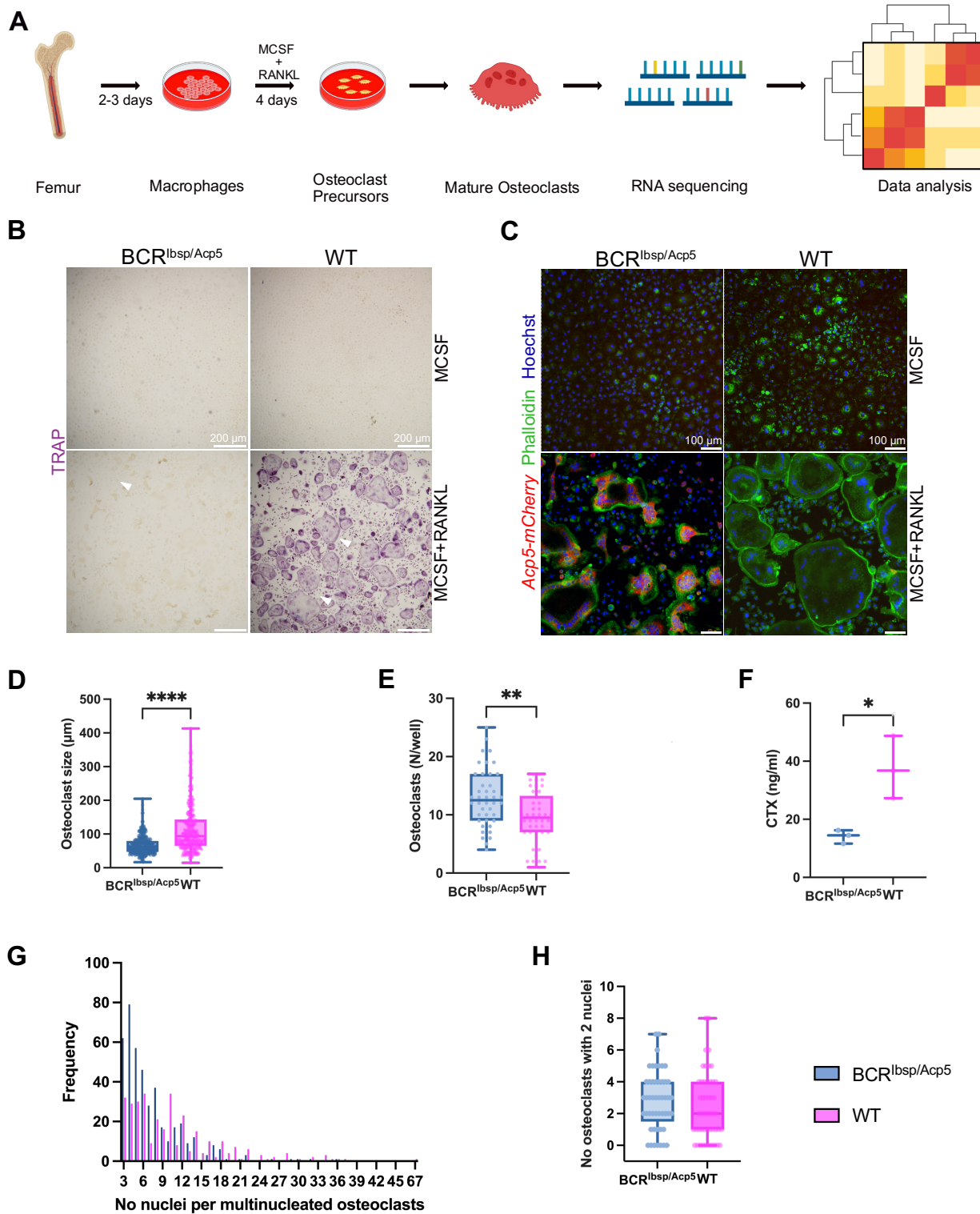
Figure 3.2 Cellular and functional properties of TRAP-deficient osteoclasts. A) Schematic showing the method for isolating and culturing primary osteoclasts from the femurs of BCR[Ibsp/Acp5] and WT mice at 5 weeks old. B) TRAP (purple) staining showed TRAP+ osteoclasts isolated from BCR[Ibsp/Acp5] and WT mice cultured in the presence of RANKL on day 4. C) Representative images of mCherry (Acp5-mCherry, red), Phalloidin (F-Actin, green), and Hoechst (nucleus, blue) staining in osteoclasts isolated from BCR[Ibsp/Acp5] and WT mice cultured in the presence of RANKL on day 4. D) Size of Phalloidin and Hoechst positive

multinucleated cells generated from macrophages isolated from BCR$^{Ibsp/Acp5}$ and WT mice in the presence of RANKL on day 4. E) Number of Phalloidin and Hoechst positive multinucleated cells generated from macrophages isolated from BCR$^{Ibsp/Acp5}$ and WT mice in the presence of RANKL on day 4. F) Measured CTX protein levels of osteoclasts derived from BCR$^{Ibsp/Acp5}$ and WT mice cultured on the bone disks in the presence of RANKL on day 4. G) Number of nuclei per multinucleated osteoclasts (>2 nuclei) from BCR$^{Ibsp/Acp5}$ and WT mice cultured in the presence of RANKL on day 4. Data represent mean ± s.d., (n=3 mice/group), ****<0.0001 by Kolmogorov-Smirnov test. H) Number of nuclei per osteoclast with two nuclei from BCR$^{Ibsp/Acp5}$ and WT mice cultured in the presence of RANKL on day 4. Box plots represent max and min values with data points, (n=3 mice/group). Significance was determined by two-tailed unpaired t-test, *p<0.05, **p<0.01, ***p<0.001.

To gain further insights into the characteristics of TRAP-deficient osteoclasts, we performed bulk RNA sequencing (RNA-seq) analysis of cells obtained from BCR$^{Ibsp/Acp5}$ and WT mice that were isolated and cultured *in vitro*. Principal component analysis (PCA) of the RNA-seq data indicated a 92% variation between the BCR$^{Ibsp/Acp5}$ and WT samples that fell into two groups: macrophages (BCR$^{Ibsp/Acp5}$-M, WT-M) and osteoclasts (BCR$^{Ibsp/Acp5}$, WT). Within each group, gene expression levels exhibited less variations (Figure 3.3A). Gene set enrichment analysis revealed a downregulation in BCR$^{Ibsp/Acp5}$ mice of essential signaling pathways promoting growth and proliferation, such as Hippo, fibroblast growth factor receptors (FGFR), and negative regulators of the Wnt signaling pathway (Figure 3.3B). Consistent with the immunostaining results, *TRAP* (*Acp5*) was downregulated in osteoclasts from BCR$^{Ibsp/Acp5}$ mice, whereas genes important for osteoclastogenesis such as *Ctsk*, *Calcr*, *Nfatc1*, and *Tnfrsf11a*, exhibited the same degree of expression in osteoclasts of BCR$^{Ibsp/Acp5}$ and WT mouse osteoclasts (Figure 3.3C-D). Taken together, these results indicated that reduced TRAP activity did not alter the expression of other essential osteoclast-associated genes (Figure 3.3D).
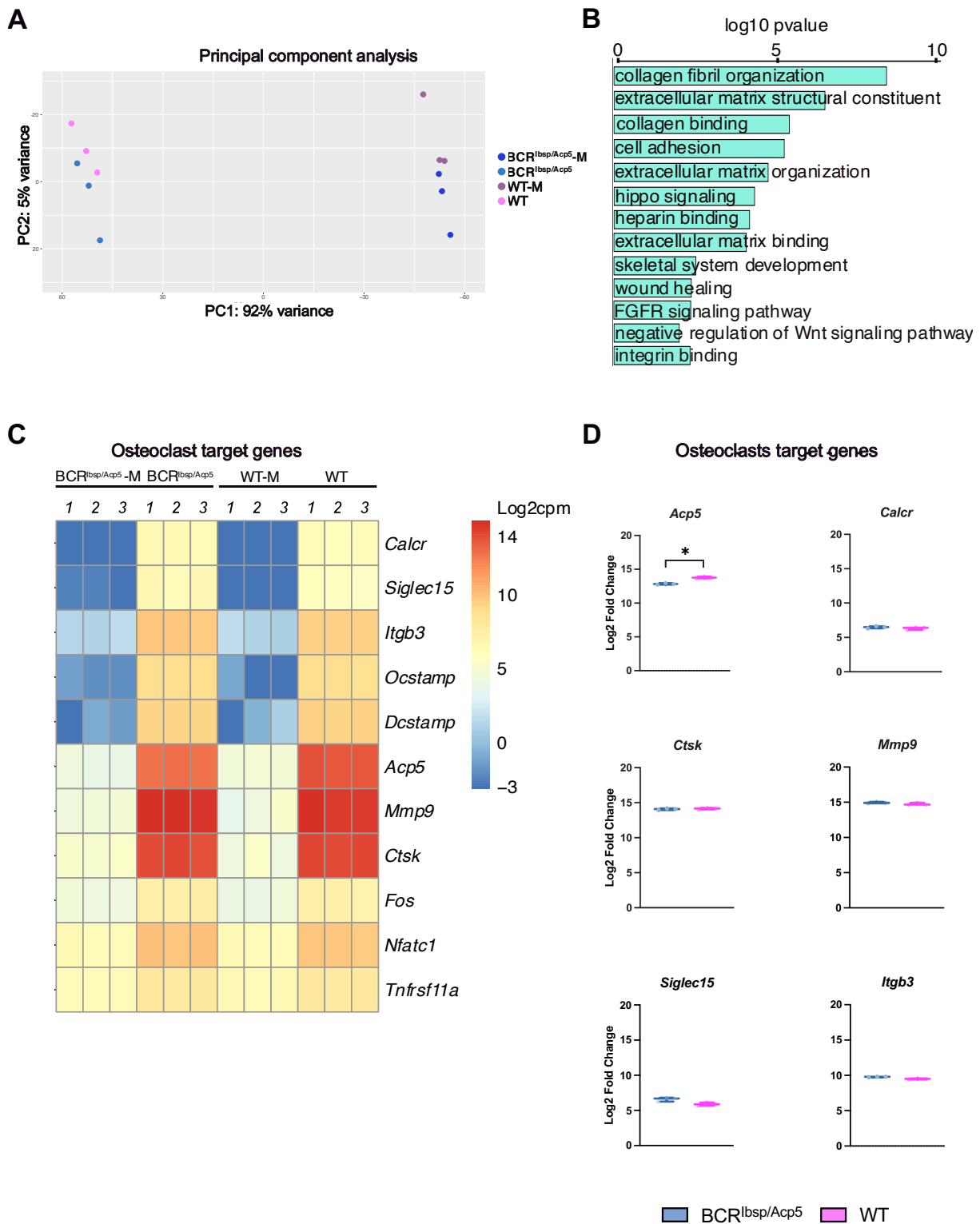
Figure 3.3 Transcriptional landscape and gene expression pattern of osteoclasts from BCR[Ibsp/Acp5] mice. A) Principal component analysis of RNA-sequencing data using the top 500 most variable genes across the samples. The first component exhibits 92% variance (PC1), and the second component (PC2) shows 5% variance within sample groups. B) Downregulated signaling pathway components between primary osteoclasts derived from BCR[Ibsp/Acp5] and WT mice (in the presence of RANKL). C) Heatmap of osteoclasts target genes in primary osteoclast derived from BCR[Ibsp/Acp5] and WT mice (in the presence of RANKL) and macrophages (in the

presence of MCSF without RANKL). Color intensity indicates normalized log2(cpm) expression values. D) Differentially regulated osteoclasts target genes (*Acp5, Calcr, Ctsk, Mmp9, Siglec15, Itgb3*) in BCR$^{Ibsp/Acp5}$ vs. WT mice. Data represent the normalized Log2 (cpm) of RNA seq data, mean ± s.d., (n=3 mice/group). Significance was determined by Mann-Whitney test, *$p<0.05$, **$p<0.01$, ***$p<0.001$.

BCR$^{Ibsp/Acp5}$ mice exhibit a similar response to in vivo mechanical loading as WT mice

Next, we investigated the mechanosensitivity of BCR$^{Ibsp/Acp5}$ mice using an *in vivo* tail-loading model (Figure 3.4A). To explore how bone adapts to mechanical cues, we employed weekly time-lapsed micro-CT images complemented by micro-FE analysis. This approach sheds light on tissue-level responses and provides insights into the activities of osteoblasts and osteoclasts despite the observed morphological deformities in the trabecula and the skeleton of BCR$^{Ibsp/Acp5}$ mice.

Figure 3.4B displays the representative micro-CT images illustrating the disparity between the last (week 4) and the initial (week 0) time points of loading and reveals the thickening of the trabecula and cortex in both BCR and WT mice in contrast to their respective controls. Time-lapsed micro-CT images indicated a similar increase in static parameters in loaded BCR$^{Ibsp/Acp5}$ and WT mice compared to their sham-loaded (control) counterparts (Figure 3.4B-C, Table 3.S3). In response to four weeks of loading, the trabecular bone volume fraction (BV/TV) exhibited a remarkable increase of +22% in loaded BCR$^{Ibsp/Acp5}$ mice and +12% in loaded WT mice compared to their respective controls (Figure 3.4B). This change in BV/TV was accompanied by a significant increase in trabecular thickness (+10% in BCR$^{Ibsp/Acp5}$, and +3% in WT mice), as well as cortical thickness (+6% in BCR$^{Ibsp/Acp5}$, and +5% in WT mice), and cortical bone area fraction (+6% in both BCR$^{Ibsp/Acp5}$ and WT mice) (Figure 3.4B-C). Furthermore, the difference in trabecular BV/TV between the last and the initial time points accentuated the anabolic effect of mechanical loading within the loaded mice that was distinctly noticeable through a substantial increase in BV/TV after 4 weeks (+27% in BCR$^{Ibsp/Acp5}$, +16% in WT) (Figure 3.4D). In contrast, a decrease in BV/TV indicated the catabolic effect of loading in sham-loaded mice (-4% in BCR$^{Ibsp/Acp5}$ and, -3% in WT mice, respectively) (Figure 3.4D). Additionally, tissue mineral density (TMD) in both loaded mice increased at the end of 4 weeks of loading compared to their corresponding controls (+0.2% in BCR$^{Ibsp/Acp5}$ and +0.01% in WT mice, respectively) (Figure 3.4E) Considering the dynamic parameters that quantify the bone formation and resorption activities from time-lapsed micro-CT images, Figure 3.5A illustrates

a representative visualization of a caudal vertebra, indicating bone remodeling sites (formation, resorption, and quiescence) and their corresponding local mechanical signals that are presented as effective strain [26]. Based on the analysis of parameters linked to bone formation events, the bone formation rate (BFR) was notably higher in loaded BCR[Ibsp/Acp5] and WT mice compared to their sham-loaded counterparts (+34% in BCR[Ibsp/Acp5] and +11% in WT mice) (Figure 3.5B). Moreover, mineral apposition rate [27] that indicates the thickness of the formation packages, was not notably different between the loaded and sham-loaded groups for both BCR[Ibsp/Acp5] and WT mice (+11% in BCR[Ibsp/Acp5] and +3% in WT mice). In contrast, the mineralizing surface [28] that refers to the area of formation sites, was significantly higher in both loaded groups (+30% in BCR[Ibsp/Acp5] and +19% in WT mice) (Figure 3.5B). Focusing on the analysis of bone resorption events, it is noteworthy that, the bone resorption rate (BRR) exhibited a pronounced increase in the sham-loaded groups compared to that in loaded mice (+65% in BCR[Ibsp/Acp5] and +52% in WT mice). Mineral resorption rate (MRR), indicating the depth of the resorption cavities, exhibited no significant differences between loaded and sham-loaded mice for both groups (-5% in BCR[Ibsp/Acp5] and -4% in WT mice). The surface area of the eroded surfaces (ES) decreased considerably with loading for the loaded groups (-47% in BCR[Ibsp/Acp5] mice and -40% in WT mice) (Figure 3.5B). Moreover, the net remodeling rate that signifies the difference between BFR and BRR demonstrated that loaded mice exhibited a constant positive remodeling trend throughout all weeks (+1.2% per day in BCR[Ibsp/Acp5] mice and +0.6% per day in WT mice), thus indicating a bone gain. In contrast, sham-loaded mice exhibited a negative remodeling (-0.2% per day in BCR[Ibsp/Acp5] and -0.3% in WT), that was associated with bone loss (Figure 3.5B).

In order to gain a deeper understanding of the cellular-level mechano-molecular mechanism, we also examined the expression of cellular mechanotransduction markers. As YAP1 and TAZ-Hippo pathway effectors have been demonstrated to function as mechanotransducers where they modulate mechano-responsive gene transcription programs that govern cellular functions[29, 30], we assessed TAZ expression in response to mechanical loading on the caudal vertebrae. Hoechst staining highlighted the vertebral architecture of loaded and sham-loaded BCR[Ibsp/Acp5] and WT sections (Figure 3.S3A). Immunostaining for TAZ exhibited significantly higher expression around the trabeculae in loaded groups than in the sham-loaded controls, particularly in BCR[Ibsp/Acp5] mice (Figure 3.S3B-C). Moreover, the serum CTX protein levels in loaded and sham-loaded BCR and WT mice indicated normal levels and were not significantly different between the groups despite low CTX levels observed *in vitro* (Figure 3.S3D).
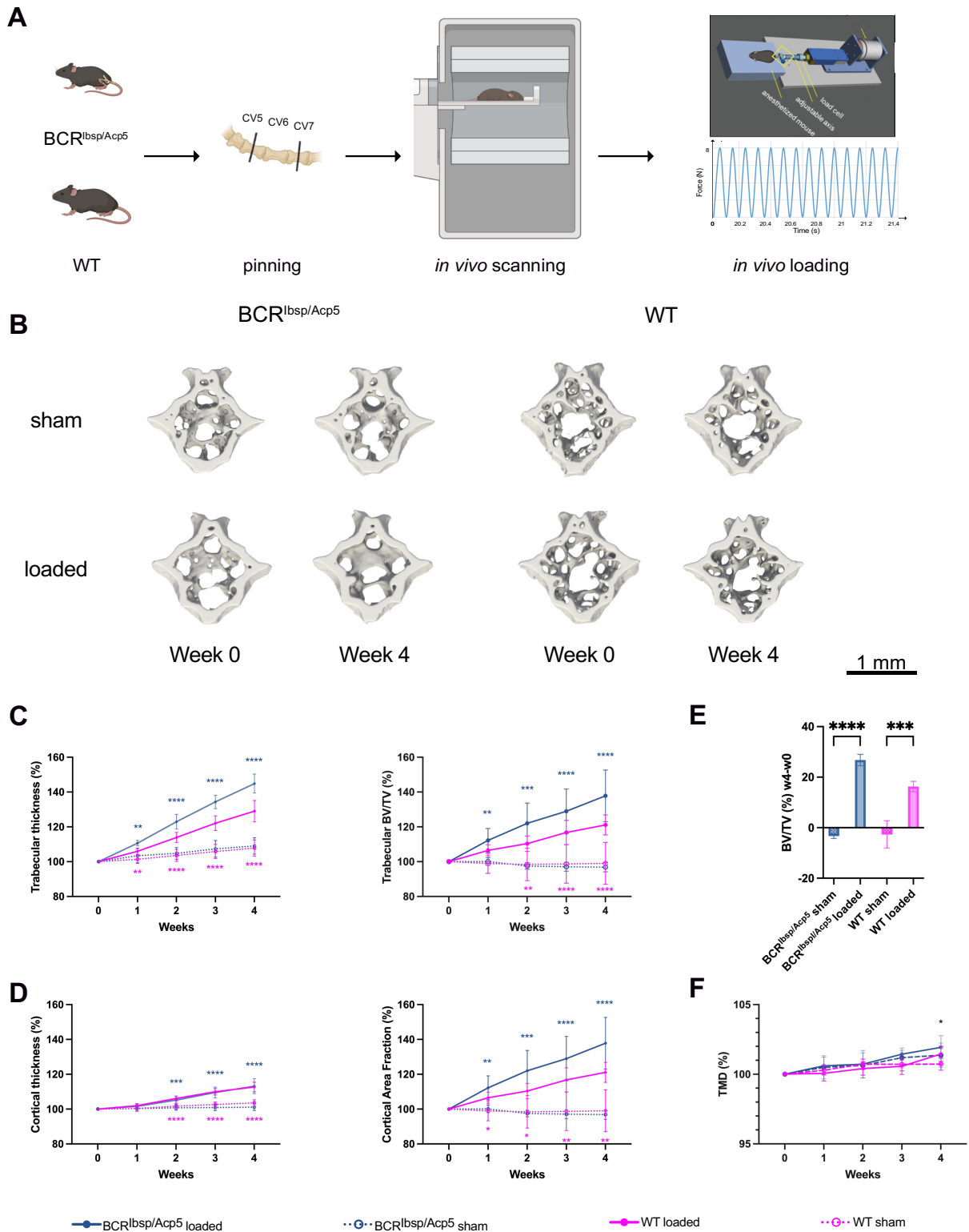
Figure 3.4 Micro-CT-based evaluation of static bone parameters upon cyclic mechanical loading. A) Schematic showing the in vivo tail loading setup: the application of force is controlled through two pins inserted in the neighboring vertebrae (CV5 and CV7) connected to a mechanical loading device, and the 6th caudal vertebra (CV6) was either cyclically loaded by a force of 8N or sham loaded (0N). All mice were scanned weekly with micro-CT for 4 weeks. B) Representative micro-CT images from the sham and loaded groups of BCR[Ibsp/Acp5]

and WT mice were taken at two time points: the initial time point (week 0) and the final time point (week 4) during the 4-week loading period. *In vivo* micro-CT scans were conducted to capture the changes in bone microstructure. For loading groups, thickening of the trabecular structure can be observed, while on the sham groups minimal changes in the bone structure between two time points can be seen. C-D) Changes in the structural bone morphometric parameters over the 4-week tail loading: trabecular thickness, trabecular bone volume fraction (BV/TV), cortical thickness, and cortical area fraction, normalized to the first time point and shown as percentages. E) Change of bone volume fraction from week 4 to week 0 (BV/TV week 4/week 0). F) Changes in the tissue mineral density (TMD) over the 4-week tail loading. Normalized to the first time point and shown as percentages. Data represent mean $\pm$ s.d., (n=9-10 mice/group). Significance was determined by two-way ANOVA with Dunnett correction, *p<0.05, **p<0.01, ***p<0.001, ****p<0.0001.
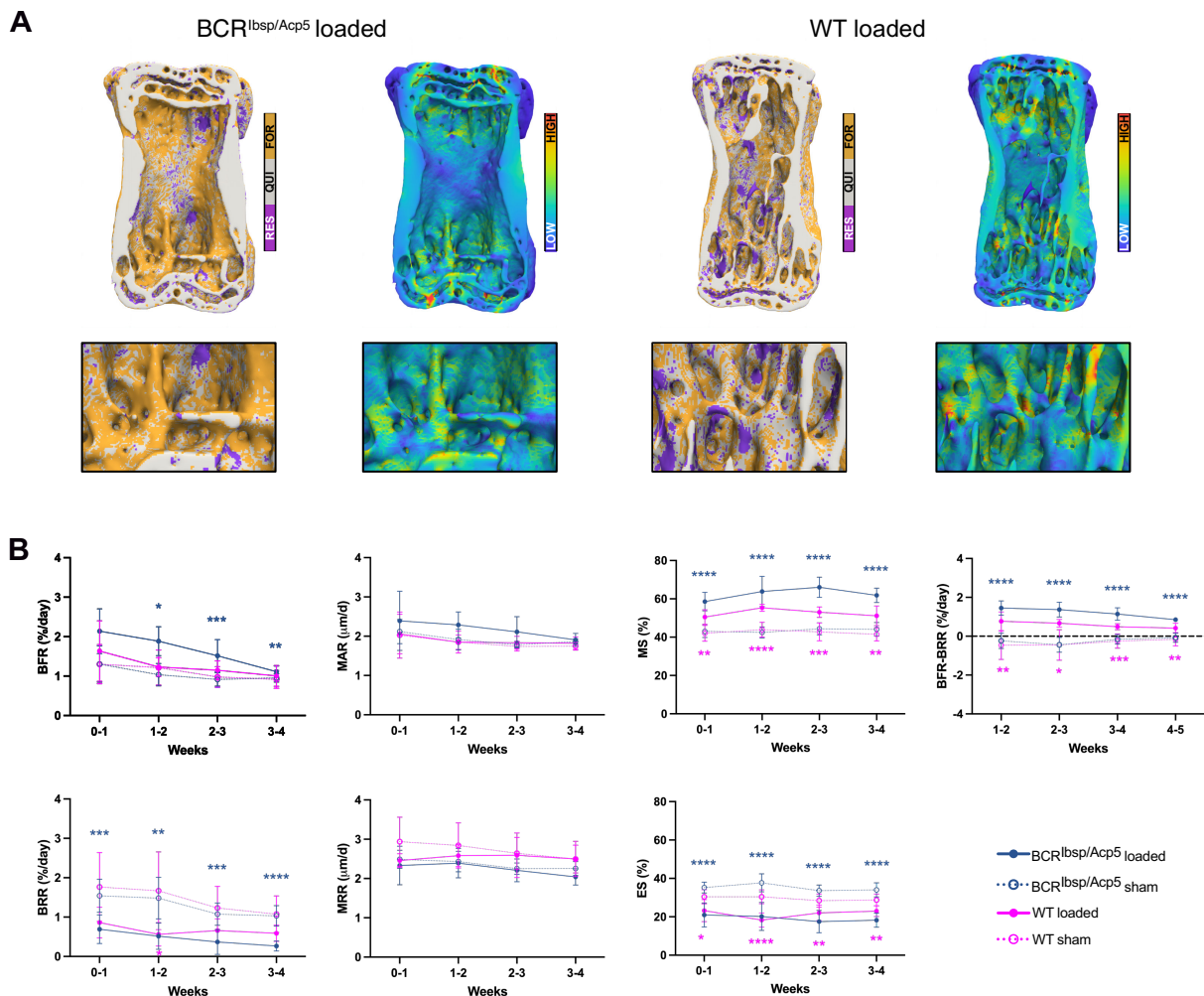
Figure 3.5 Mechanically driven regulation of the bone remodeling activity of BCR[Ibsp/Acp5] mice. A) Visualization of bone remodeling sites (formation, quiescence, and resorption) in the caudal vertebra in vivo. Overlay of time-lapsed micro-CT image showing sites of bone formation (orange), quiescence (grey), and resorption (purple) at week 2. The corresponding map of the effective strain highlights the spatial distribution of mechanical strains showing higher and lower (blue) strain regions computed by micro-FE analysis. B) Dynamic bone morphometric parameters in the trabeculae over 4-week tail loading assessed by in vivo micro-CT: formation events as BFR, MAR, MS; resorption events as BRR, MRR, and ES. Changes

in the net remodeling rate were shown as the difference between BFR and BRR over the 4-week loading period. Data represent mean ± s.d., (n=9-10 mice/group). Significance was determined by two-way ANOVA with Dunnett correction, *p<0.05, **p<0.01, ***p<0.001.

Bone adaptation in BCRIbsp/Acp5 mice is also controlled by the local mechanical in vivo environment

Finally, to investigate bone mechanoregulation in BCR[Ibsp/Acp5] mice, the association between remodeling events and the local mechanical *in vivo* environment was analyzed. Bone resorption sites were associated with lower effective strain values compared to quiescent clusters in all groups and loading regimens, with the exception of sham-loaded BCR[Ibsp/Acp5] mice at weeks 3-4 (Figure 3.6A). For each remodeling event, the effective strain values for the loaded groups exhibited lower variability, as indicated by narrower interquartile ranges compared to those of the sham-loaded groups, thus highlighting a distinct response to mechanical loading and association with remodeling events (Figure 3.6A). Similar results were observed in the conditional probability curves that were associated likelihood of observing each remodeling event for a given mechanical signal value. Between weeks 0-4, resorption events were strongly associated with lower normalized effective strains (below 25% for BCR[Ibsp/Acp5] and below 27% for WT mice), whereas a higher probability of formation events was concurrent with higher mechanical signal values (Figure 3.6B). The loaded groups exhibited a clear separation between formation and quiescence events for higher normalized effective strains (greater than 60%), and there was a narrower separation between remodeling events in the same interval for sham-loaded groups, particularly for the BCR[Ibsp/Acp5] mice, where the curves were close to the random probability of 0.33. For all groups and time points, the correct classification rate [24, 31] values determined from the conditional probability curves were above 0.33, thus supporting a non-random association between the magnitude of effective strain and remodeling events. Additionally, there were significant differences between loaded and sham-loaded BCR[Ibsp/Acp5] mice up to week 3 (Figure 3.6C), and this was consistent with the strong anabolic response presented in Figure 5B. Although the loaded WT mice had greater CCR values compared to their sham-loaded counterparts, the differences were not statistically significant.

Furthermore, we assessed mechanoregulation using remodeling velocity (RmV) curves that associate the average remodeling surface velocity with effective strain. The RmV curves obtained for each week resembled the mechanostat function proposed by Frost [5], and they were accurately fitted with hyperbolic functions with normalized root mean squared errors (NRMSE) to below 5% (Table 3.S4). From these curves, biologically meaningful remodeling

parameters were derived and included the formation and resorption saturation levels (FSL and RSL respectively) that determine the magnitude of these events. Additionally, the remodeling threshold (RmT) and velocity modulus (RmVM) provided a quantitative measure of the mechanosensitivity of the model to the applied loading. The loaded $BCR^{Ibsp/Acp5}$ mice exhibited the highest FSL values across all weeks (Figure 3.6D) that were significantly different from those observed in the other groups (Table 3.S5). Similarly, loaded WT mice exhibited significant differences in FSL compared to that of both sham-loaded groups. The RSL values were consistently higher for both loaded groups up to week 2 compared to their sham-loaded counterparts, given the increasing number of formation events for this loading condition that shifted the range of the RmV curves towards positive values. Significant differences in RSL were observed between the sham-loaded and loaded groups of $BCR^{Ibsp/Acp5}$ mice during weeks 1-2 and 2-3. However, when comparing the loaded groups of $BCR^{Ibsp/Acp5}$ and WT mice, the differences in RSL were significant only during weeks 2-3 (Table 3.S5).

Focusing on the mechanosensitivity descriptors, the RmVM values were consistently higher in the loaded groups than they were in the sham-loaded groups. As expected, cyclic loading created a closely regulated mechanically driven environment, which emphasizes the dependency of the RmV values on the magnitude of the local effective strains (Table 3.S5). Indeed, there were significant differences between loaded and sham-loaded groups for both $BCR^{Ibsp/Acp5}$ and WT mice up to weeks 2 and 3, respectively in contrast to the comparisons between the loaded or sham-loaded WT and $BCR^{Ibsp/Acp5}$ mice. In weeks 3-4, the loaded groups had adapted to the supraphysiological loading condition, as supported by an increase over time in the Pearson correlation coefficient (PCC) between the RmV curves of loaded and sham-loaded $BCR^{Ibsp/Acp5}$ and WT mice. In particular, these values increased from 0.895 and 0.949 (p < 0.0001) at weeks 0-1 to 0.966 and 0.978 (p < 0.0001) at weeks 3-4, for $BCR^{Ibsp/Acp5}$ and WT mice, respectively, supporting comparable bone remodeling responses between these groups except for differences in RmT. Comparably, the RmV curves between the loaded groups also evolved towards a more uniform bone remodeling response based on the increase in the PCC between the loaded $BCR^{Ibsp/Acp5}$ and WT mice from 0.910 at weeks 0-1 to 0.955 at weeks 3-4. Regarding the RmT parameter, the sham-loaded groups exhibited consistently higher values in comparison to loaded groups. This indicates that in a mechanically driven environment, there is a precise regulation on the threshold to initiate formation that restricts resorption events to a narrower interval of effective strain values. $BCR^{Ibsp/Acp5}$ loaded, and sham-loaded mice exhibited significant differences for all weeks, whereas discrepancies

between WT mice were significant only at weeks 1-2 and 2-3. Importantly, there were no significant differences were observed between BCR[Ibsp/Acp5] and WT mice in either the sham-loaded or loaded groups at any time point, except for the comparison between the loaded groups at weeks 3-4. The similarities in the responses observed in the conditional probability curves and between parameters obtained from the remodeling velocity curves from BCR[Ibsp/Acp5] and WT mice reinforce the comparable mechanoregulation between these mice.
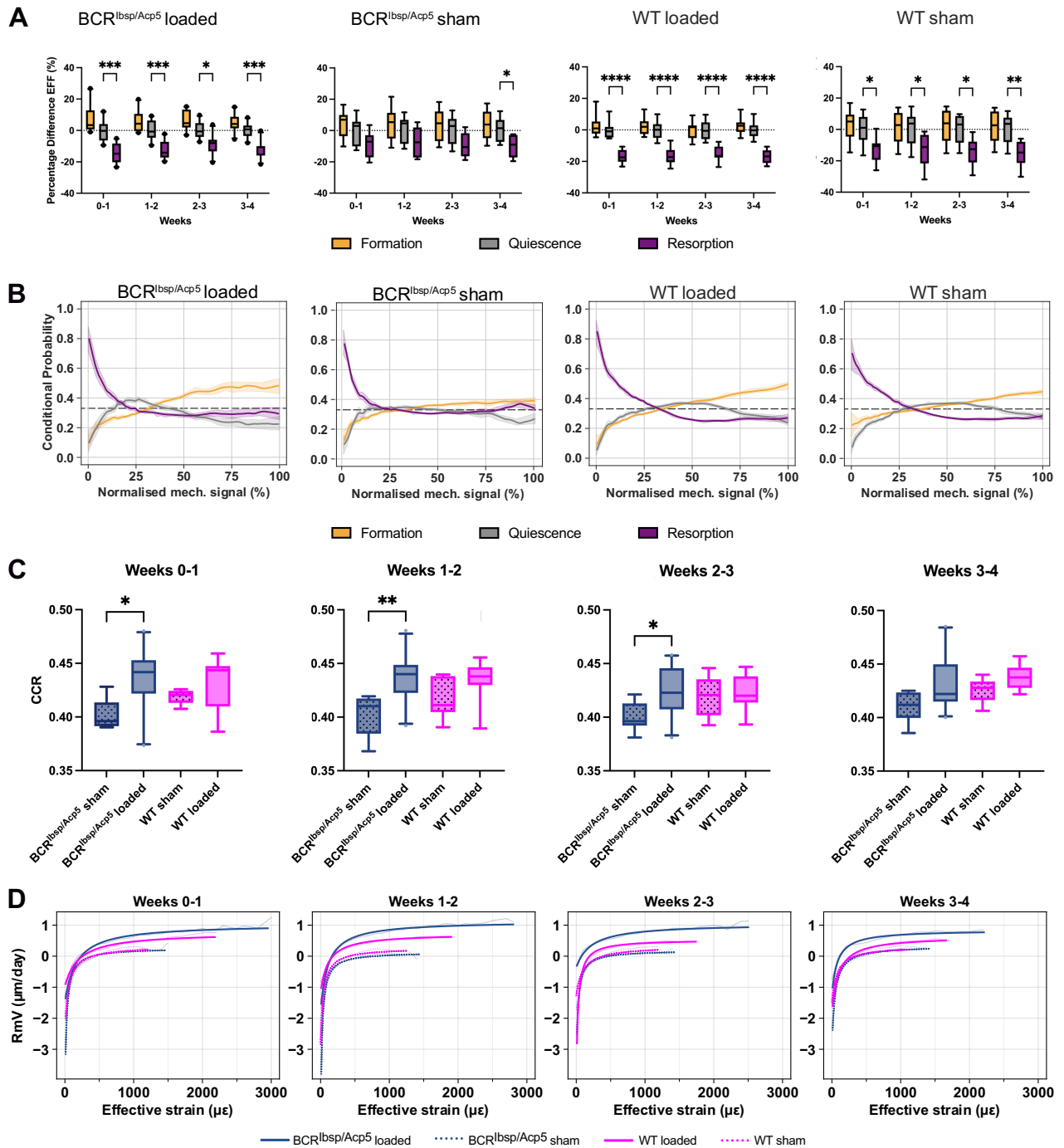
Figure 3.6 Quantification of mechanoregulation information from time-lapsed *in vivo* micro-CT images of the 6th caudal vertebrae. A) Mean effective strain at formation, quiescent, and resorption sites expressed as the percentage difference from the mean quiescent effective strain for all weekly time points. B) Conditional probability curves connecting the mechanical environment expressed as normalized effective strain with remodeling events, computed for all groups using micro-FE with homogeneous material properties. The plots show the mean probability line per group after applying a LOWESS operation for the interval 0-4 weeks and its corresponding 95% confidence interval. The dashed line at 0.33 identifies the probability of a random event for a ternary classification case. C) Comparison of correct classification rate values obtained from conditional probability curves for 0–4 weeks. Higher CCR values indicate a higher sensitivity to retrieve mechanoregulation information. D) Estimated mechanostat remodeling velocity curves fitted with continuous hyperbola functions for weekly time points and all groups. Data points are filtered such that at least three mice are averaged per group for each mechanical signal value. Effective strain values are also obtained from micro-FE analysis using homogeneous material properties. Data represents mean differences, (n=9-10 mice/group). Significance was determined by two-tailed student t-test, *p<0.05, **p<0.01, ***p<0.001.

3.1.3 Discussion

Numerous studies have provided evidence for the involvement of TRAP in essential molecular processes, including cell recruitment [32], cell attachment [15], and the development of long bones [32, 33]. However, the role of TRAP in multiscale bone mechanoregulation remained incompletely understood. Here, we demonstrated that TRAP is not a critical regulator of mechano-regulated trabecular bone remodeling and adaptation. Our findings demonstrate the feasibility of employing CRISPR-Cas9 mediated fluorescent reporter (BCR[Ibsp/Acp5]) mice to facilitate the identification, tracking, and characterization of TRAP-deficient osteoclasts and osteoblasts fluorescently *in vivo* and *in vitro*. However, despite the absence of TRAP activity, the unchanged expression of other critical osteoclast-associated genes enabled functional trabecular bone remodeling in a controlled, mechanically driven environment in BCR[Ibsp/Acp5] mice.

TRAP expression in our mice is not expected to be limited to osteoclasts but can also be found in macrophages and other immune cell types. However, the observed phenotypes of BCR[Ibsp/Acp5] mice in our study, including trabecular bone impairments and reduced resorption capacity *in vitro,* were still remarkably similar to those observed in TRAP knock-out mice [18, 34-37]. Moreover, TRAP deficiency in our mice appeared to compromise the trabecular bone structure without altering mineral density, and this was inconsistent with the findings from the previous TRAP knock-out mouse studies. These studies have suggested that the deficiency in acid phosphatase activity in TRAP knock-out mice impacts the regulation of osteoclast to the

mineralization front through the partial dephosphorylation of osteopontin (OPN) and bone sialoprotein (BSP), thereby potentially resulting in increased mineralization [18.] The difference observed in our mouse model could potentially be attributed to the underestimation of tissue mineral density values acquired through micro-CT, as TMD is an average value computed over the entire image. This diminishes its specificity.

In addition to providing insights into the skeletal morphology of our TRAP-deficient mice, it is important to characterize fluorescent TRAP-deficient osteoclasts. Notably, distinct disparities were observed between osteoclasts from BCR$^{Ibsp/Acp5}$ and WT mice; TRAP-deficient osteoclasts exhibited smaller and irregular shapes and were more abundant than the osteoclasts from WT mice. Additionally, BCR$^{Ibsp/Acp5}$ mice also exhibited a lower number of nuclei in their osteoclasts than that of osteoclasts from WT mice. However, there was no observable difference in the number of pre-osteoclasts containing two nuclei between the groups, thus indicating that the formation of large, highly nucleated osteoclasts was compromised whereas the formation of pre-osteoclasts remained unaffected in BCR$^{Ibsp/Acp5}$ mice. Additionally, these discrepancies observed in the osteoclasts of BCR$^{Ibsp/Acp5}$ mice may indicate that the fusion process of osteoclasts or their maturation does not proceed as expected, and this likely contributes to the observed clustering of smaller osteoclasts. Furthermore, this potentially disrupted fusion process strongly reduced CTX levels *in vitro*, thus implying a decreased capacity for bone resorption. However, unchanged serum CTX levels in our TRAP-deficient mice, combined with the outcomes from the *in vivo* loading indicated that the bone resorption capacity remained unaffected.

Despite the downregulation of TRAP expression, other key genes involved in osteoclastogenesis showed unchanged expression levels (*Calcr, Ctsk, Mmp9*) in both TRAP-deficient and WT osteoclasts. Expression levels of *Calcr, Ctsk, and Mmp9,* being essential for bone resorption and remodeling, displayed only slight differences between the osteoclasts of BCR$^{Ibsp/Acp5}$ and WT mice. Therefore, these small distinctions may contribute to maintaining the stability of osteoclast function for bone resorption in BCR$^{Ibsp/Acp5}$ mice but might not trigger significant alterations in overall osteoclast function and the associated bone phenotype for TRAP deficiency.

Furthermore, we showed that TRAP-deficient BCR$^{Ibsp/Acp5}$ mice exhibited robust mechanosensitivity during caudal vertebra loading, on par with WT mice. Structural and dynamic bone morphometric parameters resulted in equivalent outcomes in both mice with no

significant differences observed between the genotypes, demonstrating that loading exerted an anabolic effect on the bone for both mice, as previously observed [20, 38, 39]. The trabecular bone deformity observed in the BCR[Ibsp/Acp5] mice, along with their lower trabecular BV/TV explains their stronger response to mechanical loading. Despite receiving the same mechanical dose, BCR[Ibsp/Acp5] mice, which had lower trabecular BV/TV than WT mice, exhibited an increased area of high local surface strains. These high local surface strains are known to be associated with an increased likelihood of bone formation events. Therefore, the altered trabecular bone structure in BCR[Ibsp/Acp5] mice contributes to their increased response to mechanical loading, ultimately leading to increased bone formation in response to mechanical stimuli. The observed increase in BV/TV is in agreement with prior findings, where loads of 4N resulted in substantial BV/TV increases compared to sham and 2N [40]. Notably, the reported increase with an 8N load was significantly greater. This suggests that the 8N load in BCR mice is deemed supraphysiological, and surpasses the threshold for pronounced anabolic responses, even within the initially lower trabecular BV/TV. Additionally, *in silico* bone loading estimations based on micro-FE have determined an axial compressive force of approximately 4N as the equivalent loading acting on sham-loaded mice during the loading experiment [41]. This value can be deemed as an upper bound for physiological loading, thus supporting our assumption that a force of 8N can be considered supraphysiological. Moreover, the quantification of bone formation and resorption sites indicated that cyclic mechanical loading primarily influenced the surface area of these events. Therefore, an increase in the area of mineralized surfaces and a reduction in eroded surfaces may also suggest an increased osteoblast activity in BCR[Ibsp/Acp5] mice. This notion aligns with previous findings where TRAP knock-out mice displayed signs of premature maturation of osteoblasts [33] and higher mineralization of the bone matrix due to the partial dephosphorylation of OPN and BSP mentioned earlier [15]. Thus, downregulation of TRAP in osteoclasts from BCR[Ibsp/Acp5] mice could increase anabolic responses due to increased activity of osteoblasts.

We further provided evidence for the comparable expression of mechano-molecular markers at the cellular level. TAZ expression increased in loaded WT and BCR[Ibsp/Acp5] mice, and this increase was more prominently in BCR[Ibsp/Acp5] mice thus indicating a robust reaction of TRAP-deficient mice to cellular mechanical cues. Upon osteoblast differentiation, TAZ activity was increased, ultimately leading to its interaction with Runx2 and subsequent activation of the Runx2 gene transcription pathway, and thereby playing a significant role in the regulation of

osteoblastogenesis [42, 43]. In our study, increased TAZ expression in loaded BCR$^{Ibsp/Acp5}$ mice might suggest a potential link to increased osteoblast activity in response to mechanical stimuli.

Consistent with these results, we observed comparable mechanoregulation in the BCR$^{Ibsp/Acp5}$ and WT mice. Previous studies have used mechanoregulation analysis to evaluate the effects of cyclic mechanical loading on the vertebrae [8, 44, 45], femur [24, 46], and tibia [21, 47] of C57Bl/6J mice. Similarly, this analysis highlighted a similar EFF distribution of remodeling clusters between our TRAP-deficient and WT mice, where the mean EFF at formation sites was higher than that at quiescent sites and lower than that at resorption sites in both the loaded and sham groups. In both loading groups, these differences were significant, thus suggesting that mechanical cues strongly influenced the remodeling. As the CCR values, remodeling velocity curves, and derived parameters were indicated to capture distinct responses to cyclic mechanical loading at varying loading frequencies, we anticipate that this analysis are sensitive to differences in mechanically driven bone adaptation between BCR$^{Ibsp/Acp5}$ and WT mice. Notably, lower RmVM values for sham groups described a flatter RmV response, aligning with the observations from conditional probability curves where formation and quiescent events were closer to the random probability for higher normalized effective strains and suggesting an increased number of non-targeted remodeling events that are rather stochastic than mechanically-driven.[48, 49] Concurrently, the increase in formation events in response to supraphysiological loading shifted RmV curves towards higher velocity values and was followed by lower RmT values. As RmV curves describe bone remodeling events at the micrometer scale, RmT values mark the transition between low strains where resorption is primarily observed and high strains where the formation, on average, occurs more often and to a greater extent. Importantly, the trends observed in our data align with the original predictions of Frost [5], who argued that increased mechanical demands could decrease the magnitude of this parameter. Frost further argued that the region around RmT would define an adapted window [5], also described as lazy zone [47], that is a range of strains where bone formation and resorption would balance each other. In the mouse bone and with the resolution of the micro-CT used here, non-targeted remodeling and mechanically driven modeling events were analyzed collectively. Such an interval, if existent, would appear as a uniform RmV region bounded by monotonic changes in RmV for lower and higher effective strains. In agreement with previous results [8, 21, 23], our findings provided no evidence of a lazy zone for any group or loading condition.

Conversely, mechanical unloading, often performed through hindlimb suspension or immobilization, leads to loss of bone mass and strength [50]. This loss of bone induced by unloading stems from the decoupling of bone turnover, where bone formation diminishes, while bone resorption increases [51]. In BCR[Ibsp/Acp5] mice, already afflicted with TRAP deficiency impairing their osteoclast function *in vivo*, unloading could lead to significant bone loss. TRAP plays a vital role in osteoclast function, and its absence in BCR[Ibsp/Acp5] mice potentially renders them susceptible to bone loss during unloading. However, considering their smaller osteoclasts with reduced resorptive capacity *in vitro*, TRAP might also play a protective role against unloading bone loss.

Exercise is well-known to exert a positive influence on bone health [52]. Weight-bearing activities and resistance training have been scientifically demonstrated to stimulate bone remodeling and enhance bone density [52]. In the context of BCR[Ibsp/Acp5] mice, their response to exercise would likely resemble the results observed after *in vivo* mechanical loading, where they exhibit increased bone formation similar to that of WT mice. This connection is based on the findings that exercise, particularly resistance training such as treadmill running, has been demonstrated to increase bone formation and tissue-level mechanical properties in young mice [52]. Despite the TRAP deficiency that affects the osteoclast function in BCR[Ibsp/Acp5] mice, the beneficial effects of exercise on bone formation may persist. Consequently, exercise could potentially play a role in maintaining or even improving bone mass in our TRAP-deficient mice, thus aligning their response to that of WT mice in terms of increased bone formation.

Hence, our findings provide novel insights into bone mechanoregulation and emphasize that TRAP is not the primary regulator of this process. Importantly, we observed that TRAP deficiency in BCR[Ibsp/Acp5] mice did not alter the functional remodeling activities in the trabecular region. Our results shed light on the mechanomolecular mechanism of TRAP and demonstrated that TRAP-deficient mice exhibit a similar response to mechanical loading and expression of molecular markers involved in bone mechanosensitivity. Additionally, our study highlighted the feasibility of simultaneous identification and tracking of fluorescently labeled osteoblasts and TRAP-deficient osteoclasts *in vivo* and *in vitro* using CRISPR/Cas9 mediated fluorescent reporter (BCR[Ibsp/Acp5]) mice.

The ability of TRAP-deficient osteoclasts to sustain bone remodeling in a mechanically driven environment suggests that TRAP may not be an exclusive target for therapeutic strategies aimed at bone diseases. Future pharmacological interventions could explore the modulation of

associated pathways rather than direct TRAP inhibition. The observed bone remodeling and mechanosensitivity that occurred despite TRAP deficiency indicate that other genetic or environmental factors may compensate for the lack of TRAP. Therefore, it is important to focus on exploring these factors and investigating the osteoclast physiology, development, and function as novel therapeutic targets to restore the altered phenotype and activity of osteoclasts.

3.1.4 Materials and Methods

Ethics statement

All animal procedures were approved by the local authorities (animal license number ZH09/2018, Verterinäramt des Kantons Zürich, Zurich, Switzerland). All mice were maintained for animal husbandry, welfare, and monitoring at the ETH Phenomics Center (12:12 h light–dark cycle, maintenance feed and water ad libitum, three to five animals per cage).

Animal models

Bone Cell Reporter (BCR) mouse lines used in this study were initially designed as knock-in models to label osteoclasts (*Acp5*, mCherry) and osteoblasts (*Ibsp*, eGFP) respectively. BCR$^{Ibsp/Acp5}$ (*C57BL/6j.Ibsp$^{em1(ETHZ)}$.Acp5$^{em1(ETHZ)}$*) and BCR$^{Ibsp/WT}$ (*C57BL/6j.Ibsp$^{em1(ETHZ)}$*) mice were derived from four founder animals generated via CRISPR/Cas9 genome editing. Tartrate-resistant acid phosphatase type 5 - *Acp5* and integrin-binding sialoprotein - *Ibsp* were labeled with fluorescent proteins (mCherry, eGFP), respectively. Donor templates were designed to contain a furin recognition site (RAKR), a self-cleaving peptide (P2A), and the fluorescent reporter sequence (eGFP/mCherry) flanked by homology arms of 1000bp, which were specific to sequences upstream (5') and downstream (3') of the target gene's stop codon. (ensembl.org; Gene IDs, GenBank: 11433 for Acp5, 15891 for Ibsp) and inserted into puC57 vectors (ShineGene Molecular Biotech, Inc., Shanghai, China). Guide RNAs were selected based on specificity, efficiency, off-target predictions, and distance from the insertion site, using open software (http://crispor.tefor.net, https://chopchop.cbu.uib.no) [53]. After confirming the functionality of guide RNAs (Acp5: GCAGGACTCTCGTGGTGTTCAGG and Ibsp: CGGGGAGGGGGCTTCACTGATGG) and Cas9 protein through *in vitro* digestions, CRISPR/Cas9 reagents were injected into C57BL/6J zygotes (Zygotes Kit, Janvier Labs, Le Genest-Saint-Isle, France) and transferred to Swiss Webster recipient mice.

Genotyping was performed for the mouse litters using PCR followed by Sanger sequencing (Microsynth, Balgach, Switzerland). Heterozygous F1 animals were crossbred to obtain homozygous animals, and the BCR mouse lines were maintained in homozygosity. Homozygous offspring from the BCR[Ibsp/Acp5] line exhibited an intact TRAP-mCherry complex; thus, the BCR[Ibsp/Acp5] mice displayed TRAP knockdown-like characteristics at the protein level, with osteoclasts lacking TRAP expression. Despite this, both osteoblasts and osteoclasts continued to express the fluorescent proteins (eGFP and mCherry). All BCR mouse lines included in this study were genotyped prior to experiments (Transnetyx, Cordova, USA). Age-matched C57BL/6J male and female mice purchased from Janvier Labs were used as controls (WT) for all experiments [54].

Bone sample preparation and immunofluorescence staining

Femur and vertebra were harvested from 5- and 20-week-old mice and fixed immediately in ice-cold 4% paraformaldehyde (PFA) for 24 hours at 4°C. Bones were decalcified in 12.5% EDTA for 10-11 days at 4°C, followed by overnight incubation in sucrose solution (20% sucrose, 2% PVP) and embedded in OCT. Samples were stored at −80°C until sectioning. 10-50 μm-thick cryosections were obtained for immunofluorescence staining. Bone sections were hydrated with PBS 3 times in 5 min intervals and permeabilized with 0.3% Triton X-100 in PBS for 20 min at room temperature (RT). Slides were incubated in blocking solution (5% specific serum in 0.025% Triton X-100) for 45 min at RT, followed by incubation of primary antibody in blocking solution (5% bovine serum albumin (BSA) in 0.025% Triton X-100) overnight at 4°C. the following antibodies were used: mCherry (PA5-34974, Invitrogen, 1:200), GFP (ab290, Abcam, 1:200), IBSP (270457, Abcam, 1:200), TAZ (HPA007415, Sigma Aldrich, 1:100). The next day, slides were washed in PBS 3 times in 10 min intervals, followed by incubation in species-specific Alexa Fluor 647 conjugated secondary antibodies diluted (ab150075, Abcam, 1:1000), in 0.3% BSA in PBS for 75 min at RT. Slides were incubated in Phalloidin conjugated Alexa Flour 555 (A20106, Thermo Fischer, 1:1000) and Hoechst (B22126-25G, Sigma Aldrich 1:500) in 0.3% BSA in PBS for 1 hour to stain the actin cytoskeleton. Slides were washed in PBS 3 times in 10 min intervals, air-dried, mounted with Prolong Diamond mounting medium (P36961, Thermo Fischer), and the edges were sealed with nail polish.

Immunohistochemistry for bone samples

Femurs and vertebrae were fixed in 10% NBF for 24h, decalcified with 12.5% EDTA for 10 days, and embedded with paraffin. 5 μm thick paraffin sections were prepared for stainings. Slides were deparaffinized in Xylene 3 times with 5 min intervals, rehydrated in the gradient of EtOH (100% to 70% with 5 minutes intervals each), and blocked in 10% goat serum for 1h at RT. Slides were stained with mCherry antibody (PA5-34974, Invitrogen, 1:200) overnight at 4°C. After washing with PBST, the corresponding biotinylated secondary antibody (ab6720, Abcam 1:50) was added for 1 hour at RT. DAB (PK-6100, VECTASTAIN Elite ABC-HRP kit Peroxidase, Vector Laboratories) was used as chromogen, and Fast Green (F2758, Sigma Aldrich) was used as a counterstaining.

To identify osteoclasts, TRAP staining was performed according to the manufacturer's guidelines (387A, Sigma Aldirch) and Fast Green was used as a counterstaining for better visualization of bone architecture.

Calcein blue (M1255, Sigma Aldrich) staining for minerals was used to visualize bone architecture. Slides were stained in 30 mg/ml of Calcein blue prepared in 2% $NaHCO_3$ solution for 10 minutes, followed by rinsing with PBS 3 times at 10 min intervals and applying DPX (44581, Sigma Aldrich) mounting the slides.

In vitro osteoclast differentiation

Femurs were collected from 5-week-old male mice and, after removing surrounding connective tissue and epiphysis, bone marrows were flushed using culture media (αMEM containing 10% FBS, 1X GlutaMAX, and 1% Antibiotic cocktails (Streptomycin and Penicillin)). The harvested marrow cells were centrifuged at 600 x g for 5 minutes at RT for pelletization. The resulting supernatant was discarded, and the cells were rinsed using 4.5 ml of cold ddH_2O to lyse red blood cells, followed by the addition of 500 μl of 10x PBS to adjust osmolarity. Cells were centrifuged again at 600 x g for 5 min at RT resuspended in 1 ml of culture media with 10 ng/mL MCSF seeded in a non-adherent plate and incubated for 24 hours at 37°C. The following day, the supernatant is collected which contains the non-adherent hematopoietic progenitors [55, 56]. Cells were centrifuged at 600 x g for 5 min at RT and resuspended in 5mL medium (αMEM with ascorbic acid, 10% FBS, 1X GlutaMAX, and 1% Antibiotic cocktails (Streptomycin and Penicillin)) and 30 ng/ml MCSF and seeded for osteoclast differentiation.

3.1 Elucidating the mechano-molecular dynamics of TRAP activity using CRISPR/Cas9 mediated fluorescent reporter mice

Cells were counted with Trypan blue and seeded in triplicates as 5000 cells/well in a 96-well plate and supplemented with 4 ng/ml of RANKL and 30 ng/ml of MCSF without RANKL as controls. Media was changed on day 3, and multinucleated osteoclasts appeared on day 4.

F-actin and TRAP staining

To stain F-actin, BCR[Ibsp/Acp5] and WT osteoclasts (initially seeded at 5000 cells/well) were fixed on day 4 with 4% PFA for 5 minutes, permeabilized with 0.1% Triton in PBS, blocked with 2% BSA for 1 hour, and co-stained with phalloidin-conjugated with Alexa Flour 647 and Hoechst for 45 min. The cells were washed with 0.1% Triton in PBS, air-dried, and imaged with Nikon wide-field microscopy. Next, the cells were washed with 1X PBS and stained for TRAP according to the manufacturer's guidelines and were imaged using Nikon wide-field microscope.

Osteoclasts resorption assay

Bone slices (Immunodiagnostic System Ltd) were placed in a 96-well plate one day before the experiments, and the cells were seeded on them in triplicates. Cells were cultured on the bone slices following the standard osteoclast differentiation protocol (20.000 cells/well in a 96-well plate and supplemented with 4 ng/ml of RANKL and 30 ng/ml of MCSF to induce osteoclast formation, and without RANKL as controls). On day 9, bone slices were fixed with 4% PFA for 5 min at RT, and resorption pits were imaged using light microscopy. Bone slices without cells were used as the controls.

RNA extraction from osteoclasts

Cells were seeded at 10.000 cells/well and differentiated into osteoclasts following the standard protocol and were used for RNA extraction. The medium was aspirated from the cells when they were on day 4 of differentiation and the cells were washed twice with 1X PBS. Next, the cells were harvested with TRIzol, and the RNA isolation protocol was performed according to the manufacturer's guidelines (Qiagen Micro kit).

RNA sequencing and data analysis

The RNA quality from the isolated cells was assessed using a 2100 BioAnalyzer (Agilent). The TruSeq Stranded Total RNA Library Prep Kit (Illumina, San Diego, CA, USA), was used for

the preparation of sequencing libraries according to the manufacturer's instructions. Single-end sequencing of the samples was performed at Functional Genomics Center, Zürich (https://fgcz.ch/).

Quality assessment of the raw sequence data of all samples was performed using FastQC (Version: FastQC v0.11.9, (http://www.bioinformatics.babraham.ac.uk/projects/fastqc/). Raw reads were mapped to the mouse reference genome using the STAR aligner (Version=2.7.10a). The mouse genome GRCm39 was downloaded from Ensembl (https://www.ensembl.org/Musmusculus) and the mouse genome index was created from STAR genomeGenerate command [57]. The aligned reads were quantified on a per gene basis using HTSeq with the following settings (Version:HTSeq-1.99.2; [htseq-count-mode = intersection-nonemptystranded = reverse]) [58]. The RNA-sequencing data were deposited to ArrayExpress under the accession number E-MTAB-11403. To explore the similarities and dissimilarities between the samples, the quantified count data were normalized using the Variance Stabilizing Transformation (VST), and principal component analysis was performed. Further, differentially expressed genes are listed with FDR-adjusted p-value cutoff < 0.1 with different contrast (BCR$^{Ibsp/Acp5}$-M vs WT-M, BCR$^{Ibsp/Acp5}$ vs WT, WT vs WT-M, BCR$^{Ibsp/Acp5}$ vs BCR$^{Ibsp/Acp5}$-M) using DESeq2 (BioConductor version3.14The Ensembl ID was annotated to gene symbols and Entrez Gene using biomaRt (BioConductor version 3.14).

Gene-set enrichment analysis was performed using Generally Applicable Gene-set Enrichment (GAGE; BioConductor version 3.14)[59]. For functional annotation, we used gene sets from org.Mm.eg.db, a genome-wide annotation package for mice (Bioconductor, version 3.14).[60] The analysis was performed on the basis of one-on-one comparisons between BCR$^{Ibsp/Acp5}$ vs WT datasets, where WT was used as a control sample. Significant GO terms are listed using an FDR-adjusted p-value of < 0.01.

Measurement of CTX from in vitro osteoclast cultures

The degradation of C-terminal telopeptides of type I collagen (CTX) in the cell culture supernatant from BCR$^{Ibsp/Acp5}$ and WT osteoclasts was measured using a Mouse CTX-I ELISA Kit (Immunodiagnostic System Ltd) according to the manufacturer's guidelines. The results were obtained from three biological and three technical replicates per group.

Measurement of serum CTX

Blood was collected from loaded and sham-loaded BCR[Ibsp/Acp5] and WT mice by cardiac puncture under anesthesia. Subsequently, the collected blood was allowed to clot for 1 hour at RT and the resulting clot was removed by centrifugation at 2000 x g for 10 minutes at 4°C. The serum was promptly collected and stored at -80°C. The measurement of CTX levels was carried out using the Mouse CTX ELISA kit (Immunodiagnostic System Ltd) following the guidelines provided by the manufacturer.

Cyclic mechanical loading of the sixth caudal vertebra

The 6th caudal vertebra was subjected to cyclic mechanical loading as previously described[20, 39]. Stainless steel pins were inserted into the fifth and seventh caudal vertebra of 12-week-old female mice (n=37). Three weeks after pinning, the mice received either sham (0N, n=18) or 8N (n=19) cyclic loading with a 10Hz frequency for 5 min, thrice per week over four weeks.

Analysis of micro-computed tomography images

For the analysis of *ex vivo* femur and vertebra samples, femurs and vertebrae were fixed overnight in 4% PFA at 4°C and placed into 70% EtOH, and then scanned using micro-CT (micro-CT 40, Scanco Medical AG) with an isotropic voxel-size of 10 μm and 6 μm, respectively; 55 kVp, 145 μA, 200 ms integration time. A Gaussian filter (support: 1) with sigma of 0.8 and 1.2 was applied to the 3D image data, after which images were segmented with a threshold of 392 and 580 mgHA/cm^3, for femurs and vertebrae, respectively [24]. Relevant cortical and trabecular compartments were identified as previously described [20]. A mask of the outer vertebra was obtained by iterative dilation and erosion operations that smoothed and closed all holes on the surface. For the trabecular and cortical compartments, a distance transformation map was computed from the binary image of the caudal vertebra and yielded two masks. The growth plates were discarded by cropping the outer 10% of the inner mask and 12% of the outer mask. The middle 33% of the inner mask was also removed to eliminate the nearly empty space in the trabecular region. Standard bone morphometric parameters in these regions and in the whole bone were evaluated (Table 3.S1-2).

For the analysis of the 6th caudal vertebrae *in vivo,* mice were anesthetized with isoflurane (induction: 4.5-5%, maintenance: 2-2.5% isoflurane/oxygen) and were scanned weekly via *in vivo* micro-CT (vivaCT-80, Scanco Medical AG) with a resolution of 10.5 μm (55 kVp, 145 μA, 350 ms integration time) for 4 weeks. The registration of micro-CT images from

consecutive time points was performed using an image processing language (IPL Version 5.04c; Scanco Medical AG, Switzerland). Similar to the *ex vivo* analysis, standard and dynamic bone morphometric parameters were evaluated for the trabecular, cortical, and whole bone, after identifying the corresponding compartments for each image (Supplementary Table 5). Briefly, bone structural parameters were calculated using a direct 3D model-independent algorithm where spheres are fitted at each voxel to quantify trabecular thickness (Tb.Th), trabecular separation (Tb.Sp), and trabecular number (Tb.N). Additionally, the following parameters were measured using the binary bone image: total volume (Tb.TV), bone volume fraction (BV/TV), specific bone surface (BS/BV), structure model index[61], connectivity density (Conn.D) [62], and degree of anisotropy (DA) [63, 64]. Dynamic parameters were obtained by overlaying registered images thus revealing the sites of bone formation, quiescence and resorption between the time points considered. Although quiescent bone voxels were present in both images, formation sites were voxels only present in the follow-up image and resorption sites were voxels present only in the baseline image. By analyzing the voxels from each remodeling event separately, dynamic parameters describing the surface area, thickness and remodeling rates were computed, namely: mineralization surface [28], mineral apposition rate [27] and bone formation rate (BFR) for the formation and eroded surface (ES), mineral resorption rate (MRR) and bone resorption rate (BRR) for resorption.

Micro finite element analysis of the caudal vertebrae images

All time points for each sample were analyzed with micro-FE to estimate the mechanical signal in the structure in the form of effective strain [65]. The simulations used a Python pipeline that was previously developed [45], while considering homogeneous material properties for bone [39] (Young's modulus of 14.8 GPa and a Poisson's ratio of 0.3). Briefly, the image voxels were converted into 8-node hexahedral elements, and the bone was assumed to behave within the linear elastic regime. Two cylindrical discs were added at the distal ends of the vertebra model, mimicking the role of the intervertebral discs. The bottom nodes of the FE mesh were constrained in all directions, whereas the top nodes were displaced by 1% of their lengths along the z-axis (longitudinal axis of the sample). The effective strain was determined after linear rescaling to match the forces applied *in vivo*: 4N (physiological loading estimate [41]) for the sham-loaded and 8N for the loaded groups. The simulations ran on the Euler cluster operated by Scientific IT Services at ETH Zurich, using the micro-FE solver ParOSol [66], on Intel Xeon Gold 6150 processors (2.7–3.7 GHz).

3.1 Elucidating the mechano-molecular dynamics of TRAP activity using CRISPR/Cas9 mediated fluorescent reporter mice

Mechanoregulation analysis in the local in vivo environment

Mechanoregulation analysis focused on conditional probability curves and remodeling velocity curves to characterize the association between remodeling events and local mechanical signals. Conditional probabilities were computed as previously described[8], for weekly intervals (e.g., weeks 2–3 considered the micro-CT images from weeks 2 and 3 and the micro-FE from week 2) and for the 4-week observation period (considering the micro-CT images from weeks 0 and 4 to identify remodeling events and using micro-FE data from week 0). The effective strain values were normalized to the 99th percentile of all the observed values thus defining a normalized mechanical signal (%). A conditional probability of 0.33 indicates an equal probability of any remodeling event occurring. The correct classification rate [24, 31] metric summarizes the accuracy of the ternary classification problem that classifies remodeling events (formation, quiescence, and resorption) within the range of the observed local mechanical signal values. CCR values above 0.33 indicate that the mechanical signal descriptor considered can predict remodeling events with better accuracy than a random classifier.

Additionally, remodeling velocity curves associated with the expected surface velocity based on the mechanical signal were determined, as previously described [45]. Remodeling velocity curves were fitted with a hyperbolic function, from which biologically meaningful remodeling parameters can be estimated, including formation and resorption saturation levels (FSL and RSL) that bind the magnitude of these events and a remodeling threshold (RmT) and a velocity modulus (RmVM), that quantitatively characterize the mechanosensitivity of the model. The curve fit quality was assessed using the normalized root mean squared error (NRMSE, %), while considering the interval between the while considering the interval between the maximum and minimum remodeling velocities observed as the normalization factor.

Quantification and statistical analysis

Stained bone sections were imaged using Leica SP8 and ZEISS LSM 880 confocal microscopes with 10x and 20x air objectives, respectively. The selection of ROIs within the femurs and vertebrae was carefully defined as 25 to 35% of the length from the growth plate considering the differences in the growth plate (wider in BCR$^{Ibsp/Acp5}$ mice) and the length of the femurs. For both strains, we normalized the imaged area and volume to the total length of femurs to ensure the ROIs were proportionally comparable. Images were analyzed, quantified, and processed using LASX, Zen Blue, and Affinity Designer software. Images were preprocessed

using Fiji, and colocalization analysis was performed as described elsewhere [25, 67]. The total fluorescent intensity ratio was determined with Fiji software.

In vitro osteoclasts were imaged in a glass-bottom 96 well plate using a NIKON Wide-Field microscope with 5x and 10x air objectives, and the entire surface of the wells was scanned to generate a tile image. Multinucleated cells containing at least three nuclei were visually identified, and counted with Fiji using the Cell Counter plugin, and processed using Affinity Designer software. GraphPad Prism software was used for statistical analyses. All data were presented as mean ± s.d. unless indicated otherwise. The sample numbers were chosen by a power analysis of bone morphometry parameters from previous experiments [44]. Reproducibility was ensured based on several independent experiments. None of the animals were excluded from the analysis. Statistical significance for all datasets was set at $p < 0.05$. The following statistical tests that were used included two-way ANOVA with Dunnett's comparison test for *in vivo* experiments, two-tailed Student's t-test for *ex vivo* histology and Mann-Whitney test for *in vitro* experiments and one-way ANOVA with Dunnett's comparison test for *ex vivo* micro-CT analysis. Data were normally distributed and tested through the Shapiro-Wilk Test and homogeneity of variance was assessed by the Levene test.

For the in silico analysis, as previously described [45], a hyperbolic function was fitted to the remodeling velocity curves per group and weekly time points, and a balanced bootstrap approach was used to characterize the distribution of the parameters estimated from the curve fits. Group comparisons of these distributions were performed for all weekly time points and group pairs. Due to the skewed nature of some of the distributions that were generated, statistical comparisons considered the bias-corrected and accelerated bootstrapped confidence intervals [68]. As indicated above, $p < 0.05$ was considered significant and was adjusted for multiple comparisons using Bonferroni correction. Additionally, correlations between the remodeling velocity curves from different groups were assessed using the Pearson Correlation Coefficient (PCC).

The sample sizes were selected based on our previous experiments and a series of independent experiments were carried out to ensure our findings could be consistently replicated.

Acknowledgments

## Conflict of interest

The authors have no conflict of interest to declare.

Author contributions

Conceptualization and methodology: DY, FCM, PRA, PCS, GAK, EW, AS, NM, RM; investigation, methodology: DY, FCM, GAK, PCS, EW; data curation, formal analysis: DY, FCM, PCS, AS, NM, YF, GH, SZ, DG; writing - original draft: DY; writing - review and editing: DY, FCM, PRA, PCS, GAK, EW, AS, NM, RM; resources, supervision, funding acquisition, project administration RM.
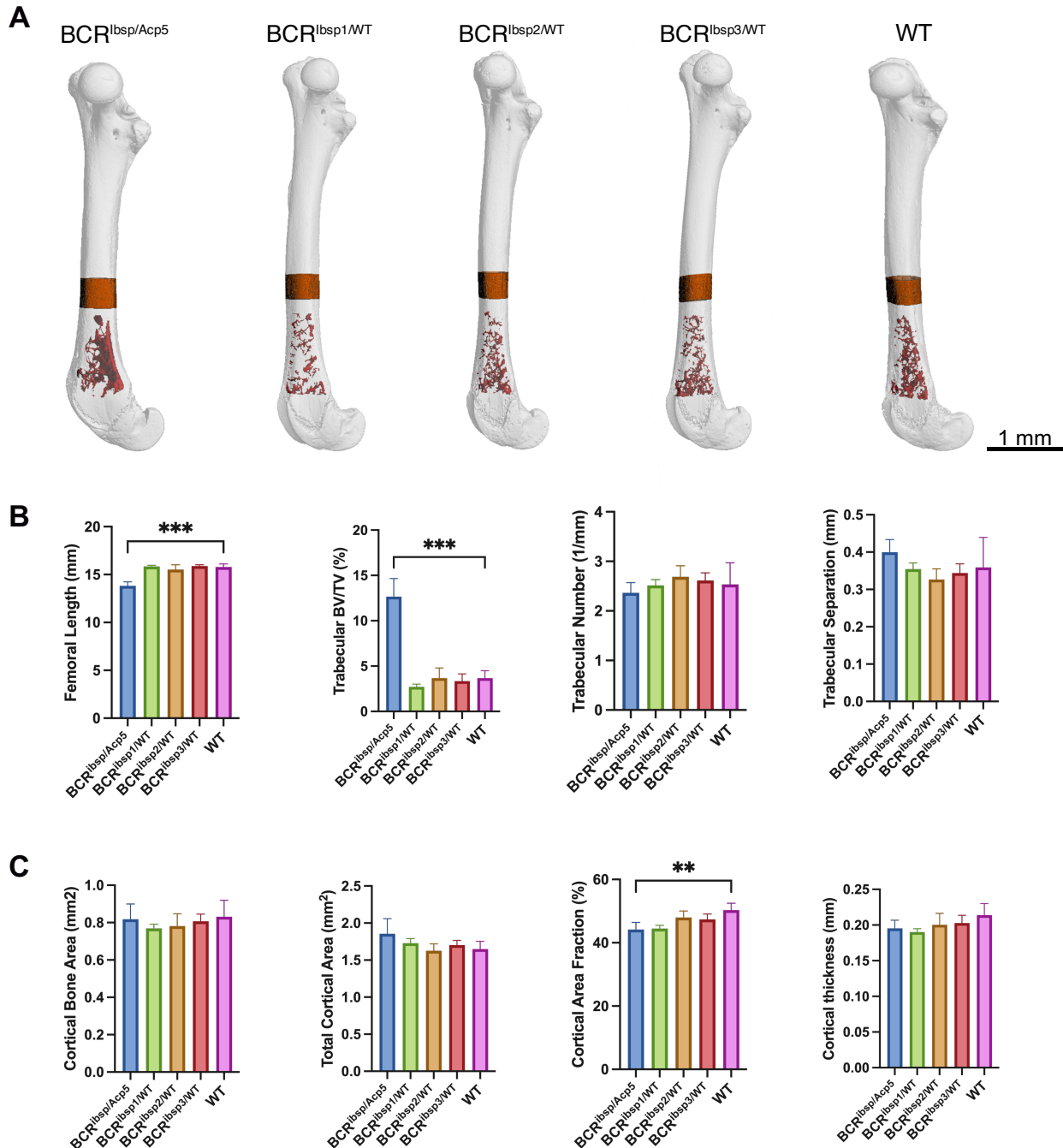
Supplementary Materials
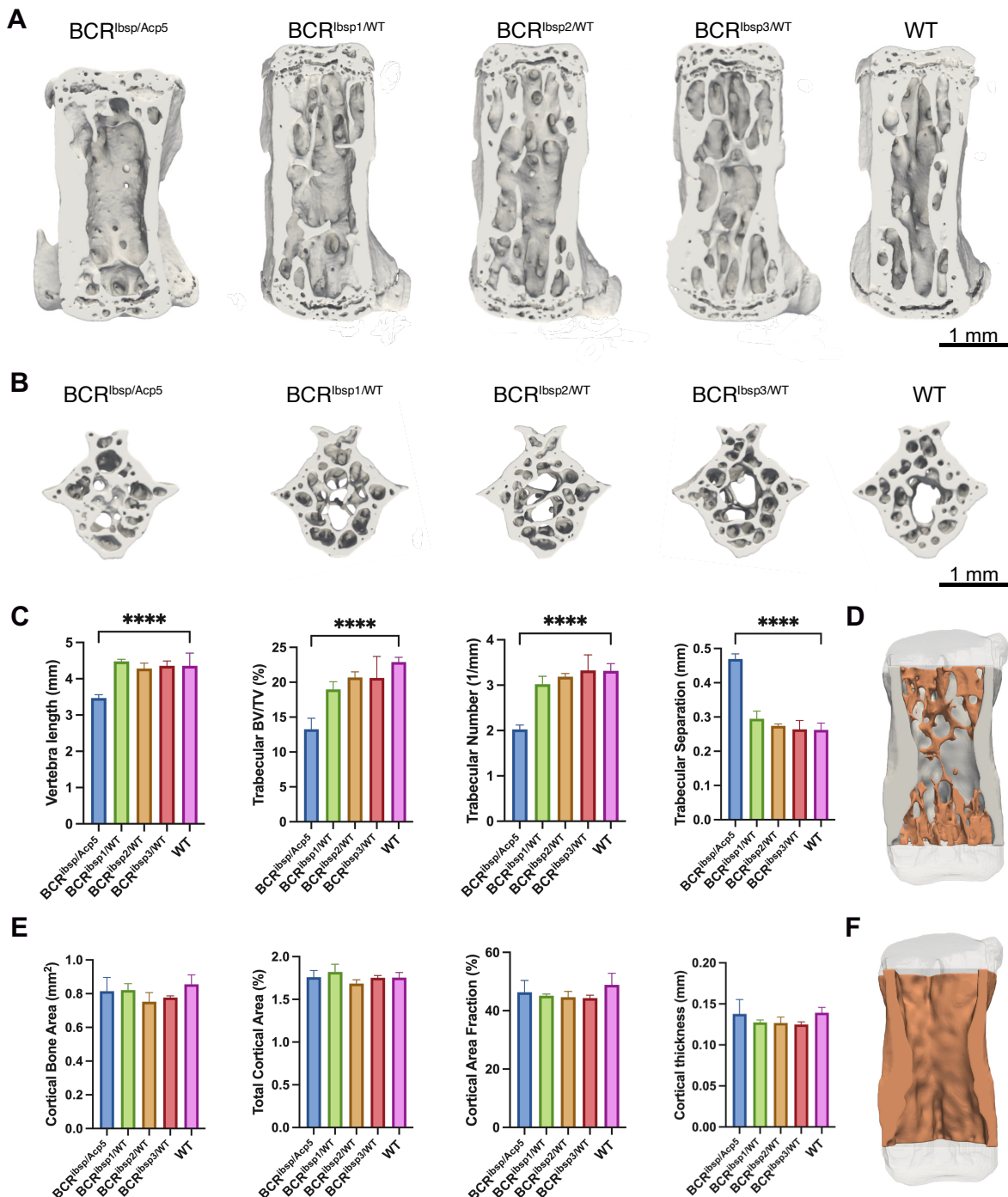
Figure 3.S1 Micro-CT-based evaluation of caudal vertebra. A) Representative 3D reconstructed longitudinal micro-CT images of the 6th caudal vertebra of BCR[Ibsp/Acp5,] BCR[Ibsp/WT,] and WT mice at 20 weeks. B) Representative 3D reconstructed cross-sectional micro-CT images of the 6th caudal vertebra of BCR[Ibsp/Acp5], BCR[Ibsp/WT], and WT mice at 20 weeks. C) Bone morphometric parameters obtained from micro-CT analysis; vertebra length, bone volume fraction (BV/TV), trabecular number, and trabecular separation. D) Representative 3D reconstructed longitudinal micro-CT images showing the trabecular mask

in orange, where the analysis for trabecular parameters was obtained. E) Cortical bone parameters: cortical bone area, total cortical area, cortical area fraction, and cortical thickness. F) Representative 3D reconstructed longitudinal micro-CT images showing the cortical mask in orange where the analysis for cortical parameters was obtained. Data represent mean ± s.d., n=4-8 mice/ group). Significance was determined by one-way ANOVA with Dunnett correction, *p<0.05, **p<0.01, ***p<0.001.

Figure 3.S2 Micro-CT-based evaluation of femurs in BCR[Ibsp/Acp5] mice. A) Representative 3D reconstructed longitudinal micro-CT images of the femurs of BCR[Ibsp/Acp5], BCR[Ibsp/WT], and WT mice at 20 weeks. B) Bone morphometric parameters obtained from micro-CT analysis; femoral length, bone volume fraction (BV/TV), trabecular number, and trabecular separation.

C) Cortical bone parameters: cortical bone area, total cortical area, cortical area fraction, and cortical thickness. Data represent mean ± s.d., (n=4-5 mice/group), Significance was determined by one-way ANOVA with Dunnett correction, *p<0.05, **p<0.01, ***p<0.001.
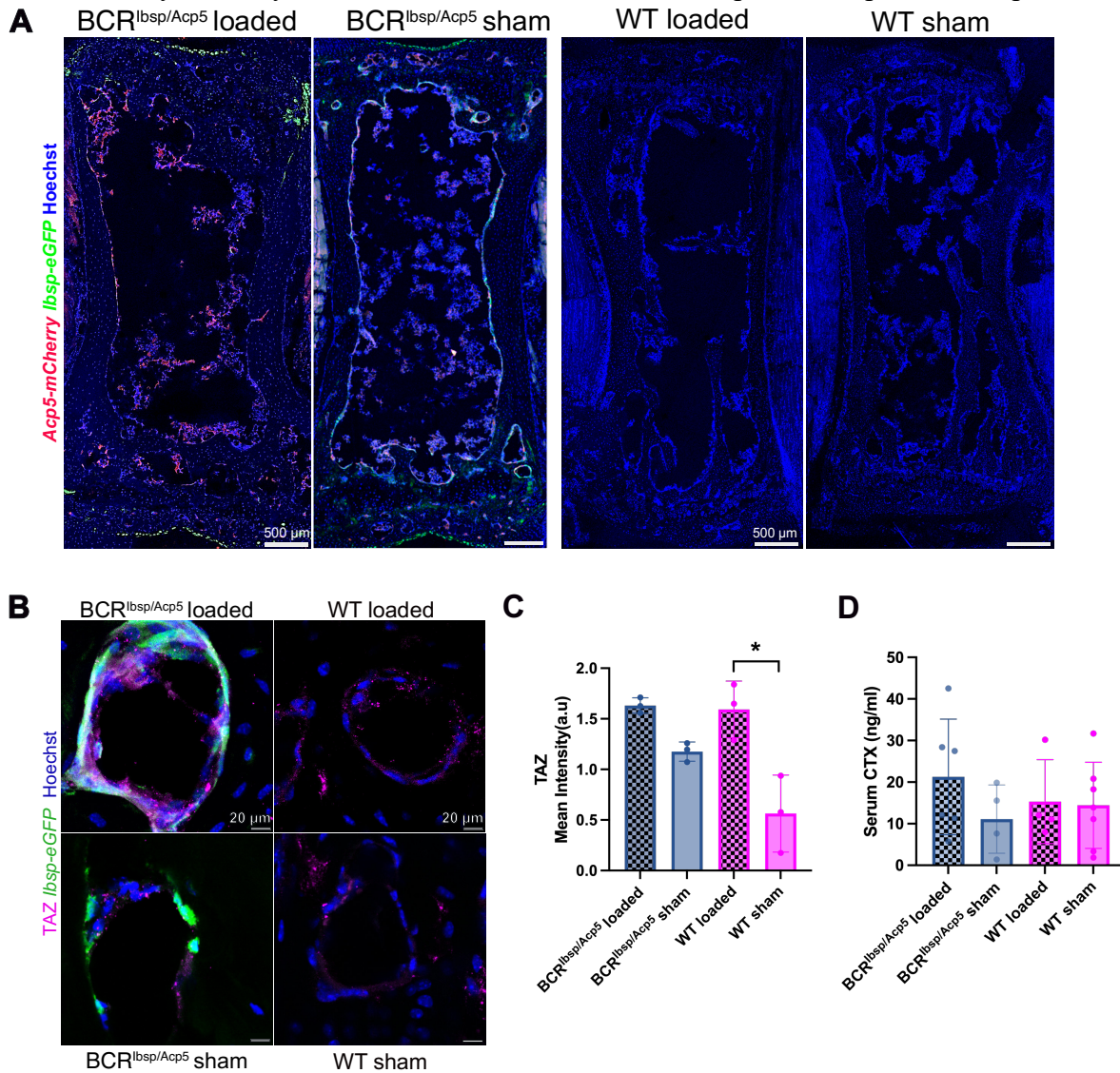
Figure 3.S3 Mechano-molecular mechanism of BCR[Ibsp/Acp5] mice *in vivo.* A) Representative tile scan confocal images indicating endogenous mCherry *(Acp5-mCherry,* red), endogenous GFP (*Ibsp-eGFP,* green) and Hoechst (nucleus, blue) staining in loaded and sham-loaded BCR[Ibsp/Acp5] and WT mice vertebrae. B) High-magnification images indicating endogenous signals of osteoblasts *(Ibsp-eGFP*, green) stained with TAZ (purple) in resorption cavities loaded and sham-loaded BCR[Ibsp/Acp5] and WT mice caudal vertebra sections. C) Mean intensity (a.u.) of TAZ signals from the resorption cavities from loaded and sham-loaded BCR[Ibsp/Acp5] and WT mice. Data represent mean ± s.d, (n=3 mice/group). Significance was determined by two-tailed unpaired t-test. p<0.05, **p<0.01, ***p<0.001. D) Measured serum CTX protein levels in loaded and sham-loaded BCR[Ibsp/Acp5] and WT mice. Data represent mean ± s.d., (n=5-7 mice/group). Significance was determined by two-tailed unpaired t-test, *p<0.05, **p<0.01, ***p<0.001.

Table 3.S1 Bone structural parameters in the full, trabecular, and cortical region of the 6th caudal vertebra assessed by ex vivo micro-CT imaging.

Parameter legend: total volume (TV), bone volume (BV), bone surface (BS), average volume density (AVD), bone surface density (BS/TV), specific bone surface (BS/BV); tissue mineral density (TMD), bone volume fraction (BV/TV), trabecular thickness (Tb.Th), trabecular number (Tb.N), trabecular separation (Tb.Sp), cortical area fraction (Ct.Ar/Tt.Ar), total cross-sectional area inside the periosteal envelope (Tt.Ar), cortical bone area (Ct.Ar), cortical thickness (Ct.Th). Data represent mean ± s.d., (n=4-8 mice/group).

Parameters	BCR$^{Ibsp/Acp5}$	BCR$^{Ibsp1/WT}$	BCR$^{Ibsp2/WT}$	BCR$^{Ibsp3/WT}$	WT
Full					
TV [mm³]	5.76±0.20	7.07±.0.25	6.35±0.25	6.61±0.08	6.60±0.36
BV [mm³]	3.44±0.29	4.14±0.17	3.74±0.27	3.84±0.12	4.18±0.25
BS [mm²]	53.24±1.52	82.53±2.20	76.04±3.21	80.82±2.96	72.48±4.60
AVD [%]	59.67±3.34	58.55±1.13	58.79±2.02	58.04±1.99	63.32±2.82
BS/TV [1/mm]	9.25±0.41	11.67±0.22	11.98±0.59	12.22±0.42	10.98±0.29
BS/BV [1/mm]	15.55±1.38	19.94±0.72	20.42±1.62	21.07±0.77	17.38±1.20
TMD [mg HA/cm³]	999.72±10.24	976.90±6.79	977.52±14.38	967.54±13.36	1002.24±7.06
Length [mm]	4.11±0.35	4.54±0.09	4.28±0.15	4.35±0.14	4.15±0.16
Trabecular					
BV/TV [%]	13.26±1.57	18.96±1.11	20.68±0.80	20.61±3.09	23.70±1.93
BS/TV [1/mm]	4.38±0.46	6.27±0.17	6.91±0.29	6.97±0.73	6.84±0.39
BS/BV [1/mm]	33.37±4.78	33.09±1.30	33.46±2.29	34.00±1.99	28.99±2.65
Tb.Sp [mm]	0.47±0.02	0.29±0.02	0.27±0.01	0.26±0.03	0.26±0.02
Tb.N [1/mm]	2.03±0.10	3.02±0.17	3.19±0.07	3.19±0.07	3.32±0.34
Tb.Th [mm]	0.08±0.01	0.08±0.00	0.08±0.01	0.08±0.00	0.09±0.01
Cortical					
BS/TV [1/mm]	4.61±0.32	5.41±0.16	5.53±0.28	5.64±0.23	5.40±0.24
BS/BV [1/mm]	10.01±1.02	11.99±0.50	12.44±1.03	12.72±0.51	11.10±0.83
Ct.Ar/Tt.Ar [%]	46.30±4.05	45.11±0.65	44.60±2.03	44.34±0.99	48.87±3.94
Tt. Ar [%]	0.81±0.08	0.82±0.04	0.75±0.05	0.78±0.01	1.65±0.10
Ct. Ar [mm²]	0.82±0.08	0.77±0.02	0.78±0.07	0.81±0.04	0.86±0.06
Ct. Th [mm]	0.14±0.02	0.13±0.00	0.13±0.01	0.12±0.00	0.14±0.01

Table 3.S2 Bone structural parameters in the full, trabecular, and cortical regions of femurs assessed by *ex vivo* micro-CT imaging.

Parameter legend: total volume (TV), bone volume (BV), bone surface (BS), average volume density (AVD), bone surface density (BS/TV), specific bone surface (BS/BV); tissue mineral density (TMD), bone volume fraction (BV/TV), trabecular thickness (Tb.Th), trabecular number (Tb.N), trabecular separation (Tb.Sp), cortical area fraction (Ct.Ar/Tt.Ar), total cross-sectional area inside the periosteal envelope (Tt.Ar), cortical bone area (Ct.Ar), cortical thickness (Ct.Th). Data represent mean ± s.d., (n=4-5 mice/group).

Parameters	BCR$^{Ibsp/Acp5}$	BCR$^{Ibsp1/WT}$	BCR$^{Ibsp2/WT}$	BCR$^{Ibsp3/WT}$	WT
Full					
TV [mm³]	31.71±3.12	36.17±1.13	33.28±1.84	35.85±1.23	34.05±1.18
BV [mm³]	16.28±1.55	16.99±0.36	16.16±1.40	17.01±0.59	17.42±1.45
BS [mm²]	173.00±14.76	188.76±3.78	180.53±5.17	190.49±4.12	173.18±4.48
AVD [%]	51.36±1.00	46.97±0.94	48.51±1.70	47.46±0.91	51.10±2.65
BS/TV [1/mm]	5.46±0.18	5.22±0.10	5.43±0.24	5.32±0. 18	5.09±0.10
BS/BV [1/mm]	10.64±0.50	11.12±0.27	11.22±0.80	11.21±0.49	9.98±0.56
TMD [mg HA/cm³]	973.56±23.52	940.82±19.56	949.65±38.95	965.12±22.52	956.38±31.60
Length [mm]	13.83±0.40	15.84±0.12	15.53±0.48	15.89±0.14	15.76±0.31
Trabecular					
BV/TV [%]	12.66±4.02	2.71±0.30	3.67±1.12	3.34±0.81	3.68±1.63
BS/TV [1/mm]	3.93±0.88	2.30±0.19	2.91±0.71	2.68±0.52	2.62±0.96
BS/BV [1/mm]	31.78±4.34	85.22±3.60	80.33±5.80	81.16±6.51	73.11±6.87
Tb.Sp [mm]	0.40±0.03	0.35±0.02	0.33±0.03	0.34±0.02	0.36±0.08
Tb.N [1/mm]	2.36±0.21	2.51±0.12	2.69±0.22	2.62±0.15	2.54±0.44
Tb.Th [mm]	0.10±0.01	0.04±0.00	0.04±0.00	0.04±0.00	0.05±0.00
Cortical					
BS/TV [1/mm]	2.25±0.13	2.36±0.06	2.40±0.03	2.39±0.07	49.69±2.17
BS/BV [1/mm]	5.09±0.36	5.31±0.14	5.01±0.20	5.06±0.33	2.48±0.22
Ct.Ar/Tt.Ar [%]	44.18±2.23	44.47±1.05	47.99±2.04	47.40±1.70	4.94±0.53
Tt. Ar [%]	1.85±0.20	1.73±0.06	1.63±0.09	1.70±0.06	1.65±0.10
Ct. Ar [mm²]	0.82±0.08	0.77±0.02	0.78±0.07	0.81±0.04	0.83±0.09
Ct. Th [mm]	0.20±0.01	0.19±0.00	0.20±0.02	0.20±0.01	0.21±0.02

Table 3.S3 Absolute values in the bone structural parameters in the trabecular and cortical region for the loaded and sham-loaded mice over the 4-week loading period.

Parameter legend: trabecular bone volume fraction (BV/TV), trabecular thickness (Tb.Th), trabecular separation (Tb.Sp), trabecular number (Tb.N), tissue mineral density (TMD), cortical area fraction (Ct.Ar/Tt.Ar), cortical bone area (Ct.Ar) and cortical thickness (Ct.Th). Data represent mean ± s.d., (n=8-10 mice/group).

Parameter	BCR$^{Ibsp/Acp5}$ loaded	BCR$^{Ibsp/Acp5}$ sham-loaded	WT loaded	WT sham-loaded
Trabecular				
BV/TV [%]				
Week 0	10.64±1.08	13.44±2.83	16.48±2.57	15.92±1.87
Week 1	11.92±1.30	13.41±2.81	17.51±2.02	15.78±2.29
Week 2	12.92±1.32	13.08±2.80	18.12±1.93	15.68±2.57
Week 3	13.70±1.76	13.05±2.94	19.14±1.90	15.73±2.80
Week 4	14.60±1.64	13.00±2.92	19.88±2.08	15.76±2.77
Tb.Th [mm]				
Week 0	0.07±0.00	0.08±0.00	0.07±0.00	0.06±0.00
Week 1	0.08±0.00	0.08±0.00	0.07±0.00	0.07±0.00
Week 2	0.09±0.00	0.08±0.00	0.08±0.00	0.07±0.00
Week 3	0.10±0.01	0.08±0.00	0.08±0.00	0.07±0.00
Week 4	0.11±0.01	0.08±0.00	0.09±0.00	0.07±0.00
Tb.Sp [mm]				
Week 0	0.49±0.04	0.46±0.04	0.32±0.03	0.31±0.02
Week 1	0.50±0.05	0.46±0.05	0.32±0.04	0.31±0.02
Week 2	0.50±0.04	0.47±0.04	0.33±0.04	0.32±0.03
Week 3	0.50±0.05	0.48±0.06	0.33±0.04	0.33±0.04
Week 4	0.50±0.05	0.48±0.06	0.33±0.04	0.33±0.04
Tb.N [1/mm]				
Week 0	1.92±0.16	2.10±0.22	2.85±0.24	2.98±0.17
Week 1	1.89±0.18	2.04±0.24	2.79±0.27	2.90±0.18
Week 2	1.86±0.18	2.02±0.23	2.76±0.24	2.83±0.23
Week 3	1.84±0.18	1.99±0.26	2.73±0.26	2.81±0.23
Week 4	1.82±0.17	1.97±0.24	2.69±0.24	2.76±0.25
TMD [mg HA/cm³]				
Week 0	1094.92±5.94	1093.39±7.13	1100.36±4.79	1097.51±9.06
Week 1	1101.52±5.30	1098.16±5.59	1101.08±6.19	1100.67±7.94
Week 2	1103.81±7.20	1100.06±4.41	1104.80±5.03	1105.41±6.38
Week 3	1110.64±4.96	1105.66±4.99	1106.66±7.20	1105.26±5.88
Week 4	1116.03±5.42	1108.10±3.87	1116.34±4.03	1105.54±8.30
Cortical				
Ct.Ar/Tt.Ar [%]				35.05±2.79
Week 0	43.56±1.78	42.49±2.51	37.23±2.09	36.18±2.83
Week 1	44.35±1.69	42.58±2.76	38.32±2.05	36.55±2.87
Week 2	45.62±1.75	42.54±2.68	40.14±2.10	36.85±2.79
Week 3	47.18±1.65	42.52±2.64	41.30±2.25	37.09±2.73
Week 4	48.32±1.75	42.48±2.63	42.34±2.12	
Ct.Ar [mm²]				
Week 0	0.78±0.05	0.78±0.05	0.68±0.02	0.66±0.06
Week 1	0.80±0.04	0.79±0.05	0.71±0.03	0.66±0.06
Week 2	0.82±0.05	0.79±0.05	0.74±0.03	0.68±0.06
Week 3	0.86±0.04	0.80±0.04	0.77±0.03	0.68±0.06
Week 4	0.88±0.03	0.80±0.04	0.79±0.03	0.69±0.06

Ct.Th [mm]				
Week 0	0.16±0.01	0.15±0.01	0.13±0.01	0.13±0.01
Week 1	0.16±0.01	0.15±0.01	0.14±0.01	0.13±0.01
Week 2	0.16±0.01	0.15±0.01	0.14±0.01	0.13±0.01
Week 3	0.17±0.01	0.15±0.01	0.15±0.01	0.13±0.01
Week 4	0.18±0.01	0.15±0.01	0.15±0.01	0.13±0.01

Table 3.S4 Parameters of the mathematical functions fitted to the estimated mechanostat group average remodeling velocity curves for all weekly intervals. Data presented as "parameter (95% confidence interval)", where the 95% confidence interval was calculated using the balanced bias-corrected and accelerated bootstrapping approach. Normalized root mean squared error (NRMSE) was used to characterize the quality of the fit, considering the range defined by the minimum and maximum observed RmV values as the normalization parameter. The row "Effective strain range" indicates the range of mechanical signal values from which the fit of the mathematical functions was derived. (n=9-10 mice/group).

Parameter legend: Resorption saturation level (RSL), Resorption velocity modulus (RVM), Resorption threshold (RT), Formation threshold (FT), Formation velocity modulus (FVM), Formation saturation level (FSL), Remodeling threshold (RmT), Remodeling velocity modulus (RmVM)

	Parameters	Unit	BCR$^{Ibsp/Acp5}$ sham	BCR$^{Ibsp/Acp5}$ loaded	WT sham	WT loaded
0-1	RSL	µm/day	-3.130 (-4.679, -1.445)	-1.388 (-1.844, -0.480)	-1.923 (-2.684, -0.692)	-0.729 (-1.211, -0.315)
	RmVM	(µm/day) x µε	114 (52, 152)	384 (170, 543)	185 (73, 282)	568 (144, 832)
	RmT	µε	386 (303, 723)	227 (191, 326)	363 (301, 881)	289 (265, 352)
	FSL	µm/day	0.202 (0.154, 0.367)	0.897 (0.834, 1.062)	0.283 (0.173, 0.594)	0.682 (0.594, 0.855)
	NRMSE	%	2.75 (2.40, 5.13)	3.94 (3.84, 6.56)	3.74 (3.43, 7.03)	3.79 (3.57, 6.43)
	Effective strain range	µε	10–1470	10–2950	10–1210	10–2180
1-2	RSL	µm/day	-3.750 (-4.272, -2.127)	-1.506 (-2.020, -0.248)	-2.799 (-4.013, -0.924)	-0.985 (-1.645, -0.327)
	RmVM	(µm/day) x µε	115 (81, 137)	318 (183, 376)	131 (35, 165)	228 (114, 334)
	RmT	µε	670 (534, 5040)	168 (136, 270)	357 (288, 11534)	184 (169, 219)
	FSL	µm/day	0.087 (0.042, 0.199)	1.035 (0.954, 1.264)	0.227 (0.058, 0.564)	0.633 (0.576, 0.807)
	NRMSE	%	1.81 (1.81, 4.15)	3.86 (3.72, 6.46)	4.10 (3.49, 6.99)	3.10 (3.13, 5.46)
	Effective strain range	µε	10–1430	10–2800	0–1250	10–1900
2-3	RSL	µm/day	-2.440 (-2.950, -1.235)	-0.180 (-0.715, 0.428)	-1.186 (-1.736, -0.410)	-2.794 (-3.898, -0.725)

Week	Parameter	Units				
	RmVM	(µm/day) x µε	111 (64, 133)	472 (75, 1120)	284 (87, 452)	118 (65, 133)
	RmT	µε	421 (378, 776)	66 (0, 157)	363 (319, 554)	194 (167, 253)
	FSL	µm/day	0.169 (0.125, 0.292)	0.985 (0.892, 1.489)	0.328 (0.281, 0.410)	0.472 (0.452, 0.538)
	NRMSE	%	2.17 (2.03, 4.60)	5.08 (4.67, 11.27)	3.81 (3.15, 9.22)	2.17 (1.83, 5.05)
	Effective strain range	µε	10–1430	10–2500	0–1190	10–1740
3-4	RSL	µm/day	-2.347 (-2.784, -1.262)	-0.949 (-1.469, 0.015)	-1.362 (-1.863, -0.654)	-1.521 (-2.284, -0.563)
	RmVM	(µm/day) x µε	150 (105, 177)	186 (72, 281)	245 (61, 337)	283 (105, 415)
	RmT	µε	366 (340, 483)	122 (98, 164)	335 (306, 434)	286 (254, 361)
	FSL	µm/day	0.263 (0.220, 0.365)	0.786 (0.749, 0.912)	0.334 (0.276, 0.453)	0.542 (0.475, 0.689)
	NRMSE	%	2.27 (2.27, 3.94)	3.93 (3.28, 7.23)	2.84 (2.70, 5.42)	3.02 (2.86, 6.33)
	Effective strain range	µε	10–1430	10–2210	0–1140	10–1660

Table 3.S5 Statistical outcomes (p values) of the pair comparisons of parameters obtained from the hyperbola functions fitted to the RmV curves, for each week and group pair. The significance was adjusted for multiple comparisons using Bonferroni correction. These comparisons considered the parameters fitted to the average curves and parameter distributions estimated using the balanced bias-corrected and accelerated bootstrapping approach described in the methods. (n=9-10 mice/group).

Parameter legend: Resorption saturation level (RSL), Resorption velocity modulus (RVM), Resorption threshold (RT), Formation threshold (FT), Formation velocity modulus (FVM), Formation saturation level (FSL), Remodeling threshold (RmT), Remodeling velocity modulus (RmVM). p-value> 0.05 are highlighted in bold.

Weeks	Group comparison	Parameter			
		RSL	RmVM	RmT	FSL
0-1	BCR[Ibsp/Acp5] sham – BCR[Ibsp/Acp5] loaded	0.29200	**0.00109**	**0.03433**	**0.00001**
	BCR[Ibsp/Acp5] sham – WT sham	0.98784	0.06902	0.43463	0.81011
	BCR[Ibsp/Acp5] sham – WT loaded	0.14340	**0.00119**	0.07198	**0.00660**
	BCR[Ibsp/Acp5] loaded – WT sham	0.04999	0.91072	0.82559	**0.00001**

	BCR$^{Ibsp/Acp5}$ loaded – WT loaded	0.84749	0.11589	0.26757	**0.00073**
	WT sham – WT loaded	0.64182	**0.01775**	0.08072	**0.02298**
1-2	BCR$^{Ibsp/Acp5}$ sham – BCR$^{Ibsp/Acp5}$ loaded	**0.03813**	**0.00001**	**0.00001**	**0.00001**
	BCR$^{Ibsp/Acp5}$ sham – WT sham	0.79458	0.14307	0.11353	0.96187
	BCR$^{Ibsp/Acp5}$ sham – WT loaded	**0.00001**	**0.00001**	**0.00001**	**0.00001**
	BCR$^{Ibsp/Acp5}$ loaded – WT sham	**0.01934**	0.50233	0.93048	**0.00001**
	BCR$^{Ibsp/Acp5}$ loaded – WT loaded	0.78424	0.78935	0.54723	**0.00001**
	WT sham – WT loaded	0.22901	**0.03181**	**0.01932**	**0.00001**
2-3	BCR$^{Ibsp/Acp5}$ sham – BCR$^{Ibsp/Acp5}$ loaded	**0.02657**	**0.00907**	**0.00001**	**0.00001**
	BCR$^{Ibsp/Acp5}$ sham – WT sham	0.60730	**0.00145**	0.32990	0.10227
	BCR$^{Ibsp/Acp5}$ sham – WT loaded	0.16744	0.20277	**0.00001**	**0.00001**
	BCR$^{Ibsp/Acp5}$ loaded – WT sham	**0.02519**	0.70416	**0.00001**	**0.0001**
	BCR$^{Ibsp/Acp5}$ loaded – WT loaded	**0.00026**	0.51138	0.15333	**0.00001**
	WT sham – WT loaded	**0.01028**	0.44383	**0.00027**	**0.00001**
3-4	BCR$^{Ibsp/Acp5}$ sham – BCR$^{Ibsp/Acp5}$ loaded	0.23250	0.13044	**0.00001**	**0.00001**
	BCR$^{Ibsp/Acp5}$ sham – WT sham	0.58683	**0.04209**	0.58523	0.87816
	BCR$^{Ibsp/Acp5}$ sham – WT loaded	0.85009	**0.02283**	**0.00441**	**0.02986**
	BCR$^{Ibsp/Acp5}$ loaded – WT sham	0.11580	0.12690	**0.00001**	**0.00001**
	BCR$^{Ibsp/Acp5}$ loaded – WT loaded	0.06675	0.10081	**0.00001**	**0.00001**
	WT sham – WT loaded	0.18647	0.19926	0.05884	0.39030

References

1.   Berendsen, A.D. and B.R. Olsen, Bone development. Bone, 2015. 80: p. 14-18.

2.   Angel, N.Z., et al., Transgenic mice overexpressing tartrate-resistant acid phosphatase exhibit an increased rate of bone turnover. J Bone Miner Res, 2000. 15(1): p. 103-10.

3.   Vaaraniemi, J., et al., Intracellular machinery for matrix degradation in bone-resorbing osteoclasts. J Bone Miner Res, 2004. 19(9): p. 1432-40.

4.   Niedzwiedzki, T. and J. Filipowska, Bone remodeling in the context of cellular and systemic regulation: the role of osteocytes and the nervous system. J Mol Endocrinol, 2015. 55(2): p. R23-36.

5.   Frost, H.M., The mechanostat: a proposed pathogenic mechanism of osteoporoses and the bone mass effects of mechanical and nonmechanical agents. Bone Miner, 1987. 2(2): p. 73-85.

6.   Wolff, J., The law of bone remodeling. Maqet P., Furlong R., (Translation). 1986, Berlin, Germany: Springer Verlag.

7.   Robling, A.G., et al., Modulation of appositional and longitudinal bone growth in the rat ulna by applied static and dynamic force. Bone, 2001. 29(2): p. 105-13.

8.   Schulte, F.A., et al., Local mechanical stimuli regulate bone formation and resorption in mice at the tissue level. PLoS One, 2013. 8(4): p. e62172.

9.   Boyle, W.J., W.S. Simonet, and D.L. Lacey, Osteoclast differentiation and activation. Nature, 2003. 423(6937): p. 337-42.

10.   Dong, L.L., et al., Mechanical stretch induces osteogenesis through the alternative activation of macrophages. Journal of Cellular Physiology, 2021. 236(9): p. 6376-6390.

11.   Zhao, B. and L.B. Ivashkiv, Negative regulation of osteoclastogenesis and bone resorption by cytokines and transcriptional repressors. Arthritis Research & Therapy, 2011. 13(4): p. 234.

12.   Radzun, H.J., H. Kreipe, and M.R. Parwaresch, Tartrate-resistant acid phosphatase as a differentiation marker for the human mononuclear phagocyte system. Hematol Oncol, 1983. 1(4): p. 321-7.

13.   Ljusberg, J., B. Ek-Rylander, and G. Andersson, Tartrate-resistant purple acid phosphatase is synthesized as a latent proenzyme and activated by cysteine proteinases. Biochemical Journal, 1999. 343(1).

14.   Janckila, A.J., et al., Tartrate-resistant acid phosphatase as an immunohistochemical marker for inflammatory macrophages. Am J Clin Pathol, 2007. 127(4): p. 556-66.

15. Ek-Rylander, B., et al., Dephosphorylation of osteopontin and bone sialoprotein by osteoclastic tartrate-resistant acid phosphatase. Modulation of osteoclast adhesion in vitro. J Biol Chem, 1994. 269(21): p. 14853-6.

16. Mira-Pascual, L., et al., A Novel Sandwich ELISA for Tartrate-Resistant Acid Phosphatase 5a and 5b Protein Reveals that Both Isoforms are Secreted by Differentiating Osteoclasts and Correlate to the Type I Collagen Degradation Marker CTX-I In Vivo and In Vitro. Calcif Tissue Int, 2020. 106(2): p. 194-207.

17. Briggs, T.A., et al., Spondyloenchondrodysplasia Due to Mutations in ACP5: A Comprehensive Survey. J Clin Immunol, 2016. 36(3): p. 220-34.

18. Hayman, A.R., et al., Mice lacking tartrate-resistant acid phosphatase (Acp 5) have disrupted endochondral ossification and mild osteopetrosis. Development, 1996. 122(10): p. 3151-62.

19. Reinholt, F.P., et al., Osteopontin--a possible anchor of osteoclasts to bone. Proc Natl Acad Sci U S A, 1990. 87(12): p. 4473-5.

20. Lambers, F.M., et al., Mouse tail vertebrae adapt to cyclic mechanical loading by increasing bone formation rate and decreasing bone resorption rate as shown by time-lapsed in vivo imaging of dynamic bone morphometry. Bone, 2011. 49(6): p. 1340-50.

21. Birkhold, A.I., et al., Monitoring in vivo (re)modeling: a computational approach using 4D microCT data to quantify bone surface movements. Bone, 2015. 75: p. 210-21.

22. Wehrle, E., et al., Individualized cyclic mechanical loading improves callus properties during the remodelling phase of fracture healing in mice as assessed from time-lapsed in vivo imaging. Sci Rep, 2021. 11(1): p. 23037.

23. San Cheong, V., et al., A novel algorithm to predict bone changes in the mouse tibia properties under physiological conditions. Biomechanics and Modeling in Mechanobiology, 2020. 19(3): p. 985-1001.

24. Tourolle Ne Betts, D.C., et al., The association between mineralised tissue formation and the mechanical local in vivo environment: Time-lapsed quantification of a mouse defect healing model. Sci Rep, 2020. 10(1): p. 1100.

25. van Steensel, B., et al., Partial colocalization of glucocorticoid and mineralocorticoid receptors in discrete compartments in nuclei of rat hippocampus neurons. J Cell Sci, 1996. 109 (Pt 4): p. 787-92.

26. Fazeli, P.K., et al., Marrow fat and bone--new perspectives. J Clin Endocrinol Metab, 2013. 98(3): p. 935-45.

27.   Turner, C.H., et al., Mechanobiology of the skeleton. Sci Signal, 2009. 2(68): p. pt3.

28.   Hodgkinson, C.A., et al., Mutations at the mouse microphthalmia locus are associated with defects in a gene encoding a novel basic-helix-loop-helix-zipper protein. Cell, 1993. 74(2): p. 395-404.

29.   Dupont, S., et al., Role of YAP/TAZ in mechanotransduction. Nature, 2011. 474(7350): p. 179-83.

30.   Wada, K., et al., Hippo pathway regulation by cell morphology and stress fibers. Development, 2011. 138(18): p. 3907-14.

31.   Roforth, M.M., et al., Effects of age on bone mRNA levels of sclerostin and other genes relevant to bone metabolism in humans. Bone, 2014. 59: p. 1-6.

32.   Bune, A.J., et al., Mice lacking tartrate-resistant acid phosphatase (Acp 5) have disordered macrophage inflammatory responses and reduced clearance of the pathogen, Staphylococcus aureus. Immunology, 2001. 102(1): p. 103-13.

33.   Blumer, M.J., et al., Role of tartrate-resistant acid phosphatase (TRAP) in long bone development. Mech Dev, 2012. 129(5-8): p. 162-76.

34.   Suter, A., et al., Overlapping functions of lysosomal acid phosphatase (LAP) and tartrate-resistant acid phosphatase (Acp5) revealed by doubly deficient mice. Development, 2001. 128(23): p. 4899-910.

35.   Hayman, A.R. and T.M. Cox, Tartrate-resistant acid phosphatase knockout mice. J Bone Miner Res, 2003. 18(10): p. 1905-7.

36.   Hollberg, K., et al., Osteoclasts from mice deficient in tartrate-resistant acid phosphatase have altered ruffled borders and disturbed intracellular vesicular transport. Exp Cell Res, 2002. 279(2): p. 227-38.

37.   Roberts, H.C., et al., Altered collagen in tartrate-resistant acid phosphatase (TRAP)-deficient mice: a role for TRAP in bone collagen metabolism. Calcif Tissue Int, 2007. 80(6): p. 400-10.

38.   Lambers, F.M., et al., Bone adaptation to cyclic loading in murine caudal vertebrae is maintained with age and directly correlated to the local micromechanical environment. J Biomech, 2015. 48(6): p. 1179-87.

39.   Webster, D.J., et al., A novel in vivo mouse model for mechanically stimulated bone adaptation--a combined experimental and computational validation study. Comput Methods Biomech Biomed Engin, 2008. 11(5): p. 435-41.

40.   Webster, D., et al., Mechanical loading of mouse caudal vertebrae increases trabecular and cortical bone mass-dependence on dose and genotype. Biomech Model Mechanobiol, 2010. 9(6): p. 737-47.

41.   Christen, P., et al., Bone morphology allows estimation of loading history in a murine model of bone adaptation. Biomech Model Mechanobiol, 2012. 11(3-4): p. 483-92

42.   Byun, M.R., et al., FGF2 stimulates osteogenic differentiation through ERK induced TAZ expression. Bone, 2014. 58: p. 72-80.

43.   Cui, C.B., et al., Transcriptional coactivation of bone-specific transcription factor Cbfa1 by TAZ. Mol Cell Biol, 2003. 23(3): p. 1004-13.

44.   Scheuren, A.C., et al., Mechano-Regulation of Trabecular Bone Adaptation Is Controlled by the Local in vivo Environment and Logarithmically Dependent on Loading Frequency. Front Bioeng Biotechnol, 2020. 8: p. 566346.

45.   C. Marques, F., et al., Mechanostat parameters estimated from time-lapsed in vivo micro-computed tomography data of mechanically driven bone adaptation are logarithmically dependent on loading frequency. Frontiers in Bioengineering and Biotechnology, 2023. 11.

46.   Paul, G.R., et al., Tissue-Level Regeneration and Remodeling Dynamics are Driven by Mechanical Stimuli in the Microenvironment in a Post-Bridging Loaded Femur Defect Healing Model in Mice. Frontiers in Cell and Developmental Biology, 2022. 10.

47.   Razi, H., et al., Aging Leads to a Dysregulation in Mechanically Driven Bone Formation and Resorption. J Bone Miner Res, 2015. 30(10): p. 1864-73.

48.   Burr, D.B., Targeted and nontargeted remodeling. Bone, 2002. 30(1): p. 2-4.

49.   Parfitt, A.M., Targeted and nontargeted bone remodeling: relationship to basic multicellular unit origination and progression. Bone, 2002. 30(1): p. 5-7.

50.   Lloyd, S.A., et al., Interdependence of muscle atrophy and bone loss induced by mechanical unloading. J Bone Miner Res, 2014. 29(5): p. 1118-30.

51.   Bikle, D.D. and B.P. Halloran, The response of bone to unloading. J Bone Miner Metab, 1999. 17(4): p. 233-44.

52.   Gardinier, J.D., et al., Bone adaptation in response to treadmill exercise in young and adult mice. Bone Rep, 2018. 8: p. 29-37.

53.   Labun, K., et al., CHOPCHOP v2: a web tool for the next generation of CRISPR genome engineering. Nucleic Acids Res, 2016. 44(W1): p. W272-6.

54.   Bellanti, F., A. Lo Buglio, and G. Vendemiale, Mitochondrial Impairment in Sarcopenia. Biology, 2021. 10(1).

55.   Takeshita, S., K. Kaji, and A. Kudo, Identification and characterization of the new osteoclast progenitor with macrophage phenotypes being able to differentiate into mature osteoclasts. J Bone Miner Res, 2000. 15(8): p. 1477-88.

56. Chevalier, C., et al., Primary mouse osteoblast and osteoclast culturing and analysis. STAR Protoc, 2021. 2(2): p. 100452.

57. Dobin, A., et al., STAR: ultrafast universal RNA-seq aligner. Bioinformatics, 2013. 29(1): p. 15-21.

58. Anders, S., P.T. Pyl, and W. Huber, HTSeq--a Python framework to work with high-throughput sequencing data. Bioinformatics, 2015. 31(2): p. 166-9.

59. Luo, W., et al., GAGE: generally applicable gene set enrichment for pathway analysis. BMC Bioinformatics, 2009. 10: p. 161.

60. Love, M.I., W. Huber, and S. Anders, Moderated estimation of fold change and dispersion for RNA-seq data with DESeq2. Genome Biol, 2014. 15(12): p. 550.

61. Chambers, T.J., et al., Induction of bone formation in rat tail vertebrae by mechanical loading. Bone Miner, 1993. 20(2): p. 167-78.

62. Odgaard, A. and H.J. Gundersen, Quantification of connectivity in cancellous bone, with special emphasis on 3-D reconstructions. Bone, 1993. 14(2): p. 173-82.

63. Whitehead, J.C., et al., A clinical frailty index in aging mice: comparisons with frailty index data in humans. J Gerontol A Biol Sci Med Sci, 2014. 69(6): p. 621-32.

64. Harrigan, T.P. and R.W. Mann, Characterization of microstructural anisotropy in orthotropic materials using a second rank tensor. Journal of Materials Science, 1984. 19(3): p. 761-767.

65. Pistoia, W., et al., Estimation of distal radius failure load with micro-finite element analysis models based on three-dimensional peripheral quantitative computed tomography images. Bone, 2002. 30(6): p. 842-8.

66. Flaig, C. and P. Arbenz, A scalable memory efficient multigrid solver for micro-finite element analyses based on CT images. Parallel Computing, 2011. 37(12): p. 846-854.

67. Lunde, A. and J.C. Glover, A versatile toolbox for semi-automatic cell-by-cell object-based colocalization analysis. Sci Rep, 2020. 10(1): p. 19027.

68. Davison, A.C. and D.V. Hinkley, Bootstrap Methods and their Application. Cambridge Series in Statistical and Probabilistic Mathematics. 1997, Cambridge: Cambridge University Press.

Chapter 4

Hallmarks of Aging of Bone and Bone Cells in Prematurely Aged Mice

4.1. Unveiling frailty: comprehensive and sex-specific characterization in prematurely aged PolgA mice

Dilara Yılmaz[1], Amit Singh[1], Esther Wehrle[1,2], Gisela A. Kuhn[1], Neashan Mathavan[1], Ralph Müller[1]

[1]Institute for Biomechanics, ETH Zurich, Zurich, Switzerland
[2]AO Research Institute Davos, Davos Platz, Switzerland

Abstract

Frailty, a geriatric syndrome, is assessed using the frailty phenotype (FP) and frailty index (FI). While these approaches have been applied to aging mice, their effectiveness in prematurely aging mouse models such as PolgA$^{D257A/D257A}$ (PolgA) has not been completely explored. We demonstrated that frailty became evident in PolgA mice around 40 weeks, validated through body weight loss, reduced walking speed, decreased physical activity, and weaker grip strength. Moreover, we also identified sex differences in these mice with females exhibiting higher frailty compared to males. Frailty prevalence in PolgA mice at 40 weeks parallels that observed in naturally aging mice at 27 months and aging humans at 65-70 years. These findings contribute to understanding frailty onset and sex-specific patterns, emphasizing the significance of the PolgA mouse model in investigating aging and related disorders.

Keywords

Musculoskeletal aging, frailty, PolgA mice, frailty phenotype, premature aging

4.1.1. Introduction

Frailty is a complex geriatric syndrome that is characterized by a diminished ability to respond to stressors and maintain homeostasis [1]. Two widely used approaches to evaluate frailty are the frailty phenotype (FP) and the frailty index (FI) [2, 3]. The FP assesses individuals based on the presence or absence of specific criteria, which are: unintentional weight loss, slow walking speed, self-reported exhaustion, weakness, and low physical activity. Individuals, meeting three or more of these criteria are classified as frail [2]. On the other hand, the FI is based on the accumulation of health deficits, where the total number of deficits is divided by the number of deficits assessed, providing a quantitative measure of frailty [3]. Both the FP and FI are valuable approaches for identifying frailty in individuals, enabling a better understanding of its impact on health outcomes and aging research.

With the intention of investigating frailty, mouse models that accurately replicate the complex nature of frailty in humans have been developed [4]. Several research groups established frailty assessment tools designated for mice based on human criteria (FP or FI) [5-8]. Slowness (rotarod), weakness (grip strength), physical activity (rotarod), and endurance (combined rotarod and grip strength) were assessed to develop frailty in mice by adopting the FP approach for humans [7]. Similarly, frailty was defined in mice by using the clinical human FI approach, which involved 31 parameters, including basal metabolism, body composition, and activity levels in evaluating signs of discomfort [9] and the modified versions of these methods were used by other groups to assess frailty [6, 10-14]. However, the methods employed for assessing frailty in mice have primarily been applied to C57BL/6 (naturally aging) mice aged 17 months and older [15]. Therefore, it remains unclear whether these methods are equally effective in identifying frailty in prematurely aging mice.

In this regard, prematurely aging mouse models such as PolgA$^{D257A/D257A}$ (PolgA) offer numerous advantages over naturally aging mice [4]. Notably, PolgA mice demonstrate the premature manifestation of age-related phenotypes within a short time frame [16]. Around just 40 weeks of age, these mice exhibit multiple hallmarks of aging, including kyphosis, hearing impairment, progressive weight loss, osteosarcopenia, and osteoporosis [16-18]. In addition, age-related changes in these mice were evaluated in females using the clinical mouse FI method, exhibiting higher FI scores in PolgA mice compared to their age-matched wild-type littermates (WT) [18]. Although the PolgA mouse model holds promise for investigating frailty

and age-related musculoskeletal disorders, there are certain limitations in its frailty scoring. Despite being a non-invasive method, FI scoring, in general, lacks assessments such as walking speed and endurance to measure the functional abilities of mice. Moreover, the sex-dependent component of frailty has not been addressed in these mice. Therefore, our first objective is to identify the frailty phenotype in prematurely aging PolgA mice around 40 weeks by evaluating weight loss, grip strength (weakness), walking speed (slowness), and home cage walking distance (physical activity) in comparison to their age-matched WT littermates. Our second objective is to show the sex-dependent differences in frailty in PolgA mice.

4.1.2. Results

When considering age-related changes in the PolgA mice, there were notable differences compared to WT mice for both sexes (Figure 4.1.1). Firstly, PolgA males were observed to be 13% lighter than their WT counterparts ($p<0.001$), whereas this difference was 12% for females ($p<0.05$), reflecting the unintentional body weight loss observed in sarcopenia patients [19] (Figure 4.1.1A). In terms of slowness, PolgA males exhibited a 24% reduction in walking speed compared to WT males ($p<0.001$), while PolgA females showed a 18% decrease compared to WT females which was not significant (Figure 4.1.1B). Although there was no significant difference in grip strength among males, there was a significant 26% decrease in females compared to WT counterparts ($p<0.05$) (Figure 4.1.1C). In the case of physical activity assessed by average walking distance, there was a 6% and 24% decrease for males and females ($p<0.05$) respectively between PolgA and WT mice (Figure 4.1.1D). Hence, the age-related differences were notably prominent in PolgA mice, with the differences being more pronounced in females around 40 weeks.
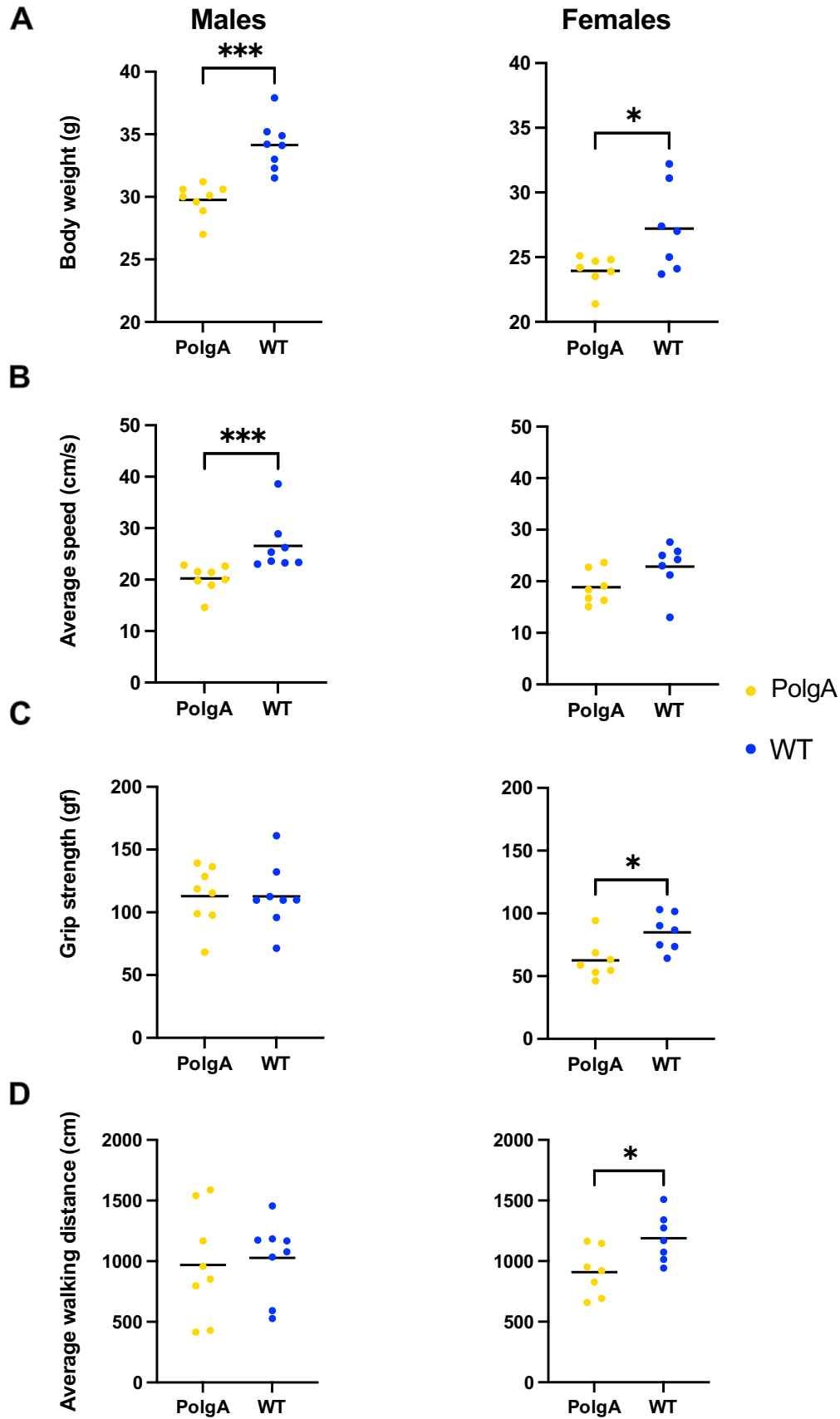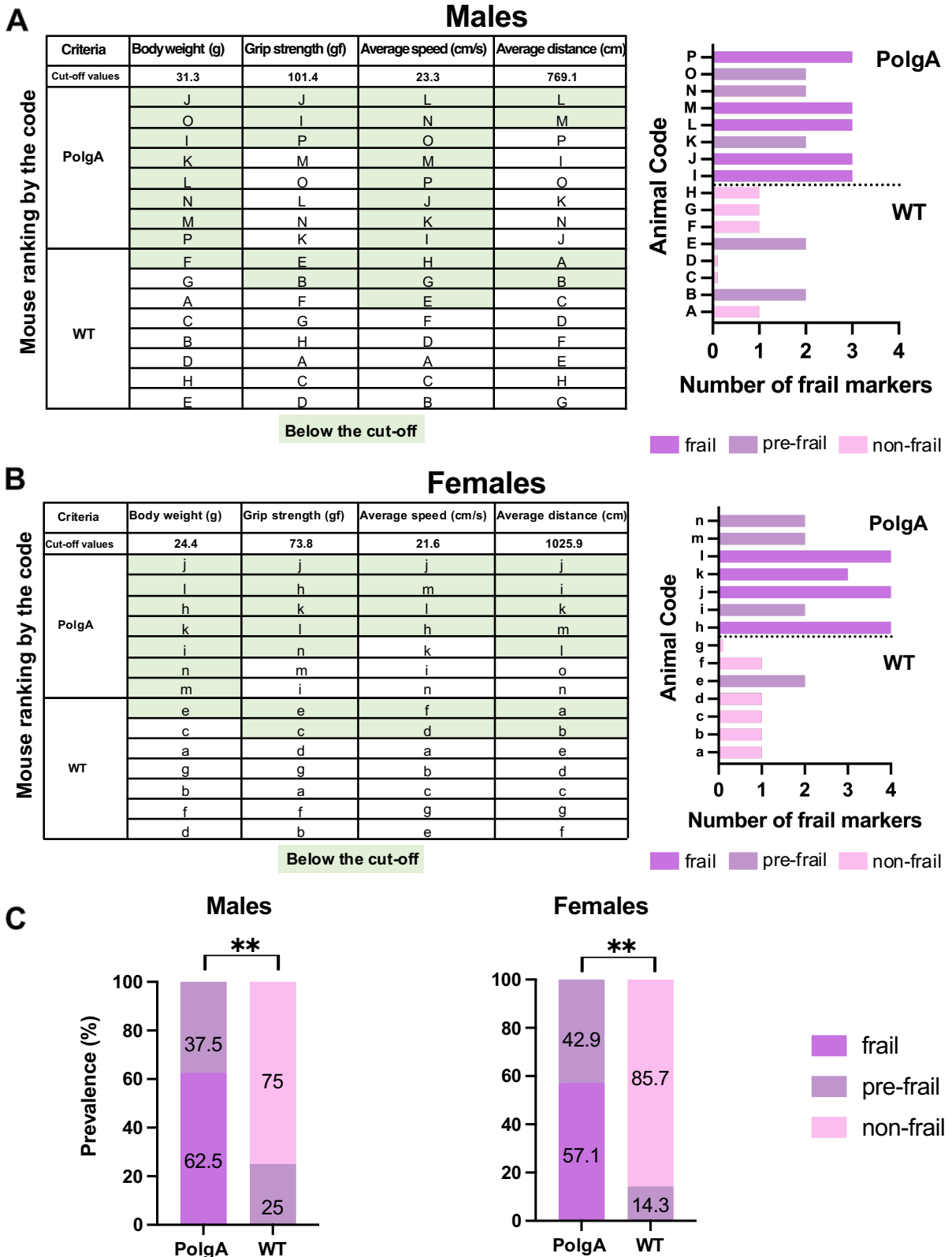
Figure 4.1.1 Age and sex-related changes in PolgA mice. Comparison of each criteria used to assess frailty phenotype between PolgA mice and WT littermates at 40 weeks: A) body weight B) average walking speed C), max grip strength and D) average walking distance. Box plots represents max and min values, (n=7-8 mice/group). Significance was determined by the Student t-test or Mann-Whitney test, *p<0.05, **p<0.01, ***p<0.001.

To assess the frailty of PolgA mice, cutoff values, and the ranking order of mice for each criterion from best to worst, were identified (Figure 4.1.2A-B). Mice were considered frail if their performance fell below the cutoff values for the designated parameters for body weight (31.3 g, 24.4 g), grip strength (101.4 gf, 73.8 gf), average speed (23.3 cm/s; 21.6 cm/s) and average distance (769.1 cm, 1025.9 cm) for male and female mice respectively using the reference values obtained from WT mice around 40 weeks. According to these criteria, 5 PolgA male mice and 4 PolgA female mice were categorized as frail, while 3 PolgA male and female mice were classified as pre-frail. None of the PolgA mice were identified as non-frail. In contrast, among the WT mice, 2 males and 1 female were designated as pre-frail, and 6 males and females were categorized as non-frail based on the same criteria. Regardless of sex, none of the WT mice were identified as frail (Figure 4.1.2A-B). In addition, these cut-off values obtained from WT mice for each sex were utilized as a reference to assess the prevalence of frailty in PolgA mice (Figure 4.1.2C). 62.5% of PolgA male mice were classified as frail, while 37.5% were categorized as pre-frail. On the other hand, 57.1% of PolgA females were identified as frail, while 42.9% were designated as pre-frail. In contrast, the majority of the WT females, 85.7%, were designated as non-frail while only 14.3% of them were identified as pre-frail. Similarly,75 % of WT males were categorized as non-frail and 25% as pre-frail (Figure 4.1.2C). The difference in frailty category (frail, pre-frail and non-frail) distribution between PolgA and WT mice are statistically significant by the Fischer-Exact test for both females (p=0.0014) and males (p=0.0031), indicating the notable effects of genetic or physiological differences of these mice on their frailty status rather than random variability (Figure 4.1.2C).

Figure 4.1.2 Frailty status of PolgA mice at 40 weeks. A) The mice were coded A-P for males and a-o for females and ranked by their performance. Frailty for PolgA mice of both sexes was calculated using reference values obtained from WT mice for each criterion. The green highlight indicates the mice in the below 20% of the performance for each criterion except body weight (below 10%). B) The number of frailty markers for each mouse at 40 weeks was

presented. Frailty was defined if a mouse exhibited three or more of the criterion markers below the cut-off values. Pre-frailty was assigned if a mouse displayed two frailty markers, while non-frailty was indicated if a mouse had one or no markers. (n=7-8 mice/group). C) Prevalence for frailty was determined using the cut-off values obtained from 40-week-old WT mice for each sex and criterion categorized as frail, pre-frail, and non-frail. Data represented as percentages, (n=7-8 mice/group). Significance was determined by the Fischer-exact test, *p<0.05, **p<0.01, ***p<0.001.

To identify the morphological differences between the mice identified as frail, pre-frail, and non-frail, we systematically compared these subgroups by evaluating each criterion to assess frailty. No distinct difference was observed in body weight within the male subgroups of PolgA and WT mice. However, non-frail female WT mice exhibited a higher body weight compared to pre-frail WT mice. Similarly, pre-frail PolgA females displayed a pattern for slightly greater body weight compared to their frail counterparts (Figure 4.1.3A). Regarding the slowness, there were no distinctive variations in walking speed among subgroups of PolgA and WT males except WT pre-frail male indicating significantly faster walking speed than pre-frail and frail PolgA mice. In contrast, female PolgA frail mice indicated a trend for slower walking speed in comparison to the pre-frail group while no significance was observed (Figure 4.1.3B). For comparison of the weakness of the grip strength, pre-frail PolgA mice manifested a tendency towards higher grip strength compared to frail PolgA mice regardless of sex. Subsequently, non-frail WT mice for both sexes exhibited a trend for higher grip strength compared to pre-frail mice WT and PolgA mice and frail mice (Figure 4.1.3C). A similar pattern was observed for comparison of physical activity assessed by average walking distance. Pre-frail PolgA mice indicated a pattern for increased walking distances compared to frail PolgA mice, irrespective of sex for both groups while non-frail WT mice covered longer distances compared to their pre-frail counterparts (Figure 4.1.3D). The results indicated morphological differences in subcategories evaluated between WT and PolgA mice, across similar frailty statuses.
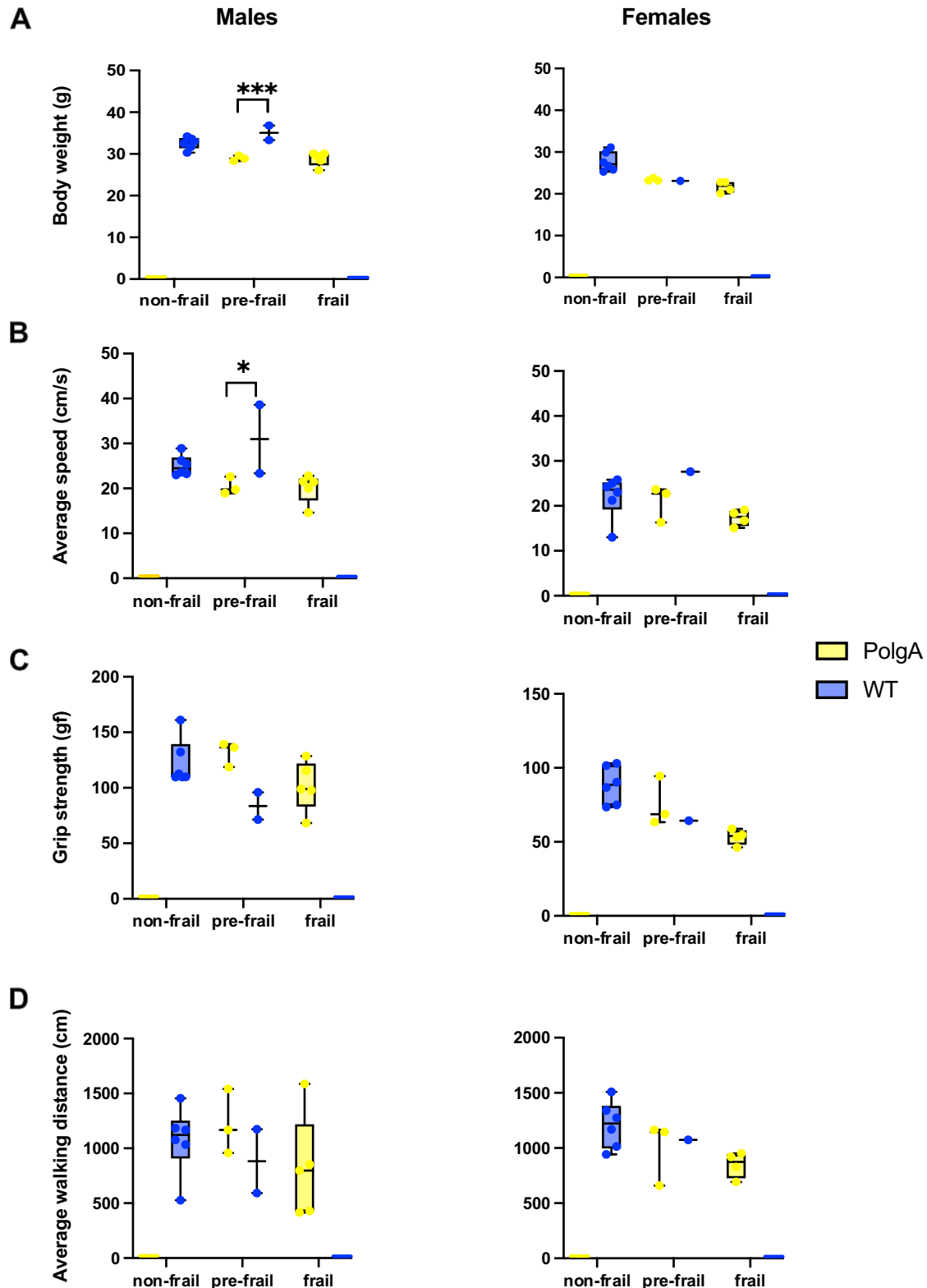
Figure 4.1.3 Age-related differences between frail, pre-frail, and non-frail mice. Mice that were identified as frail, pre-frail, and non-frail at 40 weeks were compared for each criterion used to evaluate the frailty phenotype in PolgA and WT mice: A) body weight, B) average speed, C) grip strength, D) average walking distance. Box plots represent max and min values with data points, (n=1-6 mice/group). Significance was determined by two-way ANOVA

corrected for multiple comparisons by false discovery rate (FDR) using a two-stage linear step-up procedure of Benjamini, Krieger, and Yekutieli, (*p<0.05, **p<0.01, ***p<0.001).

Furthermore, individual frailty scores were calculated as percentages, determined by dividing the total number of failed tests by the total number of tests performed for each group [20] (Table 4.1.S1). PolgA males had a frailty score of 65.6%, while females had a score of 75%. In contrast, the frailty scores for WT mice were 25% for both males and females, indicating a tendency for a higher level of frailty in female PolgA mice compared to males and WT females.

The calculation of frailty scores has revealed that primary contributors to frailty in our study include alterations in body weight, walking speed, and grip strength (Table 4.1.S2). Therefore, we compared these primary contributors used to evaluate frailty across different ages (Figure 4.1.4). Body weight gradually increases with aging in PolgA and WT mice from 12 to 40 weeks, with a more pronounced increase in WT mice. However, PolgA mice begin to experience weight loss after 40 weeks for both sexes. The differences in body weight between PolgA and WT mice become statistically significant at 34 (p<0.0001) and 40 weeks for males (p<0.001), while for females this significance is observed only at 40 weeks (p<0.01) (Figure 4.1.4A). Considering the slowness, there was no distinct difference between PolgA and WT mice males until 40 weeks. However, at 40 weeks, a significant decrease in walking speed is observed between WT and PolgA mice (p<0.01). In females, although there is a trend of decreasing speed with age in PolgA females, there is no notable difference between WT mice at any age (Figure 4.1.4A). Regarding the grip strength, there were no notable differences in males. However, in females, PolgA mice showed a gradual decrease over time, and at 40 weeks, this decrease was significant compared to WT females (p<0.05) (Figure 4.1.4A).

Finally, we assessed FI in PolgA mice at these various ages. Our results showed a trend that the frailty of PolgA male and female mice increased with age. PolgA male mice demonstrated a higher FI compared to their WT (p<0.001) and female counterparts (p<0.01) at 40 weeks while no significant differences between the genotypes were observed at earlier time points (Figure 4.1.4B). This particular outcome might be associated that females can exhibit greater impairments in physical functions at 40 weeks while males accumulated a higher cumulative burden of health deficiencies although they performed better in these physical function measures.
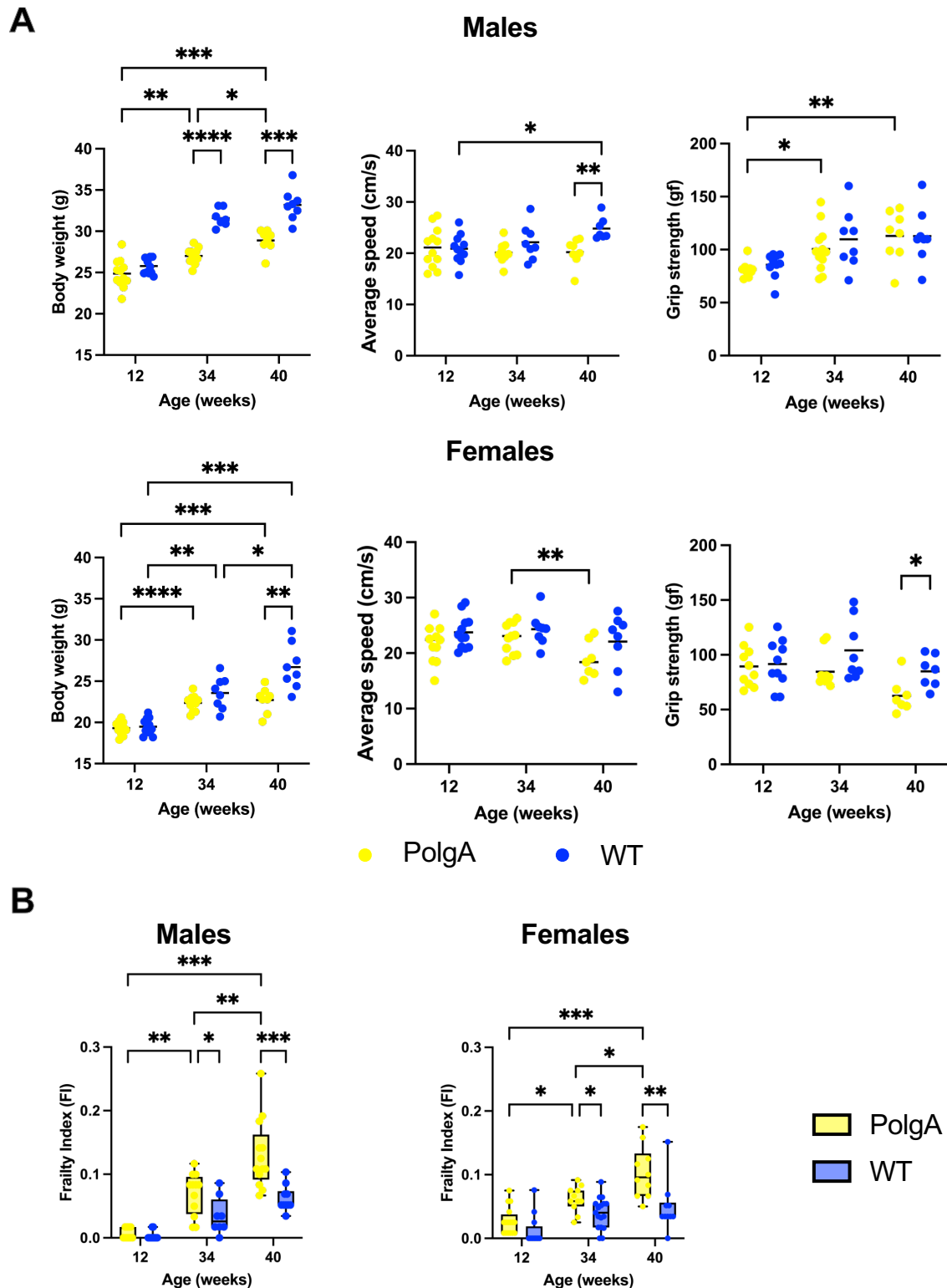
Figure 4.1.4 Comparison of key frailty phenotype parameters and frailty index across various age groups in PolgA mice A) Assessment of the primary contributors used to evaluate frailty: body weight, slowness (average speed) and weakness (grip strength) B) frailty index (FI) in PolgA and wild type (WT) at 12, 34, and 40 weeks. Data are presented as mean ± s.d., (n=7-13 mice/group). Significance was determined by two-way ANOVA by Bonferroni correction, *p<0.05, **p<0.01, ***p<0.001.

4.1.3. Discussion

Frailty measurement, utilizing both the FP and FI, is crucial for advancing our understanding of the aging process and developing interventions that can enhance health span. The FP, typically defined by physical characteristics such as reduced activity and weight loss, alongside the FI, which aggregates a broad range of health deficits, offers a comprehensive approach to assessing vulnerability to adverse outcomes [2,3]. Previous research on frailty in mice underscores the reliability of these measurements in capturing comparable aging phenomena observed in humans, demonstrating their critical role in translational aging research [5-8]. Furthermore, Feridooni et al. (2016) particularly investigated the reproducibility of FI scores done by different raters and concluded that mice have overall comparable FI scores [30].

In this study, we applied the human frailty phenotype approach [2] to evaluate frailty characteristics of prematurely aging PolgA mice by assessing body weight loss, impaired strength, reduced walking speed, and limited physical activity. By applying this approach, we were able to effectively identify the onset and prevalence of frailty in PolgA mice and further elucidate the sex differences. Previous studies had evaluated frailty in WT mice as early as 17 months old, indicating the onset of frailty at approximately 27 months [6]. In contrast, PolgA mice developed frailty as early as 40 weeks, roughly equivalent to 20-23 months in C57BL/6 mice and correspond to frailty onset at 65–70 years in humans [2, 21, 22].

At 29 months of age, 52.4% of WT mice were shown to be frail and another study reported frailty rates of 44.4%, for males and 73.7% for females at 26 months [6, 11]. Using a similar assessment method, PolgA mice exhibited a prevalence of frailty approximately at 40 weeks with rates of 63% for males and 57% for females. In addition, the calculated frailty scores for PolgA mice were 65.6 % for males and 75% for females while the frailty score for the prematurely aging mice was previously reported as 40% [20].

Collectively, our data show that PolgA mice have higher frailty scores compared to their age-matched WT counterparts irrespective of sex. Furthermore, the prevalence of frailty among PolgA mice at 40 weeks is comparable to that observed in WT mice at around 27 months of age. Considering the sex differences, female PolgA is frailer compared to male PolgA. This observation parallels with what was similarly observed in humans, where women were known to exhibit higher frailty compared to men [23]. While there has been some controversy regarding increased frailty in female mice, some studies have indicated no significant sex

differences while some demonstrated female C57BL/6 mice were frailer compared to males[8, 9, 11]. Moreover, it was argued that the prevalence of frailty increases with age, ultimately resulting in early mortality among frail mice, regardless of sex [10, 11, 13, 24]. Nevertheless, our findings may indicate the existence of sex differences in aging PolgA mice.

One limitation of our study is the small sample size contributing to non-significant results and altering the outcomes for the prevalence of frailty. In addition, the average walking distance of males might be impacted by their single housing conditions, potentially leading to no notable differences between the groups. Moreover, our frailty phenotype assessment is based on the 4 criteria adopted from the mouse frailty phenotype approach, which was derived from the human approach [2, 7]. However, the mouse FP approach lacked a weight factor and did not include an established endurance test. On that note, we could have incorporated an endurance test into our studies to provide a more comprehensive overview of the frailty phenotype status of PolgA mice. However, the traditional treadmill running test used to evaluate exhaustion in animals has faced significant scrutiny from an animal welfare point-of-view due to the stress it imposes on the animals.

In conclusion, our study comprehensively characterized frailty in prematurely aging PolgA mice. The onset of frailty in PolgA mice was evident around 40 weeks, thereby confirming the validity of the observed frailty phenotypes including body weight loss, reduced walking speed, grip strength, and physical activity. FI scoring corroborated these findings and highlighted an age-associated increase in frailty with the onset observed at 40 weeks in PolgA mice.

Furthermore, our study revealed sex differences, with females displaying a slightly higher susceptibility to frailty compared to males. We contextualized these results by comparing them with their WT littermates and referencing established literature on natural aging in mice and humans, emphasizing PolgA mice as a valuable model for investigating aging and age-related disorders.

4.1.4. Materials and Methods

Animal models

All animal procedures were carried out by the regulations set by the local authorities (license: ZH35/2019) and approved by the Verterinäramt des Kantons Zürich, Zurich, Switzerland. A

colony of mice expressing an exonuclease-deficient version of the mitochondrial DNA polymerase γ (PolgAD257A, B6.129S7(Cg)-Polgtm1Prol/J, JAX stock 017341, The Jackson Laboratory) was bred and maintained at the ETH Phenomics Center. The mice were housed under standard conditions, including a 12:12 h light-dark cycle, with access to maintenance feed and water ad libitum, and three to five animals per cage. The mice were bred as previously described [18] and genotyped before the experiments (Transnetyx, Cordova, USA). Homozygous PolgA mice and age- and sex-matched WT littermates (controls) were used for all experiments.

Grip strength

Grip strength was assessed using a force tension apparatus (Grip Strength Meter, model 47200, Ugo Basile) approximately at 40 weeks in female and male PolgA and WT mice as previously described [18]. The mice held the stationary bar with their forepaws and were then gently pulled horizontally by their tail until they released their grip. This procedure was repeated five times for each mouse, and the maximum force (gram-force) value was used for the analysis. All measurements were conducted by the same trained operator.

Gait analysis

Gait data was collected from female and male PolgA and WT mice around 40 weeks of age using the Noldus CatWalk XT system. Run speed, stand, duty cycle, swing speed, maximum variation, and stride length were analyzed to assess the gait characteristics of the mice.

Physical activity

The average distance was measured from the PhenoMaster experiment and used to assess physical activity level. PhenoMaster metabolic cage system was utilized to record various physiological and behavioral measurements including the measurement of drinking and feeding amounts, CO_2 and O_2 consumption, walking speed, and walking distance. For this manuscript, only the average walking distance from PhenoMaster analysis were used.

Quantification of frailty index

The FI in the study was quantified by implementing the Mouse Clinical Frailty Index consisting of a comprehensive evaluation of 31 non-invasive clinical parameters [9]. Each parameter except body weight and body surface temperature received a score of 0 for absence, 0.5 for a

mild deficit, and 1 for a severe deficit. Body weight and body surface temperature were scored relative to the standard deviations from a reference mean in young adult mice (12 weeks old). However, body surface temperature was excluded in the calculation of the FI due to a lack of appropriate tools for measurement.

Frailty phenotype criteria

To establish a frailty phenotype, we identified four criteria that are indicative of frailty: body weight loss, grip strength, walking speed, and physical activity. These criteria were deliberately chosen due to their similarity to the clinical criteria for assessing frailty in humans [2]. By incorporating these key indicators, we aimed to create a comprehensive and reliable frailty phenotype that aligns closely with established clinical mouse and human frailty standards (Table 4.1). For each parameter, a 20% cut-off value was chosen, except for body weight. In the case of body weight, which was measured prior to the experiments, a 10% cut-off value was applied. This choice was made to maintain alignment with established human criteria and to ensure consistency in assessments between mice and humans, as indicated in the previous publication [2, 25-28].

Table 4.1 The criteria for defining mouse frailty for PolgA mice based on the human frailty criteria.

Human frailty criteria	Mouse frailty criteria	Cut off values
Unintentional weight loss	Weight loss: Body weight (g) Males: 31.3 g Females: 24.4 g	Lowest 10%
Weakness - Low grip strength	Weakness: Grip strength (gf) Males: 101.4 gf - Females: 73.8 gf	Lowest 20%
Slow walking speed	Slowness: Average walking speed (cm/s) Males: 23.3 cm/s Females: 21.6 cm/s	Lowest 20%
Low physical activity level	Low physical activity: Average walking distance (cm) Males: 769.1 cm Females: 1025.9 cm	Lowest 20%

Statistical analysis

Data analysis was performed using GraphPad Prism software. Given the small sample sizes within the frailty category data, Fisher's exact test was utilized to compare the frailty prevalence between genotypes. For the analysis of frailty phenotype parameters within sub-frailty groups, a two-way ANOVA corrected for multiple comparisons by false discovery rate (FDR) using a two-stage linear step-up procedure of Benjamini, Krieger, and Yekutieli was used. For the remaining comparisons involving two independent samples, Student's t-test or Mann-Whitney test was used based on the normality. Comparisons involving more than two groups were analyzed using a two-way ANOVA, corrected with Bonferroni or Sidak's post hoc test. Statistical significance was determined for $p<0.05$.

Acknowledgments

Conflict of interest

The authors have no conflict of interest to declare.

Author Contributions

Conceptualization and methodology: GAK, RM; investigation, methodology: GAK; data curation, formal analysis: DY, AS, NM; writing - original draft: DY, writing - review and editing: DY, GAK, NM, AS, EW, RM; resources, supervision, funding acquisition, project administration RM.

Supplementary Materials

Table 4.1.S1 Calculation of frailty score in PolgA mice and WT littermates.

The frailty score was calculated using reference values obtained from WT mice for each sex and criterion with A representing the total number of mice below designated the cut-off value for the specific criterion, and B representing the total number of mice included in the analysis for that criterion. Frailty score is expressed as a percentage.

Criteria	Males				Females			
	PolgA		WT		PolgA		WT	
	A	B	A	B	A	B	A	B
Body weight (g)	8	8	1	8	7	7	1	7
Average walking speed (cm/s)	8	8	3	8	4	7	2	7
Grip strength (gf)	3	8	2	8	5	7	2	7
Average walking distance (cm)	2	8	2	8	5	7	2	7
Total	21	32	8	32	21	28	7	28
Frailty Score (%) (A/B) x 100	65.6		25		75		25	

Table 4.1.S2 Calculation of frailty score in PolgA mice and WT littermates using 3 frailty criteria:

The calculated frailty scores (abcd) for PolgA mice and WT littermates, derived from the method presented in Table 4.1.S1, were extended to assess frailty using a combination of three criteria: Body weight (a), Average speed (b), Grip strength (c), and Average walking distance (d), representing a subset of the four criteria used in Table 4.1.S1

Criteria	Frailty Score (%)			
	Males		Females	
	PolgA	WT	PolgA	WT
abcd	65.6	25	75.0	25.0
abc	79.2	25	76.2	23.8
abd	75.0	25	76.2	23.8
acd	54.2	20.8	81.0	23.8
bcd	54.2	29.2	66.7	28.6

References

1.   Milte, R. and M. Crotty, Musculoskeletal health, frailty and functional decline. Best Pract Res Clin Rheumatol, 2014. 28(3): p. 395-410.

2.   Fried, L.P., et al., Frailty in older adults: evidence for a phenotype. J Gerontol A Biol Sci Med Sci, 2001. 56(3): p. M146-56.

3.   Rockwood, K., et al., A global clinical measure of fitness and frailty in elderly people. CMAJ, 2005. 173(5): p. 489-95.

4.   Yilmaz, D., et al., Mouse models of accelerated aging in musculoskeletal research for assessing frailty, sarcopenia, and osteoporosis - a review. Ageing Res Rev, 2023: p. 102118.

5.   Baumann, C.W., et al., Age-induced oxidative stress: how does it influence skeletal muscle quantity and quality? J Appl Physiol (1985), 2016. 121(5): p. 1047-1052.

6.   Baumann, C.W., D. Kwak, and L.V. Thompson, Phenotypic Frailty Assessment in Mice: Development, Discoveries, and Experimental Considerations. Physiology (Bethesda), 2020. 35(6): p. 405-414.

7.   Liu, H., et al., Clinically relevant frailty index for mice. J Gerontol A Biol Sci Med Sci, 2014. 69(12): p. 1485-91.

8.   Parks, R.J., et al., A procedure for creating a frailty index based on deficit accumulation in aging mice. J Gerontol A Biol Sci Med Sci, 2012. 67(3): p. 217-27.

9.   Whitehead, J.C., et al., A clinical frailty index in aging mice: comparisons with frailty index data in humans. J Gerontol A Biol Sci Med Sci, 2014. 69(6): p. 621-32.

10.   Baumann, C.W., D. Kwak, and L.V. Thompson, Assessing onset, prevalence and survival in mice using a frailty phenotype. Aging (Albany NY), 2018. 10(12): p. 4042-4053.

11.   Baumann, C.W., D. Kwak, and L.V. Thompson, Sex-specific components of frailty in C57BL/6 mice. Aging (Albany NY), 2019. 11(14): p. 5206-5214.

12.   Gomez-Cabrera, M.C., et al., A New Frailty Score for Experimental Animals Based on the Clinical Phenotype: Inactivity as a Model of Frailty. J Gerontol A Biol Sci Med Sci, 2017. 72(7): p. 885-891.

13.   Kwak, D., C.W. Baumann, and L.V. Thompson, Identifying Characteristics of Frailty in Female Mice Using a Phenotype Assessment Tool. J Gerontol A Biol Sci Med Sci, 2020. 75(4): p. 640-646.

14.   Sukoff Rizzo, S.J., et al., Assessing Healthspan and Lifespan Measures in Aging Mice: Optimization of Testing Protocols, Replicability, and Rater Reliability. Curr Protoc Mouse Biol, 2018. 8(2): p. e45.

15.   von Zglinicki, T., et al., Frailty in mouse ageing: A conceptual approach. Mech Ageing Dev, 2016. 160: p. 34-40.

16.   Trifunovic, A., et al., Premature ageing in mice expressing defective mitochondrial DNA polymerase. Nature, 2004. 429(6990): p. 417-23.

17.   Kujoth, G.C., C. Leeuwenburgh, and T.A. Prolla, Mitochondrial DNA mutations and apoptosis in mammalian aging. Cancer Res, 2006. 66(15): p. 7386-9.

18.   Scheuren, A.C., et al., Hallmarks of frailty and osteosarcopenia in prematurely aged PolgA((D257A/D257A)) mice. J Cachexia Sarcopenia Muscle, 2020. 11(4): p. 1121-1140.

19.   Bales, C.W. and C.S. Ritchie, Sarcopenia, weight loss, and nutritional frailty in the elderly. Annu Rev Nutr, 2002. 22: p. 309-23.

20.   Martinez de Toda, I., et al., Frailty Quantified by the "Valencia Score" as a Potential Predictor of Lifespan in Mice. J Gerontol A Biol Sci Med Sci, 2018. 73(10): p. 1323-1329.

21.   Dutta, S. and P. Sengupta, Men and mice: Relating their ages. Life Sci, 2016. 152: p. 244-8.

22.   Justice, J.N., et al., Comparative Approaches to Understanding the Relation Between Aging and Physical Function. J Gerontol A Biol Sci Med Sci, 2016. 71(10): p. 1243-53.

23.   Gordon, E.H., et al., Sex differences in frailty: A systematic review and meta-analysis. Exp Gerontol, 2017. 89: p. 30-40.

24.   Kane, A.E., et al., Sex Differences in Healthspan Predict Lifespan in the 3xTg-AD Mouse Model of Alzheimer's Disease. Front Aging Neurosci, 2018. 10: p. 172.

25.   Hill, J.O., Can a small-changes approach help address the obesity epidemic? A report of the Joint Task Force of the American Society for Nutrition, Institute of Food Technologists, and International Food Information Council. Am J Clin Nutr, 2009. 89(2): p. 477-84.

26.   Hill, J.O., J.C. Peters, and H.R. Wyatt, Using the energy gap to address obesity: a commentary. J Am Diet Assoc, 2009. 109(11): p. 1848-53.

27.   Koch, A., et al., Establishment of Early Endpoints in Mouse Total-Body Irradiation Model. PLoS One, 2016. 11(8): p. e0161079.

28.   Leibel, R.L., Molecular physiology of weight regulation in mice and humans. Int J Obes (Lond), 2008. 32 Suppl 7(Suppl 7): p. S98-108.

29.   Liang, H., et al., Genetic mouse models of extended lifespan. Exp Gerontol, 2003. 38(11-12): p. 1353-64.

30.   Feridooni, H.A., et al., Reliability of a Frailty Index Based on the Clinical Assessment of Health Deficits in Male C57BL/6J Mice. J Gerontol A Biol Sci Med Sci, 2015. 70(6):

4.2 Age- and sex-specific deterioration of bone and osteocyte lacuno-canicular network in prematurely aged PolgA mice

Dilara Yılmaz[1], Francisco C. Marques[1]*, Lorena Gregorio[1]*, Jérôme Schlatter[1], Christian Gehre[1], Thurgadevi Pararajasingam[1], Wanwan Qiu[1], Xiao-Hua Qin[1], Esther Wehrle[1,2], Gisela A. Kuhn[1], Ralph Müller[1]

[1]Institute for Biomechanics, ETH Zurich, Zurich, Switzerland
[2]AO Research Institute Davos, Davos Platz, Switzerland

*equal contribution

Under Review

Abstract

Age-related osteoporosis, a condition characterized by reduced bone density and increased fracture susceptibility in older individuals, necessitates a better understanding of underlying molecular and cellular mechanisms. Osteocytes are the pivotal orchestrators of bone remodeling and they have emerged as novel therapeutic targets for age-related bone loss. Our study uses the prematurely aged PolgD257A/D257A (PolgA) mouse model to scrutinize age- and sex-related alterations in bone and particularly the osteocyte lacuno-canicular network (LCN). Moreover, we introduced a novel staining method for undecalcified fresh frozen bone sections coupled with quantitative in silico approaches to evaluate the alterations in the osteocyte network with aging. Our findings underscore the pronounced degenerative changes in the bone and the osteocyte LCN in PolgA mice as early as 40 weeks with slightly more pronounced changes observed in aged PolgA males. Our findings suggest that the PolgA mouse model serves as a valuable tool for studying the cellular mechanisms underlying age-related bone loss, given the comparable age-related degeneration of the bone and the osteocyte network observed in aged mice and humans.

4.2 Age and sex-specific deterioration of bone and osteocyte lacuna-canalicular network in prematurely aged PolgA mice

Keywords

4.2.1. Introduction

Age-related bone loss is a major health concern among older individuals characterized by decreased bone density, leading to increased susceptibility to fractures and compromised skeletal integrity [1-3]. Understanding the intricate cellular processes underlying this condition is paramount since emerging evidence suggests that osteocytes represent a promising therapeutic target for mitigating age-related osteoporosis [4-7]. Osteocytes, the most abundant cells and mechanosensors in bone, play a crucial role in regulating bone remodeling [8, 9]. These cells reside in small pocket-like spaces known as lacunae within the mineralized bone matrix and communicate through a complex network called the lacuno-canalicular network (LCN). In response to mechanical cues, the osteocytes transmit signals that influence bone formation or resorption, thereby altering the bone microenvironment and regulating homeostasis. This mechanism is enabled through the gap junctions, secretory cell activities, and direct cell-to-cell contact via their dendrites [5, 6, 10-12]. Therefore, gaining insight into how osteocyte LCN changes within its native milieu during the aging process offers a deeper understanding of its pivotal role in age-related bone loss.

Advanced imaging techniques provided valuable insight into the age-related morphological changes in osteocytes and LCN in both humans and rodents. Micro-computed tomography (micro-CT) imaging allowed precise quantifications of the lacunar morphometry, illustrating a decline in lacunar density with aging on undecalcified bone samples [13-16]. Additionally, the assessment of osteocyte morphology and connections (connectomics) through confocal microscopy imaging combined with computational analysis showcased degenerations in the osteocyte and lacunar morphology in aging [17-21]. Hence, impairments in dendrites and LCN significantly compromise osteocyte function, thereby contributing to the age-related decline of bone.

An understanding of how aging is associated with changes in the osteocyte network may uncover new strategies to prevent age-related bone loss in older individuals. Our group has recently established the prematurely aged $Polg^{D257A/D257A}$ (PolgA) mouse model to characterize age-related alterations in females [7, 22]. The PolgA mice displayed a naturally accelerated aging phenotype and developed clinically relevant musculoskeletal aging characteristics, including kyphosis, alopecia, graying, and osteosarcopenia [23-25]. Yet the underlying mechanism driving the age- and sex-associated changes in the osteocyte network

remains unclear. Therefore, this study investigates these changes in bone and associated degeneration of the osteocyte network considering both age and sex factors in PolgA mice. We performed detailed bone morphometric analysis and quantitative assessment of the osteocyte network. This involved the development of a specialized staining method for undecalcified fresh frozen bone sections and utilized multiphoton confocal imaging, followed by in-depth *in silico* quantitative approaches. Given the key role of osteocytes in maintaining bone homeostasis [26], a comprehensive understanding of the age-related deterioration of the osteocyte network is essential for unraveling the intricate mechanisms contributing to bone loss in older individuals.

4.2.2. Results

Structural impairments in bone with age in prematurely aged PolgA mice

To investigate the changes in the bone with aging, we performed micro-CT imaging on the right femurs for PolgA mice and their WT littermates at the ages of 20 and 40 weeks and evaluated standard morphometric parameters at each point. Micro-CT analysis revealed the changes in the structural composition of femurs with aging. Representative 3D reconstructed micro-CT images demonstrated a thinner and porous cortical bone and reduced trabecula in PolgA mice at 40 weeks compared to their age-matched WT littermates and young counterparts (Figure 4.2.1A-C, Table 4.2S1). Bone morphometry analysis illustrated the notable changes in both trabecular and cortical bone. Cortical area fraction (Ct.Ar/Tt.Ar) was significantly reduced both in male and female PolgA mice in comparison to the WT littermates ($p<0.001$) and young PolgA mice ($p<0.0001$) (Figure 4.2. 1D). Additionally, cortical area (Ct.Ar) and thickness (Ct.Th) were decreased ($p<0.001$) in PolgA male and female mice compared to age- and sex-matched WT and young mice (Figure 4.2.1E-F). In parallel to the observations in cortical bone, trabecular bone parameters were drastically altered in aged PolgA mice (Figure 4.2.1G-I). A particularly noticeable decreased trabecular bone volume fraction (BV/TV) in females was observed (Figure 4.2.1G). With aging, BV/TV was decreased in PolgA mice for both sexes; however, this difference was less apparent in females due to their lower trabecular density. Moreover, trabecular thickness (Tb.Th) was significantly reduced in male ($p<0.001$) but not in female PolgA while trabecular spacing (Tb.Sp) was increased only for females ($p<0.001$). At 20 weeks, no differences were observed in bone phenotype and morphometric characteristics between PolgA and WT mice. However, at 40 weeks, PolgA mice showed compromised bone

structure compared to age-matched WT littermates and young mice, with striking differences identified between males and females of the PolgA group (Figure 4.2.1).
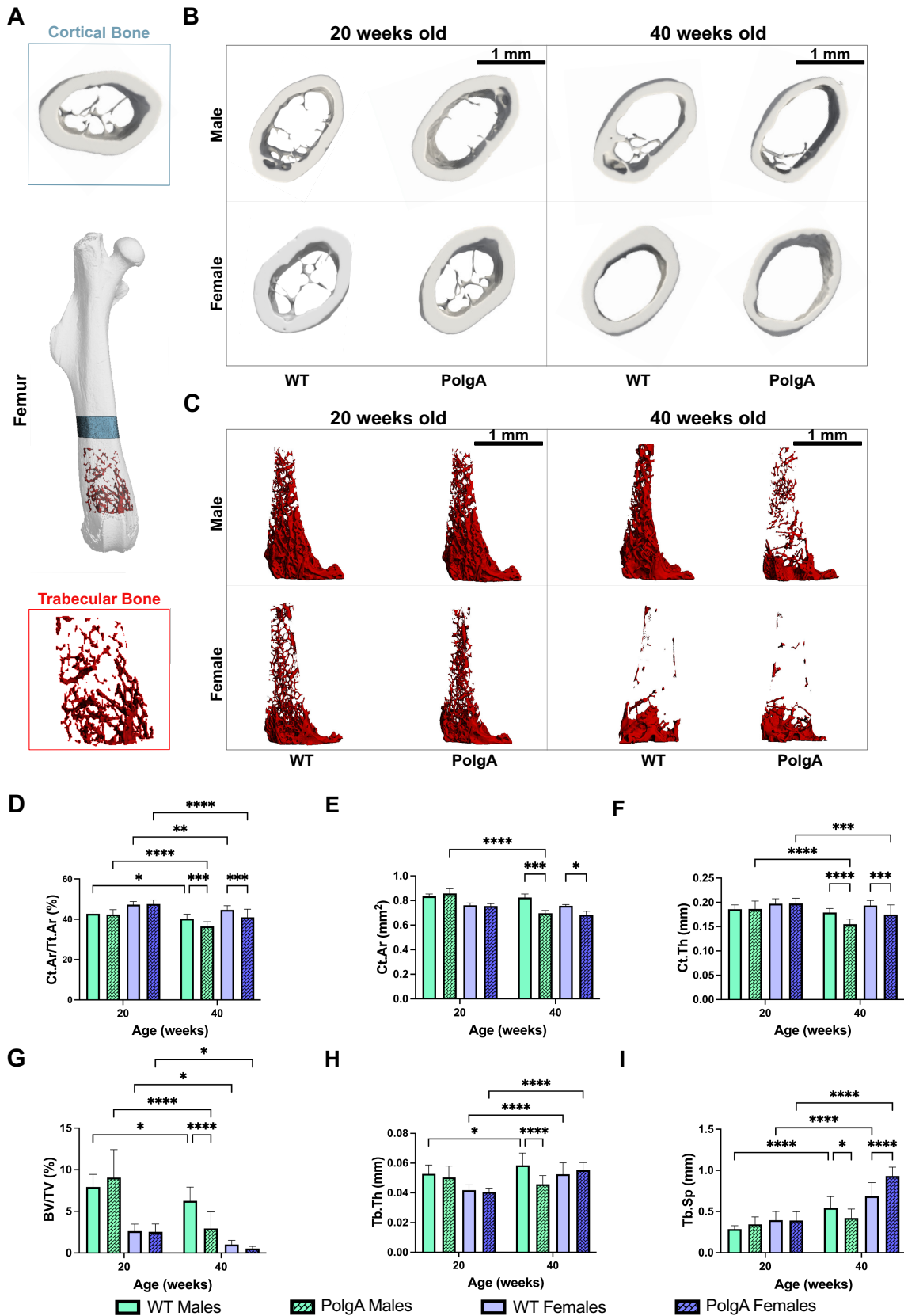
Figure 4.2.1 Age-specific structural impairments in bone in prematurely aged PolgA mice A) Representative 3D reconstructed longitudinal micro-CT image of right femurs showing cortical and trabecular bone regions used for analysis. B) 3D cortical bone images of male and female PolgA mice at 20 and 40 weeks indicating the thinning of cortical bone and increased cortical bone area with aging. C) 3D trabecular bone images of male and female PolgA mice at 20 and 40 weeks showing the reduced trabecular bone with age. D) Decreased cortical bone parameters with aging in PolgA mice: cortical area fraction (Ct.Ar/Tt.Ar), E) cortical area (Ct.Ar), and F) cortical thickness (Ct.Th). G) Altered trabecular bone parameters with age in PolgA mice: bone volume fraction (BV/TV) H) trabecular thickness (Tb.Th) and I) trabecular space (Tb.Sp). Data represents mean ± s.d., (n=8-16 mice/group). Sign ificance was determined two-way ANOVA corrected by Uncorrected Fischer's LSD, *p< 0.05, **p< 0.01, ***p< 0.001, ****p<0.0001.

Age- and sex-related deterioration of osteocyte network in PolgA mice

To investigate the impact of aging on osteocyte morphology, we performed Phalloidin/Hoechst staining to label osteocytes and their dendrites and quantified the stained sections from confocal image stacks through Fiji (ImageJ) and IMARIS filament tracing software by adapting the implementation of neuronal filament analysis [27-29]. Through these approaches, we were able to analyze and evaluate the morphology and characteristics of osteocytes and their dendrites robustly and quantitatively. In PolgA mice, the quantification of confocal image stacks demonstrated a notable reduction in osteocyte connectivity as they aged (Figure 4.2A, 4.2S1A). At 40 weeks, both male and female PolgA mice exhibited reduced osteocyte connectivity (Figure 4.2A). Furthermore, analysis of the confocal image stacks identified instances of disconnected osteocytes and empty cell bodies with only dendrites, predominantly in aged PolgA mice. Moreover, significant reductions in the dendrite number, area and length, and osteocyte area in aged PolgA mice compared to aged-matched WT littermates and young PolgA counterparts were observed (Figure 4.2B-F).
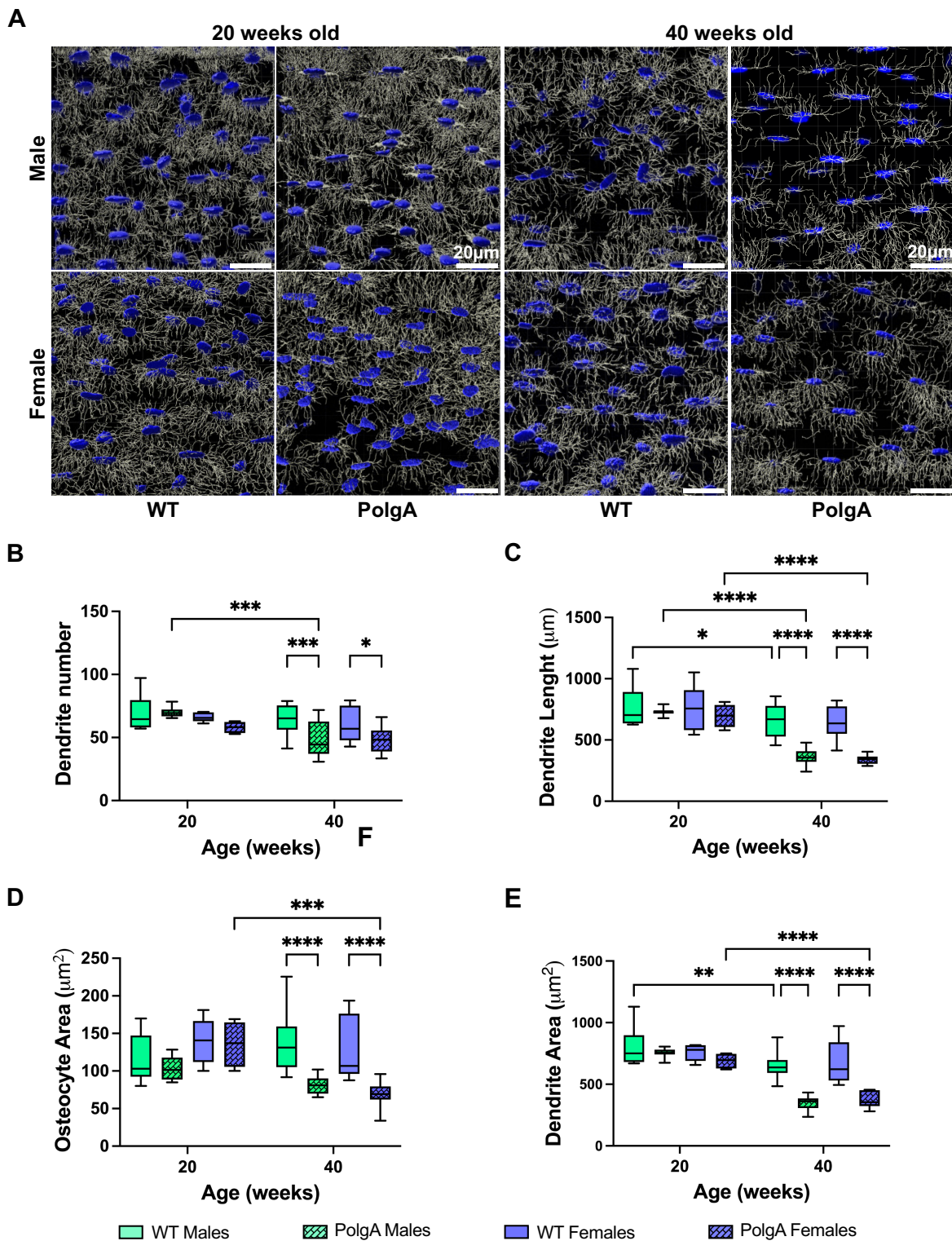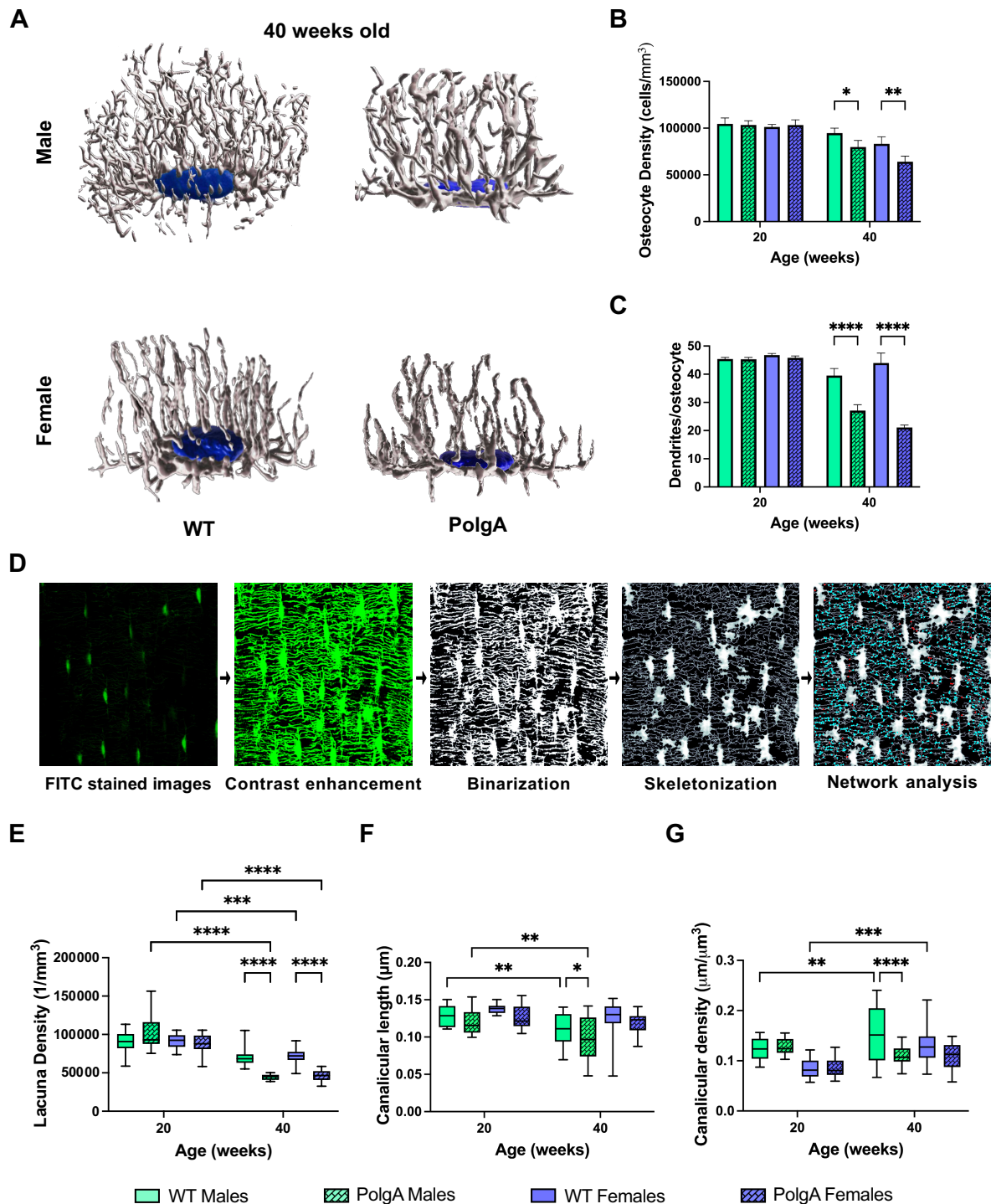
Figure 4.2.2 Age- and sex-related changes in osteocyte network of PolgA mice: A) Representative 3D reconstructed Phalloidin-Hoechst stained images showing altered osteocytes and their dendrites with age in male and female PolgA mice using automated filament tracing in IMARIS. B) Quantification of osteocytes and their dendrites from 3D Phalloidin-Hoechst image stacks of male and female PolgA mice indicating the degenerated osteocyte and dendrite features: dendrite number C) dendrite length D) osteocyte area E) dendrite length. Box plots represent max and min values, (n=3-4 mice/group). Significance

was determined by two-way ANOVA corrected by Uncorrected Fischer's LSD, * p< 0.05, **p < 0.01, *** p< 0.001.

Furthermore, a notable decline in the osteocyte density and dendricity (number of dendrites per osteocyte) was observed in PolgA mice, slightly greater in males (Figure 4.2.3B-C). 3D images of osteocytes support the evident degenerative changes of osteocytes with aging in PolgA mice, illustrating the decrease in dendrites and an elongated and flattened osteocyte body (Figure 4.2.3A).

Figure 4.2.3 Degeneration of osteocyte and LCN with age. A) Representative 3D reconstructed Phalloidin-Hoechst stained images showing altered osteocytes and their dendrites with age in male and female PolgA mice 40 weeks. B) Quantification of osteocyte showing the reduction in osteocyte density and C) dendricity of male and female PolgA mice at 40 weeks. D) Image processing workflow for the connectomics analysis of LCN showing, FITC stained confocal images, contrast enhancement, binarization, and skeletonization steps for osteocyte network analysis. E) Quantification of LCN parameters showing degeneration with aging in PolgA mice at 40 weeks: lacuna density F) canalicular length G) canalicular density. Box plots represent max and min values, (n=3-4 mice/group). Significance was determined by two-way ANOVA corrected by Uncorrected Fischer's LSD, *p< 0.05, **p< 0.01, ***p< 0.001.

Disrupted LCN architecture and reduced connectivity within aging

For a more in-depth analysis of the osteocyte network, we performed FITC staining on undecalcified thick, optically cleared femur sections. Since Phalloidin specifically labels the actin filaments of the osteocytes, its visualization is restricted to the dendrites, whereas FITC can permeate the bone matrix and fill spaces like lacunae and canaliculi, thereby facilitating a detailed visualization of LCN. Therefore, by quantifying the FITC-stained images, we demonstrated the structural alterations of the LCN with aging (Figure 4.2S1B, 4.2.3D-G and 4.2.4). LCN network in aging bone was sparser and less connected (Figure 4.2S1B) aligning with the findings in the aforementioned osteocyte analysis with Phalloidin-stained images. Lacuna density was significantly reduced in PolgA mice compared to their controls at 40 weeks (Figure 4.2.3E). Moreover, the shortening of canaliculi and decline in the canaliculi density were apparent in aged PolgA mice in comparison to their littermates and young counterparts (Figure 4.2.3F-G). Moreover, using connectomics analysis [19, 20], we quantified nodes in addition to a 3D osteocyte network of young and aged PolgA compared to WT littermates (Figure 4.2.4). The mean number of nodes decreased with aging for both PolgA and WT mice, however; this reduction was greater in the PolgA group compared to controls and young mice, indicating the loss of network interaction in aging (Figure 4.2.4B). In contrast, the mean node degree, showing the number of connected nearest neighbors remained similar across all groups, suggesting that the network is preserved at a similar level despite the changes in the osteocyte connectivity (Figure 4.2.4C). The proportion of all node types: tree nodes (t, c = 0), cluster nodes (c, cc > 0.5), and end nodes remained constant among all groups indicating the overall robustness and resilience of network architecture with different age groups (Figure 4.2.4D-F). Furthermore, distances within the LCN network were quantified. Aged bone displayed lower canalicular length, resulting in increased molecule travel distance from the extracellular matrix (ECM) to LCN, thereby d_{LC} was greater significantly in aged PolgA mice compared to their respective controls and young mice, while other variables describing the distance to the nearest

cell directly through the matrix (d_L) and the distance within the LCN to the nearest lacuna through the network (d_{net}) remained unaffected by the age-related alteration in LCN (Figure 4.2.4G-J). Hence, analysis of LCN features revealed degenerative alterations in aged PolgA mice when compared to aged-matched WT littermates at 40 weeks, as well as in young PolgA mice, indicating degenerative changes in the osteocyte network of PolgA mice with age.
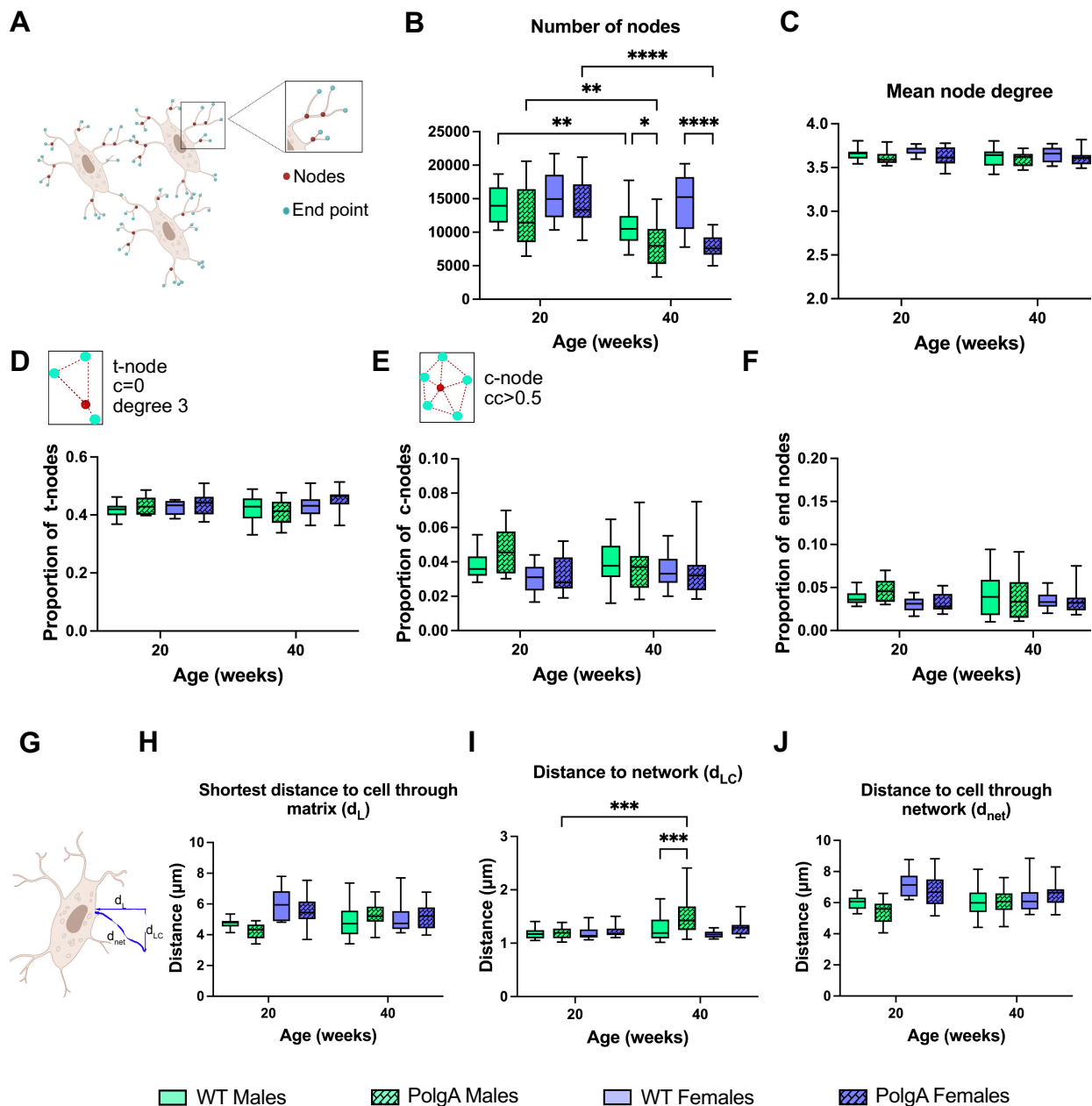
Figure 4.2.4 Disrupted LCN connectivity with aging in PolgA mice: Changes in the nodal analysis of osteocyte network in PolgA mice showing A) classification of nodes from the connectomics analysis B) the number of nodes indicating the loss of network connection with aging. C) Mean node degree (connections per node) showing the maintenance of network architecture. D) Proportion of tree (t) nodes E) Proportion of cluster (c) nodes F) Proportion of

endpoint nodes G) Illustration of the distance of the bone matrix from lacunae and the canalicular network H) distance to the nearest cells through the matrix I) the average distance to LCN from the matrix J) distance of the network from the next lacuna. Box plot represents max and min values, (n=3-4 mice/group). Significance was determined by two-way ANOVA corrected by Uncorrected Fischer's LSD, *p < 0.05, ** p< 0.01, ***p< 0.001.

4.2.3. Discussion

In this study, a detailed analysis was conducted to investigate the age- and sex-related changes in the bone and the osteocyte network in prematurely aged PolgA mice. Our findings revealed that the PolgA mice demonstrated age-related impairments in bone at 40 weeks compared to their WT littermates and young counterparts. In particular, our data demonstrated the degeneration of the osteocytes and their dendrites in PolgA mice with more prominently observed in males using the semi-automatic quantification through IMARIS software. Furthermore, we illustrated the disrupted LCN connectivity with aging in PolgA mice by employing the combination of novel FITC staining for fresh frozen sections and *in silico* connectomics analysis. Hence, we showcased the degeneration of osteocytes LCN and bone in prematurely aged PolgA mice as early as 40 weeks which is parallel with the findings from aged mice roughly 23 months and approximately 75-year-old humans [7, 30, 31].

At 40 weeks, age-related alterations in the bone of PolgA mice closely resembled those observed in both aged C57Bl/6 mice and humans [32-35]. These changes included increased cortical area fraction, diminished cortical thickness, and a reduction in trabecular BV/TV. However, in C57BL/6 mice, age-related changes were reported to be more pronounced in females exhibiting a greater loss in trabecular bone and increased cortical porosities compared to males [32]. In contrast, in our PolgA mouse model, age-related impairments in bone were notably more pronounced in male mice at 40 weeks of age compared to females.

Consistent with previous findings, aging alters the osteocyte network in PolgA mice where the osteocyte density and dendricity were reduced at 40 weeks similarly observed in C57Bl/6 mice at 22-23 months and in aged humans at 60-75 years [21, 36, 37]. However, deteriorations of the osteocyte network were observed to be slightly more pronounced in aged male PolgA mice, contrasting to the findings in C57Bl/6 mice and humans.

Additionally, through semi-automated quantification with IMARIS, we successfully captured detailed information on the degeneration of dendrites and osteocytes. IMARIS filament tracing method, originally designed for 3D tracking and high throughput analysis of neurons, was adeptly repurposed for osteocyte cell counting and dendrite quantification due to its precise object detection and accurate morphological analysis [27, 38-40]. This approach allowed for

robust and in-depth evaluation while obtaining additional information about osteocytes and their dendrites including dendrite volume, area and length, and osteocyte area [28].

Furthermore, connectomics analysis revealed the canalicular loss and degeneration of LCN with aging in PolgA mice, akin to the findings in aged C57Bl/6 mice and mice with disrupted TGF-b pathway [20]. Their findings emphasized the loss of canaliculi with aging without taking into account the changes in the lacunae that was consistent with earlier findings, where no reduction in the number of lacunae was observed, thus underlining the significant role the canalicular network in osteocyte function [20, 41-43]. However, in our study, we briefly assessed the changes in the lacunae as well to underscore that alterations in both the canaliculi and lacunae contribute to osteocyte function and overall bone health.

Furthermore, we developed a novel FITC staining method specifically tailored for fresh frozen undecalcified sections for the connectomics analysis. This enabled the high-contrast labeling of the bone, which was further enhanced with 2,2′-thiodiethanol (TDE) optical clearing and multiphoton confocal imaging. This combination minimizes imaging artifacts and enhances resolution, allowing precise identification of canaliculi within the deep mineralized bone matrix without requiring tedious sample processing with acid-etching of resin-embedded bone or *in vivo* dye injections [18, 37, 44-46]. Moreover, the challenges associated with visualizing the 3D network in 2D paraffin sections stained for LCN were overcome through connectomics analysis applied to FITC-stained 3D image stacks.

Furthermore, our connectomics analysis exhibited impaired LCN architecture in PolgA mice at 40 weeks, with reduced lacunar density, canalicular density, and length similar to the findings from aged mice and humans [47-50]. On the other hand, the nodal analysis of PolgA mice showed a similar extent of changes as observed in the aged WT mouse bone [20]. This could be attributed to the comprehensive nature of our connectomics analysis including a larger region to quantify osteocyte networks than the previous publications [17, 19, 20]. While our study did not particularly focus on predicting fluid mechanics or investigating mechanotransduction of osteocytes concerning the age-related changes in LCN, it is possible to achieve these by combining confocal imaging of osteocyte LCN with connectomics analysis and further applying 3D finite element (FE) modeling [51-54]. Hence *in silico* approach for the analysis of osteocyte network offers a unique opportunity to overcome experimental challenges in investigating the connection between osteocyte and LCN structure.

Although PolgA mice do not fully capture the complex relationship between LCN degeneration leading to osteocyte death and the subsequent bone deterioration caused by osteocyte loss, our

study with this model reveals the age- and sex-specific degeneration of bone, osteocyte, and LCN as early as 40 weeks, similar to those observed in aged mice and humans. Consequently, our findings suggest that the PolgA mouse model could serve as a robust model for investigating the molecular mechanisms responsible for age-related bone loss. Furthermore, it underscores the critical contribution of osteocytes to bone remodeling and health.

4.2.4. Materials and methods

Animal model

All animal procedures adhered to the regulations established by local authorities and received approval from the Veterinäramt des Kantons Zürich, Zurich, Switzerland (license: ZH35/2019). A mouse colony expressing an exonuclease-deficient version of the mitochondrial DNA polymerase γ (PolgAD257A, B6.129S7(Cg)-Polgtm1Prol/J, JAX stock 017341, The Jackson Laboratory) was bred and maintained at the ETH Phenomics Center. The mice were housed under standard conditions, featuring a 12:12 h light-dark cycle, access to ad libitum maintenance feed and water, and three to five animals per cage following previously outlined protocols [22]. Genotyping was performed before experiments by Transnetyx (Cordova, USA). Homozygous PolgA mice, along with age- and sex-matched wild-type (WT) littermates (controls), were used for all experiments [55].

Micro-CT image analysis

Right femurs were fixed for 4h in 4% PFA at 4°C and were subjected to micro-CT scanning in PFA (micro-CT 45, Scanco Medical AG) with an isotropic voxel-size of 10 μm; 55 kVp, 145 μA, 200 ms integration time. A Gaussian filter (support: 1) with a sigma of 0.8 was applied to 3D image data and segmented with a threshold of 392 mgHA/cm [56]. Cortical and trabecular compartments were identified following the previously described method [57]. Standard bone morphometric parameters were evaluated (Table 3.S1).

Bone immunohistochemistry

As previously described, femurs harvested from 20 to 40-week-old PolgA mice and their age-matched WT littermates were fixed immediately in ice-cold 4% paraformaldehyde (PFA) for 24 hours at 4°C. Right femurs were decalcified in 12.5% EDTA for 10-11 days at 4°C, and left femurs were undecalcified. Bones went through overnight incubation in sucrose solution (20%

sucrose, 2% PVP) and embedded in OCT. Samples were stored at −80°C until sectioning. 50 μm-thick cryosections were obtained for stainings [55].

Bone sections were hydrated with PBS three times at 5 min intervals, followed by permeabilization with 0.3% Triton X-100 in PBS for 20 min at room temperature (RT) [16]. Sections were immersed in blocking solution (5% bovine serum albumin (BSA) in 0.025% Triton X-100) for 45 min at RT. Following the sections were co-incubated with Phalloidin conjugated Alexa Flour 555 (ab176756, Abcam, 1:1000) and Hoechst (94403, Sigma Aldrich, 1:500) in 0.3% BSA in PBS for 1 hour to stain the actin cytoskeleton. Sections underwent a triple wash in PBS at 10 min intervals, followed by air-drying and, mounting with Prolong Diamond antifade mountant (P36961, Thermo Fischer), and the edges were sealed with nail polish.

For FITC staining, undecalcified bone sections were hydrated with gradually increasing concentration of EtOH for 5 min each on a shaker and then incubated with a freshly prepared 0.01% fluorescein isothiocyanate isomer I (FITC) solution (F7250, Sigma Aldrich) for 2 days in the dark. The FITC solution was renewed, and the sections were further incubated for an additional 3 days on a shaker in the dark. Subsequently, the sections were washed with 100% ethanol three times for 15 min each, followed by air-drying. Next, sections were hydrated with PBS for 5 min twice. Following rehydration, the sections were optically cleared with a gradually increasing concentration of 2,2'-thiodiethanol (TDE) (166782, Sigma Aldrich) for 2 hours each, followed by an overnight incubation in a 97% TDE solution. Finally, the sections were mounted in 97% TDE, and the edges were sealed with nail polish.

The right femurs, which were scanned using micro-CT, underwent a decalcification process and were then used for staining with Phalloidin and Hoechst. On the other hand, the left femurs were not decalcified and were used for staining with FITC.

Image acquisition and quantitative analysis

Phalloidin-Hoechst stained sections were imaged on midshaft and distal regions with Leica SP8 confocal microscopy while FITC stained sections were imaged on midshaft region with Leica SP8 MP multiphoton microscopy with the dimensions of 0.2 μm x 0.2 μm. Z-stacks images with the depth of 32.21 μm were processed and 3D-reconstructed using IMARIS (Oxford Instruments). The filament tracer tool in IMARIS was utilized for the reconstruction

and quantification of dendrites. Consistent threshold parameters were applied to both PolgA and WT mice across all age groups and sexes. Dendrite area, volume, length, and osteocyte area were used for statistical analysis. Additionally, osteocyte number, dendrite number, osteocyte area, and density were quantified using Fiji for comparison with IMARIS. Output from IMARIS was used for this paper. Image processing steps comply with *Nature's* Guide for digital images.

Prior to connectomics network analysis, images were pre-processed in Python (Python 3.11.6, scipy 1.10.1, scikit-image 0.20.0) to enhance the details of the LCN network. First, the brightness of each section in a z-stack was adjusted using a Python implementation adapted from Fiji's "Auto brightness correction" function in a sliding-window approach (kernel: 50 µm and stride: 8 µm), followed by Gauss-filtering to reduce noise (sigma determined as: 3.25 x pixel size in µm). After intensity normalization, contrast-limited adaptive histogram equalization was applied (kernel: 6 µm) to enhance lacunae and canaliculi details. Subsequently, contrast adjustment based on sigmoid correction was performed with an image-specific cut-off value that scaled the range of the intensity histogram to the interval (0, 1). Finally, images were rescaled to an isotropic resolution of 0.4 µm and binarized (threshold: 0.6). Images were analyzed in MATLAB (MATLAB 2022a, Mathworks), as described previously [17]. An initial random subset of 5 images was used to calibrate the parameters of the MATLAB connectomics analysis, based on visual inspection of the lacunae and canaliculi identified and comparison to the number of lacunae counted manually. For subsequent analysis of the entire dataset, the lacunae identification values were set as distance threshold to identify potential lacunae as 5, minimum object size in voxels as 25, distance threshold for dilation as 2, and limit fraction for dilation as 0.1.

Statistical analysis

Data analysis was performed with GraphPad Prism software. Significant differences were determined with two-way ANOVA corrected by Uncorrected Fischer's LSD. 8-16 mice per group were used for bone morphometry and for each staining, 3-4 mice per group with 6-10 regions per mouse were used for analysis. Significant differences were determined $p < 0.05$.

Acknowledgments

European Research Council (ERC Advanced MechAGE- ERC-2016-ADG-741883) as well as the Swiss National Science Foundation (no. 188522).

Conflict of Interest

The authors have no conflict of interest to declare.

Author Contributions

Conceptualization and methodology: DY, GAK, RM; investigation, methodology: DY, FCM; data curation, formal analysis: DY, FCM, LOG, JS, TP, WQ; writing - original draft: DY; writing - review and editing: DY, FCM, CG, XHQ, WQ, JS, GAK, EW, RM; resources, supervision, funding acquisition, project administration: RM, XHQ.

Supplementary Materials
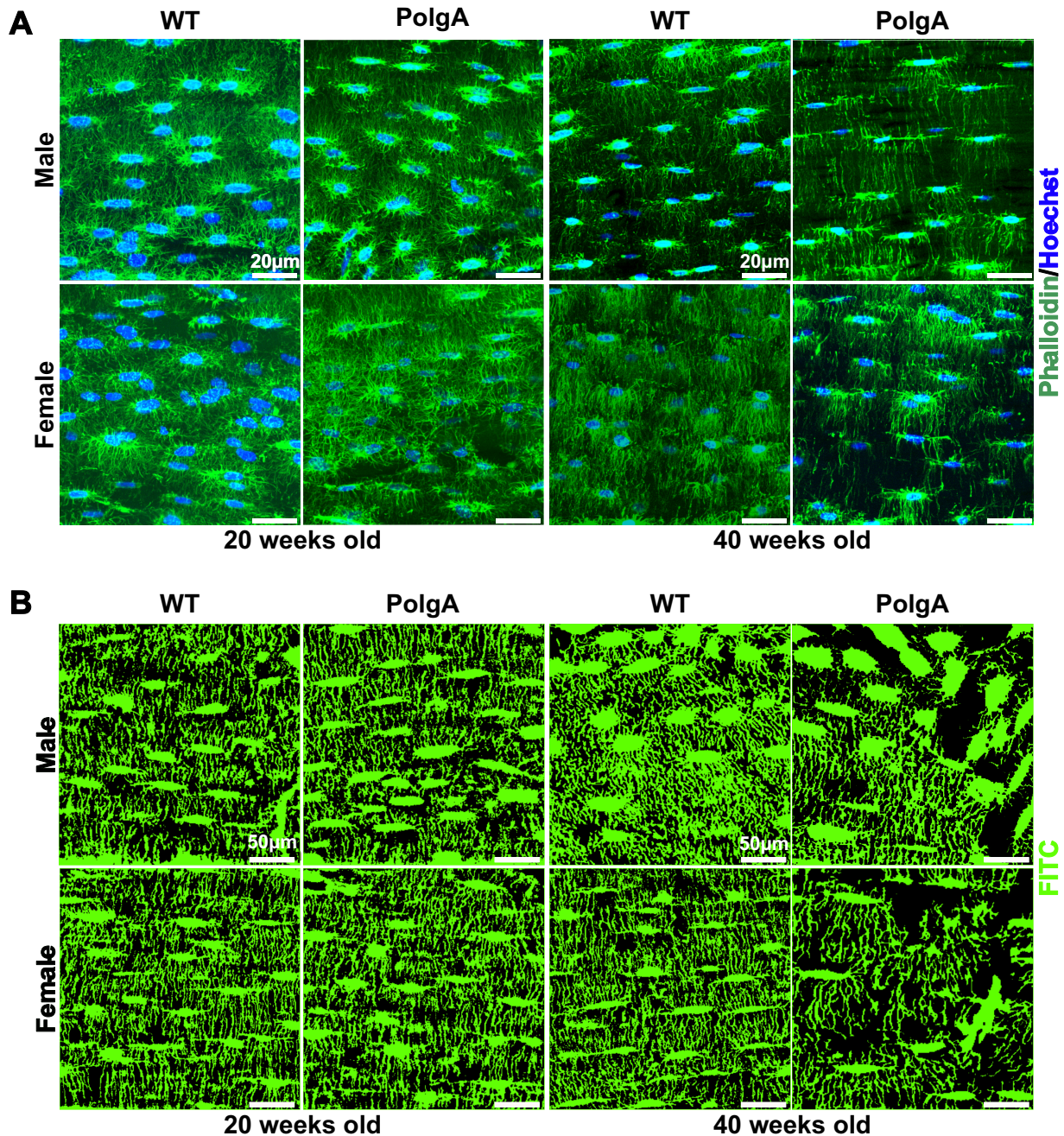
Figure 4.2.S1 Degeneration of osteocyte network and LCN connectivity with aging in PolgA mice: A) Representative high magnification images of Phalloidin (F-actin, green) and Hoechst (nucleus, blue) stained sections illustrating degeneration of osteocyte networks and B) representative maximum intensity projection images of FITC stained sections showing LCN disruption in male and female PolgA mice and their WT littermates at 20 and 40 weeks.

Table 4.2S1 Bone structural parameters in the full, trabecular, and cortical regions of the femurs of PolgA mice and WT littermates at 20 and 40 weeks assessed by ex vivo micro-CT. Parameter legend: average volume density (AVD), bone volume fraction (BV/TV), trabecular thickness (Tb.Th), trabecular number (Tb.N), trabecular separation (Tb.Sp), cortical area fraction (Ct.Ar/Tt.Ar), total cross-sectional area inside the periosteal envelope (Tt.Ar), cortical bone area (Ct.Ar), cortical thickness (Ct.Th). Data represent mean ± s.d., (n=8-16 mice/group).

	20 weeks			
	Males		Females	
	PolgA	WT	PolgA	WT
Parameters				
AVD [%]	46.05±3.48	47.26±2.19	46.83±2.05	46.74±0.82
BV/TV [%]	9.05±3.33	7.92±1.55	2.58±0.94	2.62±2.94
Tb.Sp [mm]	0.34±0.09	0.29±0.04	0.39±0.10	0.39±0.10
Tb.N [1/mm]	3.16±0.36	2.83±0.50	2.40±0.47	2.39±0.45
Tb.Th [mm]	0.04±0.00	0.06±0.00	0.05±0.00	0.05±0.00
Ct.Ar/Tt.Ar [%]	42.38±2.41	42.74±1.39	47.56±2.01	47.25±1.55
Tt. Ar [%]	2.01±0.20	1.95±0.14	1.58±0.07	1.61±0.12
Ct. Ar [mm²]	0.85±0.12	0.83±0.06	0.75±0.03	0.77±0.02
Ct. Th [mm]	0.18±0.00	0.18±0.00	0.19±0.00	0.19±0.00

	40 weeks			
	Males		Females	
	PolgA	WT	PolgA	WT
Parameters				
AVD [%]	37.27±3.35	46.65±2.53	39.29±2.77	45.54±1.64
BV/TV [%]	2.94±1.98	6.25±1.62	0.53±0.26	1.01±0.50
Tb.Sp [mm]	0.42±0.10	0.54±0.13	0.93±0.10	0.68±0.16
Tb.N [1/mm]	1.91±0.37	2.29±0.54	0.99±0.11	1.37±0.32
Tb.Th [mm]	0.04±0.00	0.05±0.00	0.05±0.00	0.05±0.00
Ct.Ar/Tt.Ar [%]	36.46±2.33	40.29±2.24	40.95±4.02	44.66±2.05
Tt. Ar [%]	1.91±0.22	2.05±0.22	1.67±0.10	1.69±0.09
Ct. Ar [mm²]	0.68±0.08	0.78±0.04	0.69±0.07	0.82±0.08
Ct. Th [mm]	0.15±0.01	0.18±0.00	0.17±0.02	0.19±0.01

References

1.   Almeida, M., Aging mechanisms in bone. Bonekey Rep, 2012. 1.

2.   Rachner, T.D., S. Khosla, and L.C. Hofbauer, Osteoporosis: now and the future. Lancet, 2011. 377(9773): p. 1276-87.

3.   Eastell, R., et al., Postmenopausal osteoporosis. Nat Rev Dis Primers, 2016. 2: p. 16069.

4.   Cui, J., et al., Osteocytes in bone aging: Advances, challenges, and future perspectives. Ageing Res Rev, 2022. 77: p. 101608.

5.   Schaffler, M.B., et al., Osteocytes: master orchestrators of bone. Calcif Tissue Int, 2014. 94(1): p. 5-24.

6.   Schaffler, M.B. and O.D. Kennedy, Osteocyte signaling in bone. Curr Osteoporos Rep, 2012. 10(2): p. 118-25.

7.   Yilmaz, D., et al., Mouse models of accelerated aging in musculoskeletal research for assessing frailty, sarcopenia, and osteoporosis - A review. Ageing Res Rev, 2024. 93: p. 102118.

8.   Cowin, S.C., Bone Mechanics Handbook. 2nd ed. 2001: CRC Press.

9.   Bonewald, L.F., The amazing osteocyte. J Bone Miner Res, 2011. 26(2): p. 229-38.

10.   Bonewald, L.F., Mechanosensation and Transduction in Osteocytes. Bonekey Osteovision, 2006. 3(10): p. 7-15.

11.   Doty, S.B., Morphological evidence of gap junctions between bone cells. Calcif Tissue Int, 1981. 33(5): p. 509-12.

12.   Bonewald, L.F., Osteocytes: a proposed multifunctional bone cell. J Musculoskelet Neuronal Interact, 2002. 2(3): p. 239-41.

13.   Goff, E., et al., Large-scale quantification of human osteocyte lacunar morphological biomarkers as assessed by ultra-high-resolution desktop micro-computed tomography. Bone, 2021. 152: p. 116094.

14.   Hemmatian, H., et al., Age-related changes in female mouse cortical bone microporosity. Bone, 2018. 113: p. 1-8.

15.   Peyrin, F., et al., Micro-CT examinations of trabecular bone samples at different resolutions: 1 4, 7 and 2 micron level. Technology and Health Care, 1998. 6(5-6): p. 391-401.

16.   Carter, Y., et al., Femoral osteocyte lacunar density, volume and morphology in women across the lifespan. J Struct Biol, 2013. 183(3): p. 519-526.

17.   Kollmannsberger, P., et al., The small world of osteocytes: connectomics of the lacuno-canalicular network in bone. New Journal of Physics, 2017. 19(7).

18.   Kamel-ElSayed, S.A., et al., Novel approaches for two and three dimensional multiplexed imaging of osteocytes. Bone, 2015. 76: p. 129-40.

19.   Weinkamer, R., P. Kollmannsberger, and P. Fratzl, Towards a Connectomic Description of the Osteocyte Lacunocanalicular Network in Bone. Curr Osteoporos Rep, 2019. 17(4): p. 186-194.

20.   Schurman, C.A., S.W. Verbruggen, and T. Alliston, Disrupted osteocyte connectivity and pericellular fluid flow in bone with aging and defective TGF-beta signaling. Proc Natl Acad Sci U S A, 2021. 118(25).

21.   Tiede-Lewis, L.M., et al., Degeneration of the osteocyte network in the C57BL/6 mouse model of aging. Aging (Albany NY), 2017. 9(10): p. 2190-2208.

22.   Scheuren, A.C., et al., Hallmarks of frailty and osteosarcopenia in prematurely aged PolgA((D257A/D257A)) mice. J Cachexia Sarcopenia Muscle, 2020. 11(4): p. 1121-1140.

23.   Kujoth, G.C., et al., Mitochondrial DNA mutations, oxidative stress, and apoptosis in mammalian aging. Science, 2005. 309(5733): p. 481-4.

24.   Trifunovic, A., et al., Premature ageing in mice expressing defective mitochondrial DNA polymerase. Nature, 2004. 429(6990): p. 417-23.

25.   Chien, K.R. and G. Karsenty, Longevity and lineages: toward the integrative biology of degenerative diseases in heart, muscle, and bone. Cell, 2005. 120(4): p. 533-44.

26.   Webster, D., et al., Mechanical loading of mouse caudal vertebrae increases trabecular and cortical bone mass-dependence on dose and genotype. Biomech Model Mechanobiol, 2010. 9(6): p. 737-47.

27.   Kuljis, D.A., et al., Fluorescence-Based Quantitative Synapse Analysis for Cell Type-Specific Connectomics. eNeuro, 2019. 6(5).

28.   Ren, Y., et al., A novel way to statistically analyze morphologic changes in Dmp1-null osteocytes. Connect Tissue Res, 2014. 55 Suppl 1(0 1): p. 129-33.

29.   Viana da Silva, S., et al., Early synaptic deficits in the APP/PS1 mouse model of Alzheimer's disease involve neuronal adenosine A2A receptors. Nat Commun, 2016. 7: p. 11915.

30.   Dutta, S. and P. Sengupta, Men and mice: Relating their ages. Life Sci, 2016. 152: p. 244-8.

31.   Fried, L.P., et al., Frailty in older adults: evidence for a phenotype. J Gerontol A Biol Sci Med Sci, 2001. 56(3): p. M146-56.

32.   Seeman, E., Age- and menopause-related bone loss compromise cortical and trabecular microstructure. J Gerontol A Biol Sci Med Sci, 2013. 68(10): p. 1218-25.

33.   Halloran, B.P., et al., Changes in bone structure and mass with advancing age in the male C57BL/6J mouse. J Bone Miner Res, 2002. 17(6): p. 1044-50.

34.   Glatt, V., et al., Age-related changes in trabecular architecture differ in female and male C57BL/6J mice. J Bone Miner Res, 2007. 22(8): p. 1197-207.

35.   Gabet, Y. and I. Bab, Microarchitectural changes in the aging skeleton. Curr Osteoporos Rep, 2011. 9(4): p. 177-83.

36.   Kobayashi, K., et al., Mitochondrial superoxide in osteocytes perturbs canalicular networks in the setting of age-related osteoporosis. Sci Rep, 2015. 5: p. 9148.

37.   Milovanovic, P., et al., Osteocytic canalicular networks: morphological implications for altered mechanosensitivity. ACS Nano, 2013. 7(9): p. 7542-51.

38.   Miranda-Angulo, A.L., et al., Rax regulates hypothalamic tanycyte differentiation and barrier function in mice. J Comp Neurol, 2014. 522(4): p. 876-99.

39.   Ando, K., et al., Inside Alzheimer brain with CLARITY: senile plaques, neurofibrillary tangles and axons in 3-D. Acta Neuropathol, 2014. 128(3): p. 457-9.

40.   Haberl, M.G., et al., Structural-functional connectivity deficits of neocortical circuits in the Fmr1 (-/y) mouse model of autism. Sci Adv, 2015. 1(10): p. e1500775.

41.   Heveran, C.M., et al., Chronic kidney disease and aging differentially diminish bone material and microarchitecture in C57Bl/6 mice. Bone, 2019. 127: p. 91-103.

42.   Lai, X., et al., The dependences of osteocyte network on bone compartment, age, and disease. Bone Res, 2015. 3: p. 15009-.

43.   Dole, N.S., et al., Osteocyte-Intrinsic TGF-β Signaling Regulates Bone Quality through Perilacunar/Canalicular Remodeling. Cell Reports, 2017. 21(9): p. 2585-2596.

44.   Ashique, A.M., et al., Lacunar-canalicular network in femoral cortical bone is reduced in aged women and is predominantly due to a loss of canalicular porosity. Bone Rep, 2017. 7: p. 9-16.

45.   Coutu, D.L., et al., Multicolor quantitative confocal imaging cytometry. Nat Methods, 2018. 15(1): p. 39-46.

46.   Greenbaum, A., et al., Bone CLARITY: Clearing, imaging, and computational analysis of osteoprogenitors within intact bone marrow. Sci Transl Med, 2017. 9(387).

47.   Tiede-Lewis, L.M. and S.L. Dallas, Changes in the osteocyte lacunocanalicular network with aging. Bone, 2019. 122: p. 101-113.

48.   Qiu, S., et al., Age and distance from the surface but not menopause reduce osteocyte density in human cancellous bone. Bone, 2002. 31(2): p. 313-8.

49.   Mullender, M.G., et al., Osteocyte density changes in aging and osteoporosis. Bone, 1996. 1   8(2): p. 109-13.

50.   Heveran, C.M., et al., A new open-source tool for measuring 3D osteocyte lacunar geometries from confocal laser scanning microscopy reveals age-related changes to lacunar size and shape in cortical mouse bone. Bone, 2018. 110: p. 115-127.

51.   Verbruggen, S.W., T.J. Vaughan, and L.M. McNamara, Strain amplification in bone mechanobiology: a computational investigation of the in vivo mechanics of osteocytes. J R Soc Interface, 2012. 9(75): p. 2735-44.

52.   van Tol, A.F., et al., Network architecture strongly influences the fluid flow pattern through the lacunocanalicular network in human osteons. Biomech Model Mechanobiol, 2020. 19(3): p. 823-840.

53.   Dallas, S.L. and D.S. Moore, Using confocal imaging approaches to understand the structure and function of osteocytes and the lacunocanalicular network. Bone, 2020. 138: p. 115463.

54.   Qing, H., et al., Demonstration of osteocytic perilacunar/canalicular remodeling in mice during lactation. J Bone Miner Res, 2012. 27(5): p. 1018-29.

55.   Yılmaz, D., et al., Unraveling the Mechano-Molecular Mechanisms of TRAP Activity Using CRISPR/Cas9 Mediated Fluorescent Reporter Mice. iScience, 2023.

56.   Tourolle Ne Betts, D.C., et al., The association between mineralised tissue formation and the mechanical local in vivo environment: Time-lapsed quantification of a mouse defect healing model. Sci Rep, 2020. 10(1): p. 1100.

57.   Lambers, F.M., et al., Mouse tail vertebrae adapt to cyclic mechanical loading by increasing bone formation rate and decreasing bone resorption rate as shown by time-lapsed in vivo imaging of dynamic bone morphometry. Bone, 2011. 49(6): p. 1340-50.

Chapter 5

Spatially Resolved Bone Mechanomics and Mechanoregulation in Prematurely Aged Mice

5.1. Spatially resolved age- and sex-specific alterations in bone mechanomics and mechanoregulation in prematurely aged PolgA mice

Dilara Yılmaz[1], Neashan Mathavan[1], Francisco C. Marques[1], Charles Ledoux[1], Daniele Boaretti[1], Danielle Whittier[1], Esther Wehrle[1,2], Gian N. Schädli[1], Amit Singh[1], Gisela A. Kuhn[1], Ralph Müller[1]

[1]Institute for Biomechanics, ETH Zurich, Zurich, Switzerland
[2]AO Research Institute Davos, Davos Platz, Switzerland

In Preparation

Abstract

Aging is a multifactorial process associated with the decline of physiological functions, leading to an increased risk of frailty, sarcopenia, and osteoporosis conditions that severely impair the quality of life in older adults. Bone adaptation plays a crucial role in maintaining skeletal integrity; however, this dynamic process becomes compromised with age, resulting in an imbalanced remodeling. Understanding the molecular mechanisms that drive bone adaptation in response to mechanical stimuli, and how this process is influenced by aging and differs between sexes, is insufficiently understood. Here, we leverage the Polg$^{D257A/D257A}$ (PolgA) mouse model, exhibiting premature aging, to elucidate the age- and sex-specific responses to mechanical signals during bone adaptation. Furthermore, by coupling spatial transcriptomics analysis, we aim to map gene expression changes that correspond with these age- and sex-dependent responses to mechanical loading. Our research indicated that PolgA mice displayed a multifaceted age-related decline, with male mice showing more pronounced characteristics. While young mice, particularly females, exhibited a robust response to mechanical loading, this adaptive response was absent in aged PolgA mice of both sexes. In addition, young mice displayed increased gene expression levels related to bone formation (*Bglap, Col1a1, Sparc, Tnfrsf11b*), and mechanosensation (*Fgf23, Gja1, Piezo1, Piezo2*) with loading while aged mice exhibited decrease in these gene expressions with a shift towards adipogenesis (*Adipog, Lipe,*

Lpl, Plin1). These findings suggest PolgA mouse as an invaluable tool for studying the effects of age and sex differences on bone adaptation.

Keywords

Mechanoregulation, PolgA mice, premature aging, spatial gene expression, aging, frailty, age-related osteoporosis, sex difference in aging.

133

5.1.1 Introduction

Aging is a complex, multifaceted process characterized by a gradual decline in physiological functions, leading to increased vulnerability to diseases. The key hallmarks of aging include frailty, sarcopenia, and osteoporosis, conditions that notably impair quality of life in older individuals [1-3.]. These conditions manifest differently across age and sex demographics: frailty presents as a syndrome of decreased reserve and resistance to stressors; sarcopenia is characterized by the loss of muscle mass and strength; and osteoporosis is defined by reduced bone mass and density [4-6]. The simultaneous presence of these conditions in older individuals can increase the risk of falls and fractures, emphasizing the need for an in-depth understanding of their underlying mechanism [7, 8].

Mechanoregulation of bone adaptation plays a pivotal role in the aging process because of its essential role in maintaining bone remodeling and health [14, 17, 22-25]. Mechanically driven bone adaptation is a dynamic process, in which bone tissue undergoes remodeling to accommodate mechanical demands and ensure structural efficiency [9-12]. The intricate interplay between the mechanical environment and bone adaptation involves the transduction of mechanical forces into biochemical signals that drive the remodeling process [13-15]. With age, the efficiency of both bone adaptation and mechanosensation declines, leading to alterations in bone remodeling, also resulting in a net loss of bone density and mass, therefore increasing the risk of osteoporosis and fractures in older adults [14, 16-18]. Postmenopausal women are particularly vulnerable due to the drastic decrease in estrogen, a hormone pivotal in preserving bone density, which is critical for maintaining bone mass [19-21]. Although molecular mechanisms that underpin bone adaptation to mechanical stimuli are recognized, how these processes are influenced by age and sex remains poorly understood.

This study aims to investigate age- and sex-specific changes in physical functions and bone adaptation responses to mechanical stimuli by mapping spatially resolved gene expression profiles in prematurely aged PolgA$^{D257A/D257A}$ (PolgA) mice. We employed phenotyping experiments including frailty scoring, grip strength, and gait analysis, followed by time-lapsed *in vivo* mechanical loading and spatial transcriptomics analysis. These comprehensive approaches may lead to the development of strategies to mitigate age-related musculoskeletal decline and improve the quality of life in older populations.

5.1.2 Results

Multifaceted age-related declines in physiological functions of PolgA mice

To characterize the age-related musculoskeletal phenotypes of PolgA mice, body weight, clinical mouse frailty index (FI), forelimb grip strength, and gait analysis were measured at 12, 19, 34, and 42 weeks for both male and female PolgA mice (Figure 5.1A). The chosen time points correlate with the subsequent *in vivo* mechanical loading experiments: 12 weeks marked the beginning while 19 weeks was the completion of the experiments for the young group. In parallel, 34 weeks was the beginning, and 42 weeks indicated the termination of the experiments in the aged cohort.

Analysis of body weight changes indicated an increase until 34 weeks, followed by a significant decline from 34 to 42 weeks for both sexes of PolgA mice (males: -7.4 % and females: -2.6 %), with a particularly greater decrease in males (Figure 5.1B). Concurrently, FI increased with age, indicating a significant increase at 42 weeks (males mean FI: 0.13 ± 0.05 and females mean FI: 0.10 ± 0.04) (Figure 5.1C). Additionally, grip strength decreased in aged (34 and 42 weeks) (males: -13.8% and females: -17.7%) but not in young (12 and 19 weeks) PolgA mice (Figure 5.1D). In parallel, a notable decrease in walking speed from 34 to 42 weeks in PolgA mice was observed for both sexes (males: -27.7% and females: -32.2%) (Figure 5.1E).

Concerning the remaining gait analysis parameters, we observed a pronounced decline in stride length from 34 to 42 weeks for each limb for both males and females (right forelimb (RF): -12.4%, -17.7%, right hindlimb (RH): -12.5%, -21.4% left forelimb (LF): -11,9%, 17.4% and left hindlimb (LH): -23.9%, -18.7% respectively). Likewise, a reduction in swing speed was observed for aged PolgA mice from 34 to 42 weeks (RF: -18.8%, -33.4%, RH: -26.2%, -36.8%, LF: -15,3%, -50.6% and LH: -29.6%, -47.6% for males and females respectively), indicating reduced mobility as they age (Figure 5.S1A). Reduced stride length exhibited that the mice took shorter steps for all paws upon aging, while decreased swing speed indicates that aged PolgA mice moved their limbs slower during the swing phase of locomotion (Figure 5.S1A-B).

Duty cycle is the percentage of the gait cycle that a foot is in contact with the ground [30]. During the period from 34 to 42 weeks, aged male PolgA mice exhibited increased duty cycle in both RF and LF; whereas female mice demonstrated no significant alterations in the duty

cycle for any limb at the defined period (RF: -7.5% and LF: -9.6%). At 42 weeks, an increased duty cycle indicated that aged PolgA mice's feet remained in contact with the ground for longer periods during each step (Figure 5.S1C). This was more pronounced in aged male PolgA mice, who exhibited a greater decline in their physical condition compared to females. However, females displayed substantially greater impairment in their gait. The decreased stride length and swing speed suggest that aged PolgA mice may need to maintain foot contact with the ground longer to ensure stability and prevent falls, indicating a reduction in motor coordination and agility. Overall, these findings align with the clinical manifestations of sarcopenia observed in humans.
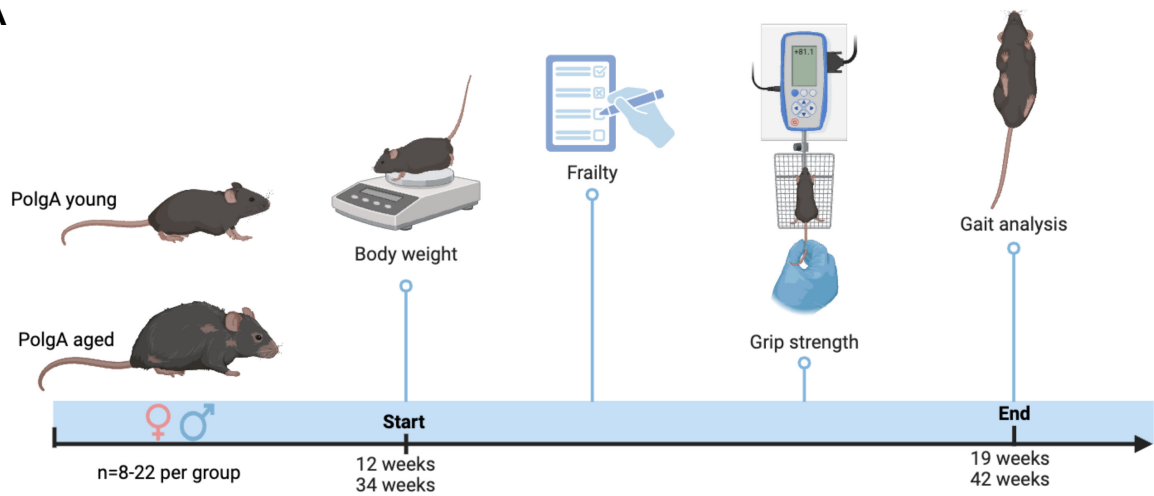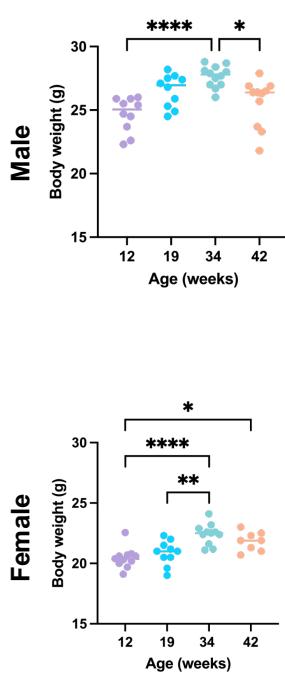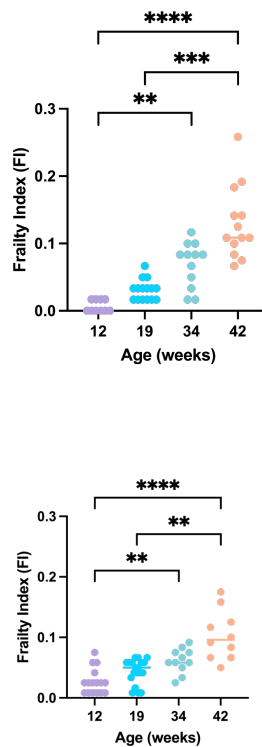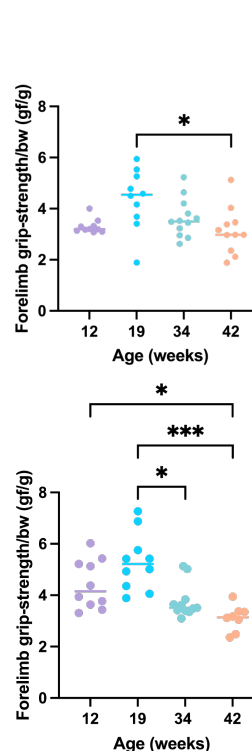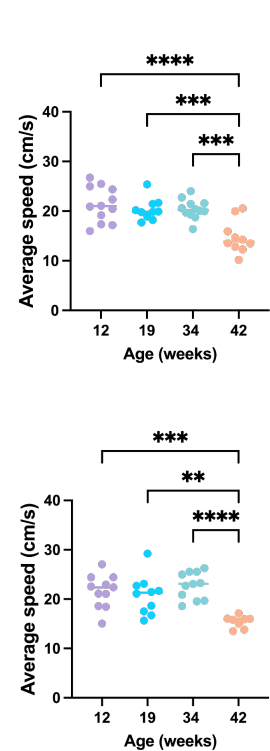
Figure 5.1 Assessing musculoskeletal phenotypes of PolgA mice across different ages and sexes. A) Schematic illustrating the study design for the phenotypic experiments to evaluate B) body weight changes C) frailty index (FI) D) forelimb grip strength E) average walking speed. Box plot represented, (n=9-22 mice/group). Significance was determined by two-way ANOVA by Tukey's corrections, *p<0.05, **p<0.01, ***p<0.001.

Reduced age- and sex-specific bone adaptation to in vivo mechanical loading in PolgA

Given the observed age- and sex-dependent declines in musculoskeletal phenotype in PolgA mice, we utilized an *in vivo* tail-loading model to investigate the alterations in bone mechanoregulation. Longitudinal micro-CT imaging facilitated the assessment of bone adaptation in response to mechanical stimuli across different ages and sexes. This robust approach sheds light on the nuanced alterations in bone mechanoregulation with aging. Within this model, the fifth and seventh caudal vertebrae were pinned, performed at 12 weeks of age for the young and at 34 weeks for the aged cohort, to enable the loading on the sixth caudal vertebra (CV6). Changes in the bone microarchitecture of CV6 from 15 to 19 weeks in young mice and from 38 to 42 weeks in aged mice were monitored, allowing for a detailed observation of bone adaptation over time (Figure 5.1.2).

Bone morphometric analysis revealed significant changes between the initial (week 0) and final time points (week 4) in the static parameters among loaded young PolgA mice compared to their sham counterparts, with particularly notable differences observed in females (Figure 5.2A-D). Young loaded male PolgA mice exhibited an average increase of 8.8% of ΔBV/TV (trabecular bone volume fraction) compared to a 3.3% increase in their sham counterparts. For young loaded females, the ΔBV/TV was notably higher at average 17.9% (p<0.001), highlighting the anabolic impact of mechanical loading, while sham females displayed a 1.8% increase (Figure 5.2A). In contrast, aged mice regardless of sex exhibited negative ΔBV/TV indicating catabolic effects: males (sham: -1.1%, loaded: -0.2%); females (sham: -8.2%, loaded: -5.5%). This increase in ΔBV/TV was accompanied by a significant increase in ΔTb.Th (trabecular thickness), with loaded males experiencing average 6.9% compared to 2.3% increase in their sham counterparts. Similarly, loaded young females exhibited a remarkable 28.4% increase (p<0.0001) in ΔTb.Th compared to a 4.9% increase in young sham females (Figure 5.2B). Conversely, the aged cohort exhibited either no change or decrease in ΔTb.Th upon loading: males (sham: -0.7%, loaded: 0.1%); females (sham: -8.4%, loaded: -4.1%). In addition, ΔTb.N (trabecular number) significantly decreased with a 7.4% (p<0.0001) in young

loaded females compared to sham females with a 2.4% decrease. In contrast, young males displayed 1.2% increase in ΔTb.N in comparison to their sham counterparts with a 0.5% increase (Figure 5.2C). Whereas, loaded aged groups experienced either no change or slight increase in ΔTb.N compared to their sham counterparts: males (sham: -0.1%, loaded: -0.3%); females (sham: 1.3%, loaded: 0.3%). Subsequently, ΔMV (marrow volume) decreased with loading for both young groups as males showing 6.1% decrease (p<0.001) while females indicated 8.2% reduction (p<0.0001) compared to their sham counterparts with 0.0% decrease and 1.7% increase for males and females respectively (Figure 5.2D). In contrast, aged loaded mice experienced a 0.4% decrease in marrow volume compared to their sham counterpart showing 1.9% increase. Likewise, aged, loaded females exhibited 1.8% decrease in comparisons to the sham controls showing 7.4% increase.

Thus, aged mice exhibited deteriorative changes in bone microarchitecture, characterized by sparser, thinner, and more disconnected trabeculae within the trabecular bone. In contrast, younger mice, particularly females, exhibited thicker trabeculae with increased bone volume fraction (BV/TV). Similar findings observed in the cortical bone as well. Thus, these findings highlight an age-related decline in the structural integrity of bone in both sexes.
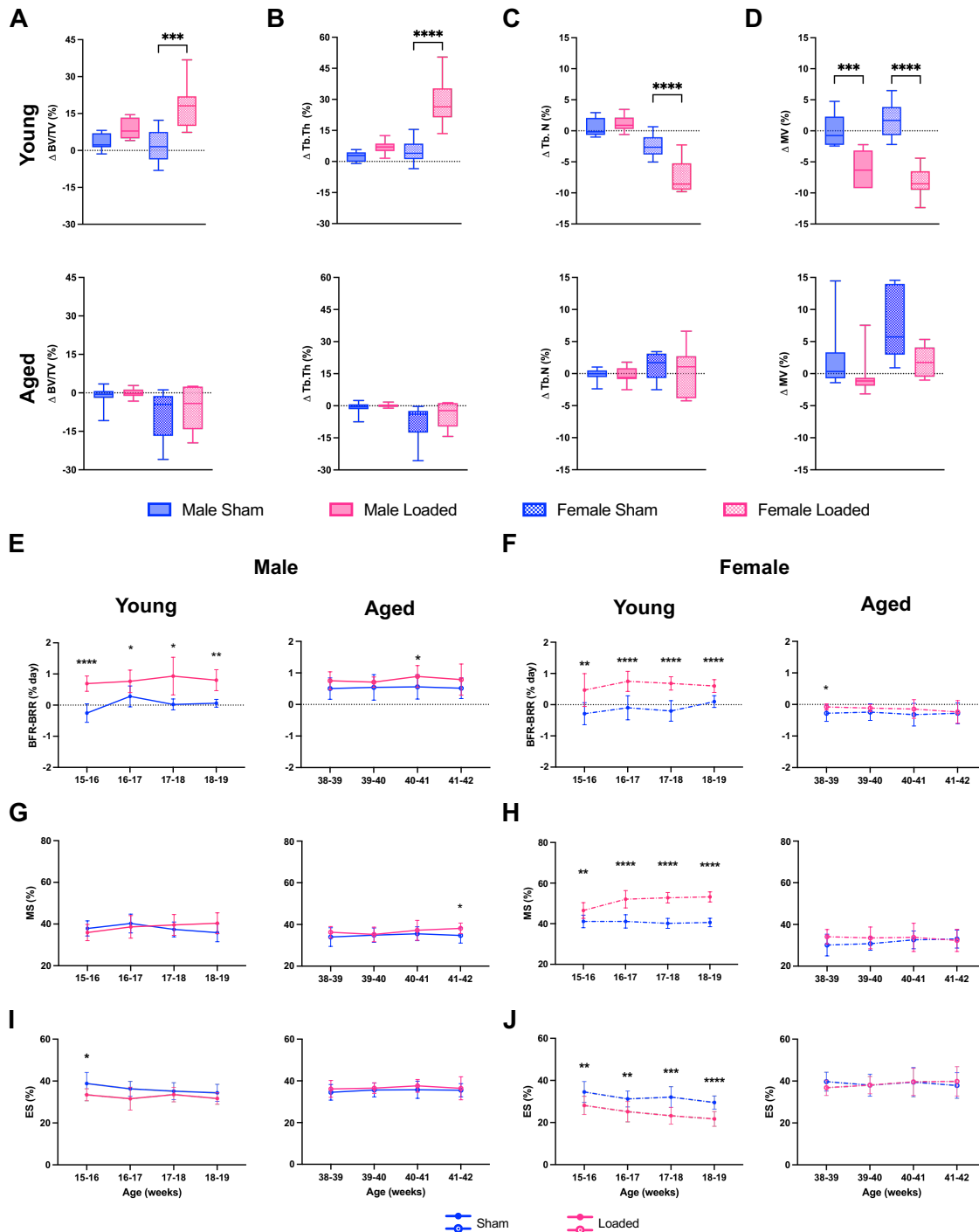
Figure 5.2 Age- and sex-dependent impacts of mechanical loading on bone and bone remodeling dynamics in PolgA mice. A) Changes in the trabecular bone volume fraction (BV/TV) B) trabecular thickness (Tb.Th) C) trabecular number (Tb.N) D) marrow volume (MV) from week 0 to week 4. E-F) Changes in the net remodeling rate were shown as the difference between BFR and BRR over the 4-week loading period, G-H) Changes in the mineralization surfaces (MS), I-J) changes in the eroded surfaces (ES). Data represent mean ± s.d. and are shown as percentages, (n=6-10 mice/group). Statistical significance was determined by two-tailed unpaired t-test and by two-way ANOVA corrected with Sidak's tests, *p<0.05, **p<0.01, ***p<0.001.

139

Age-related decline in bone remodeling in PolgA mice

We quantified the dynamic parameters to elucidate the changes in bone formation and resorption activities using weekly micro-CT images. A representative 3D illustration of a caudal vertebra highlighted the specific sites of bone remodeling activities as formation, resorption, and quiescence. Additionally, the local mechanical signals at these sites were illustrated as effective strains (Figure 5.3A-D). In line with trends observed in static parameters, the most significant changes were detected in the young group. The bone formation rate (BFR) was substantially increased with 0.8% in males and 1.5% in females on average per week compared to the sham-loaded group, showing a 1.1% increase for both sexes. Moreover, mineral apposition rate (MAR), indicating the thickness of formation packages, did not show a significant difference between the loaded and sham-loaded young mice. Conversely, mineralizing surface (MS), indicating the area of the formation sites, was considerably higher in loaded female young mice, with a 51.1% (p<0.0001) increase compared to sham counterparts showing a 40.7% increase. However, there were no distinct differences in MS between the loaded and sham groups of young male mice (Figure 5.2G-H). Regarding bone resorption events, a pronounced increase in bone resorption rate (BRR) was observed in the sham-loaded groups compared to the loaded young mice showing 0.6% and 0.8% increase for males and females respectively, with a significant increase of 1.1% in males and 1.3% in females. Similar to the MAR, the mineral resorption rate (MRR), which reflects the depth of resorption cavities, did not differ significantly between the loaded and sham-loaded young mice in either group. Mechanical loading resulted in a substantial reduction in the surface area of eroded surfaces (ES) among the loaded groups of young female PolgA mice, with a decrease of an average of 24.6% (p<0.0001) compared to an average of 31.8% in the sham group. However, there were no distinct alterations observed between young male loaded and sham groups. (Figure 5.2I-J).

Furthermore, the net remodeling rate (BFR-BRR), representing the difference between bone formation rate (BFR) and bone resorption rate (BRR), revealed a consistent positive remodeling trend in loaded young mice, with a daily increment of 0.79 in males (p<0.01) and 0.62 in females (p<0.0001). Conversely, the sham-loaded mice tend to display a negative remodeling trend, indicative of bone loss for males with a daily increment of 0.02 and -0.12 for females (Figure 5.2E-F).

On the other hand, aged PolgA mice of both sexes exhibited no notable difference in the dynamic bone morphometry parameters which contrast with their younger counterparts. The net remodeling rate (BFR-BRR) in loaded young male mice showed a daily increment of 0.78, while loaded females indicated a decrease of -0.14. In contrast, sham counterparts in young mice displayed a daily increase of 0.52 for males and a decrease of -0.28 for females. Despite minimal changes in the net remodeling rate between the sham and loaded groups among aged mice, aged female PolgA mice exhibited negative values, whereas aged males showed positive values (Figure 5.2E-F).

MAR and MS remained constant over time in aged mice, without significant differences between the loaded and sham groups or across sexes (Figure 5.2G-H). Similarly, MRR and ES, bone resorption indicators, displayed no significant changes over time for aged PolgA mice (Figure 5.2I-J). Collectively, these data indicate that aged PolgA mice did not respond to mechanical loading resulting in reduced bone remodeling and bone turnover with negligible sex-specific differences. In contrast, the young group had an increase in bone formation activities in response to loading with effects being particularly pronounced in female PolgA mice; complementing the findings obtained from static morphometry.
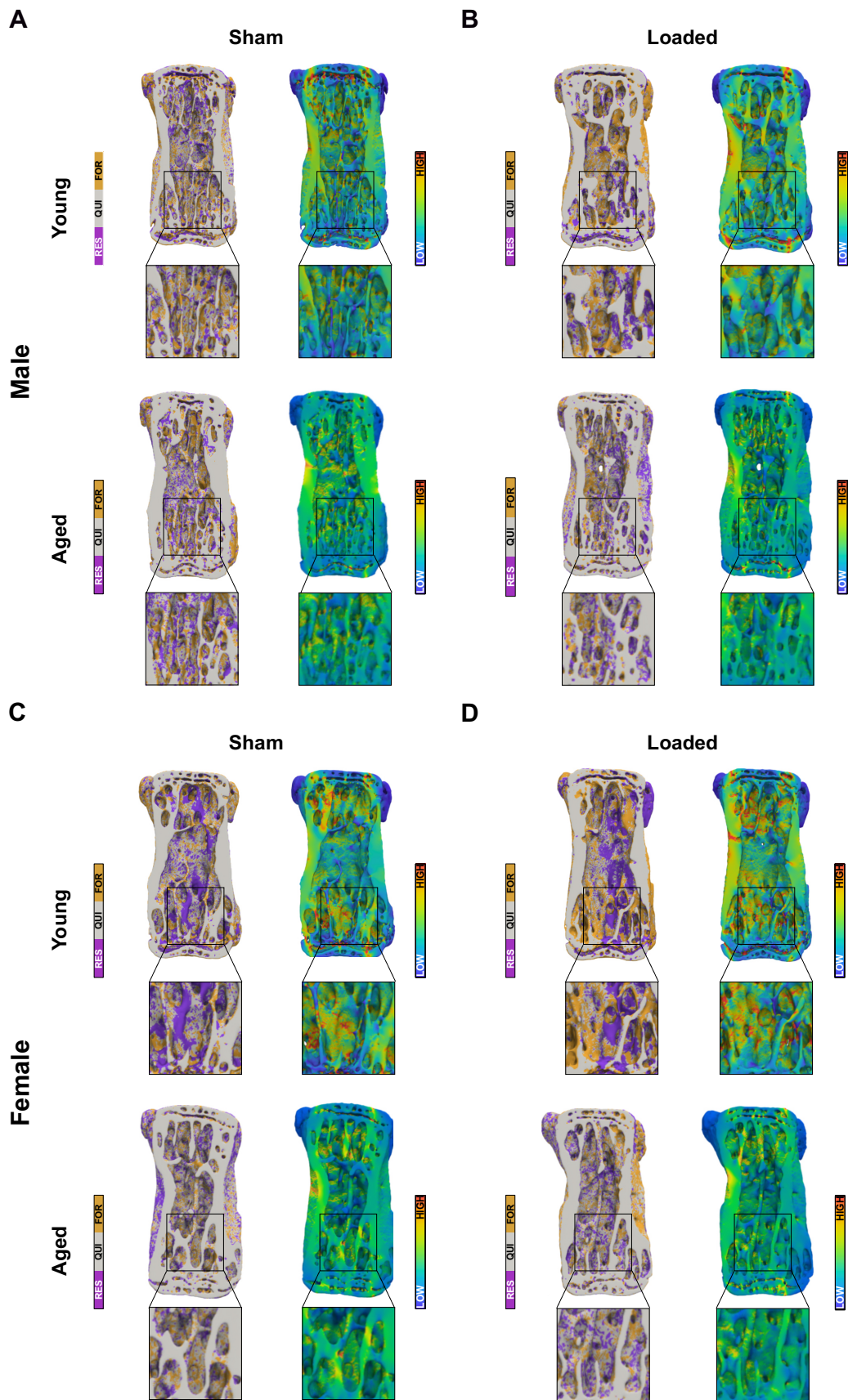
Figure 5.3 Age- and sex-specific mechanically regulated bone remodeling in young and aged, male, and female PolgA mice. Representative 3D micro-CT image of caudal vertebra

indicating bone remodeling sites (formation, quiescence, and resorption) and the corresponding map of the effective strain showing the spatial distribution of mechanical strains as higher and lower strain regions for male (top) and female (bottom), young (upper rows) and aged (lower rows) A-C) sham and B-D) loaded PolgA mice at week 2.

Mapping differential gene expression across age and sex in PolgA mice through spatial transcriptomics analysis

To identify the contribution of the specific gene alterations that correspond with age- and sex-related responses to mechanical loading, we utilized spatial transcriptomics analyses. Regions for the analysis were defined by selecting all spots in the caudal vertebrae and categorizing them as bone (trabecular and cortical bone), bone marrow, muscle and interverbal disc region within each section (Figure 5.3A). In these defined regions, clusters were identified across all areas; however, the primary focus for investigating differential gene expression levels and subsequent comparative analysis was the whole bone region, which encompassed the combined spots in the bone and bone marrow areas (Figure 5.3B).

In the whole bone region 1401 genes from aged female, 2556 genes from aged male, 3408 genes from young female and 2313 genes from young male were identified when comparing sham versus loaded conditions and included in the DEG analysis (FDR-adjusted p value cutoff < 0.1; absolute log2 fold change > 0.5). In the young cohort, there was an upregulation of the genes related to osteoblastogenesis including *Col1a1, Sparc, Spp1, Bglap* while genes linked to osteoclastogenesis such as *Acp5, Ctsk,* and *Mmp9* were downregulated (Figure 5.3C). In contrast, aged mice exhibited the upregulated of adipogenesis-associated genes such as *Adipoq, Lipe, Plin1* alongside a downregulation of osteoclastogenesis-associated genes including *Acp5* and *Ctsk* indicating a shift toward adipogenic rather than osteogenic activity with aging (Figure 5.3C). The spatial distribution of these gene expressions further corroborates these findings, highlighting the patterns of gene expression levels across different age and sex groups in response to mechanical loading (Figure 5.4). Higher expression of osteoblast differentiation and activity markers, such as *Bglap* and *Col1a1*, was observed in response to mechanical loading in young mice, particularly females (Figure 5.4A). Additionally, genes related to osteoclastogenesis (*Nfatc1 and Acp5*) and mechanosensation (*Sost and Fgf11*) were upregulated in the young loaded groups but not in the aged cohort, regardless of sex (Figures 5.4B-C). Conversely, genes associated with adipogenesis, such as *Lipe* and *Adipoq,* were upregulated only in aged mice of both sexes (Figure 5.4D).
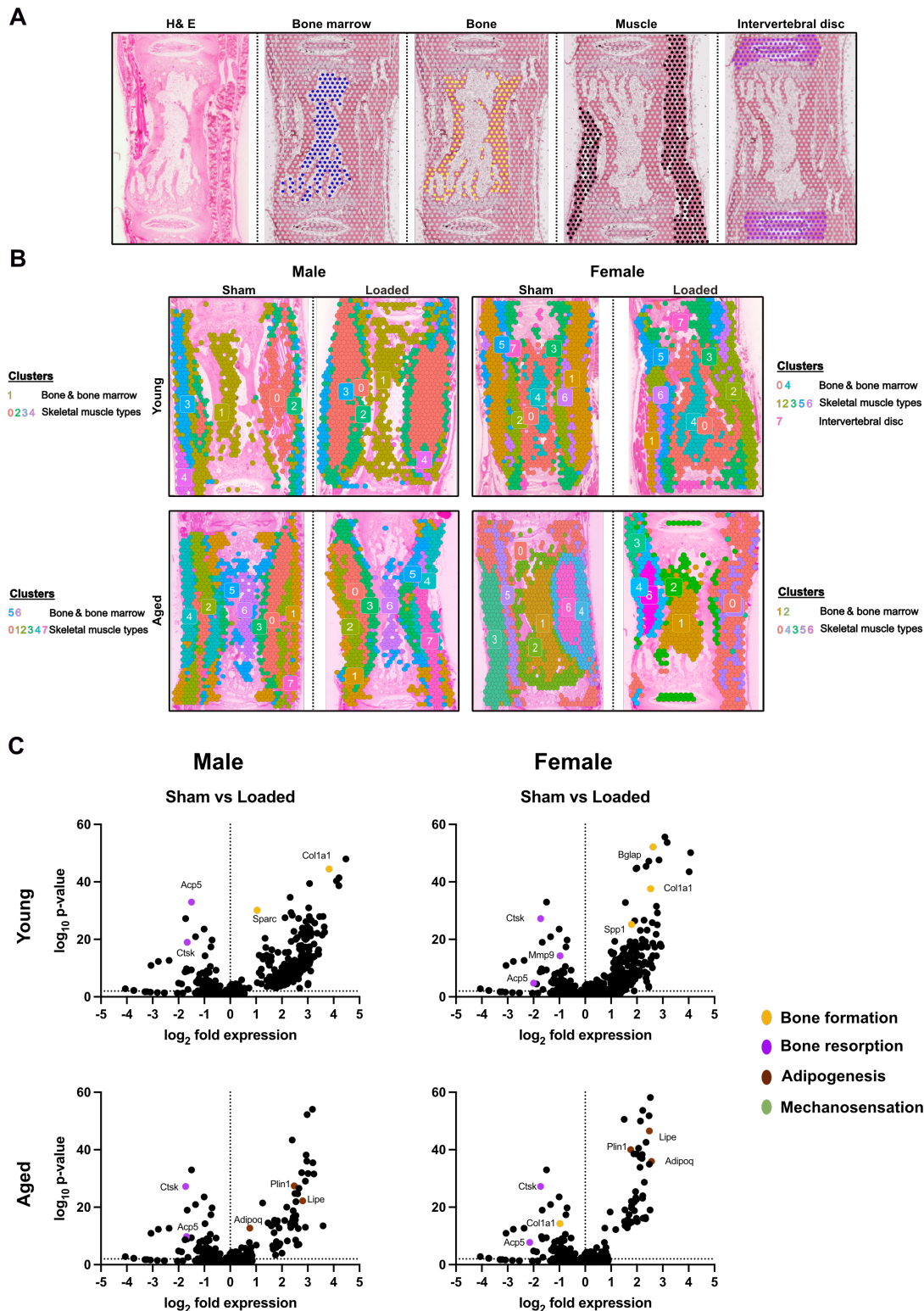
Figure 5.3 Differential gene expression profiling was conducted across young and aged, male and female PolgA mice in both sham and loaded conditions. A) Representative H & E stained CV6 section contains the spatially captured transcriptome and the defined areas of interest: bone marrow, bone, muscle and intervertebral disc regions for the analysis B) Spatial feature plots of H&E-stained sections overlaid with the number of genes per spatial spot showing the

identified clusters for analysis C) Differentially expressed genes (DEGs) were identified based on significance criteria: FDR-adjusted p-value cutoff < 0.1 and an absolute log2 fold change > 0.5. Significant DEGs associated with bone formation are shown as orange, bone resorption in purple, adipogenesis in brown and mechanosensation in green.

Figure 5.S2 Spatial gene expression profiles in response to loading in young and aged, female and male PolgA mice A) Visualization of the spatial expression patterns of genes associated with bone formation *(Col1a1 and Bglap)* B) bone resorption (*Ctsk and Acp5)* C) mechanosensation *(Sost and Fgfr1)* D) adipogenesis *(Lipe and Adipoq)*.

Moreover, we analyzed the expression levels of genes that are indicative of bone formation, resorption, adipogenesis, and mechanosensation, highlighting the variations in gene expression associated with age and sex in response to mechanical loading (Figure 5.5). The bone formation-associated genes *Alpl, Col1a1, Bglap* (osteocalcin) and *Tnfrsf11b* (osteoprotegerin, OPG) were upregulated in response to loading in young mice, while in the aged cohort, these genes were downregulated, indicating age-dependent differences in bone to mechanical cues in aged PolgA mice (Figure 5.5A). Concurrently, genes associated with bone resorption, such as *Ctsk, Acp5, Calcr,* and *Mmp9*, were upregulated in response to mechanical loading as well

in young mice, underscoring their role in promoting resorptive activities within the bone remodeling cycle. However, downregulation of these genes in the aged cohort suggests a diminished responsiveness to mechanical stimuli and indicates a decline in bone turnover with age (Figure 5.5B). In addition, genes that facilitate adipogenesis, such as *Lipe, Plin1, Lpl, and Adipoq,* were upregulated in aged PolgA mice upon loading, suggesting a preferential shift towards adipogenic rather than osteogenic lineages (Figure 5.5C). This inclination towards adipogenic commitment, coupled with the downregulation of osteogenesis-associated genes, further implies that mechanical loading did not promote bone formation in the aged mice. Finally, genes essential to mechanosensation, including *Gja1* (connexin 43), *Fgf23, Piezo1*, and *Piezo2*, were upregulated in young mice, indicating an active mechanotransductive response. Conversely, these genes were minimally expressed or downregulated in aged mice, highlighting a diminished mechanosensory reaction with advancing age (Figure 5.5D). Collectively, the data suggests that young mice exhibited an active bone remodeling response to mechanical loading. On the other hand, aged mice showed a tendency toward adipogenic differentiation over osteogenic activity and exhibited a reduced response to mechanical stimuli.
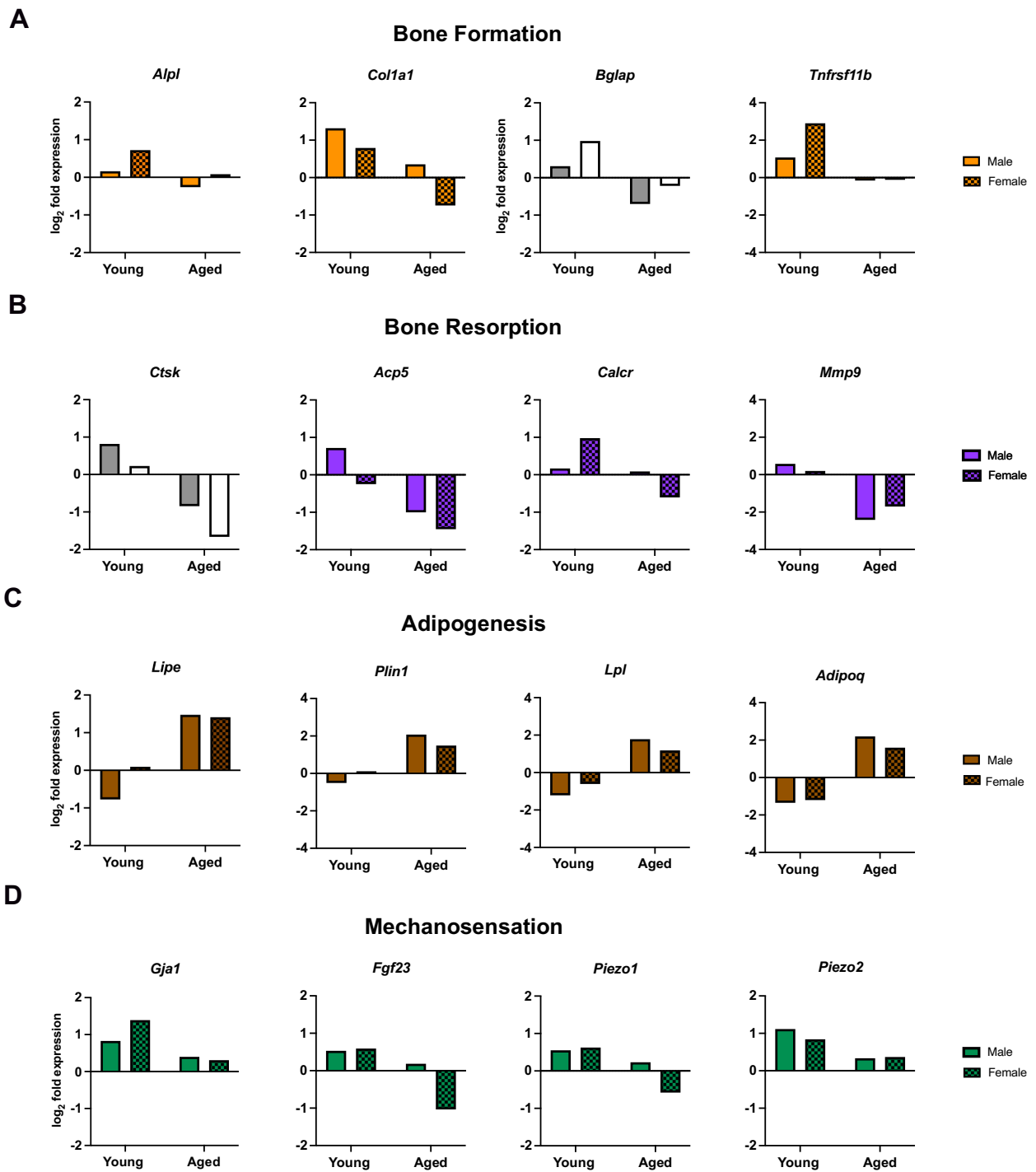
Figure 5.5 Variations in gene expression in response to mechanical stimuli in PolgA mice were analyzed using spatial transcriptomics. A) Gene expression profiling in vertebra associated with bone formation B) bone resorption C) adipogenesis and D) mechanosensation within the whole bone region (trabecular and cortical bone and bone marrow) in both sham and loaded conditions.

5.1.3 Discussion

In this study, we elucidated the complex interplay between age- and sex-specific bone adaptation to mechanical loading and the corresponding spatial gene expression changes in the prematurely aged PolgA mouse model. Our findings illustrated several key points: 1) Age-related decline was multifaced and exhibited a sex-specific disparity with males showing slightly more decrease in physical functions. 2) Young mice, particularly females demonstrated a robust response to mechanical loading, in contrast to aged mice which displayed a blunted response, indicating a reduced mechanosensitivity and a decline in bone turnover with aging regardless of sex. 3) Active remodeling in young mice was also evident from the spatial gene expression associated with bone formation and mechanosensation. In contrast, aged mice displayed a decrease in these genes and showed a shift toward adipogenesis, indicating reduced osteogenic activity in response to mechanical loading.

PolgA mice exhibited various hallmarks of aging over time including body weight loss, increased accumulation of frailty, weakened grip strength and impaired gait. It has been shown that 40-week-old female PolgA mice exhibited mean frailty index (FI) scores of 0.15, which was significantly higher than their age-matched wild-type littermates, who had a mean FI score of 0.06 [29]. Moreover, previous studies have reported that FI of 0.24 for individuals over 65 years of age, while WT mice between 15 to 20 months of age displayed a mean FI score of 0.21 and those older than 20 months exhibited a mean FI of 0.29 [5, 31-37]. In contrast, in our study, male PolgA mice at 42 weeks of age exhibited a mean FI score of 0.15, while female PolgA mice had a slightly lower score of 0.10. We utilized an FI scoring system based on 30 parameters, which yielded lower FI values compared to those quantified with 31 parameters. Despite this difference, the FI scores for PolgA mice potentially align with the range expected for WT mice aged between 15 to 20 months. Among the parameters scored for frailty, the most noticeable changes observed were alterations in fur color from black to brown and the onset of baldness. Furthermore, literature presents mixed results regarding sex differences in frailty, with some studies reporting higher FI scores in female mice, while others found no significant disparities between sexes [32, 34-37]. Our findings align with the notion that signs of aging appear earlier in males than in females [38]. Moreover, the standardized breeding scheme used in our study, which involved a single generation of mutation accumulation, may have resulted in a delayed onset of the accelerated aging phenotype in PolgA mice compared to other studies.

In terms of grip strength, aged PolgA females exhibited a slightly weaker grip, consistent with previous findings, compared to their age-matched male counterparts [39] Additionally, grip strength, a measure of muscle function [29], decreased at 42 weeks for both sexes, which reflect the progressive weakening of the musculoskeletal system consistent with earlier findings [39-41]. Concerning the gait analysis, there was a decline in average speed, stride length, and swing speed, with more pronounced deficits observed in females, indicating an impaired gait associated with aging.

Although frailty quantified in these mice through phenotypic assessment became pronounced at around 40 weeks, confirmed by body weight loss, reduced walking speed, reduced physical activity, and weaker grip strength compared to their age-matched WT littermates [2], these results indicate that PolgA mice underwent a decline in physiological function that mirrors the complex, age-related progression of sarcopenia observed in humans.

Regarding the age- and sex-related changes in bone adaptation and mechanoregulation dynamics in these mice, young female PolgA mice demonstrated a more pronounced anabolic response to mechanical loading compared to their male counterparts, as evidenced by significant increases in trabecular and cortical parameters, BFR, MS and net remodeling rate. These findings, consistent with previous studies, highlight the anabolic effect of mechanical loading in young bones [21-23, 42]. In contrast, aged mice exhibited reduced responsiveness to mechanical loading, with both male and female mice displaying minimal changes in static and dynamic parameters between their respective controls. This could be attributed to the notion that the response of aged bone to mechanical stimuli differ from that of young bone, potentially requiring different magnitudes or loading frequencies for achieving similar effects in bone remodeling. Similarly, because male bones are larger than females, a greater force or higher frequency might be necessary to attain a comparable effect in bone remodeling. In aged PolgA females, the combination of natural hormonal changes due to aging and the accelerated aging phenotype may have contributed to the reduced response to mechanical loading.

The application of spatial transcriptomics in our study has provided a nuanced understanding of the genetic underpinnings that mediate bone adaptation to mechanical cues, highlighting pronounced age and sex differences. Spatial transcriptomics offers distinct advantages over single cell sequencing by maintaining the spatial context of gene expression, crucial for understanding the complex organization of tissues, such as bone [44, 45]. This method allows

for the visualization of gene expression patterns within their native tissue architecture, enabling the study of cellular interactions and the spatial heterogeneity of tissues. Analyses of the defined bone and muscle regions, distinct gene expression profiles were identified. Young mice showed upregulation of osteoblastogenesis-related genes such as *Col1a1, Sparc, Spp1, and Bglap,* and downregulation of osteoclastogenesis-linked genes including *Acp5, Ctsk, and Mmp9*, suggesting increased osteogenic activity in response to mechanical loading, especially in young females. In contrast, aged mice displayed upregulated expression of genes associated with adipogenesis, such as *Adipoq, Lipe,* and *Plin1,* indicating a shift in cellular differentiation from osteogenic to adipogenic pathways with aging.

The decreased response to mechanical loading in aged PolgA mice suggests that aging process may impair the mechanotransduction pathways crucial for bone remodeling [17]. This result aligns with other studies indicating that the downregulation of osteogenic and mechanosensory genes leads to a weakened anabolic response to mechanical stimuli and reduced bone turnover with age [46-48]. Conversely, the upregulation of mechanosensation genes in young mice indicates a robust and responsive mechanotransducive signaling network.

Moreover, age-related decline in bone regeneration may stem from both decreased osteogenic potential and mechanosensitivity of osteoprogenitor cells [17, 49]. Previous studies have demonstrated that aged bones display a reduced ability to increase bone formation in response to mechanical loading due to an age-related decline in the sensitivity of the mechanotransduction pathways and a decrease in the proliferative and differentiative capacity of mesenchymal stem cells (MSCs)[14, 17, 50].

Collectively, utilizing the prematurely aged PolgA mouse model, our study demonstrated that signs of aging manifest earlier in males than in females. Furthermore, mechanical loading induced a robust bone-forming response in young, particularly female mice, while aged mice displayed a decline in this osteogenic reaction, instead exhibiting an increase in adipocyte-related gene expression. These findings suggest that age-specific therapeutic approaches may be necessary to effectively counteract musculoskeletal aging.

5.1.4 Materials and Methods

Animal experiments

All animal experiments were performed in accordance with the local authorities and approved by the Verterinäramt des Kantons Zürich, Zurich, Switzerland (license: ZH36/22). A mouse colony expressing an exonuclease-deficient version of the mitochondrial DNA polymerase γ (PolgAD257A, B6.129S7(Cg)-Polgtm1Prol/J, JAX stock 017341, Jackson Laboratory) was established and maintained at the ETH Phenomics Center (EPIC). The mice were kept under standard conditions, including a 12:12 h light-dark cycle, with access to food and water, and were housed in groups of three to five animals per cage. The mice were bred according to the established breeding protocol and genotyped before the experiments (Transnetyx, Cordova, USA) as described previously [2, 29]. Homozygous PolgA mice and their age- and sex-matched WT littermates (controls) were used for all experiments.

Quantification of frailty index

The Frailty Index (FI) was quantified at 12, 19, 34, and 42 weeks in PolgA mice and their WT littermates for both sexes by employing the mouse FI. This consists of a comprehensive evaluation of 31 non-invasive clinical parameters [29, 34, 51]. Each parameter was assigned a score of 0 for absence, 0.5 for a mild deficit, and 1 for a severe deficit with the exception of body weight and body surface temperature, which were scored relative to the standard deviations from a reference mean in young adult mice (12 weeks old) [52]. Body surface temperature was excluded from the calculation of the FI due to the unavailability of suitable measurement tools.

Grip strength

Grip strength was evaluated using a force tension apparatus (Grip Strength Meter, model 47200, Ugo Basile) at 12, 19, 34, and 42 weeks in female and male PolgA mice and WT littermates as previously described [29]. The mice grasped a stationary bar with their forepaws and were subsequently pulled horizontally by their tail until they released their grip. From the five measurements taken for each mouse, the maximum force (in gram-force) value was recorded and used for the analysis. The same trained operator performed all grip strength measurements.

Gait analysis

Gait analyses were conducted on both female and male PolgA and WT mice at 12, 19, 34, and 42 weeks of age. Noldus CatWalk XT system was utilized to analyze several critical gait parameters including run speed, standing duration, duty cycle, swing phase speed, maximum variation, and stride length to assess the gait characteristics of the mice thoroughly.

Cyclic mechanical loading of the 6th caudal vertebra

Cyclic mechanical loading was applied to the 6th caudal vertebra as previously described [23, 42]. Surgical insertion of stainless-steel pins was performed on the adjacent 5th and 7th vertebrae in 12- and 34-week-old female and male PolgA mice and their WT littermates (young mice n=41, aged mice n=33). Following a three-week recovery from pinning, the mice were divided into control with sham loading (0N) or loaded (8N) with cyclic mechanical loading with a 10Hz frequency for 5 min, three times per week for four weeks.

Analysis of micro-computed tomography images

Mice underwent anesthesia through the administration of isoflurane (induction: 4.5-5%, maintenance: 2-2.5% isoflurane/oxygen) and weekly scanned for 4 weeks using *in vivo* micro-CT (viva CT 80, Scanco Medical AG). The scanning parameters were 10.5 μm resolution, 55 kVp, 145 μA, 350 ms integration time. Micro-CT images from each week were registered with the consecutive time points through an image processing language (IPL Version 5.04c; Scanco Medical AG, Switzerland). Standard and dynamic bone morphometric parameters were evaluated for the trabecular, and cortical bone as described previously [21, 23, 53].

Tissue Sectioning, Visium Library Preparation, and Sequencing

24 hours after the final session of the mechanical loading in the fourth week, all mice were euthanized. Subsequently, spatially resolved transcriptomics analyses were conducted on representative vertebrae from each group (sham n = 1, loaded n = 1) using the CytAssist Visium Spatial Gene Expression platform designed for formalin-fixed paraffin-embedded (FFPE) samples (10x Genomics, Pleasanton, USA). The explanted vertebrae were immediately preserved in 10% neutrally buffered formalin at 4°C for 24 hours, then decalcified with 12.5% EDTA (pH 7.5) for 11 days at the same temperature, processed through a tissue processor, and finally embedded in paraffin. To verify RNA integrity, RNA was extracted from each sample using the Qiagen RNeasy FFPE Kit (Hilden, Germany), and the DV 200 value, indicating the

percentage of RNA fragments exceeding 200 nucleotides, was measured for each sample using Agilent 4200 Tape Station (Waldbronn, Germany). Spatial gene expression analysis was reserved for samples with a greater than 30% DV 200 value, as recommended by the guidelines. Longitudinal sections of 5 μm thickness from each vertebra were positioned on 3D Hydrogel coated slides (Schott Nexterion™ 3-D Hydrogel (H) coated) and then transferred to 11 x 11 mm capture areas of a CytAssist Visium Spatial Gene Expression slide. These sections underwent deparaffinization, staining with hematoxylin and eosin (H&E), imaging, and decrosslinking, all following the protocols provided by 10x Genomics. Probe hybridization completed (10x Genomics, CytAssist Visium Mouse Transcriptome Probe Set v1.0), after which spatial transcriptomics libraries were compiled. Sequencing of these libraries was performed using an Illumina NovaSeq X Plus System (Illumina, San Diego, USA), obtaining a sequencing depth of approximately 26,016 mean reads under tissue per spot per sample.

Spatial transcriptome sequence alignment and data processing

After sequencing, the raw data of Illumina was demultiplexed into fastq files using Space Ranger's pipeline 'mkfastq' (10x Genomics Space Ranger v2.0.0). The tissue section within the fiducial frame (microscopic image) was manually aligned using the Loupe Browser (version 6.3.0 of 10x Genomics Loupe Browser). Following, the raw data alignment was performed using the mouse reference genome, and the generation of spatial feature count matrices were generated with barcode filtering using Space Ranger's 'count' pipeline. The prob set, reference genome, and layout file for the visium slide were downloaded from 10x Genomics (Support/Space Ranger/ Download Center) and used in alignment steps. The counting data were further processed using R (version 4.3.1) with the Seurat package (version 5) [54].

For the downstream analysis, spots containing mitochondrial and ribosomal reads were excluded by filtering each sample separately based on the number of UMIs (nCount_Spatial >= 500) and genes (nFeature_Spatial >= 250). Data were normalized, scaled, and significant variable genes were identified using SC Transform [55]. Dimensionality reduction technique was applied to the dataset and cell clusters were identified (resolution = 0.5). Cell clustering was visualized using uniform manifold approximation and projection for dimension reduction (UMAP). The data was processed in the Euler-Scientific Computing platform from ETH Zurich.

Spatial transcriptomics gene expression analysis

Regions of interest (ROIs) were defined in the Loupe Browser, focusing on the spots in the trabecular and cortical bone, bone marrow, and muscle tissue in H&E-stained histological images. This spot selection area was performed to facilitate the analysis of differentially expressed genes between sham-loaded and mechanically loaded conditions. Differential gene expression analysis was conducted using DESeq2 [56], with scaling normalization performed via deconvolution of size factors using the scran [57]. A likelihood ratio test (LRT) was applied to identify significant genes, with an FDR-adjusted P-value cutoff of <0.1 for each comparison.

Statistical analysis

Data analysis was performed with GraphPad Prism software. Depending on whether the distribution of the data was normal or non-normal, appropriate statistical tests were chosen. Significant differences were determined with Student t-test for the comparison of two variable and two-way ANOVA corrected with Tukey's or Sidak's correction for the comparison of multiple variables. The sample size of 9-22 mice per group was used for bone morphometry whereas 6-10 mice per group was used for morphometric analysis. Data represented as mean ± s.d, and p<0.05 was considered significant. For spatial transcriptomics analysis, a single representative sample per group (1 sham-loaded, 1 loaded) was used.

Acknowledgments

Conflict of Interest

The authors have no conflict of interest to declare.

Author Contributions

References

1.   Yılmaz, D., et al., Mouse models of accelerated aging in musculoskeletal research for assessing frailty, sarcopenia, and osteoporosis - A review. Ageing Res Rev, 2024. 93: p. 102118.

2.   Yılmaz, D., et al., Unveiling Frailty: Comprehensive and Sex-Specific Characterization in Prematurely Aging PolgA Mice. bioRxiv, 2024: p. 2024.02.15.580562.

3.   Almeida, M., Aging mechanisms in bone. Bonekey Rep, 2012. 1.

4.   Walston, J.D., Sarcopenia in older adults. Curr Opin Rheumatol, 2012. 24(6): p. 623-7.

5.   Fried, L.P., et al., Frailty in older adults: evidence for a phenotype. J Gerontol A Biol Sci Med Sci, 2001. 56(3): p. M146-56.

6.   Chandra, A. and J. Rajawat, Skeletal Aging and Osteoporosis: Mechanisms and Therapeutics. Int J Mol Sci, 2021. 22(7).

7.   Greco, E.A., P. Pietschmann, and S. Migliaccio, Osteoporosis and Sarcopenia Increase Frailty Syndrome in the Elderly. Front Endocrinol (Lausanne), 2019. 10: p. 255.

8.   Hirschfeld, H.P., R. Kinsella, and G. Duque, Osteosarcopenia: where bone, muscle, and fat collide. Osteoporos Int, 2017. 28(10): p. 2781-2790.

9.   Birkhold, A.I., et al., Monitoring in vivo (re)modeling: a computational approach using 4D microCT data to quantify bone surface movements. Bone, 2015. 75: p. 210-21.

10.   Cheong, V.S., et al., A novel algorithm to predict bone changes in the mouse tibia properties under physiological conditions. Biomech Model Mechanobiol, 2020. 19(3): p. 985-1001.

11.   Reinholt, F.P., et al., Osteopontin--a possible anchor of osteoclasts to bone. Proc Natl Acad Sci U S A, 1990. 87(12): p. 4473-5.

12.   Robling, A.G. and C.H. Turner, Mechanical signaling for bone modeling and remodeling. Crit Rev Eukaryot Gene Expr, 2009. 19(4): p. 319-38.

13.   Turner, C.H., et al., Mechanobiology of the skeleton. Sci Signal, 2009. 2(68): p. pt3.

14.   Wang, L., et al., Mechanical regulation of bone remodeling. Bone Res, 2022. 10(1): p. 16.

15.   Thompson, W.R., C.T. Rubin, and J. Rubin, Mechanical regulation of signaling pathways in bone. Gene, 2012. 503(2): p. 179-93.

16.   Boskey, A.L. and R. Coleman, Aging and bone. J Dent Res, 2010. 89(12): p. 1333-48.

17.   Javaheri, B. and A.A. Pitsillides, Aging and Mechanoadaptive Responsiveness of Bone. Curr Osteoporos Rep, 2019. 17(6): p. 560-569.

18.   Kanis, J.A., Diagnosis of osteoporosis and assessment of fracture risk. Lancet, 2002. 359(9321): p. 1929-36.

19.   Manolagas, S.C., From estrogen-centric to aging and oxidative stress: a revised perspective of the pathogenesis of osteoporosis. Endocr Rev, 2010. 31(3): p. 266-300.

20.   Ji, M.X. and Q. Yu, Primary osteoporosis in postmenopausal women. Chronic Dis Transl Med, 2015. 1(1): p. 9-13.

21.   Yılmaz, D., et al., Unraveling the Mechano-Molecular Mechanisms of TRAP Activity Using CRISPR/Cas9 Mediated Fluorescent Reporter Mice. iScience, 2023.

22.   Lambers, F.M., et al., Bone adaptation to cyclic loading in murine caudal vertebrae is maintained with age and directly correlated to the local micromechanical environment. J Biomech, 2015. 48(6): p. 1179-87.

23.   Lambers, F.M., et al., Mouse tail vertebrae adapt to cyclic mechanical loading by increasing bone formation rate and decreasing bone resorption rate as shown by time-lapsed in vivo imaging of dynamic bone morphometry. Bone, 2011. 49(6): p. 1340-50.

24.   Schulte, F.A., et al., Local mechanical stimuli regulate bone formation and resorption in mice at the tissue level. PLoS One, 2013. 8(4): p. e62172.

25.   Klein-Nulend, J., R.G. Bacabac, and M.G. Mullender, Mechanobiology of bone tissue. Pathol Biol (Paris), 2005. 53(10): p. 576-80.

26.   Dobson, P.F., et al., Mitochondrial dysfunction impairs osteogenesis, increases osteoclast activity, and accelerates age related bone loss. Sci Rep, 2020. 10(1): p. 11643.

27.   Trifunovic, A., et al., Premature ageing in mice expressing defective mitochondrial DNA polymerase. Nature, 2004. 429(6990): p. 417-23.

28.   Kujoth, G.C., et al., Mitochondrial DNA mutations, oxidative stress, and apoptosis in mammalian aging. Science, 2005. 309(5733): p. 481-4.

29.   Scheuren, A.C., et al., Hallmarks of frailty and osteosarcopenia in prematurely aged PolgA((D257A/D257A)) mice. J Cachexia Sarcopenia Muscle, 2020. 11(4): p. 1121-1140.

30.   Broom, L., et al., Shifts in Gait Signatures Mark the End of Lifespan in Mice, With Sex Differences in Timing. Front Aging Neurosci, 2021. 13: p. 716993.

31.   Fried, L.P., Interventions for Human Frailty: Physical Activity as a Model. Cold Spring Harb Perspect Med, 2016. 6(6).

32.   Parks, R.J., et al., A procedure for creating a frailty index based on deficit accumulation in aging mice. J Gerontol A Biol Sci Med Sci, 2012. 67(3): p. 217-27.

33.   Rockwood, K. and A. Mitnitski, Frailty defined by deficit accumulation and geriatric medicine defined by frailty. Clin Geriatr Med, 2011. 27(1): p. 17-26.

34.   Whitehead, J.C., et al., A clinical frailty index in aging mice: comparisons with frailty index data in humans. J Gerontol A Biol Sci Med Sci, 2014. 69(6): p. 621-32.

35.   Kane, A.E., et al., Sex Differences in Healthspan Predict Lifespan in the 3xTg-AD Mouse Model of Alzheimer's Disease. Front Aging Neurosci, 2018. 10: p. 172.

36.   Scheuren, A.C., G.A. Kuhn, and R. Muller, Effects of long-term in vivo micro-CT imaging on hallmarks of osteopenia and frailty in aging mice. PLoS One, 2020. 15(9): p. e0239534.

37.   Kane, A.E., et al., Impact of Longevity Interventions on a Validated Mouse Clinical Frailty Index. J Gerontol A Biol Sci Med Sci, 2016. 71(3): p. 333-9.

38.   Blagosklonny, M.V., Why men age faster but reproduce longer than women: mTOR and evolutionary perspectives. Aging (Albany NY), 2010. 2(5): p. 265-73.

39.   Fischer, K.E., et al., A cross-sectional study of male and female C57BL/6Nia mice suggests lifespan and healthspan are not necessarily correlated. Aging (Albany NY), 2016. 8(10): p. 2370-2391.

40.   Ge, X., et al., Grip strength is potentially an early indicator of age-related decline in mice. Pathobiol Aging Age Relat Dis, 2016. 6: p. 32981.

41.   Sheth, K.A., et al., Muscle strength and size are associated with motor unit connectivity in aged mice. Neurobiol Aging, 2018. 67: p. 128-136.

42.   Webster, D.J., et al., A novel in vivo mouse model for mechanically stimulated bone adaptation--a combined experimental and computational validation study. Comput Methods Biomech Biomed Engin, 2008. 11(5): p. 435-41.

43.   Windahl, S.H., et al., Estrogen receptor-alpha is required for the osteogenic response to mechanical loading in a ligand-independent manner involving its activation function 1 but not 2. J Bone Miner Res, 2013. 28(2): p. 291-301.

44.   D'Ercole, C., et al., Spatially resolved transcriptomics reveals innervation-responsive functional clusters in skeletal muscle. Cell Rep, 2022. 41(12): p. 111861.

45.   Xiao, X., et al., Spatial transcriptomic interrogation of the murine bone marrow signaling landscape. Bone Res, 2023. 11(1): p. 59.

46.   Corrado, A., et al., Molecular Basis of Bone Aging. Int J Mol Sci, 2020. 21(10).

47.   Nagaraja, M.P. and H. Jo, The Role of Mechanical Stimulation in Recovery of Bone Loss-High versus Low Magnitude and Frequency of Force. Life (Basel), 2014. 4(2): p. 117-30.

48.   Rubin, J., C. Rubin, and C.R. Jacobs, Molecular pathways mediating mechanical signaling in bone. Gene, 2006. 367: p. 1-16.

49.   Fang, H., et al., The Mechanism of Bone Remodeling After Bone Aging. Clin Interv Aging, 2022. 17: p. 405-415.

50.   Roberts, S., et al., Ageing in the musculoskeletal system. Acta Orthop, 2016. 87(sup363): p. 15-25.

51.   Liu, H., et al., Clinically relevant frailty index for mice. J Gerontol A Biol Sci Med Sci, 2014. 69(12): p. 1485-91.

52.   Martinez de Toda, I., et al., Frailty Quantified by the "Valencia Score" as a Potential Predictor of Lifespan in Mice. J Gerontol A Biol Sci Med Sci, 2018. 73(10): p. 1323-1329.

53.   Webster, D., et al., Strain energy density gradients in bone marrow predict osteoblast and osteoclast activity: a finite element study. J Biomech, 2015. 48(5): p. 866-74.

54.   Hao, Y., et al., Integrated Analysis of Multimodal Single-Cell Data. Cell, 2021, 184 (13): p. 3573–3587.

55.   Hafemeister, C., Satija, R., Normalization and Variance Stabilization of Single-Cell RNA-Seq Data Using Regularized Negative Binomial Regression. Genome biology, 2019. *20* (1): p. 296.

56.   Love, M. I., et al., Moderated Estimation of Fold Change and Dispersion for RNA-Seq Data with DESeq2. Genome biology, 2014. 15: p. 1–21.

57.   Lun L., et al., Pooling across Cells to Normalize Single-Cell RNA Sequencing Data with Many Zero Counts. Genome biology, 2016 17: p. 1–14.

Supplementary Material
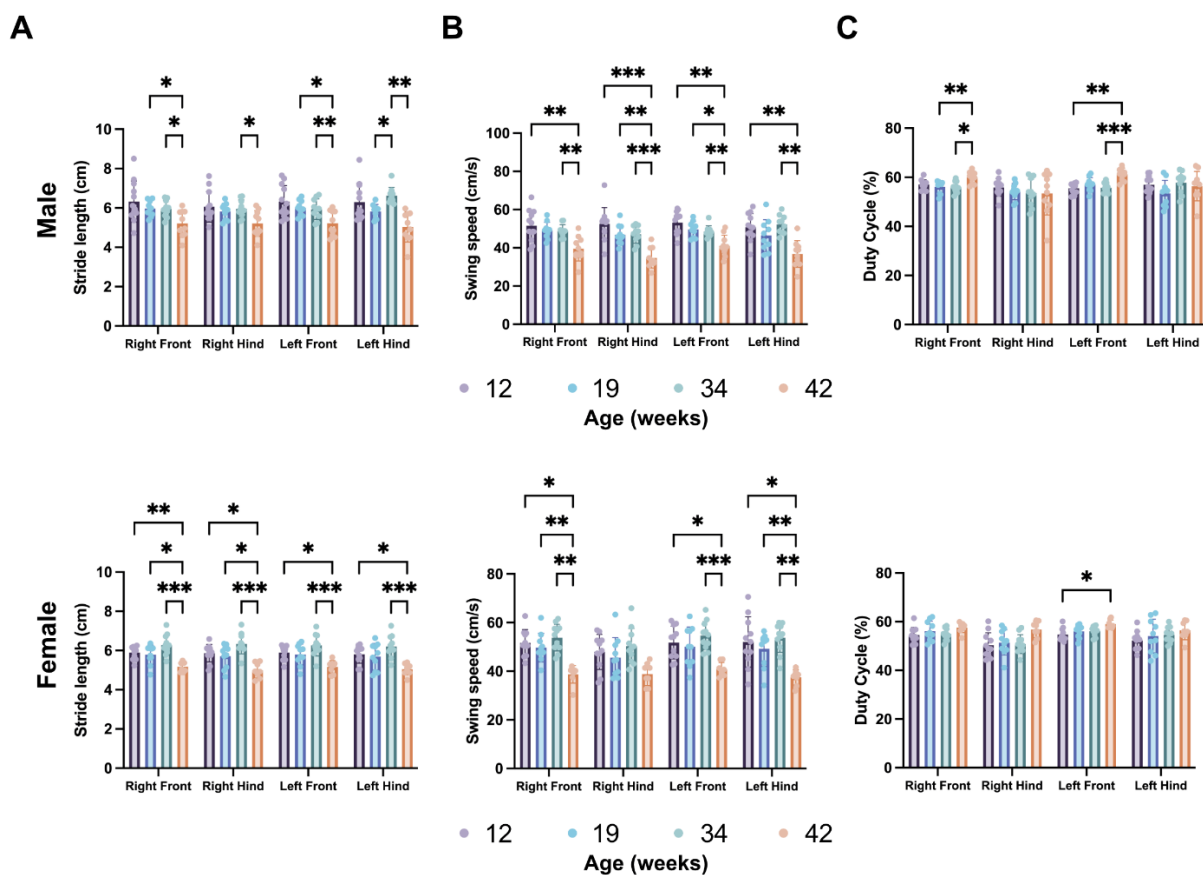
Figure 5.S1 Analysis of the age- and sex-related changes in the gait parameters indicating A) stride length (cm) B) swing speed (cm/s) C) duty cycle (%) for each limb of male and female PolgA mice across different ages. Data represents mean ± s.d, (n=8-12 mice/group). Significance was determined by two-way ANOVA with Tukey's correction, *p<0.05, **p<0.01, ***p<0.001.

Chapter 6

Synthesis

6.1 Background

Aging is a multifaceted process that results in a decline in physiological functions and an increased susceptibility to diseases, with profound implications for the skeletal system [1]. Bone remodeling, a dynamic interplay of bone-resorbing osteoclasts, bone-forming osteoblasts, and osteocytes-the mechanosensors, is essential for maintaining skeletal integrity and adapting to mechanical demands [2-5]. As individuals age, the balance between bone formation and resorption is often compromised, leading to a net loss of bone mass and increased fragility [6]. This imbalance elevates the risk of osteoporosis and associated fractures, with women being more susceptible due to the postmenopausal decline in estrogen levels [7]. On the other hand, mechanoregulation is a process by which the bones adapt to their structure in response to mechanical forces, which is an important factor in preventing age-related bone loss [8, 9]. Adaptive responses of bone to mechanical cues, along with the changes of these responses by aging and sex differences remain insufficiently investigated. Consequently, understanding the molecular mechanisms governing these processes is essential for the development of targeted therapies for age-related osteoporosis and the diseases associated with the impairment in the function of the bone cells. Addressing these concerns requires an in-depth exploration of the dynamics of bone cells within bone adaptation and mechanoregulation, as well as understanding age- and sex- differences, for which current *in vivo* mouse models are insufficient.

In this regard, the objective of this thesis was to elucidate the mechanisms of bone adaptation and mechanoregulation, focusing on osteoclast dynamics and the changes in the age and sex-related responses to mechanical stimuli, using novel *in vivo* mouse models.

First part of this thesis aimed to investigate the role of tartrate-resistant acid phosphatase (TRAP) and osteoclast dynamics in bone adaptation utilizing CRISPR/Cas9 mediated reporter mice. Tartrate-resistant acid phosphatase (TRAP Acp5) is a principal enzyme predominantly located in osteoclasts, playing a critical role in osteoclast differentiation, activation, and proliferation, with its secretion being indicative of resorptive activity [10, 11]. Understanding the involvement of TRAP in bone adaptation and mechanoregulation provides the development of targeted therapeutics for osteoclast-related diseases. By employing CRISPR/Cas9 genome engineering, fluorescent reporter mice with TRAP deficiency were generated, enabling *in vivo* and *in vitro* tracking of the TRAP-deficient osteoclasts. Furthermore, their morphology and

gene expression profiling were characterized through *ex vivo* histological analysis, *in vitro* assays, and RNA sequencing. Given the well-known anabolic effects of mechanical loading on bone [3, 12-14], mechanoregulation in the TRAP-deficient mice was evaluated by combining *in vivo* mechanical loading and *in vivo* micro-CT imaging, thereby linking bone remodeling to the mechanical environment.

For the second part of the thesis, the focus was on prematurely aged PolgA mice to investigate hallmarks of aging in bone. Polg$^{D257A/D257A}$ mouse model (PolgA), characterized by a mutation that induces mitochondrial dysfunction, mimicking accelerated aging with pronounced symptoms such as kyphosis, alopecia, and osteosarcopenia, which occur earlier than those observed in naturally aging mice [15-18]. Although frailty and its link to age-related osteoporosis [1, 19-24], an important hallmark of aging, have been studied in humans and naturally aging mice, they remain understudied in the prematurely aging mouse models. To investigate this hallmark of aging, the frailty characteristics in these mice were assessed using human frailty phenotype approach [25], thereby helping to bridge the gap in our understanding of sex differences and functional performance metrics such as physical activity levels and walking speed.

An understanding of how aging is associated with changes in the osteocyte network may uncover new strategies to prevent age-related osteoporosis in older individuals since the underlying mechanism driving the age- and sex-associated changes in the osteocyte network remains unclear. Therefore, we investigated the age- and sex-related changes in the bone and osteocyte network in prematurely aged PolgA mice. Bone structural differences associated with aging and sex were assessed using micro-CT-based bone morphometric evaluation. Additionally, we employed quantitative *in silico* methods for an in-depth analysis of the osteocyte network in the context of aging. The dendrite tracking method, originally developed for neuron tracing, was adapted to capture detailed information on the deterioration of the osteocyte and their dendrites [26, 27] and the *in silico* connectomics approach assessed the changes in the lacuno-canalicular network (LCN) [28, 29].

After establishing PolgA mice as a prominent model for age-related osteoporosis, we investigated spatially resolved age- and sex-specific alterations in bone mechanomics and mechanoregulation in PolgA mice. Understanding the molecular mechanisms underlying bone adaptation to mechanical stimuli and how these mechanisms are modulated by age and sex is critical for developing therapies to enhance bone health and prevent age-related deterioration.

Utilizing the previously established *in vivo* tail loading model [30] combined with spatial transcriptomics analysis, we evaluated the spatially resolved gene expression changes in response to mechanical loading considering age- and sex-related differences. Additionally, *in vivo* micro-CT imaging [5], permitted longitudinal monitoring of bone adaptation in each mouse, providing insight into the changes in bone architecture due to mechanical loading. Finally, combining i*n vivo* micro-CT imaging with spatial transcriptomics analysis allowed for the visualization of spatial gene profiling alterations in response to mechanical loading, highlighting age- and sex-related differences. This approach also facilitated the investigation of cellular interactions and heterogeneity within the native bone tissue.

6.2 Main findings and implications

This thesis represents a significant advancement in our understanding of bone mechano-adaptation, aging, and sex-specific responses in musculoskeletal health. It elucidates the interplay between cellular dynamics and mechanical stimuli within the aging skeleton using innovative *in vivo* mouse models.

Chapter 2 presents a comprehensive evaluation of four accelerated aging mouse models, which emulate musculoskeletal aging phenotypes related to frailty, sarcopenia, and osteoporosis. These phenotypes mirror those found in both wild-type mice (WT) and humans, substantiating the relevance of the models to the hallmarks of aging. Notably, the PolgA mouse model exhibited early-onset frailty, as well as reduced bone and muscle mass closely resembling human musculoskeletal aging.

Chapter 3 introduces a novel mouse model, generated via CRISPR/Cas9 technology in order to investigate the osteoclast dynamics and TRAP activity during bone remodeling. A serendipitous development within this model allows for *in vivo* and *in vitro* tracking of osteoclasts with TRAP deficiency. Moreover, in line with the anabolic responses observed in loaded WT mice [2, 11-13], [30], these TRAP-deficient mice exhibited a similar anabolic response. Our study showcased the *in vivo* and *in vitro* identification of TRAP-deficient osteoclasts for the first time. Specifically, this study illustrated that gene expression related to osteoclastogenesis remained unaltered despite downregulation of TRAP, thus enabling functional trabecular bone remodeling in a mechanically driven environment in these mice. Additionally, our results indicated that TRAP may not be playing a critical regulatory role in trabecular bone remodeling and adaptation.

Subsequent chapters focused on the prematurely aged PolgA mouse model. Chapter 4 investigated the aging hallmarks in the bone. Although the prematurely aging phenotype characteristics in these mice have already been assessed [15-18], this study was the first to evaluate the frailty phenotype considering sex differences. Our findings demonstrated that frailty became evident around 40 weeks in PolgA mice, validated through body weight loss, reduced walking speed, decreased physical activity, and weaker grip strength compared to their WT littermates at the same age, with aged female PolgA mice exhibiting a trend for higher levels of frailty. The prevalence of frailty in PolgA mice at 40 weeks corresponds with that seen in naturally aging mice and older individuals [19, 32, 33]. These findings deepen our understanding of the onset of frailty and its sex-specific manifestations, underscoring the value of the PolgA model in aging research.

In the following section, Chapter 4.2 addressed the age- and sex-related alterations in bone and particularly osteocyte lacuno-canalicular network (LCN) using the PolgA mouse model. The study indicated that at 40 weeks, PolgA mice exhibited significant impairments in bone structure relative to their age-matched WT littermates and young mice. In particular, our data demonstrated the degeneration of the osteocytes and their dendrites in PolgA mice, more prominently observed in males. At 40 weeks, alterations in bone structure in PolgA mice closely resembled those seen in aged WT mice and older humans, including changes such as decreased cortical thickness and trabecular bone volume fraction (BV/TV) [34-37]. Additionally, age-related alterations in these mice disrupted the osteocyte network, mirroring the changes observed in aged WT mice and humans [38-40]. The deterioration of the osteocyte network, while slightly more observed in aged male PolgA mice, was quantified using IMARIS. This imaging software, originally designed for neuron analysis, was successfully adapted for osteocyte counting and dendrite quantification. Additionally, a new staining technique, tailored for fresh frozen undecalcified bone sections, facilitated the connectomics analysis. This analysis underscored the compromised LCN architecture in aged PolgA mice, with reductions in lacuna density and canaliculi length, akin to those observations in aged mice and older humans [30, 39-41]. Our study showed that the quantification of osteocyte LCN is accurately achievable without the complexities of tedious sample processing or the use of advanced imaging methods. Thus, PolgA mice may be proposed as a model for age-related osteoporosis, as they display key hallmarks of aging, including reduced physical functionality (observed in frailty phenotype) and alterations in bone and bone cells similar to those seen in human aging process.

In the final chapter, Chapter 5, we assessed the age- and sex-specific responses to mechanical stimuli during bone adaptation. Prior to this, we conducted a thorough evaluation of the musculoskeletal aging-related phenotypes in these mice, considering sex-specific differences. This comprehensive analysis provided a complete understanding of the aging signs they exhibit before assessing their response to mechanical loading. Our findings revealed an age-related musculoskeletal decline in PolgA mice, with males showing a slightly more pronounced decrease in physical condition compared to females, aligning with the clinical manifestations of sarcopenia in humans.

The next achievement in this chapter was to evaluate age- and sex-related differences in bone adaptation in response to loading. It was observed that young mice, particularly females displayed a strong response to mechanical loading, while aged mice exhibited reduced response. This indicates a decline in mechanosensitivity and bone turnover with age, regardless of sex. Moreover, active remodeling in young mice was correlated with the upregulation of genes associated with bone formation and mechanosensation. Conversely, aged mice exhibited downregulation of these genes, shifting towards adipogenesis, indicative of a reduced osteogenic response to mechanical loading. These findings significantly demonstrated the spatial, gene-specific responses to mechanical loading while accounting for both sex and age differences. Collectively, our study indicated that the prematurely aged PolgA mouse model could serve as a robust model for elucidating the intricacies of musculoskeletal aging, thereby potentially facilitating the development of age-specific therapeutic approaches to mitigate these effects.

6.3 Limitations and future research

With respect to the limitations and future directions of the thesis, Chapter 2 could include a discussion on murine mouse models of age-related bone loss compared to ovariectomy driven bone loss to provide a more comprehensive overview. Chapter 3 primarily focused on trabecular bone adaptation, highlighting the necessity for a detailed examination of the effects of TRAP deficiency on cortical bone. The RNA sequencing results could be validated with qPCR to confirm the differential regulation of osteoclast target genes and TRAP expression levels. Additionally, the extent to which osteoclasts from BCR[Ibsp/Acp5 mice] can match the fusion process observed in the WT osteoclasts has not been explored, as they were only cultured for four days. Small sample size used in the gene expression analysis affected the statistical power.

Future studies with larger sample sizes are needed to validate and reinforce the findings. A more in-depth analysis of the interaction between osteoblasts and TRAP-deficient osteoclasts is also required for a more thorough understanding of the cellular mechanisms involved and their impact on bone remodeling and mechanosensitivity.

In Chapter 4.1, the small sample size in the study may contribute to non-significant results, affecting the outcomes of frailty prevalence. Our assessment of the frailty phenotype was based on four criteria instead of five, as adopted from the mouse frailty model, which may have altered quantification of the frailty phenotype. Future studies should consider increasing sample sizes and incorporating an endurance test to evaluate exhaustion as a fifth criterion. In Chapter 4.2, the study did not assess changes in lacuna morphology with age and sex, except for lacuna density at 40 weeks. Additionally, the relationship between dendrite degeneration and subsequent bone loss due to osteocyte death was not fully explored. Performing a membrane staining such as Tetramethylindocarbocyanine Perchlorate (Dil) could help with quantifying osteocyte bodies and identifying the osteocytes without dendrites.

For the last chapter (Chapter 5), notable inconsistencies were observed in the frailty outcomes among PolgA mice, contrasting with earlier findings in Chapter 2. Specifically, male PolgA mice were identified as frailer at 42 weeks when evaluated using the Frailty Index (FI) method, whereas PolgA females were observed to be frailer at 40 weeks according to the Frailty Phenotype (FP) method. This could be attributed to the variations in methods since FI reflects cumulative health deficits, whereas the FP assesses functionality, potentially explaining why male mice appeared less functionally frail despite showing more signs of aging. Future studies should consider increasing the sample size and inclusion of all frailty criteria for better quantification of frailty. Moreover, the inclusion of the analysis of the whole-body fat composition by micro-CT scanning could provide the complete musculoskeletal phenotype assessment of PolgA mice.

Another limitation was that aged PolgA mice exhibited reduced response to mechanical loading, in contrast to young mice. Within the young group, male and female mice did not achieve similar bone remodeling effect. Future studies might consider applying different forces or frequencies tailored to each sex and age group. Regarding the spatial transcriptomics analysis, future studies could benefit from increasing the number of histological sections for a more robust statistical analysis. Extending the analysis to include muscle tissues could offer valuable insights into age- and sex-related variations in muscle response to mechanical loading.

Lastly, standardized breeding scheme for PolgA mice used in our studies might lead to a delayed onset of accelerated aging phenotype of these mice.

6.4 Conclusions

In conclusion, this thesis has provided significant insights into the bone mechano-adaptation process by examining osteoclast dynamics using a CRISPR/Cas9-mediated reporter mouse model with TRAP deficiency. It has shed light on the aging hallmarks within bone and osteocytes, while also unveiling intricate age- and sex-specific spatial mechano-adaptive responses in prematurely aged PolgA mice.

Regarding the CRISPR/Cas9 mediated TRAP-deficient mice, findings revealed that bone remodeling and mechanosensation were maintained regardless of TRAP deficiency, despite observed impairments in bone structure and reduced osteoclast function. This suggests that TRAP may not serve as a key regulator within this context, thus broadening our understanding of the role of TRAP in bone remodeling.

Delving into the aging aspect, we identified the frailty phenotype in prematurely aged PolgA mice, characterized by a notable onset of frailty at 40 weeks, particularly pronounced in female mice. This indicates that age-related physiological changes in these mice are equivalent to approximately 27 months in aged WT mice and a 65-year lifespan in humans. Moreover, significant degenerative changes in the bone and osteocyte network were observed at 40 weeks with a greater extent in males.

Furthermore, investigating age and sex-related responses to mechanical loading revealed that young PolgA mice, particularly females, had a stronger response to loading, while aged PolgA mice displayed reduced responses regardless of sex. Coupled with spatial gene expression profiling, this finding indicated that young mice had upregulation of bone formation markers, demonstrating osteogenic responses. In contrast, aged mice illustrated increased adipogenic gene expression, suggesting a shift from an osteogenic to adipogenic fate.

Hence, PolgA mouse model exhibited a multifaceted age-related decline, including frailty and a diminished in physical functionality, slightly more accentuated in males. Furthermore, age

and sex-related deterioration in bone in response to mechanical stimuli, was observed regardless of sex. These collective findings underscore the robustness of the PolgA mouse model in studying the effects of aging on the musculoskeletal system.

This thesis contributes to understanding the relationship between age, sex changes in bone and the underlying cellular mechanism in bone remodeling. It provides foundations for future research and the development of effective interventions aimed at targeted therapeutic approaches in musculoskeletal aging to improve bone health.

References

1.   Fulop, T., et al., Aging, frailty and age-related diseases. Biogerontology, 2010. 11(5): p. 547-63.

2.   Hadjidakis, D.J. and Androulakis, II, Bone remodeling. Ann N Y Acad Sci, 2006. 1092: p. 385-96.

3.   Lambers, F.M., et al., Bone adaptation to cyclic loading in murine caudal vertebrae is maintained with age and directly correlated to the local micromechanical environment. J Biomech, 2015. 48(6): p. 1179-87.

4.   Niedzwiedzki, T. and J. Filipowska, Bone remodeling in the context of cellular and systemic regulation: the role of osteocytes and the nervous system. J Mol Endocrinol, 2015. 55(2): p. R23-36.

5.   Schulte, F.A., et al., Local mechanical stimuli regulate bone formation and resorption in mice at the tissue level. PLoS One, 2013. 8(4): p. e62172.

6.   Raisz, L.G. and E. Seeman, Causes of age-related bone loss and bone fragility: an alternative view. J Bone Miner Res, 2001. 16(11): p. 1948-52.

7.   Vaananen, H.K. and P.L. Harkonen, Estrogen and bone metabolism. Maturitas, 1996. 23 Suppl: p. S65-9.

8.   Fang, H., et al., The Mechanism of Bone Remodeling After Bone Aging. Clin Interv Aging, 2022. 17: p. 405-415.

9.   Javaheri, B. and A.A. Pitsillides, Aging and Mechanoadaptive Responsiveness of Bone. Curr Osteoporos Rep, 2019. 17(6): p. 560-569.

10.   Radzun, H.J., H. Kreipe, and M.R. Parwaresch, Tartrate-resistant acid phosphatase as a differentiation marker for the human mononuclear phagocyte system. Hematol Oncol, 1983. 1(4): p. 321-7.

11.   Ljusberg, J., B. Ek-Rylander, and G. Andersson, Tartrate-resistant purple acid phosphatase is synthesized as a latent proenzyme and activated by cysteine proteinases. Biochemical Journal, 1999. 343(1).

12.   Lambers, F.M., et al., Mouse tail vertebrae adapt to cyclic mechanical loading by increasing bone formation rate and decreasing bone resorption rate as shown by time-lapsed in vivo imaging of dynamic bone morphometry. Bone, 2011. 49(6): p. 1340-50.

13.   Webster, D., et al., Mechanical loading of mouse caudal vertebrae increases trabecular and cortical bone mass-dependence on dose and genotype. Biomech Model Mechanobiol, 2010. 9(6): p. 737-47.

14.   Webster, D.J., et al., A novel in vivo mouse model for mechanically stimulated bone adaptation--a combined experimental and computational validation study. Comput Methods Biomech Biomed Engin, 2008. 11(5): p. 435-41.

15.   Dobson, P.F., et al., Mitochondrial dysfunction impairs osteogenesis, increases osteoclast activity, and accelerates age related bone loss. Sci Rep, 2020. 10(1): p. 11643.

16.   Kujoth, G.C., et al., Mitochondrial DNA mutations, oxidative stress, and apoptosis in mammalian aging. Science, 2005. 309(5733): p. 481-4.

17.   Scheuren, A.C., et al., Hallmarks of frailty and osteosarcopenia in prematurely aged PolgA((D257A/D257A)) mice. J Cachexia Sarcopenia Muscle, 2020. 11(4): p. 1121-1140.

18.   Trifunovic, A., et al., Premature ageing in mice expressing defective mitochondrial DNA polymerase. Nature, 2004. 429(6990): p. 417-23.

19.   Fried, L.P., et al., Frailty in older adults: evidence for a phenotype. J Gerontol A Biol Sci Med Sci, 2001. 56(3): p. M146-56.

20.   Kwak, D., C.W. Baumann, and L.V. Thompson, Identifying Characteristics of Frailty in Female Mice Using a Phenotype Assessment Tool. J Gerontol A Biol Sci Med Sci, 2020. 75(4): p. 640-646.

21.   Liu, H., et al., Clinically relevant frailty index for mice. J Gerontol A Biol Sci Med Sci, 2014. 69(12): p. 1485-91.

22.   Rockwood, K. and A. Mitnitski, Frailty defined by deficit accumulation and geriatric medicine defined by frailty. Clin Geriatr Med, 2011. 27(1): p. 17-26.

23.   Rockwood, K., et al., A global clinical measure of fitness and frailty in elderly people. CMAJ, 2005. 173(5): p. 489-95.

24.   von Zglinicki, T., et al., Frailty in mouse ageing: A conceptual approach. Mech Ageing Dev, 2016. 160: p. 34-40.

25.   Fried, L.P., Interventions for Human Frailty: Physical Activity as a Model. Cold Spring Harb Perspect Med, 2016. 6(6).

26.   Miranda-Angulo, A.L., et al., Rax regulates hypothalamic tanycyte differentiation and barrier function in mice. J Comp Neurol, 2014. 522(4): p. 876-99.

27.   Ando, K., et al., Inside Alzheimer brain with CLARITY: senile plaques, neurofibrillary tangles and axons in 3-D. Acta Neuropathol, 2014. 128(3): p. 457-9.

28.   Kollmannsberger, P., et al., The small world of osteocytes: connectomics of the lacuno-canalicular network in bone. New Journal of Physics, 2017. 19(7).

29. Schurman, C.A., S.W. Verbruggen, and T. Alliston, Disrupted osteocyte connectivity and pericellular fluid flow in bone with aging and defective TGF-beta signaling. Proc Natl Acad Sci U S A, 2021. 118(25).

30. Scheuren, A.C., et al., Mechano-Regulation of Trabecular Bone Adaptation Is Controlled by the Local in vivo Environment and Logarithmically Dependent on Loading Frequency. Front Bioeng Biotechnol, 2020. 8: p. 566346.

31. Dutta, S. and P. Sengupta, Men and mice: Relating their ages. Life Sci, 2016. 152: p. 244-8.

32. Justice, J.N., et al., Comparative Approaches to Understanding the Relation Between Aging and Physical Function. J Gerontol A Biol Sci Med Sci, 2016. 71(10): p. 1243-53.

33. Gabet, Y. and I. Bab, Microarchitectural changes in the aging skeleton. Curr Osteoporos Rep, 2011. 9(4): p. 177-83.

34. Glatt, V., et al., Age-related changes in trabecular architecture differ in female and male C57BL/6J mice. J Bone Miner Res, 2007. 22(8): p. 1197-207.

35. Halloran, B.P., et al., Changes in bone structure and mass with advancing age in the male C57BL/6J mouse. J Bone Miner Res, 2002. 17(6): p. 1044-50.

36. Seeman, E., Age- and menopause-related bone loss compromise cortical and trabecular microstructure. J Gerontol A Biol Sci Med Sci, 2013. 68(10): p. 1218-25.

37. Kobayashi, K., et al., Mitochondrial superoxide in osteocytes perturbs canalicular networks in the setting of age-related osteoporosis. Sci Rep, 2015. 5: p. 9148.

38. Milovanovic, P., et al., Osteocytic canalicular networks: morphological implications for altered mechanosensitivity. ACS Nano, 2013. 7(9): p. 7542-51.

39. Tiede-Lewis, L.M., et al., Degeneration of the osteocyte network in the C57BL/6 mouse model of aging. Aging (Albany NY), 2017. 9(10): p. 2190-2208.

40. Tiede-Lewis, L.M. and S.L. Dallas, Changes in the osteocyte lacunocanalicular network with aging. Bone, 2019. 122: p. 101-113.

Curriculum Vitae

DILARA YILMAZ

Education

05/2019-Present **Doctoral Candidate, ETH Zurich, Zurich, Switzerland**

Institute for Biomechanics, Laboratory for Bone Biomechanics, supervised by Prof. Dr. Ralph Müller

09/2015-10/2017 **M.Sc, Regenerative Biology and Medicine, TU Dresden, Germany**

Thesis: Harvard University, Cambridge, USA

08/2010-06/2015 **B.Sc, Molecular Biology and Genetics, Bilkent University, Turkey**

Thesis: Massachusetts Institute of Technology (MIT), Cambridge, USA

Honors & Awards

2021, 2023 ASBMR Travel Grant (750 USD)

2021, 2023 Runner up for ECTS New Investigator Award

2022 Moderator at ECTS Congress Symposium 3: Mechanobiology session

2021 ECTS Travel Award

2018 Life Science Zurich Graduate School Acceptance (top 5% of applicants)

2017 Promos Scholarship (monthly 500 EUR)

2015-2017 German Scholarship (monthly 300 EUR)

2013-2014 TUBITAK Research Grant (highest money award, 2000 TRY)

2011-2015 Bilkent University Honor & High Honor List

Publications

Yılmaz D, Marques F.C., Fischer Y., Zimmermann S., Hwang G, P. R. Atkins, et al. Elucidating the mechano-molecular dynamics of TRAP activity using CRISPR/Cas9 mediated fluorescent reporter mice. Heliyon 2024, doi: 10.1016/j.heliyon.2024.e32949.

Yılmaz D., Mathavan N., Wehrle E., Kuhn G. A., Müller R., Mouse models of accelerated aging in musculoskeletal research for assessing frailty, sarcopenia, and osteoporosis - a review. Ageing Res Rev., 2023., doi: 10.1016/j.arr.2023.102118.

Original Research Articles in Submission

Yılmaz D., Marques F. C., Gregorio L., Schlatter J., Gehre C., Pararajasingan T., Qiu W., Qin X-H., Wehrle E., Kuhn G. A., Müller R., Age- and sex-specific deterioration of bone and osteocyte lacuna-canalicular network in prematurely aged PolgA mice. Under Review, Bone Research, 2024.

Yılmaz D., Singh A., Wehrle E., Kuhn G. A., Mathavan N., Müller R., Unveiling frailty: comprehensive and sex-specific characterization in prematurely aged PolgA mice. Under Review. Front. Aging., 2024.

Yılmaz D., Mathavan N., Marques F. C., Ledoux C., Boaretti D., Whittier D., Wehrle E., Schädli G. N., Singh A., Kuhn G. A., Müller R., Spatially resolved age- and sex-specific alterations in bone mechanomics and mechanoregulation in prematurely aged PolgA mice. In preparation, 2024.

Conference Proceedings and Abstracts

Yılmaz D., Marques F. C., Boaretti D., Gehre C., Qin X-H., Wehrle E., Kuhn G. A., and Müller. R., Unveiling Age- and Sex-Specific Impairments in Mechanical Adaptation of Prematurely Aged PolgA Mice. Abstracts 51st Annual European Calcified Tissue Society Congress (ECTS 2024), Marseille, France, May 25-28, Bone Rep., accepted, 2024

Yılmaz D., Mathavan N., Marques F.C., Ledoux C., Boaretti D., Whittier D., Wehrle E., Schädli G. N., Kuhn G. A., and Müller R., Spatially Resolved Age- and Sex-Specific Alterations in Bone Mechanomics and Mechanoregulation in Prematurely Aged PolgA Mice. Abstracts ASBMR 2024 Annual Meeting, Toronto, Canada, September 27-30, J. Bone Miner. Res., accepted, 2024

Yılmaz D., Mathavan N., Marques F.C., Ledoux C., Boaretti D., Whittier D., Wehrle E., Schädli G.N., Kuhn G.A., and Müller R., Spatially Resolved Age- and Sex-Specific Alterations in Bone Mechanomics and Mechanoregulation in Prematurely Aged PolgA Mice. Abstracts ISBM 2024 Annual Meeting, Toronto, Canada, October 1-3, accepted, 2024

Marques F. C., **Yılmaz D.,** Schlatter J., Gehre C., Qin X-H., Wehrle E., Kuhn G. A., and Müller R., An automated image pre-processing pipeline to identify lacunar-canalicular networks from FITC-stained confocal microscopy images. Abstracts 51st Annual European Calcified Tissue Society Congress (ECTS 2024), Marseille, France, May 25-28, Bone Rep., accepted, 2024

Yılmaz D., Parajasingam T., Gregorio L., Gehre C., Marques F.C., Mathavan N., Qin X-H., Wehrle E., Kuhn G. A., and Müller R., Prematurely Aged PolgA Mice Exhibit Hallmarks of Frailty and A Disrupted Osteocyte Network. Abstracts ASBMR 2023 Annual Meeting, Vancouver, BC, Canada, October 13-16, J. Bone Miner. Res., accepted, 2023

Yılmaz D., Schlatter J., Marques F.C, Gehre C., Qin X-H., Wehrle E., Kuhn G.A., and. Müller, R., Degenerated 3D osteocyte lacuno-canalicular network in a mouse model of premature aging. Abstracts 50th Annual European Calcified Tissue Society Congress (ECTS 2023), Liverpool, UK, May 15-18, Bone Rep., accepted, 2023

Marques F.C., **Yılmaz D.,** Çakmak G.R., Wehrle E., Kuhn G.A., and Müller. R., Osteocytes identified with 2D high-resolution confocal images can be positioned in their 3D local mechanical environment and associated with tissue-level remodeling events. Abstracts 50th Annual European Calcified Tissue Society Congress (ECTS 2023), Liverpool, UK, May 15-18, Bone Rep., accepted, 2023

Mathavan N., Paul G.R., **Yılmaz D**., Kuhn G.A., Müller R., and Wehrle E., Assessing the use of the PolgA mouse model of premature aging to investigate the effects of aging on bone

fracture healing. Abstracts 50th Annual European Calcified Tissue Society Congress (ECTS 2023), Liverpool, UK, May 15-18, Bone Rep., accepted, 2023.

Yılmaz D., Gregorio L., Gehre C., Whittier D., Qin X-H., Wehrle E., Kuhn G.A., and Müller, R., Prematurely aging PolgA mice display sex-dependent degenerative changes in their osteocyte network. Abstracts ASBMR 2022 Annual Meeting, Austin, USA, September 9-12, J. Bone Miner. Res., accepted, 2022

Marques F.C., Schroeder B., **Yılmaz D.,** Wehrle E., and Müller R., A correlative multimodal imaging approach for multiscale analysis of bone regeneration and adaptation. Abstracts 27th Congress of the European Society of Biomechanics (ESB), Porto, Portugal, June 26-29, accepted, 2022.

Marques F.C., **Yılmaz D.,** Wehrle E., and Müller R., Large-scale quantification of osteocyte morphometry and protein expression from murine bone histology. Abstracts 27th Congress of the European Society of Biomechanics (ESB), Porto, Portugal, June 26-29, accepted, 2022.

Yılmaz D., Marques F.C., Wehrle E., Kuhn G.A., and Müller. R., Mechanoregulation of CRISPR/Cas9 mediated bone cell reporter mice under cyclic mechanical loading. Abstracts 27th Congress of the European Society of Biomechanics (ESB), Porto, Portugal, June 26-29, accepted, 2022.

Mathavan N., McLennan C., **Yılmaz D.,** Kuhn G.A., Wehrle E., and Müller R., Analyzing gait adaptations to surgically induced fractures in young and old mice. Abstracts 23rd Annual Alberta Biomedical Engineering Conference, Banff, Canada, October 21-22, p. 99, 2022.

Yılmaz D., Fischer Y., Zimmermann S., Hwang G., Müller R., and Wehrle E., CRISPR/Cas9 mediated dual fluorescent reporter mice to study spatial bone genomics of osteoblasts and osteoclasts in the local in vivo environment. Abstracts 48th Annual European Calcified Tissue Society Congress (ECTS 2021), Online, May 6-8, Bone Rep., accepted, 2021.

Mathavan, N., Wehrle, E., Paul, G., **Yılmaz D.,** Kuhn G.A., and Müller. R., Individualized cyclic mechanical loading enhances the regenerative response of bone in a mouse model of aging. Abstracts 26th Congress of the European Society of Biomechanics (ESB), Online, Milan, Italy, July 11-14, accepted, 2021.

Yılmaz D., Marques F.C., Wehrle E., Kuhn G.A., and Müller R., CRISPR/Cas9 mediated dual fluorescent reporter mice response to in vivo mechanical loading. Abstracts ASBMR 2021 Annual Meeting, San Diego, USA, October 1-4, J. Bone Miner. Res., 37(S1):206-206, 2021.

Yılmaz D., Gregorio L., Gehre C., Wehrle E., Qin X-H., Kuhn G.A., and Müller. R., Prematurely aging male PolgA mice display structural and cellular hallmarks of senile osteoporosis. Abstracts ASBMR 2021 Annual Meeting, San Diego, USA, October 1-4, J. Bone Miner. Res., 37(S1):209-209, 2021. 683.

Mathavan, N., Paul G.R., Marques F.C., **Yılmaz D.,** Kuhn G.A., Wehrle E., and Müller R. Individualized cyclic mechanical loading significantly augments the regenerative response of bone in a mouse model of premature aging. Abstracts ASBMR 2021 Annual Meeting, San Diego, USA, October 1-4, J. Bone Miner. Res., 37(S1):339-340, 2021.

Yılmaz D., Fischer Y., Müller R., and Wehrle E., Genotypic and phenotypic characterization of CRISPR/Cas9 mediated fluorescent osteoclast reporter mice. Abstracts ASBMR 2020 Annual Meeting, Online, J. Bone Miner. Res., 35(1):267, 2020.